

2011

A numerical and experimental study of in-situ NO formation in laminar NH₃-seeded syngas diffusion flames

Miao Li
Iowa State University

Follow this and additional works at: <https://lib.dr.iastate.edu/etd>

 Part of the [Mechanical Engineering Commons](#)

Recommended Citation

Li, Miao, "A numerical and experimental study of in-situ NO formation in laminar NH₃-seeded syngas diffusion flames" (2011).
Graduate Theses and Dissertations. 10434.
<https://lib.dr.iastate.edu/etd/10434>

This Dissertation is brought to you for free and open access by the Iowa State University Capstones, Theses and Dissertations at Iowa State University Digital Repository. It has been accepted for inclusion in Graduate Theses and Dissertations by an authorized administrator of Iowa State University Digital Repository. For more information, please contact digirep@iastate.edu.

A numerical and experimental study of *in-situ* NO formation
in laminar NH₃-seeded syngas diffusion flames

by

MIAO LI

A dissertation submitted to the graduate faculty
in partial fulfillment of the requirements for the degree of

DOCTOR OF PHILOSOPHY

Major: Mechanical Engineering

Program of Study Committee:
Terrence R. Meyer, Major Professor
Song-Charng Kong
Hui Hu
Rodney O. Fox
Gap-Yong Kim

Iowa State University

Ames, Iowa

2011

Copyright © Miao Li, 2011. All rights reserved.

To my parents, my wife and my daughter

TABLE OF CONTENTS

LIST OF TABLES	vii
LIST OF FIGURES	viii
ACKNOWLEDGEMENTS	xvi
ABSTRACT	xvii
CHAPTER 1: INTRODUCTION	1
1.1 BACKGROUND	1
1.2 PLANAR LASER INDUCED FLUORESCENCE	4
1.3 MOTIVATION	8
1.4 OBJECTIVES	9
1.5 OUTLINE	10
CHAPTER 2: LITERATURE REVIEW	12
2.1 NO FORMATION MECHANISM	12
2.1.1 THERMAL NO	13
2.1.2 PROMPT NO	13
2.1.3 FUEL NO	15
2.1.4 NO FORMATION VIA N ₂ O	16
2.1.5 NO FORMATION VIA NO ₂	16
2.1.6 NO FORMATION VIA NNH	17
2.2 PLIF APPLICATION IN NO DETECTION	17

2.3 NH₃ DOPANT EFFECT	21
2.4 CHEMICAL KINETICS COMPARISON	24
2.5 NO EMISSION OF SYNGAS DIFFUSION FLAMES	29
2.6 SYNGAS COMPOSITION EFFECTS	30
CHAPTER 3: EXPERIMENTAL SETUP	32
3.1 LASER DIAGNOSTICS SETUP	33
3.1.1 BURNER SETUP	34
3.1.2 FLOW CONTROL SYSTEM	35
3.1.3 LASERS	36
3.1.4 LASER SHEET FORMING	38
3.1.5 DETECTION OPTICS	38
3.1.6 OPTICAL ACCESS	40
3.1.7 DATA COLLECTION SYSTEM	41
3.2 OH-PLIF SETUP	42
3.3 NO-PLIF SETUP	43
3.4 CALIBRATION	45
3.5 FLOW CONDITIONS	46
3.6 DATA PROCESSING	49
3.6.1 2-D OH- AND NO-PLIF IMAGING	49
3.6.2 DATA PROCESSING AND REDUCTION	51
3.7 SELECTION OF EXCITATION STRATEGIES	53
3.7.1 EXCITATION SCHEMES FOR OH-PLIF	53
3.7.2 EXCITATION SCHEMES FOR NO-PLIF	55
3.8 SUMMARY	57

CHAPTER 4: CHEMICAL KINETICS MODELING	59
4.1 GOVERNING EQUATIONS	62
4.2 CHEMICAL KINETICS	64
4.3 THERMODYNAMICS AND TRANSPORT PROPERTIES	65
4.4 BOUNDARY CONDITIONS	66
4.5 CONTROL VOLUME AND FINITE DIFFERENCE SCHEMES	69
4.6 NUMERICAL PROCEDURE	72
4.7 THERMAL RADIATION MODEL	73
4.8 GRID SIZE	74
4.9 PHYSICAL MODEL	76
4.10 DEPENDENCE OF INLET TEMPERATURE	77
4.11 SUMMARY	79
CHAPTER 5: RESULTS: LAMINAR CH₄/AIR DIFFUSION FLAMES	80
5.1 OH PROFILES: COMPARISON OF EXPERIMENTAL AND SIMULATED PLIF SIGNALS	81
5.2 MECHANISM COMPARISON FOR OH PROFILES (GRI-MECH 3.0 VS. TIAN ET AL.)	86
5.3 NO-PROFILES: COMPARISON OF EXPERIMENTAL AND SIMULATED SIGNALS	90
5.4 MECHANISM COMPARISON FOR NO PROFILES (GRI-MECH 3.0 VS. TIAN ET AL.)	95
5.5 RELATIVE CONTRIBUTION OF NO FORMATION SUB-MECHANISMS	101
5.6 SUMMARY	104
CHAPTER 6: RESULTS: LAMINAR SYNGAS DIFFUSION FLAMES	106
6.1 OH PROFILES: COMPARISON OF EXPERIMENTAL AND SIMULATED PLIF SIGNALS	107
6.2 NO PROFILES: COMPARISON OF EXPERIMENTAL AND SIMULATED SIGNALS	114

6.3 MECHANISM COMPARISON FOR OH PROFILES (GRI-MECH 3.0 VS. TIAN ET AL.)	124
6.4 EFFECTS OF SYNGAS COMPOSITION WITH VARIOUS LEVELS OF NH₃ SEEDING	129
6.5 RELATIVE CONTRIBUTION OF NO FORMATION SUB-MECHANISMS	144
6.6 SUMMARY	160
CHAPTER 7: CONCLUSIONS AND RECOMMENDATIONS FOR FUTURE WORK	163
7.1 CONCLUSIONS	163
7.2 RECOMMENDATIONS FOR FUTURE WORK	165
REFERENCES	167
APPENDIX A: ERROR ANALYSIS	181
APPENDIX B: DETAILED REACTION PATHWAYS OF TIAN MECHANISM	189

LIST OF TABLES

Table 2-1: Fraction contributions of thermal NO and prompt NO mechanisms to total NO formation in different flames.	15
Table 3-1: Hardware and settings used for OH-PLIF measurements.	43
Table 3-2: The hardware and setting used for NO-PLIF measurements.....	44
Table 3-3: Flow rates for methane/air diffusion flames at atmospheric pressure.	47
Table 3-4: Flow rates for syngas diffusion flames at atmospheric pressure.....	48
Table 4-1: Variable ϕ , transport coefficients and source terms in governing equations. .	62
Table 5-1: Percentages of NO sub-mechanisms in CH ₄ /air flames with 0% and 1% NH ₃ doped for the first and second peaks in Fig. 5-15.....	104
Table 6-1: Percentage contributions of NO sub-mechanisms to peak(s) of XNO along centerlines of flames.....	154
Table 7-1: Relative contributions of NO sub-mechanisms.....	165

LIST OF FIGURES

Figure 1-1: Diffusion flame structure.....	2
Figure 1-2: Laminar premixed flame (left) and diffusion flame (right) from a tube burner. 4	4
Figure 2-1: A simple Planar Laser-Induced Fluorescence (PLIF) configuration.....	18
Figure 2-2: NH ₃ Oxidation mechanism, reproduced from [32]	23
Figure 3-1: Schematic of general PLIF experimental setup.	33
Figure 3-2: Schematic of a laminar diffusion flame from a tube burner.....	35
Figure 3-3: A typical arrangement for dye lasers	36
Figure 3-4: Typical field of view. The camera is able to see about 6.5 cm height above the burner tube, which is denoted by the two little triangles at the bottom. The central part of the camera chip is avoided due to damage on the detector.....	41
Figure 3-5: Schematic of OH-PLIF setup.....	42
Figure 3-6: Schematic of NO-PLIF setup.....	44
Figure 4-1: Evolution of temperature, OH concentration, and NO concentration in a H ₂ /air jet diffusion flame at axial location 80 mm above nozzle exit. Contour table is given at the top.....	60
Figure 4-2: Detailed boundary conditions in the simulations.	67
Figure 4-3: Schematic diagrams of the FVM/FDM schemes, courtesy of Katta et al. [94]. 70	70
Figure 4-4: Temperature profiles along the "axisymmetric axis" boundary.	75
Figure 4-5: A comparison of 2-D temperature distribution, which shows that the temperature distributions are almost identical within the domain.	75
Figure 4-6: A schematic of the physical domain and grids used in the simulations.....	77
Figure 4-7: Top: Simulated OH-PLIF signal; Bottom: Temperature profile in case of different inlet temperature.	78

- Figure 5-1: Experimental (left) and simulated (right) OH fluorescence signal of CH₄/air laminar diffusion flames without NH₃. The physical domain covers horizontally from the centerline to 0.03m and axially from zero to 0.06m above the tube exit. This simulation was performed with GRI-Mech 3.0.....82**
- Figure 5-2: Experimental OH-PLIF images with different amounts of NH₃ seeding.84**
- Figure 5-3: Experimental (left) and computational (right) OH profile of CH₄/air laminar diffusion flames with 40 vol% NH₃. CFD result incorporates the detailed chemical kinetics using GRI-Mech 3.0.....85**
- Figure 5-4: Simulated fluorescence signal with NH₃ seeding level ranging from 0.0% to 40%. The simulated signal does not show any fluctuation.....86**
- Figure 5-5: Comparison of simulated centerline temperature profiles for laminar diffusion flames with different amounts of NH₃ seeding using GRI-Mech 3.0 mechanism (top) and Tian mechanism (bottom). Horizontal axis is the distance from fuel nozzle, and vertical axis is the temperature. Only the temperature profiles at the centerlines are plotted for ease of comparison.87**
- Figure 5-6: Comparison of simulated centerline OH mole fraction profiles for laminar diffusion flames with different amounts of NH₃ seeding using GRI-Mech 3.0 mechanism (top) and Tian mechanism (bottom). Only OH mole fraction profile in each flame centerline is plotted for ease of comparison.....89**
- Figure 5-7: A premixed CH₄/air calibration flame. Horizontal axis is the seeded NO concentration in ppm and vertical axis is the signal intensity in arbitrary units.....91**
- Figure 5-8: Experimental 2-D NO-PLIF signals in CH₄/air diffusion flames with different amounts of NH₃ seeding.92**
- Figure 5-9: Comparison between 2-D NO-PLIF signal and 2-D simulated NO fluorescence signal in CH₄/air diffusion flame with 100-ppm NH₃ seeding.92**

- Figure 5-10: Experimental (left) and computational (right) NO fluorescence signal of CH₄/air laminar diffusion flames with 1000-ppm NH₃ doping. CFD simulation was performed using GRI-Mech 3.0 mechanism.94**
- Figure 5-11: Experimental (left) and computational (right) NO fluorescence signal of CH₄/air laminar diffusion flames with 20 vol% NH₃ seeding. CFD simulation was performed using GRI-Mech 3.0 mechanism.95**
- Figure 5-12: Comparison of measured and simulated NO concentration in the centerline of CH₄/air diffusion flames doped with 100-ppm NH₃. Green lines for GRI-Mech 3.0 mechanism. Blue lines for Tian mechanism97**
- Figure 5-13: Comparison of measured and simulated NO concentration in the centerline of CH₄/air diffusion flames doped with 1000-ppm NH₃. Green lines for GRI-Mech 3.0 mechanism. Blue lines for Tian mechanism97**
- Figure 5-14: Comparison of measured and simulated NO concentration in the centerline of CH₄/air diffusion flames doped with 20 vol% NH₃. Green lines for GRI-Mech 3.0 mechanism. Blue lines are for Tian mechanism.....98**
- Figure 5-15: Comparison of simulated centerline NO mole fraction profiles for laminar diffusion flames with different amounts of NH₃ seeding by GRI-Mech 3.0 mechanism (top) and by Tian mechanism (bottom).100**
- Figure 5-16: Relative contributions of NO-sub-mechanisms in CH₄/air diffusion flames without NH₃ seeding. CFD simulation was performed using GRI-Mech 3.0 mechanism.102**
- Figure 5-17: Relative contributions of NO-sub-mechanisms in CH₄/air diffusion flames with 1 vol% NH₃ seeding. CFD simulation was performed using GRI-Mech 3.0 mechanism.103**

Figure 5-18: Relative contributions of NO-sub-mechanism in CH₄/air diffusion flames with 1 vol% NH₃ seeding. CFD was performed using Tian mechanism.....	103
Figure 6-1: Experimental (left) and computational (right) OH profile of syngas diffusion flames without NH₃ seeding. CFD simulation was performed using Tian's mechanism.	110
Figure 6-2: Experimental OH-PLIF images from 0% to 50% NH₃ seeding.	111
Figure 6-3: Simulated OH-PLIF images from 0% to 50% NH₃ seeding.....	112
Figure 6-4: Experimental (left) and computational (right) OH profile of syngas laminar diffusion flames with 50% NH₃. CFD simulation was performed using Tian's mechanism.	113
Figure 6-5: Experimental 2-D NO-PLIF signals with different amounts of NH₃ seeding. Since these laminar diffusion flames are symmetric, only halves on left are shown.....	115
Figure 6-6: Experimental (left) and computational (right) NO profile of syngas laminar diffusion flames without NH₃. CFD simulation was performed using Tian mechanism.	117
Figure 6-7: Experimental (left) and computational (right) NO profile of syngas laminar diffusion flames with 1% NH₃. CFD simulation was performed using Tian mechanism.	118
Figure 6-8: Experimental (left) and computational (right) NO profile of syngas laminar diffusion flames with 30% NH₃. CFD simulation was performed using Tian's mechanism.	119
Figure 6-9: Comparison of absolute NO concentration in centerline un-doped flames with CFD. Green lines for GRI-Mech 3.0 mechanism. Blue lines for Tian mechanism	121

- Figure 6-10: Comparison of measured NO concentration in centerline 1% NH₃ flames with CFD. Green lines use GRI-Mech 3.0 mechanism. Blue lines use Tian mechanism.122**
- Figure 6-11: Comparison of measured NO concentration in centerline with 30% NH₃ doped flames with CFD. Green lines for GRI-Mech mechanism. Blue lines for Tian mechanism123**
- Figure 6-12: Comparison of simulated centerline temperature profiles for laminar syngas (45% H₂, 45% CO, 10% CH₄) diffusion flames with various amounts of NH₃ seeding by two mechanisms. X axis is the axial distance from fuel nozzle, and Y axis is the temperature.126**
- Figure 6-13: Comparison of simulated centerline OH mole fraction profiles for laminar syngas (45%H₂, 45%CO, 10% CH₄) diffusion flames with different amounts of NH₃ seeding using GRI-Mech 3.0 mechanism (top) and by Tian mechanism (bottom). ..127**
- Figure 6-14: Comparison of simulated centerline NO mole fraction profiles for laminar (45% H₂, 45% CO, 10% CH₄) syngas diffusion flames with different amounts of NH₃ seeding using GRI-Mech 3.0 mechanism (top) and by Tian mechanism (bottom). Only NO mole fraction profile in each flame centerline is plotted for ease of comparison.....128**
- Figure 6-15: Comparison of the predicted major species and temperature of two syngas mixtures without NH₃ seeding.....132**
- Figure 6-16: Comparison of the predicted minor species and temperature of two syngas mixtures without NH₃ seeding.....133**
- Figure 6-17: Comparison of the predicted major species and temperature of two syngas mixtures with 1 vol% NH₃ seeding in fuel stream.134**

Figure 6-18: Comparison of the predicted minor species and temperature of two syngas mixtures with 1 vol% NH ₃ seeding in fuel stream.	135
Figure 6-19: Comparison of the predicted major species and temperature of two syngas mixtures with 2 vol% NH ₃ seeding in fuel stream.....	136
Figure 6-20: Comparison of the predicted minor species and temperature of two syngas mixtures with 2 vol% NH ₃ seeding in fuel stream.....	137
Figure 6-21: Comparison of the predicted temperature of two syngas mixtures with various levels of NH ₃ seeding.....	138
Figure 6-22: Comparison of the predicted OH mole fraction of two syngas mixtures with various levels of NH ₃ seeding	141
Figure 6-23: Comparison of the predicted NO mole fraction of two syngas mixtures with various levels of NH ₃ seeding.	142
Figure 6-24: CH radical (top) and C ₂ H ₂ radical (bottom) profiles on centerline of F1 and F2 diffusion flames. Solid lines “—” denote the quantities without NH ₃ seeding, dash-dot lines “- . -” denote the quantities with 1 vol% NH ₃ seeding and dash-dot-dot lines “- .. -” denote the quantities with 2 vol% NH ₃ seeding.	146
Figure 6-25: CH, C ₂ H ₂ , CH ₃ radicals and net productoin rate of NO by reaction 551, 552 and 566 in Tian’s mechanism in case of 1% NH ₃ doped in the syngas fuel stream. Top figure is in case of F1 and bottom is in case of F2 flame.....	147
Figure 6-26: Comparison of the relative contribution of NO-sub-mechanism in two syngas mixtures without NH ₃ seeding.....	148
Figure 6-27: Comparison of the relative contribution of NO-sub-mechanism in two syngas mixtures with 1 vol% NH ₃ seeding in the fuel stream.....	149
Figure 6-28: Percentages of each NO formation sub-mechanisms to the total NO mole fraction on the centerline of the F1 flame without NH ₃ seeding.....	151

Figure 6-29: Percentage contributions of NO formation sub-mechanisms to the total NO mole fraction along the centerline of the F1 flame with 1 vol% NH ₃ in the fuel stream.	152
Figure 6-30: Percentage contributions of NO formation sub-mechanisms to the total NO mole fraction along the centerline of the F1 flame with 5 vol% NH ₃ in the fuel stream.	152
Figure 6-31: Percentage contributions of NO formation sub-mechanisms to the total NO mole fraction along the centerline of the F1 flame with 20 vol% NH ₃ in the fuel stream.	153
Figure 6-32: Fuel NO with respect to NH ₃ doping in case of F1 (top) and F2 (bottom). ...	155
Figure 6-33: Thermal vs. NH ₃ doping in case of F1 (top) and F2 (bottom).	156
Figure 6-34: Prompt NO vs. NH ₃ seeding in case of F1 (top) and F2 (bottom).	157
Figure 6-35: N ₂ O-intermediate vs. NH ₃ doping in case of F1 (top) and F2 (bottom).	158
Figure 6-36: NNH-intermediate vs. NH ₃ doping in case of F1 (top) and F2 (bottom).	159
Figure A-1: X _{NO} on centerline of CH ₄ /air diffusion flame without NH ₃ seeding into the fuel stream.	182
Figure A-2: The Boltzmann fraction f_B , fluorescence efficiency η_{fluor} , total corrections $\times 10^6$ and temperature on the centerline of CH ₄ /air diffusion flame, with zero NH ₃ seeded to fuel stream.	183
Figure A-3: The stretched temperature T _{CFD,STRETCHED} , original temperature T _{CFD} ; The stretched and original X _{NO-PLIF} ; The stretched X _{NO-PLIF,STRETCHED} and and X _{NO,CFD}	184
Figure A-4: Laser profile, its curve fitting and fitting error.	185
Figure A-5: The relative spatial error by multi-gaussian curve fitting.	185

Figure A-6: Top: The original X_{NO} and its filtered signal, in case of zero NH_3 doping.

Bottom: The error between the original and filtered signal. It could be seen that

the error level is increasing.....187

ACKNOWLEDGEMENTS

This work couldn't be completed without the help from a number of people. First of all, I would like to express my gratitude to my major professor, Dr. Terrence R. Meyer, for his illuminating guidance and persistent encouragement that contributed to the completion of this thesis. Moreover, he is also an expert in stimulating me to achieve a level of independent thinking.

I would like to thank my committee members, Dr. Rodney O. Fox, Dr. Song-Chang, Kong, Dr. Hui Hu and Dr. Gap-Yong Kim. It is a great honor having you in my Doctoral committee. Your reviews and constructive comments contributed significantly to this research and thesis.

My special thanks go to Dr. Viswanath R. Katta for his patient and persistent help in my CFD research. His extensive knowledge of combustion and profound understanding of CFD greatly enhanced my perception of current combustion phenomena, my CFD research productivity, and in turn my confidence to complete my thesis.

I also would like to express my appreciation to all of my warmhearted labmates Mark Johnson, Chloe Dedic, Praveen Kumar, Matthias Veltman, and Cuong Huynh for their help and discussion; Special thanks to Joseph Miller, because not only that my PLIF couldn't be set up without his help, but also that he triggered my interest in playing with laser diagnostics and optics; Special thanks to Jordan Tiarks for his considerate dedication and excellent instrumentation skills.

My final thanks go to my wife, Dr. Chengyun Guo for her sacrifice, persistent love, support, and excellent management of my family throughout my years as a student!

ABSTRACT

Oxides of nitrogen formed during combustion are significant threats to our environment. They result in the formation of “acid rain”, smog, and depletion of the ozone layer. These combustion systems often include diffusion flames of hydrocarbon and air, where the NO can be formed at high levels (100’s to 1000’s of parts per million). In fuels produced from biomass or waste streams, small amounts of ammonia (NH_3) can significantly enhance the production of NO. However, the chemical kinetic mechanisms for NO formation in the presence of NH_3 are not well understood or validated. In the current work, a series of laminar diffusion flames of CH_4 /air and syngas/air are investigated using *in situ* measurements and detailed numerical simulations with varying levels of NH_3 to understand the dominant mechanisms of NO formation.

For these flames, the 2-D flame structure, as well as the 2-D NO formation and distribution within the flame are of major interest. This includes investigation of (1) the basic flame structure in the meridian plane of flames, (2) the NO distribution in the meridian plane of flames, (3) Relative contributions of each NO-formation sub-mechanism (e.g. thermal NO, prompt NO, N_2O intermediate, NNH intermediate, fuel NO), (4) effects of syngas composition on NO formation, and (5) effects of fuel-bound nitrogen (such as NH_3) on NO formation.

Numerically, a well-validated research code – UNICORN (UNsteady Ignition and COMbustion with ReactionNs) is used to solve 2-D axisymmetric equations of continuity, momentum, enthalpy, and species. Two detailed chemical mechanisms – GRI-Mech 3.0 and Tian are incorporated into UNICORN to describe the chemical reactions in flames.

Experimentally, an *in-situ* laser-diagnostics technique -- Planar Laser Induced Fluorescence (PLIF) is implemented to diagnose the 2-D OH concentration profiles qualitatively, and then NO concentration profiles quantitatively. Qualitative measurement of the OH radical assures agreement between the CFD simulation and experiment, in terms of flame structure. Quantitative measurement of NO concentration is compared with the CFD simulation to validate predictions with respect to NH₃ concentrations in CH₄/air and syngas/air flames.

The amounts of NH₃ in the fuel stream are varied to investigate the effects of fuel-bound nitrogen on NO formation. Two syngas mixtures (F1: 10 vol% CH₄, 45 vol% CO, 45 vol% H₂ vs. F2: 50 vol% CO, 50 vol% H₂) are used to study composition effects.

Results of the current work can be summarized as follows:

1. Both CFD and PLIF agreed well on the diffusion flame structure on the meridian plane of studied flames.
2. Both CFD and PLIF agreed well on the “one-peak” and “two-peak” structures of NO radical concentration on the centerlines of CH₄/air and syngas/air diffusion flames.
3. Peak(s) of the NO radical concentration along the centerline of flames are due to different NO-formation sub-mechanisms. This depends on the amount of seeded NH₃ and syngas composition (F1 vs. F2).
4. For each test/simulation condition, NO-formation sub-mechanisms are numerically investigated, in terms of their relative contributions.
5. GRI-Mech 3.0 is relatively successful in predicting CH₄/air flames, while the Tian mechanism is effective for syngas/air flames.

CHAPTER 1 INTRODUCTION

In this thesis, the two-dimensional flame structure and NO formation characteristics of laminar CH₄ and syngas diffusion flames seeded with NH₃ (ammonia) were investigated numerically and experimentally. Numerically, the conservation equations of mass, momentum, species, and energy were solved by a well-validated two dimensional, reacting computational fluid dynamics code – UNICORN. In order to predict detailed chemical reactions in flame, two chemical kinetics, GRI-Mech 3.0 and Tian et al., were incorporated into UNICORN. The numerical results were compared with *in situ* laser-based measurements. The relative contributions of each NO sub-mechanism, such as thermal NO, prompt NO, fuel NO, N₂O-intermediate, and NNH-intermediate were numerically evaluated with varying levels of NH₃ (100ppm through 50%) and CH₄ (0.0% and 10%) in CH₄ and syngas diffusion flames. Experimentally, spatially-resolved quantitative planar OH and NO mole fraction profiles of CH₄ and syngas diffusion flames were obtained using a *in situ* laser diagnostics technique -- Planar Laser-Induced Fluorescence (PLIF) technique.

In the following sections, background information about diffusion flames, PLIF, and NO formation mechanisms are briefly introduced. In addition, motivations for studying NO_x emission in these flames are summarized. At the end, the objectives and outline of this thesis are presented.

1.1 Background

In combustion systems, flames can be categorized into premixed, non-premixed (or diffusion), and partially premixed flames [1]. In terms of the premixed flame, the fuel and oxidizer streams are well-mixed before entering the reaction/combustion zone,

which is why it is termed as “premixed.” For non-premixed flames, the fuel and oxidizer streams enter separately and diffuse into the reaction zone where the reaction is occurring concurrently. Near the interface between fuel and oxidizer, mixing takes place by diffusion and/or convection. The flame speed of diffusion flame is limited by the rate of diffusion or mixing. The mixture is combustible or flammable only in a limited range of fuel/oxidizer ratio. Fuel/oxidizer ratios that are too high or too low are not combustible. Approximately in the middle of the flame sheet, there is a stoichiometric line, where the fuel and oxidizer are mixed at the stoichiometric ratio; higher temperature (adiabatic flame temperature) and hydroxyl (OH) concentration are expected in the neighborhood of this line. Diffusion flames are relatively safe since they don’t propagate back into the fuel or oxidizer stream (“flashback”). The direct applications of diffusion flames include candle flames, wood fires, diesel engines, and fire spread.

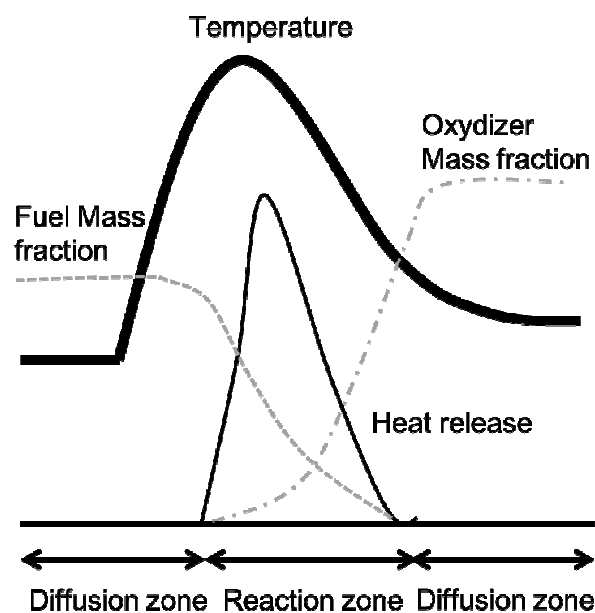


Figure 1-1: Diffusion flame structure.

Laminar diffusion flames are commonly used to study chemical mechanisms. The essential features of laminar diffusion flames from a tube burner are illustrated in Figure 1-2, together with laminar premixed flames as a comparison [2]. For laminar diffusion flames (right), as the fuel flows along the flame axis, it diffuses outward in the radial direction, while the oxidizer (e.g. air) diffuses inward. The flame surface is defined where the fuel and oxidizer meet in stoichiometric proportions and the equivalence ratio $\phi = 1.0$. The flame length is indeed proportional to the volumetric flow rate and inversely proportional to the stoichiometric fuel mass ratio.

For laminar premixed flames (left), since fuel and air are already mixed within the burner tube, a premixed flame will propagate inward towards the burner until it balances the flame speed (or burning velocity) of the fuel/oxidizer mixture. In a steady state Bunsen cone, for instance, the laminar burning velocity is equal to the flow velocity normal to the flame front. Further downstream, the unburnt species, such as CO and H₂, mix with the coflow air and lead to post flame oxidation and radiation. Laminar premixed flames appear to be blue if mixed near stoichiometric ratio, whereas diffusion flames usually appear to be bright yellow. The blue color of a premixed flame is due to chemiluminescence of excited species, whereas the yellow color of diffusion flames is due to radiating soot particles. Please note that highly stretched diffusion flames also appear blue since the local residence time is too short for soot particles to be formed. Thus, the color of a flame is a characteristic of the available residence time, not only the type of mixing.

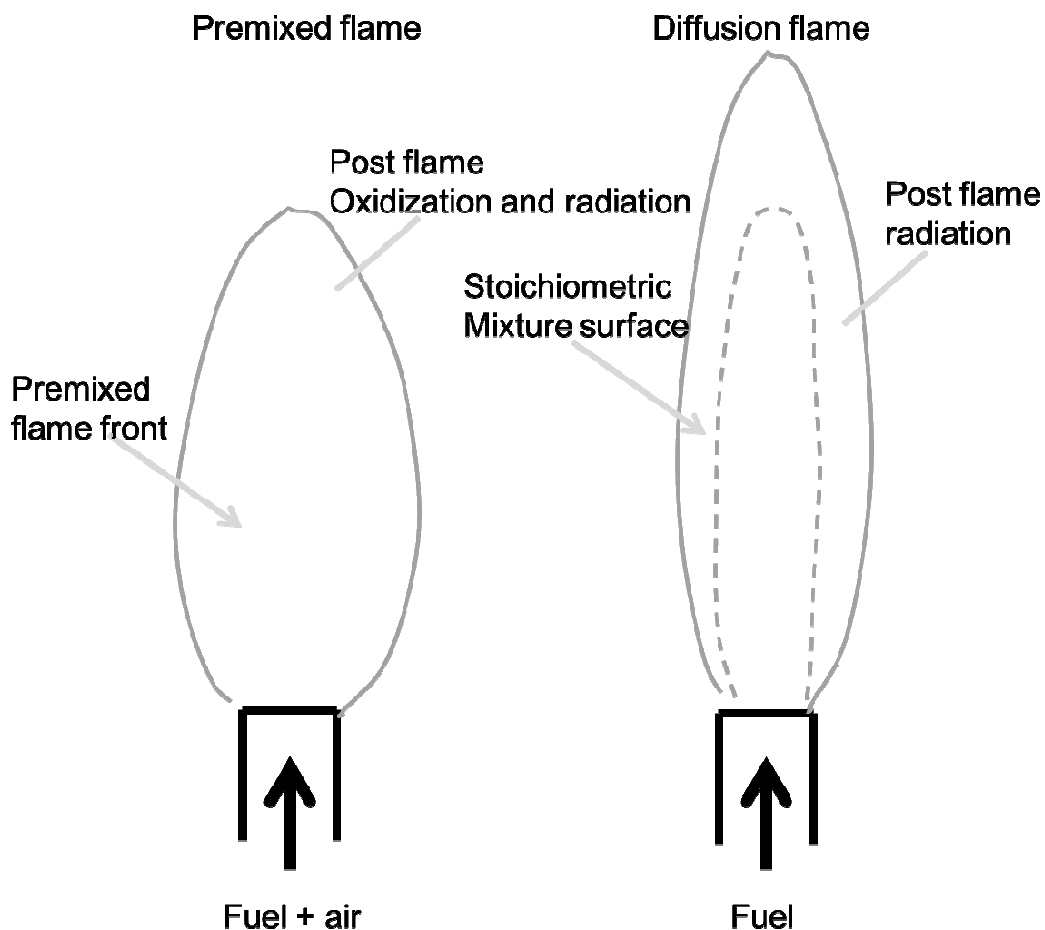


Figure 1-2: Laminar premixed flame (left) and diffusion flame (right) from a tube burner.

1.2 Planar Laser Induced Fluorescence

Detailed experimental studies of combustion flame structure have been performed for over 150 years, beginning with some phenomena related to a candle flame. It started from simple visual inspection of a flame, then gradually to detailed analysis of the entire combustion process/system with a compilation of various sophisticated techniques. Today, quantitative measurements of concentration, velocity, temperature, heat release rate, NO_x emission, etc. are common topics for combustion

scientists and engineers. Laser diagnostics can be used to make continuous or high-speed discrete measurements with high spatial and temporal resolution in the flame, which help scientists to understand the fundamentals of combustion mechanisms [3]. Typically, temperature, concentrations of major species and key intermediates in the combustion zone should be available for detailed comparison with the simulation results.

In order to study detailed chemical mechanisms, Laser-Induced Fluorescence (LIF) is used to detect important species in both a qualitative and quantitative manner [3]. It is an *in situ*, non-intrusive, well-established, and sensitive technique widely used in combustion research to perform real-time measurements for species. It is a sensible probe to detect species down to parts per million (ppm) levels; moreover it is able to visualize the 2-dimensional (or even 3-dimensional) quantitatively species' distribution inside the flame.

The challenge for this type of study is usually the chemical complexity. For instance, when it comes to PLIF imaging, up to thousands of reactions and hundreds of species may be involved and only up a few critical intermediates (e.g., OH, NO, CH, etc.) can be captured simultaneously. Even as these species are detected, in order to determine quantitative concentration or mole fractions, temperature, the concentrations of major species and key intermediates must be recorded as well.

As noted above, the major problem of Planar Laser-Induced Fluorescence is how quantitative results can be derived from measured signals. Meaningful PLIF imaging involves data collection from the targeted species without any interference from other species. Another problem is the competition of collisional quenching of LIF signals with the radiation process that leads to the observable signal. Laser-Induced Fluorescence is

affected by quenching with other major species and key intermediates. Temperature variations have a strong effect on a molecule's excitation intensity, and thus its fluorescence intensity. Hence, traditional LIF images of species profiles in laminar diffusion flames must be corrected for quenching rate, Boltzmann effects, absorption of laser energy along the beam path, as well as inherent laser inhomogeneity.

In a PLIF measurement, the fluorescence signal is obtained by exciting the targeted molecules from the ground electronic state up to an excited state. This transition between specific electronic and rovibrational states corresponds to specific frequencies, say $\nu_{\text{excitation}}$, of absorbed photons. The frequency of incident laser photons, say $\nu_{\text{laser source}}$, for the excitation is tuned to match $\nu_{\text{excitation}}$, which means that the frequency of the laser source $\nu_{\text{laser source}} = \nu_{\text{excitation}}$. Once excited, the molecules in the excited energy state depopulate with spontaneous emission of photons with frequency ν_{emission} . Due to vibrational and rotational energy transfer, this emission frequency can be equal or not equal to the excited frequency $\nu_{\text{excitation}}$.

When the laser pulse duration is long enough compared to time scale for absorption, emission and collisional quenching, the fluorescence process is supposed to be at steady state. The fluorescence signal intensity, S_f , is proportional to the species concentration or species number density. At steady state, when laser intensity is below the saturation limit, the fluorescence is in the linear regime, thus S_f is proportional to incident laser intensity, but is still dependent on the quenching rate and Boltzmann fraction (i.e., population of the transition). When the laser intensity is too high, it approaches the saturation limit, and S_f is independent of both laser intensity and quenching rate.

In recent years, NO PLIF, literally the measurement of NO molecules by PLIF has attracted increasing attention. Besides temperature and NO concentration measurement, other important flame radicals and intermediates can be measured quantitatively as well, such as OH, CH, CN, HCN, HCO and HCCO. Often experimental results are combined with numerical simulation of the combustion process, based on more detailed understanding of individual facets.

NO formation is complicated, it involves numerous aspects, such as fluid mechanics, mass transfer, heat transfer, mixing, chemistry, etc. Full understanding cannot be obtained only experimentally. It is necessary to conduct advanced numerical studies combined with experiments to obtain useful information on NO formation and emissions. Turbulent combustion with detailed chemical reaction mechanisms are rarely conducted due to the requirement of extensive computational resources for turbulent flows and detailed chemistry. This is one of the reasons that laminar, instead of turbulent flames, were selected for the current study. Numerical simulations of laminar diffusion flames require solving just two-dimensional (e.g., r- and z- direction for axisymmetric flame) partial differential equations because of the relatively simple geometry and lower Reynolds number. Detailed chemical mechanisms can be incorporated to describe chemical reactions and flow-chemistry interactions. By manipulating the incorporated chemical mechanism, various sub-mechanism of NO formation can be estimated, such as thermal NO, prompt NO, fuel NO, N_2O -intermediate, and NNH-intermediate.

Since syngas gasified from solid fuel potentially contains fuel nitrogen in volatile, and this amount of fuel nitrogen could lead to significant NO formation, it is important to

understand NO formation and destruction/reburn mechanisms of fuel-bound nitrogen in diffusion flames. One of the common strategies to simulate the fuel-bound nitrogen's effect on NO formation mechanisms is to seed the fuel stream with model nitrogen additives, such as HCN, NH₃, etc. Despite the importance of fuel NO, its formation in diffusion flames (especially syngas flames) has not been thoroughly investigated.

1.3 Motivation

In the past few decades, concerns have been growing about subsequent environmental effects of burning fossil or biomass fuel, such as acid rain and ozone layer destruction. One of the most disastrous pollutants is NO_x, which is a collective term of both Nitric Oxide (NO) and Nitrogen Dioxide (NO₂), with the NO as major species of NO_x. Once released into atmosphere, NO_x converts into highly corrosive nitric acid (HNO₃), which can further be absorbed by water droplets in the air and result in the "acid rain". In stratospheric layer, the NO catalyzes the ozone destruction reaction and leads to ozone depletion. Thus, increasingly stringent rules are set up by the Environmental Protection Agency and state authorities to regulate NO_x emissions. For example, 2ppm NO_x emission from a single gas-turbine facility is required in California. Low-NO_x regulations and environmental considerations are one of the primary motivations for modern combustion system design, and an important motivation of the current research.

Based on the above discussion, laminar diffusion flames will be used to represent numerous modern combustion systems that utilize alternative fuels, such as syngas. Thus, a detailed understanding of NO formation in these flames becomes imperative. Literature review indicates that a fundamental understanding of NO

formation in these flames is still lacking, especially the detailed chemical mechanisms concerning fuel NO, which could be the dominant NO formation mechanism for biomass combustion if fuel-bound nitrogen is available. Specifically, PLIF is used to measure OH or NO distributions in the combustion process; numerical simulations are employed with two different detailed chemical kinetics mechanisms (GRI-Mech 3.0 and Tian mechanism). In this thesis, CH₄ is first selected as the baseline fuel, since it is the simplest model hydrocarbon fuel and has been extensively studied. Syngas is then used to construct diffusion flames following studies of CH₄ flames. Syngas is the product gas from gasification of solid fuels, such as coal, at high temperature. It contains a mixture of H₂ and CO as the major combustible components and other components (e.g. CH₄, CO₂ and H₂O). In this thesis, two types of syngas composition (without CH₄ or with CH₄) were chosen for comparison; differences in results show that the presence of CH₄ has a significant effect on NO_x formation.

1.4 Objectives

The present thesis has three main objectives:

1. To investigate NO formation characteristics of laminar CH₄ diffusion flames doped with NH₃. Here, the NH₃ doping effects on NO_x formation are characterized by comprehensive numerical models with detailed chemistry. *In-situ* PLIF is used to measure OH and NO concentrations. The numerical results are compared with experimental data to validate the chemical kinetics mechanisms. The relative contributions of NO sub-mechanisms e.g. thermal, prompt, fuel, NNH, and N₂O to total NO formation are also evaluated.

2. To obtain quantitative absolute NO mole fractions in CH₄ or syngas diffusion flames by two-dimensional NO-PLIF imaging. Here, the laser excitation scheme, detection scheme, and filters are carefully selected to achieve the best signals. The signals are converted and corrected into mole fraction distributions based on calibration flames and CFD calculations. The two dimensional OH and NO profiles are further compared with numerical results. The absolute NO mole fraction profiles along flame centerline derived from experimental NO PLIF and computational fluid mechanics (CFD) are further used to validate NO emission mechanisms.
3. To investigate NO_x formation characteristics of laminar syngas diffusion flames doped with NH₃. Here, the NH₃ seeding effect and NO formation are investigated by CFD with detailed chemistry (Tian mechanism). OH and NO-PLIF are used to measure *in-situ* OH and NO concentrations. Syngas flames with two different compositions are compared to evaluate the contribution of CH_i radicals to NO_x formation. The relative contributions of NO_x sub-mechanisms e.g. thermal, prompt, fuel, NNH and N₂O to total NO_x formation are also evaluated.

1.5 Outline

In the following, Chapter 2 summarizes the literature review and background information. Chapter 3 discusses the experimental setup, including OH-PLIF, NO-PLIF, data collection, calibration, and data processing. Chapter 4 summarizes the Computational Fluid Dynamics (CFD) models used for combustion simulation, including governing equations, boundary conditions, detailed chemical kinetics, and detailed numerical procedures. Chapter 5 discusses results of CH₄ flames, including NO_x formation characteristics and NH₃ dopant effect on NO_x formation and destruction.

Chapter 6 discusses results on syngas flames with two different type of composition.

Chapter 7 concludes and talks about recommendations for future work.

CHAPTER 2 LITERATURE REVIEW

It has been a hot topic to study NO formation with different types of laser diagnostics. In this thesis, we demonstrate experimental and numerical studies of NO_x formation in laminar non-premixed methane and syngas flames doped with varying amounts of NH₃.

In this chapter, Literature review will start with a summary of NO formation mechanisms. In addition, various PLIF applications of studying NO formation are summarized, followed by two-dimensional PLIF imaging technique development in recent years. Moreover, research with detailed chemical kinetic mechanism comparisons will be summarized, along with the characteristics of NO formation in syngas flames.

2.1 NO Formation Mechanism

The concepts underlying many NO_x reduction technologies can be understood in terms of reaction mechanisms of formation and removal of various nitrogen oxides. The formation of NO is strongly influenced by temperature, and radical species concentrations. Thermal NO, Prompt NO, fuel NO, N₂O-intermediate, and NNH-intermediate mechanisms are considered major NO_x formation routes [5]. In order to distinguish the contributions from the respective NO formation routes, a separation method was introduced proposed by Nishioka et al. [6]. The detailed chemical reaction routes for each process are summarized as follows.

2.1.1 Thermal NO

Since this mechanism is only effective in high temperature, oxygen rich condition with longer residence time. The name “thermal” here refers to the high temperature condition. The following are the major reactions of the thermal NO mechanism:



Among these three reactions, the rate-limiting reaction is Eq. (2.1). Using a steady state N-atom approximation and assuming that the O-atom concentration can be calculated from equilibrium considerations, the maximum NO formation rate can be expressed as follows:

$$\frac{d[\text{NO}]}{dt} = 1.45 \times 10^{17} T^{-\frac{1}{2}} e^{-\frac{69460}{T}} [\text{O}_2]_{\text{eq}} [\text{N}_2]_{\text{eq}} \quad (2.4)$$

This equation shows that the NO formation rate is strongly related to temperature T and weakly related to O₂ concentration in the burned gas. Actually, the high activation energy of 319 kJ/mol of this reaction results in extreme temperature dependence for this thermal route. At temperatures below 1500K, this process is usually negligible. In order to accurately predict the contribution of the thermal NO mechanism, peak temperature and O₂ concentrations in the flame are the keys.

2.1.2 Prompt NO

Prompt NO is defined as the NO formed faster than equilibrium thermal NO and doesn't require high temperature, which is why it is termed as “prompt.” There are three sources of prompt NO in hydrocarbon fuel combustion:

1. Non-equilibrium O and OH concentration in the reaction zone.
2. A reaction sequence which initiates from the reactions of hydrocarbon radicals with molecular nitrogen in or near the reaction zone (also called Fenimore Prompt NO).
3. Reactions of O atom with N₂ to form N₂O in a two-step reaction as follows:



The relative importance of these sources depends on conditions in the combustor. In non-premixed flames, acceleration of NO formation by non-equilibrium O and OH concentration is most important. Fenimore's Prompt NO mechanism is dominant in fuel-rich premixed flames and hydrocarbon diffusion flames. The N₂O mechanism is most important when the overall NO is low, and usually occurs when temperature is low or the fuel/air ratio decreases.

Thermal and prompt NO are formed spatially differently in the physical domain, such as in the combustion chamber. Thermal NO is formed in the hot burned gases with a continuous increase in concentration along with residence time. In contrast, pure prompt NO should result in a sharp and sudden increase near or even upstream of the flame front. Many researchers have investigated thermal NO and prompt NO contributions to total NO formation in different combustors and at different flame conditions [7-9].

Table 2-1 shows representative contributions of thermal NO and prompt NO mechanisms from experimental data in laminar premixed flames, laminar diffusion flames, turbulence diffusion flames, and well-stirred combustors.

Table 2-1: Fraction contributions of thermal NO and prompt NO mechanisms to total NO formation in different flames.

Flame	Flame Conditions		Total NO (ppmv)	Thermal	Super-equilibrium	HC-N ₂	N ₂ O
Premixed laminar CH ₄ /air [9]	$\phi=1$	P=0.1atm	9@5 ms	0.03	0.22	0.72	0.01
	$\phi=1$	P=1atm	111@5	0.50	0.35	0.10	0.05
	$\phi=1$	P=10atm	315@5	0.57	0.15	0.21	0.10
Premixed laminar CH ₄ /air [10]	$\phi=1.05$	P=1atm	29@5 mm	0.53	0.30	0.17	--
	$\phi=1.16$	P=1atm	20@5 mm	0.30	0.20	0.50	--
	$\phi=1.27$	P=1atm	20@5 mm	0.05	0.05	0.90	--
	$\phi=1.32$	P=1atm	23@5 mm	0.02	0.03	0.95	--
Nonpremixed laminar CH ₄ /N ₂ /air [11]	$\alpha^*=10s^{-1}$	P=1atm	120 max	--	0.20	0.69	0.11
	$\alpha=36s^{-1}$	P=1atm	65 max	--	0.07	0.86	0.07
	$\alpha=70s^{-1}$	P=1atm	43 max	--	0.05	0.90	0.05
Well stirred reactor CH ₄ /air [12]	$\phi=0.7$	P=1atm	12@5 ms	0.15	0.65	0.05	0.35
	$\phi=0.8$	P=1atm	20@5 ms	--	0.85	0.10	0.05
	$\phi=1$	P=1atm	70@5 ms	--	0.70	0.30	--
	$\phi=1.2$	P=1atm	110@5	--	0.10	0.90	--
	$\phi=1.4$	P=1atm	55@5 ms	--	--	1.0	--
Well stirred reactor CO/air [13]	$\phi=0.6$	P=0.92atm	34@7 ms	0.15	0.75	--	0.10
Nonpremixed turbulent CO/H ₂ /air [14]	--	P=1atm	7peak@ x/d=100	0.40	0.60	--	--
	--	P=10atm	--	0.74	0.26	--	--

* is the strain rate

2.1.3 Fuel NO

An important source of NO_x formation in the combustion of fuel-nitrogen-containing solid fuels is the chemically bound nitrogen in the fuel, which forms gas-phase intermediates and subsequently undergoes oxidation to form NO_x. The extent of

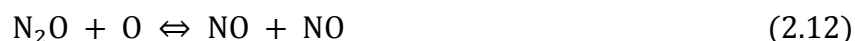
conversion of fuel-N to NO_x is dependent on temperature, stoichiometry, and the initial level of fuel-N. Experiments on fuel-N have indicated that fuel-N can first go into the intermediate HCN or NH_3 , depending on the type of fuel-N [15]. The main intermediate from coal is often HCN, and the main intermediate from biomass is often NH_3 . These two intermediates then react to form either NO or N_2 , depending on the local combustion conditions.

2.1.4 NO formation via N_2O

The N_2O mechanism was proposed by Malte et al. [13] It is used to explain NO_x formation in excess of oxygen at moderate temperatures. The principle gas-phase reactions forming N_2O in fossil fuel combustion are:



Three NO formation reactions via N_2O are summarized as following:

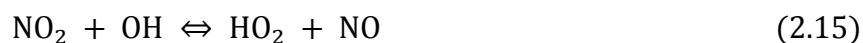


2.1.5 NO formation via NO_2

The principle NO_2 formation reaction is:



Five NO formation reactions via NO_2 are summarized as follows:





2.1.6 NO formation via NNH

In addition to other mechanisms mentioned earlier, the NNH mechanism was proposed by Bozelli and Dean [16]. The NO formation reaction is :



and they proposed NNH is formed via:



The NNH pathway would be significant in case of lean-premixed flames, especially those used in gas-turbine engines.

2.2 PLIF Application in NO Detection

Non-premixed flames remain widely used even though they have negative impacts on NO_x emission compared to fully premixed flames. In order to identify critical NO_x formation reactions and investigate the reliability of chemical mechanisms, major chemical species concentrations need to be determined and compared with proposed chemical kinetic predictions. In addition, researchers could measure species profiles with artificially doped NO, HCN or NH₃ in non-premixed flames in order to further understand NO formation chemistry.

Since PLIF involves exciting atoms or molecules to an excited state with laser radiation, the actual observation after a laser shot is the population of the excited molecules [17]. Typically, a laser sheet is formed to illuminate a thin plane in the region

of interest and the signals are detected by digital cameras. Figure 2-1 shows a simple planar imaging configuration. The advantage of Planar Laser Induced Fluorescence (PLIF) is clear, since it allows visualization of flow properties inside the flame, which is otherwise extremely difficult to observe.

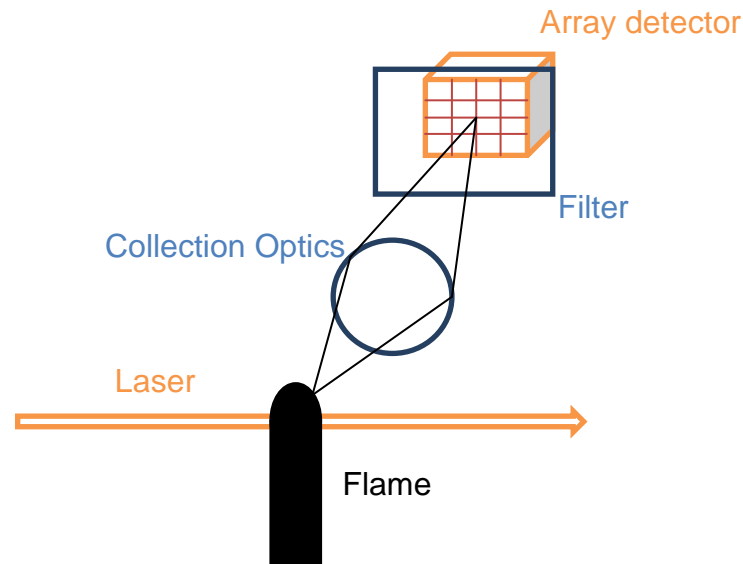


Figure 2-1: A simple Planar Laser-Induced Fluorescence (PLIF) configuration

The excitation scheme and detection scheme of NO molecules are critical as well. The NO molecule can be detected by various schemes in the ultraviolet spectral range. Excitations and detections near 193 nm (A-X (0,0) band), 226 nm (A-X (0,1) band) and 248 nm (A-X (0,2) band) has been investigated up to date. This side range can be covered by different lasers in imaging experiments,

It is important to measure not only the pulse-to-pulse fluctuations of the entire laser beam, but also the spatial intensity variations in the laser sheet, i.e. the laser sheet profile or laser sheet inhomogeneity. Empirical methods are to record an averaged

sheet profile and scale it with the individual integrated pulse energy for the corresponding measurement. Fluorescence signals are collected at right angles to the laser beam, and are usually detected with a CCD camera.

Optics are critical. They help to not only collect better signal but also improve the signal levels. For example, interference from other species such as O_2 or soot radiation can be removed very effectively by band-pass filters, though typical narrowband filters for the ultraviolet have at most 10% transmission rate. Thus, it is very important to choose filters with transmissions as high as possible in order to provide sufficient signal intensities.

The major challenge of PLIF in NO_x emission studies is the derivation of quantitative results from 2-D experimental data, i.e. deriving the 2-D absolute NO concentration or mole fractions (e.g. ppm) based on 2-D images. As known, PLIF signal is usually affected by the quenching rate, vibrational and rotational energy transfer. Other than those, temperature variations must be considered (Boltzmann fraction) in data reduction due to its considerable effects on the quenching rate. Neglecting the quenching rate in data reduction will result in misleading interpretation of experimental results. Fluorescence quenching of NO with other major species and key intermediates was studied extensively in recent years and resulted in a comprehensive understanding of quenching processes for many important quencher molecules [18].

Other than the quenching effects mentioned above, depending on experimental conditions, other corrections are needed to fully quantify the experimental results, such as laser beam profile, laser power fluctuations, signal absorption and spectral efficiency of the detection system [19].

NO emission of diffusion flames has been extensively investigated by PLIF. Hirano et al. [20] studied NO_x formation of a natural gas combustor by PLIF. In laminar CH_4/air flame cross sections at atmospheric pressure, they observed higher NO concentration at the flame front where CH, CN and NH concentrations are higher. At the same time, they observed gradual increase of NO in the outer flame where OH is high, suggesting a potential new NO formation mechanism. Plessing et al. [21] used OH-PLIF to study highly preheated combustion with exhaust gas recirculation. They found that exhaust gas recirculation leads to lower temperature, and even at significant air preheating, thermal NO is still suppressed significantly. They also found OH concentration in this condition was much lower than in non-preheated, un-diluted, turbulent, premixed flames. Ravikrishna et al. [8] investigated NO concentration of partially premixed flames by NO-PLIF and compared experimental results with numerical predictions by GRI-Mech 2.11. They found good agreement between experiments and predictions. Heberle et al. [22] measured CH and OH radical structures by PLIF in well-stabilized, laminar partially premixed Bunsen-type CH_4/air flames and found that OH and CH structures in the straight walls of inner flame cones are well described by models with detailed chemistry and the one dimensional transport model. Whereas at the tip of the inner wall, and in flames perturbed by a metal insert, OH and CH structure results deviate from simple descriptions. Naik et al. [23] measured absolute CH concentration by PLIF and Cavity Ring-down Spectroscopy (CRDS) in laminar, counterflow partially premixed and non-premixed flames at atmospheric pressure. They found that LIF and CRDS show similar CH profiles and experimental

results are in good agreement with computational predictions by both GRI-Mech 2.11 and GRI-Mech 3.0 mechanisms.

Experimentally, two-dimensional NO-PLIF has advantages of *in-situ* monitoring the spatial distribution of NO in the flame. For 2-D NO PLIF, selections of laser excitation scheme, detection scheme, and optical filters to block unwanted interference are crucial. The first 2-D NO-PLIF was reported by Kychakoff et al. [24] where the seeded NO was visualized in CH₄/air flames. The method used sheet illumination from a tunable laser to excite fluorescence, which is detected using an intensified 2-D detector. In laboratory burner setting, Laurendeau's group in Purdue University have extensively studied NO_x formation by PLIF in premixed, partially premixed, and non-premixed flames at high pressure [25, 26]. These measurements were carried out using a frequency-doubled dye laser tuned to the Q₂(26.5) transition at 225.58 nm in order to minimize the temperature dependence of the ground state population. Narrowband monochromator detection was used to suppress interference signals. For practical 2-D NO-PLIF application, e.g. in Diesel engine, Dec et al. studied in a 2-D NO-PLIF image in a direct-injection Diesel engine fueled with low-soot diesel [27], and measured semi-quantitative NO concentration throughout the combustion cycle. These measurements were carried out using a frequency-doubled OPO systems to excite P₁(23.5), Q₁+P₂₁(14.5), Q₂+R₁₂(20.5) at 226.03 nm.

2.3 NH₃ Dopant Effect

Coal and biomass fuels may contain a lot of chemically bound nitrogen (as much as 2% by mass), and these nitrogenous gases could convert in the flame into N₂ or NO_x once released from fuels during pyrolysis. In fact, oxidation of fuel-bound nitrogen is the

dominant source of NO_x formation in combustion of coal and biomass. Despite the importance of fuel-NO, little work has been done to understand conversion of reactive nitrogen species in diffusion flames.

Studies have shown that species composition of gas phase fuel nitrogen does not have a significant effect on NO emission [28]. The controlling factors of NO_x or N_2 selectivity appear to be the fuel-N dopant level and the flame configuration. Typically, the nitrogen-containing compounds consist of either HCN or NH_3 , and NH_3 is present at higher concentration compared to other fuel-nitrogen species in volatiles from biomass feedstock. Thus, a diffusion flame seeded with NH_3 is a good benchmark to study fuel-nitrogen effects.

Laminar non-premixed flames have been investigated extensively. Smooke et al. [29] successfully simulated a 2-D axisymmetric laminar diffusion flames and obtained significant insight into the structures of diffusion flames [30]. However, no study of fuel-nitrogen effects has been evaluated in these experiments. Nishioka et al. [31] correlated flame structure from simulations of 2-D coflow laminar diffusion flames with that of 1-D counterflow diffusion flames. However, when considering NO_x formation, the correlation broke down, indicating that emission characteristics of 2-D flames are different from those of 1-D flames.

The NH_3 oxidation mechanism for NO_x formation is well established. Miller et al. [10] studied nitrogen chemistry in combustion and found that fuel-nitrogen species present as NH_3 undergo hydrogen abstraction reactions. Each reaction results in NH_i radicals, which then participate in one of two competitive reaction mechanisms:

oxidation leading to NO formation or to N_2 through reactions that additionally consume NO. Figure 2-2 shows the reaction path diagram for the NH_3 oxidation mechanism.

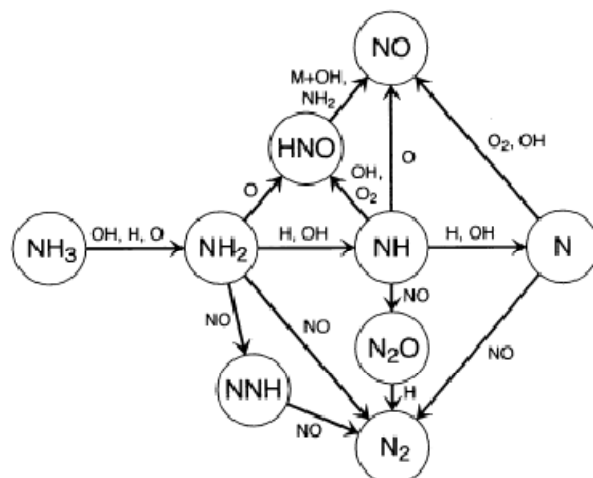


Figure 2-2: NH_3 Oxidation mechanism, reproduced from [32]

Sullivan et al. [32] reported a combined experimental and modeling investigation of NO formation in laminar, NH_3 -seeded, nitrogen-diluted, methane diffusion flames. The experiment used flue-gas sampling to measure concentrations of stable species in the exhaust gas. The computation was conducted with a 2-D CFD research code with detailed chemical kinetics. The model showed good agreement with exhaust gas concentration of NO over a wide range of NH_3 seeding. In particular, both experimental and numerical results showed that when more NH_3 is added, a greater percentage is converted into N_2 instead of NO. When comparing flames with and without seeded ammonia, it was shown that more NO is produced in the NH_3 -seeded case. They also used two different chemical kinetics mechanisms to perform the simulation comparison, and the results showed that GRI-mech 3.0 and Glarborg et al. [33] both predict experiments very well. The Glarborg mechanism produced more accurate and

consistent results, due to the inclusion of HNO formation reactions and more complete NO-recycling chemistry.

Even though Sullivan's result is very encouraging, flue data alone is insufficient for data validation. Thus, Bell et al. [34] applied in-flame measurement and PLIF to study steady laminar diffusion flames with various levels of NH_3 . For comparison with experimental data, synthetic LIF images were calculated based on numerical data accounting for temperature and fluorescence quenching effects. In the un-doped flame, four different mechanisms contribute to NO formation, and the most important pathway is prompt NO, followed by the NNH, thermal NO, and N_2O mechanisms. As the NH_3 seeding level increases, fuel-NO becomes the dominant mechanism and N_2 shifts from a net reactant to a net product.

2.4 Chemical Kinetics Comparison

The development of detailed chemical kinetics mechanisms for combustion began in the 1970s. First, several high temperature kinetics models for hydrogen, carbon monoxide, and methane oxidation were proposed based on a large quantity of experimental data [35, 36]. In the early 1980s, the first proposed chemical mechanism for C1 and C2 hydrocarbons contained 93 reversible elementary reactions and 26 chemical species [37]. This mechanism was further revised by adding elementary reactions to C1 and C2 sub-mechanisms [38]. Then, this mechanism was further expanded for ethylene chemistry and elementary reactions increased to 162 [39].

A nitrogen oxidation mechanism was first investigated by Glarborg et al. [12]. Miller et al. [10] further summarized the nitrogen oxidation mechanism as introduced in

the early part of this chapter. Baulch et al. [40, 41] later updated rate coefficients related to the oxidation of simple fuels.

In the early 1990s, Frenklach et al. [42] proposed a systematic procedure to develop a comprehensive chemical kinetics model for any fuel. These recommendations later were followed by the most recognized kinetic models such as GRI-Mech.

GRI-Mech, developed to describe methane oxidation, used a set of elementary reactions with reaction rate parameters that were provided by theoretical, experimental, and numerical data. Early versions of GRI-Mech contained 32 species and 177 reversible chemical reactions, which were constructed to describe methane combustion without nitrogen oxidation. The updated GRI-Mech 2.11 mechanism included nitrogen oxidation and contained 49 species and 279 elementary chemical reactions.

GRI-Mech 3.0 is the latest version which includes combustion of methane, ethane, and propane [43]. It contains 53 species and 325 elementary reactions. This mechanism has been validated for temperatures of 1000 K to 2500 K, pressures of 0.015 atm to 10 atm, and equivalence ratios of 0.1 to 2.5. It can be used for several combustion systems, including plug flow reactors, tube-stabilized flames, and combustion in shock tubes.

A new comprehensive kinetic mechanism was proposed by Tian et al. [44] in 2009. It is based on new observations and newly introduced intermediates. Tian's validation of this mechanism includes 11 premixed $\text{NH}_3/\text{CH}_4/\text{O}_2/\text{Ar}$ flames at low pressure (4.0 kPa) with equivalence ratio of $\phi = 1.0$. The mole ratio (R) of NH_3/CH_4 was varied from 0.0 to 1.0 to investigate effects on flame structure. CHEMKINTM PREMIX

was used to simulate the mole fractions of major and minor species and compare with experiments. Experimentally the mole fractions of these flame species were obtained by scanning the burner position at selected photon energies near ionization thresholds. Sensitivity and flow rate analysis was also conducted to determine the limiting reactions of CH₄ and NH₃ oxidation and their interaction.

The Tian mechanism contains 84 species and 703 elementary reactions involving oxidation subsets for CH₄ and NH₃, as well as a subset for hydrocarbon/nitrogen interaction. The mechanism was proposed based on recent results regarding the oxidation of C₁ and C₂ hydrocarbons [33, 45], oxidation of NH₃ and HCN [46, 47], and the interactions of these components [33, 48]. Several reactions describing hydrocarbon/NH₃ interactions were added, and the subsets for CH_{*i*} and NH_{*i*} radicals were updated.

Compared to the GRI-Mech 3.0 mechanism, the Tian mechanism includes the subsets for CH_{*i*} and NH_{*i*} radicals, which may have a considerable impact on nitrogen chemistry in CH₄ flames. CH_{*i*} radicals are very reactive, and their interaction with NH₃ can result in formation (Prompt NO) as well as reduction (reburn chemistry) of NO in flames.[10] In addition, when NH₃ concentration is high, CH_{*i*} radicals can convert amines into cyanides. Also, the key step converting the methyl radical to the methylene radical is a reaction with the hydroxyl radical. The reaction may lead to both triplet mythylene or singlet methylene, as seen following:



Between these two reactions, the singlet methylene formation reaction is the major pathway. The singlet methylene is rapidly converted into the triplet by reaction with inert molecules. The triplet may then be oxidized to CH₂O or CO by reacting with OH and O₂, or it may be converted to the CH radical through H abstraction reactions.

Compared to GRI-Mech 3.0, the Tian mechanism also includes updated subsets for NH_i radicals. NH_i radicals are important because they determine the selectivity of NH₃ to form NO or N₂ in the flame, as discussed in previous sections in this chapter.

The Tian mechanism also considers hydrocarbons and amine interactions, which are less well established than hydrocarbons/NO interactions. These reactions may involve H-abstraction reactions, such as:



Or they may involve methylamine and cyanide, such as:



Most of these reactions lack experimental validation data. Thus, rate constants of these reactions are adopted from evaluation work done by Dean et al. [49].

Other than the above two chemical mechanisms, Konnov et al. [50, 51] has developed another key mechanism that is used in combustion community. It was

initiated in the early 1980s' and been updated until the present time. The current version is 0.5, and includes 127 species and 1200 elementary reactions. Originated from methane combustion mechanisms, it was extended to cover other C1-C2 C/H/O reactions, such as methanol, acetaldehyde, ethanol and ethylene oxide. Basically it includes a multitude of C/H/N/O reaction sub-mechanisms, and is able to predict the flame structures of various $\text{NH}_3/\text{NO}/\text{N}_2\text{O}$ -seeded hydrogen and hydrocarbon flames. Its predictive capability was verified in some flames [51], but it has not been successful for other flames [52].

Other work has focused on simplifying the Konnov mechanism to reduce computational cost in combustion modeling. In order to predict the flame structure of $\text{H}_2/\text{NH}_3/\text{O}_2/\text{Ar}$ flames at elevated pressure and temperature conditions, similar to SI engine conditions, Duynslaegher [53] composed a reduced version (31 species and 245 elementary reactions) by eliminating all of carbon-related species and reactions. This approach seemed to produce good agreement. This reduced mechanism then was employed by Shmakov [54] to investigate NO and NH_3 -doped $\text{H}_2/\text{O}_2/\text{N}_2$ flames, and also led to good agreement.

However, due to significant effort and computation time required to utilize the Konnov mechanism for hydrocarbon flames, it was decided to focus the current effort on the GRI-Mech 3.0 and Tian mechanism as a starting point. In addition, the GRI-Mech 3.0 and Tian mechanisms would also be expected to perform fairly well in CH_4 and syngas flames, respectively. However, future work may certainly involve comparing the results of the current work with computations using the Konnov mechanism.

2.5 NO Emission of Syngas Diffusion Flames

Syngas, abbreviated from “synthetic gas”, is produced by gasification using variety of fuels, such as biomass, coal, and refinery residual [55]. It usually contains CO and H₂, with different amounts of CH₄ and other diluents.

There are many publications in the literature dealing with the structure and emissions characteristics of syngas diffusion flames. However, most of these studies focus on the combustion of the individual syngas components. We summarize here only studies on the combustion of syngas mixtures. Allen et al. [56] studied the oxidation chemistry of CO/H₂/N₂ mixtures. Drake et al. [57] studied numerically the effects of stretch on thermal NO in laminar CO/H₂/N₂ diffusion flames. They found that NO decreased dramatically with the increase of flame stretch. Hasegawa et al. [58] studied experimentally and numerically NH₃ removal of CO/H₂/CH₄ mixtures in a tubular flow reactor. They found that the optimum NO/NH₃ ratio for NO reduction and NH₃ decomposition is 1; the NO reduction ratio decreased with increasing H₂ concentration. Chung et al. [59] studied the extinction of CO/H₂/N₂ diffusion flames using an asymptotic approach. Fotache et al. [60] investigated numerically and experimentally the ignition characteristics of counterflow CO/H₂/N₂ diffusion flames with heated air. Charlston-Goch et al. [25] reported numerically and experimentally NO concentrations in premixed CO/H₂/CH₄/air flames at high pressures. Rumminger et al. [61] investigated experimentally and numerically burning velocities of premixed CO/H₂/O₂/N₂ flames. Natarajan et al. [62] studied experimentally and numerically the laminar flame speeds of CO/H₂/CO₂ mixtures over a range of fuel compositions, lean equivalence ratios, and reactant preheated temperatures. Natarajan et al. [63] investigated experimentally and

numerically the laminar flame speed of CO/H₂/CO₂/O₂/He mixtures over preheated temperatures and different pressures. Recently, Braun-Unkhoff et al. [64] described a reduced kinetic mechanism to predict laminar flame speed and auto ignition of syngas mixtures, and they found good agreement between experimental and calculated values. Ahn et al. [65] studied NO production mechanisms in counterflow syngas flames, and they found that the NO formation in syngas with N₂/O₂ mixtures increased dramatically at higher temperature, and that NO_x emission can be reduced efficiently using CO₂/O₂ as the oxidant.

2.6 Syngas Composition Effects

The syngas composition varies depending on fuel source, gasification process, and post-gasification treatment. In addition, the type and amount of diluents present for syngas combustion can vary significantly. Up to now, only three papers have been published on NO emissions for syngas with different compositions. Giles et al. [66] studied syngas composition and diluent effects on the flame structure and emissions characteristic of syngas diffusion flames, and they used two typical compositions (one with methane, and the other without methane). They found that the presence of methane in syngas decreased the peak flame temperature and increased prompt NO significantly. The addition of diluents, such as H₂O, CO₂ and N₂, all reduced NO formation in syngas, and the presence of methane reduced the effectiveness of these three diluents. Alavandi et al. [67] studied CO and NO_x emissions of hydrogen-syngas/methane premixed flames in a two-section porous burner, and they found that for a given adiabatic flame temperature, increasing H₂/CO content by decreasing methane amount, also decreased both CO and NO_x emissions. In addition, a higher

percentage of H_2 and CO in the fuel also decreased the temperature near the lean blow-off limit. Recently, Williams et al. [68] studied the effects syngas composition and CO_2 -diluted oxygen on performance of a premixed swirl-stabilized combustor. They found that the presence of hydrogen in syngas fuel mixtures resulted in more compact, higher temperature flames with increased flame stability and increased NO_x emissions. From the above literature review, it is obvious that understanding the combustion and emission of syngas mixtures with composition effects, and doping effect in jet diffusion flame is still lacking. Thus, further experimental and numerical investigations are needed to understand the NO_x formation of syngas mixtures and the effects of NH_3 seeding on NO formation.

CHAPTER 3 EXPERIMENTAL SETUP

Planar laser-induced fluorescence (PLIF) is a non-destructive, non-intrusive laser diagnostic tool to acquire planar snapshots of the flow field in reacting or non-reacting flow systems. PLIF is sensitive to gas dynamic properties such as species concentration, temperature, etc. PLIF images are obtained by using a laser to excite molecular species present in flow. This species either occurs naturally or can be seeded. Commonly measured species include NO, OH, CH, iodine, and acetone. The resulting fluorescence is typically imaged with a scientific-grade camera. This flow visualizations and quantitative measurements are commonly used to compare with Computational Fluid Dynamics (CFD) simulations.

The objective of PLIF measurements in this thesis is to visualize flame structure using OH PLIF and obtain quantitative NO mole fraction by NO PLIF in laminar diffusion flames. Investigation of flame structures can be used to better understand flow properties, the dynamics of laminar or turbulent structures, and reaction parameters that can be used to minimize NO formation. Measuring absolute NO can be valuable to refine rate coefficients of key chemical reactions controlling NO formation.

This Chapter will summarize the apparatus utilized to implement OH PLIF and NO PLIF. No calibration for absolute concentration was performed for OH-PLIF imaging, since qualitative visualization is good enough to understand properties related to flame structures. Instead, NO-PLIF imaging was calibrated using a standard addition technique by doping a specific amount of NO into a lean premixed flame. To obtain correct quantitative NO concentrations by PLIF, careful data processing is the key. Four issues need to be considered for NO PLIF. First, NO interference with other species,

such as O_2 and CO_2 , need to be corrected. Second, the temperature dependence of NO signals needs to be considered. Third, NO-PLIF signals need to be further corrected for the local collisional quenching rate. The details of PLIF data processing are summarized further in this chapter in the data processing section. Finally, details regarding the selection of excitation strategies for NO PLIF and OH PLIF are summarized.

3.1 Laser Diagnostics Setup

There are four main components of the laser diagnostics setup, as listed below:

1. A fuel-jet burner
2. Laser excitation optics to direct laser beam into the probe volume
3. Detection optics to measure fluorescence signal
4. A data collection system to process signals from various photo-detectors

Figure 3-1 represents a general laser diagnostics experimental setup. In this section, a general description of each component listed above will first be summarized. Then, the specific settings for OH PLIF and NO PLIF will be described.

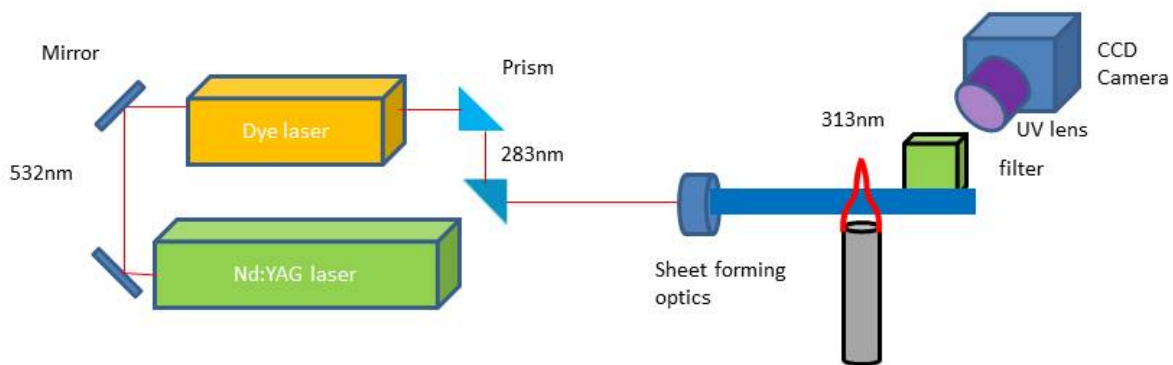


Figure 3-1: Schematic of general PLIF experimental setup.

3.1.1 Burner Setup

The burner used in this thesis is a basic fuel-jet burner. The fuel is CH₄ or syngas, which were used to form open-air laminar diffusion flames at atmospheric pressure. Figure 3-2 shows a schematic of the fuel-jet burner system used in this work. The system consists of a flow control system and a $\frac{3}{8}$ " tube (ID = 0.305", OD = $\frac{3}{8}$ "). A flow control system was used to control the mass flow rates of each fuel species (e.g. CH₄, NH₃, CO, and H₂). Each fuel is fed directly to a manifold to ensure proper mixing and then fed to a $\frac{3}{8}$ " 316 stainless steel vertical tube. The tube is insured to be long enough so the fuel stream is fully developed. On top of this tube, a diffusion flame is ignited and formed. The coordinate system used in this work is shown in Figure 3-2. The entire flame is surrounded by a 4"x4" square aluminum duct to stabilize the flame and protect it from room currents. This burner setup represents a reasonable model system to study NO formation.

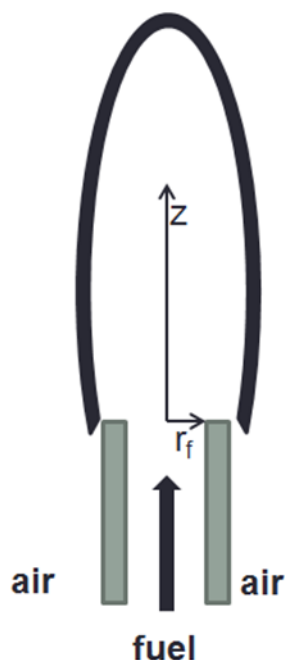


Figure 3-2: Schematic of a laminar diffusion flame from a tube burner.

3.1.2 Flow Control System

The flow rate of each species in the fuel is monitored/controlled by digital computerized Alicat[®] mass flow controllers (MFCs). They are MC series Alicat MFCs for non-corrosive gases, like CH₄, CO, and H₂, and MS series for corrosive gases or gas mixtures like NH₃, CH₄/NH₃ mixture, etc. A 1-slpm (standard liter/minute) range MFC is used for CH₄, a 5-slpm MFC range is for H₂, and a 10-slpm range is used for CO. The flow range of the MFC for corrosive NH₃ is small at 200 sccm (standard cm³/minute). All of these species are fed to a stainless steel manifold to ensure proper mixing before they are fed to the 3/8" tube. A Swagelok[®] 90° valve is used for quick shut-off in case of emergency. A LabView[®] program is used to remotely control all MFCs. Changing test conditions only requires changing mass flow rates of each of the gases, which occurs within several seconds.

3.1.3 Lasers

Laser diagnostics is used as the primary means of probing the flame chemistry in this work. Our laser system consists of an injection-seeded Nd:YAG (Neodymium Yttrium Aluminum Garnet) laser, a dye laser, and frequency conversion optics to reach the necessary UV wavelengths. Figure 3-3 shows a typical arrangement for dye lasers.

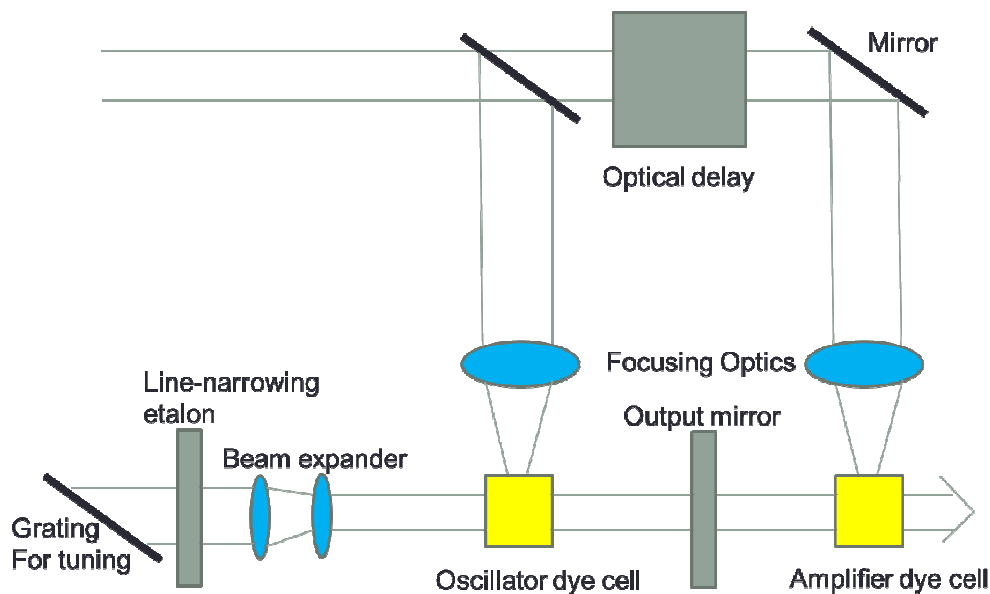
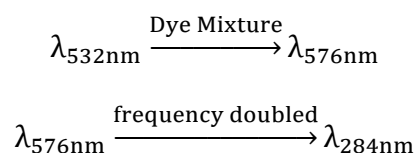


Figure 3-3: A typical arrangement for dye lasers

3.1.3.1 OH-PLIF lasers

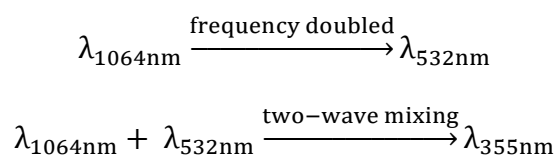
The Nd:YAG laser (Spectra-Physics[®] PIV400) is used to pump the dye laser (Continuum[®] ND 6000). The Nd:YAG laser is capable of delivering pulses of 500 mJ at wavelength of 532 nm at a frequency of 10 Hz. The laser pulses are spatially and temporally Gaussian with a beam diameter of 6.6 mm and a pulse width of 7 ns full width at half maximum (FWHM). The fundamental Nd:YAG beam, with wavelength, say , of 1064 nm is frequency doubled to generate of 532 nm as shown in the following:

A similar strategy applies inside the dye laser, which is pumped at 532 nm to generate a laser beam at 576 nm. This beam of 576 nm is then frequency doubled to generate a 283 nm beam for excitation of the OH radical. The dye solution is prepared by dissolving 300 mg of Rhodamine 590 (Exciton) dye into 700 mL of methanol for the oscillator, and 60 mg Rhodamine 590 (Exciton) dye into 700 mL of methanol for the amplifier. The following lists the procedures used to generate output at ~284 nm.



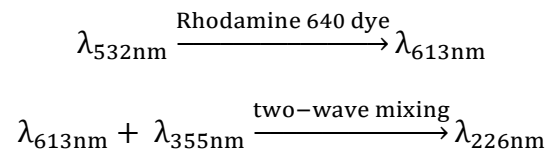
3.1.3.2 NO-PLIF lasers

The Nd:YAG laser (Spectra-Physics® PIV400) is used to pump the dye laser (Continuum® ND 6000). The Nd:YAG laser is capable of delivering pulses of 500mJ at 355nm at a frequency of 10 Hz. The laser pulses are spatially and temporally Gaussian with a beam diameter of 6.6 mm and a pulse width of 7 ns at FWHM. Inside the Nd:YAG laser, an injection seeder (Model 6350, Spectra-Physics) was used to narrow the bandwidth of fundamental, leading to narrowband second and third harmonic output. The second harmonic beam at 532 nm is mixed with the fundamental beam at 1064 nm to generate the third harmonic at 355 nm. The following lists the procedures used to generate wavelength at 355 nm.



A similar strategy applies for the dye laser. In this case, the dye laser is pumped at 532 nm utilizing a dye solution to generate a laser beam at 613 nm. This beam at

613 nm is mixed with the third harmonic from Nd:YAG laser at 355 nm to generate the 226 nm beam for excitation of the NO molecule. The dye solution was prepared by dissolving 210 mg of Rhodamine 640 dye into 700 mL of ethanol for the oscillator, and 83 mg of Rhodamine 640 dye into 700 mL of ethanol for the amplifier. The following lists the procedures used to generate laser output at 226 nm.



3.1.4 Laser Sheet Forming

In the experiment, the laser beams are directed to the flame by a set of UV reflective mirrors. After each test condition, the laser beam is directed to a power meter, and the pulse energy is recorded.

Each round laser beam is formed into a vertical sheet ~0.2-mm thick and 60-mm high by a set of lenses. This thin laser sheet then enters the flame central axis and crosses the vertical flame from side to side.

3.1.5 Detection Optics

The detection optics consists of a UV lens and filters specifically selected for OH PLIF or NO PLIF.

3.1.5.1 OH PLIF

UV-lens: a 45-mm focal length Cerco® UV objective lens with an f-number of f/1.8 is placed close to the flame to detect as much fluorescence signal as possible. The fluorescence signal encompasses a spectral width of 7 nm detected over a spectral region centered on the A-X(1, 0) band of OH at 313 nm.

Filters: The fluorescence signal occurs in a very short time span (<10 ns), whereas the intensified charge-coupled device (ICCD) camera shutter opens for 20 ns to fully detect the PLIF signal regardless of slightly drifting the laser timing. Since the camera gate is open during the laser pulse, it is essential to spectrally filter any scatter at ~ 284 nm. Two filters are used in this case. One WG295 Schottfilter (thickness of 2.0 mm) is used to fully block Rayleigh scatter. Additionally, to reduce fluorescence above 400 nm, another UG11 Schott color filter (thickness of 2.0 mm) is used. The UG11 filter also serves to further reduce signal from background visible flame emission.

3.1.5.2 NO PLIF

UV-lens: the same 45-mm focal length Cerco® UV objective lens with an f-number of f/1.8 is used and placed in the same arrangement as OH PLIF. In this case, the fluorescence signal encompass a spectral width of 11 nm detected over a spectral region centered at 248 nm. This 248 nm location corresponds to the A-X(0,2) band of NO.

Filters: LIF signals were spectrally filtered prior to detection to reject Raleigh scattering reflections from the duct surface, and fluorescence from other species such as combustion intermediates. The filter consists of a set of two mirrors with a spectrally narrow reflectivity at 248 nm, the mirrors are mounted in front of the UV objective lens. The mirrors' reflectivity is centered around the A-X(0, 2) band of NO near 248 nm with a bandwidth of approximately 22 nm to guide the fluorescence signal to the camera while allowing other light to pass through undetected.

3.1.6 Optical Access

A 7.6 cm-diameter round hole was made on the square duct's wall to allow optical access. The entire duct was painted black to reduce unwanted luminescence and scattering from the laser beam. Two 15-cm × 0.635-cm slots on the sides of the duct allow the laser sheets to pass through the flame. The camera and objective lens are then placed 90° to the laser sheet. The bottom of the laser sheets are clipped to avoid laser scatter from the metal. This reduces unwanted scattering and minimizes potential damage to ICCD camera. Based on this set up, the camera is able to view the region from the tube exit to over 6 cm above the tube, as shown in Figure 3-4. There are two small "scratches" in the image about 5 cm above the tube in the middle of the CCD chip of the camera. Hence this area is avoided and primarily the right half of the chip is used for imaging the flame.

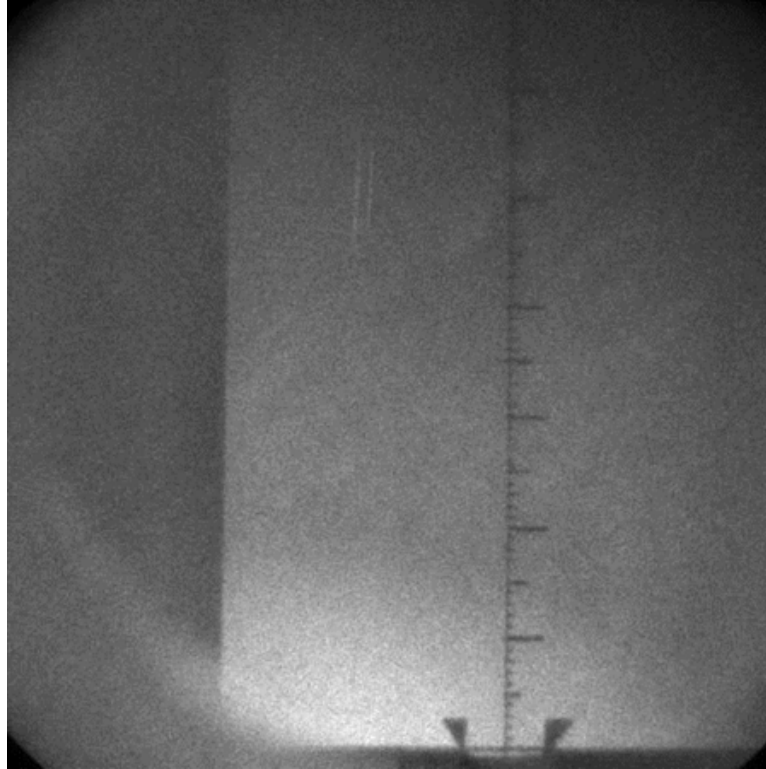


Figure 3-4: Typical field of view. The camera is able to see about 6.5 cm height above the burner tube, which is denoted by the two little triangles at the bottom. The central part of the camera chip is avoided due to damage on the detector.

3.1.7 Data Collection System

An ICCD camera (Princeton Instruments, PI-MAX II i1024) is used for 2-D PLIF image acquisition. With 2×2 pixel binning, the camera acquires monochromatic images with 512×512 pixels and a limited frame rate of 10 per second. A built-in image intensifier is used to enhance the signal-to-noise ratio. The detection system utilizes WinView 32 (Princeton Instruments) software to monitor and control the data acquisition process. After acquisition, the images are further analyzed and processed by Matlab 2010a.

Due to very weak signal levels, each NO image is obtained by accumulating 300 images onto the ICCD camera chip (300 shots per image).

3.2 OH-PLIF Setup

Figure 3-5 illustrates the OH-PLIF setup. The laser beam (10 mJ at ~284 nm) from a Nd:YAG-pumped, frequency-doubled dye laser is formed into a vertical laser sheet (60 mm × ~0.2 mm) slicing the flame vertically. It illuminates a cross-section through the vertical axis of the flame up to 6 cm above the burner nozzle. The pulse energy was monitored by a power-meter immediately after each test run. Fluorescence signals were collected at right angles to the laser sheet. LIF signals were spectrally filtered prior to detection in order to eliminate Rayleigh scattering, as discussed earlier.

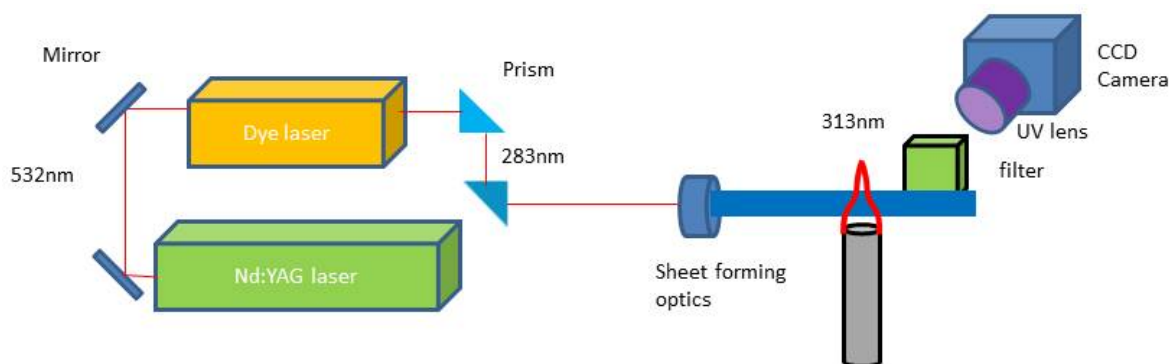


Figure 3-5: Schematic of OH-PLIF setup.

Table 3-1: Hardware and settings used for OH-PLIF measurements.

Component	Specification
Pump Laser	Nd:YAG Second Harmonic (300 mJ @ 532 nm)
Dye Laser	Two-Stage Dye Laser and BBO Crystal
Camera	Intensified CCD Camera
Lens	UV Lens, focal length $f = 45 \text{ mm}$, $f/1.8$ aperture
Optical Filters	WG-295 (high pass) and UG-11 (low pass)
Gate Time	20 ns
Gain	200x
Laser Sheet dimension	60 mm \times 0.3 mm
OH Laser Pulse Energy	10 mJ
Pulse Duration	10 ns
Excitation Wavelength	284.070 vacuum nm
Excitation Scheme	$Q_1(9) + Q_2(8) A^2\Sigma^+ - X^2\Pi(1,0)$ band
Detection Scheme	$A^2\Sigma^+ - X^2\Pi(0,0)$ band

3.3 NO-PLIF Setup

Figure 3-6 shows a schematic of the NO-PLIF setup. A laser beam ($\sim 3 \text{ mJ}$ at $\sim 226 \text{ nm}$) from a Nd:YAG-pumped, frequency-doubled dye laser is formed into a vertical light sheet (60 mm \times $\sim 0.2 \text{ mm}$) slicing the flame vertically through the central axis of the flame up to 6 cm above the burner nozzle. The pulse energy is monitored by a power-meter immediately after each test run. Fluorescence signals are collected at right angles to the laser sheet as described earlier.

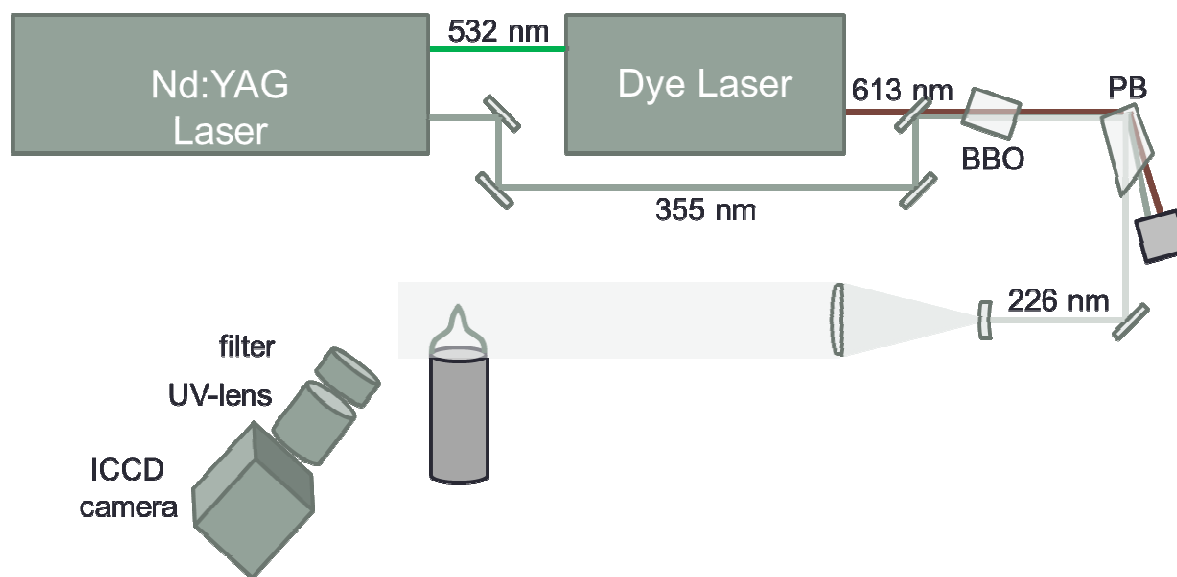


Figure 3-6: Schematic of NO-PLIF setup

Table 3-2: The hardware and setting used for NO-PLIF measurements.

Parts	Specification
Pump Laser	Nd:YAG Second Harmonic (200mJ @ 532 nm)
Dye Laser	Two-Stage Dye Laser and BBO Crystal
Camera	Princeton Instrument @ PI-MAX II i1024 ICCD Camera
Lens	UV Lens, focal length $f = 45 \text{ nm}$, $f/1.8$ aperture
Optical Filters	a set of mirrors with a spectrally narrow reflectivity curve, centered at
Gate Time	20 ns
Gain	200x
Laser Sheet dimension	60 mm 0.3 mm
Laser Pulse Energy	3 mJ
Pulse Duration	8 ns
Excitation Wavelength	226.034 vacuum nm (online) and 226.042 vacuum nm (offline)
Excitation Scheme	band
Detection Scheme	and bands

3.4 Calibration

To determine absolute NO concentration by 2-D NO-PLIF imaging, it is necessary to have an accurate calibration process. After corrections for laser-sheet inhomogeneity, PLIF interference from other species (e.g. O₂, CO₂), temperature dependence, collisional quenching and signal laser absorption, the NO signal should be proportional to the relative concentration throughout the observed area. Using a standard NO-addition technique by adding a known amount of seeded NO directly into a lean premixed flame ($\phi = 0.8$), and later comparing the fluorescence signal with the experimental NO-PLIF signal, it is possible to derive the absolute NO concentration. Detailed derivation of quantitative NO concentration is presented in later sections. In practical applications, such as engine measurements, calibration has been performed by inserting a well-characterized flame into the field of view to allow conversion of known NO concentrations to NO PLIF intensities [34, 69]. This type of *in-situ* calibration is relatively straightforward, since only the amount of seeded NO needs to be varied and monitored along with the change in NO-PLIF intensity. According to previous research on NO-PLIF [70] in premixed lean flames, NO addition in the 300-600 ppm range has a negligible influence on major species concentrations and temperature. Larger or smaller NO addition is perturbed by prompt NO or NO reburn chemistry. Thus, *in-situ* calibration in a slightly lean premixed flame with 300-600 ppm NO is more accurate than that from a calibration cell at room temperature and atmospheric pressure [71].

In the current experiment, a lean premixed CH₄/O₂/N₂/NO flame ($\phi = 0.8$) was seeded with 100 to 2000 ppm NO, with most calibration points taken in the 300 to 600

ppm range. NO then was excited at 226.030 nm at atmospheric pressure. The resulting NO fluorescence image was compared with NO fluorescence images of the flames of interest to calculate absolute NO concentrations.

3.5 Flow Conditions

For CH₄/air diffusion flames, the fuel stream consists of pure CH₄ or CH₄ seeded with NH₃. The oxidizer is the surrounding air. For syngas diffusion flames, two types of flames are used in the fuel stream. One is 45 vol% H₂, 45 vol% CO and 10 vol% CH₄, which is denoted as the F1 flame. The other is 50 vol% H₂ and 50 vol% CO, which is denoted as the F2 flame. LIF measurements are obtained at atmospheric pressure. Table 3-3 lists the flow rates for all CH₄/air diffusion flames seeded with NH₃ in this study. Table 3-4 lists the flow rates for all syngas diffusion flames seeded with NH₃ in this study.

Table 3-3: Flow rates for methane/air diffusion flames at atmospheric pressure.

Mole Fractions		Flow Rates			
CH ₄	NH ₃	NH ₃ (SCCM)			Total Flow Rates (SLPM)
16.04	17.03	MFC 9	042-07-ST	112-02-ST	
60%	40%	120	N/A	25	0.3
70%	30%	90	N/A	20	0.3
80%	20%	60	N/A	13	0.3
90%	10%	30	48	N/A	0.3
95%	5%	15	27	N/A	0.3
98%	2%	6	12	N/A	0.3
99%	1%	3	5	N/A	0.3
100%	0%	0	0	0	0.3
60%	40%	80	N/A	17	0.2
70%	30%	60	N/A	13	0.2
80%	20%	40	59	N/A	0.2
90%	10%	20	35	N/A	0.2
95%	5%	10	19	N/A	0.2
98%	2%	4	8	N/A	0.2
99%	1%	2	1	N/A	0.2
100%	0%	0	0	0	0.2

Table 3-4: Flow rates for syngas/air diffusion flames at atmospheric pressure.

	Mole Fractions				Flow Rates			
	CH4	CO	H2	NH3	CH4 (SLPM)	CO (SLPM)	H2 (SLPM)	Total Flow Rates (SLPM)
MW	16.04	28.01	2.02	17.03				
SYNGAS F1	5%	23%	23%	50%	0.020	0.09	0.090	0.4
	6%	27%	27%	40%	0.024	0.11	0.108	0.4
	7%	32%	32%	30%	0.028	0.13	0.126	0.4
	8%	36%	36%	20%	0.032	0.14	0.144	0.4
	9%	41%	41%	10%	0.036	0.16	0.162	0.4
	10%	43%	43%	5%	0.038	0.17	0.171	0.4
	10%	44%	44%	2%	0.039	0.18	0.176	0.4
	10%	45%	45%	1%	0.040	0.18	0.178	0.4
SYNGAS F2	0%	25%	25%	50%	0.000	0.10	0.100	0.4
	0%	30%	30%	40%	0.000	0.12	0.120	0.4
	0%	35%	35%	30%	0.000	0.14	0.140	0.4
	0%	40%	40%	20%	0.000	0.16	0.160	0.4
	0%	45%	45%	10%	0.000	0.18	0.180	0.4
	0%	48%	48%	5%	0.000	0.19	0.190	0.4
	0%	49%	49%	2%	0.000	0.20	0.196	0.4
	0%	50%	50%	1%	0.000	0.20	0.198	0.4
SYNGAS F1	5%	23%	23%	50%	0.030	0.14	0.135	0.6
	6%	27%	27%	40%	0.036	0.16	0.162	0.6
	7%	32%	32%	30%	0.042	0.19	0.189	0.6
	8%	36%	36%	20%	0.048	0.22	0.216	0.6
	9%	41%	41%	10%	0.054	0.24	0.243	0.6
	10%	43%	43%	5%	0.057	0.26	0.257	0.6
	10%	44%	44%	2%	0.059	0.26	0.265	0.6
	10%	45%	45%	1%	0.059	0.27	0.267	0.6
SYNGAS F2	0%	25%	25%	50%	0.000	0.15	0.150	0.6
	0%	30%	30%	40%	0.000	0.18	0.180	0.6
	0%	35%	35%	30%	0.000	0.21	0.210	0.6
	0%	40%	40%	20%	0.000	0.24	0.240	0.6
	0%	45%	45%	10%	0.000	0.27	0.270	0.6
	0%	48%	48%	5%	0.000	0.29	0.285	0.6
	0%	49%	49%	2%	0.000	0.29	0.294	0.6
	0%	50%	50%	1%	0.000	0.30	0.297	0.6

3.6 Data Processing

Data processing is summarized here in two parts. First, 2-D, OH-PLIF imaging is discussed, followed by 2-D, NO-PLIF Imaging.

3.6.1 2-D OH- and NO-PLIF Imaging

The raw OH-PLIF images from the ICCD camera are first corrected for laser sheet inhomogeneity. Quenching rate correction is performed by using experimental data on temperature-dependent quenching cross-sections from Tamura et al. [18, 74]. The processed image is further corrected for Boltzmann fraction variations with temperature. The temperature in the correction procedure is estimated from CFD results.

The average laser sheet profile to correct for inhomogeneity in excitation energy is obtained by looking at the Rayleigh scattering from air without any flame burning in the region of interest. The laser profile is then recorded at the centerline of the burner tube and used to normalize the images.

The laser sheet profile for NO PLIF is obtained in another way than OH PLIF. Because the detection wavelength is centered at 248 nm well away from the excitation wavelength ~226nm, Rayleigh scattering from air cannot be observed. In this case, a mixture of 5000 ppm NO balanced by cold N₂ is used to flood the burner tube to the height of interest. The NO-PLIF signal is recorded and averaged to extract the laser profile. The flow rate of this seeded NO is precisely controlled to make sure that the jet flow doesn't transition to turbulent flow but is still able to flood the region of interest.

The NO-PLIF signal is described as:

$$S_f = I_r \times B_{12} \times N_{NO} \times \eta_{opt} \times f_B \times \eta_{fluor} \quad (3.1)$$

where I_r is laser power density, B_{12} is Einstein absorption coefficient, N_{NO} is NO molecule number density, η_{opt} is optical collection efficiency, and f_B is the temperature-dependent Boltzmann (population) fraction of the NO excitation lines. η_{fluor} is the fluorescence efficiency, defined as:

$$\eta_{fluor} = \left(\frac{A}{Q + A} \right), \quad (3.2)$$

where Q is the total quenching rate and A is the Einstein coefficient for spontaneous emission. To obtain quantitative NO PLIF images, let “flame” denote the diffusion flames and “cal” the calibration flames, with the NO molecule number density defined as:

$$N_{NO} = X_{NO} \times N_{total} = X_{NO} \times \frac{PV}{kT} \quad (3.3)$$

Hence, the quantitative NO mole fraction is finally derived as:

$$(X_{NO})_{flame} = (X_{NO})_{cal} \frac{LIF_{flame}}{LIF_{cal}} \frac{(I_r)_{cal}}{(I_r)_{flame}} \frac{T_{flame}}{T_{cal}} \frac{(\eta_{opt})_{cal}}{(\eta_{opt})_{flame}} \frac{(f_B)_{cal}}{(f_B)_{flame}} \frac{(\eta_{fluor})_{cal}}{(\eta_{fluor})_{flame}} \quad (3.4)$$

Since the calibration flame is set up with exactly the same optical system, the ratio $\frac{(\eta_{opt})_{cal}}{(\eta_{opt})_{flame}}$ equals unity. B_{12} is canceled since same excitation and detection strategies are

used. The slope of the calibration line $k = \left(X_{NO} \times \frac{I_r}{LIF} \right)_{cal}$ is obtained from calibration flames, and temperature and quenching corrections are obtained from CFD calculations for both diffusion and calibration flames. Finally the quantitative NO is derived as:

$$X_{NO} = k \times \left(\frac{LIF}{I_r} \right)_{flame} \frac{\left(\eta_{fluor} \frac{f_B}{T} \right)_{cal}}{\left(\eta_{fluor} \frac{f_B}{T} \right)_{flame}}, \quad (3.5)$$

where the $\left(\frac{LIF}{I_r} \right)_{flame}$ is the LIF signal corrected for laser inhomogeneity.

Using the temperature estimated from CFD calculations, the corrections can be made to NO Boltzmann fraction and the quenching rate. The wavelength of 226.03 nm excites the $P_1(23.5)$, $Q_1+P_{21}(14.5)$, $Q_2+R_{12}(20.5)$ rotational transitions in the A–X(0,0) band of NO. This wavelength has been previously identified as optimal for maximum NO signal strength and minimum interference from O_2 -LIF [75].

3.6.2 Data Processing and Reduction

Based on the above information, the data acquisition procedure for the NO PLIF is as follows, e.g. four images need to be taken for each test condition:

1. The wavelength of dye-laser output beam was tuned at 226.03 nm (613.173 nm before two wave mixing), a image of flame fluorescence signal was taken, this is the image of online flame, e.g. IMG_{online_flame} .
2. Flame is turned off, the tube is flooded with cold N_2 with 5000 ppm NO at 10 SLPM. Two settings of the camera, gain factor and aperture were minimized to reduce saturation of camera chip, then a image of online flood was taken, e.g. IMG_{online_flood} . A power meter is used to monitor the power of the laser for 1 mininute and mean value is recorded.
3. Wavelength of the dye-laser output beam was adjusted to a wavelength such that the signal level is minimum, e.g. 226.09 nm (or 613.229 nm before two wave mixing). A image is recorded as the $IMG_{offline_flood}$.
4. Flood is turned off, two settings of the camera, gain factor and aperture were restored to as in step 1 above, then the flame with same condition is turned on again, a image was taken as $IMG_{offline_flame}$.

This is the basic procedure of taking NO-PLIF data. Cold flood is used to obtain the laser sheet, in the mean time, this cold flood could also cool down the potential preheating of the tube, consequently eliminate the effect of preheating on flame structure and radical distributions.

Once these four images were taken, then first of all, the laser sheet profile (or in another word the laser sheet power density $\rho_{\text{laser}}(x)$) has to be extracted. In terms of the cold N_2/NO jet, since the variations of $[\text{NO}]$, temperature and major species are minimal inside the jet, the signal intensity (e.g. $LIF(x)$) is proportional to the laser power intensity, say

$$LIF(x) \propto \rho_{\text{laser}}(x), \quad (3.6)$$

where the $LIF(x)$ is the LIF signal intensity extracted from the image manipulation ($\text{IMG}_{\text{online_flood}} - \text{IMG}_{\text{offline_flood}}$), $\rho_{\text{laser}}(x)$ is the line-power-density of laser sheet along the central axis “ x ” of the flame, i.e.

$$P = \int_{-\infty}^{\infty} \rho_{\text{laser}}(x) dx, \quad (3.7)$$

where the P is the averaged power of laser shots. In this way, it is apparent that the laser signal intensity along the central line, e.g. $LIF(x)$ has a linear relationship with the laser power density along central line, e.g. $\rho_{\text{laser}}(x)$ as:

$$LIF(x) = \frac{\rho_{\text{laser}}(x)}{P} \int_{-\infty}^{\infty} LIF(x) dx. \quad (3.8)$$

Or

$$\rho_{\text{laser}}(x) = LIF(x) \frac{P}{\int_{-\infty}^{\infty} LIF(x) dx}. \quad (3.9)$$

This is basically how the laser sheet profile is extracted raw images.

Second of all, the laser inhomogeneity, which is embedded in the $\rho_{\text{laser}}(x)$, need to be corrected. The raw images' manipulation ($\text{IMG}_{\text{online_flame}} - \text{IMG}_{\text{offline_flame}}$). The resulted image of this manipulation need to be divided by the $\rho_{\text{laser}}(x)$. In that way, the resulted images correspond to the term $\left(\frac{\text{LIF}}{I_r}\right)_{\text{flame}}$ in equation 3.5.

3.7 Selection of Excitation Strategies

This section summarizes the criteria used to select excitation strategies for OH PLIF and NO PLIF respectively. The excitation is successful if it not only has high excitation energy, but also targets a transition with high populated lower level, a low interference of other species at this wavelength, a low lifetime of the excited state for preventing quenching, and high oscillator strength to maximize fluorescence yield.

3.7.1 Excitation Schemes for OH-PLIF

3.7.1.1 The $A^2\Sigma^+ - X^2\Pi (0, 0)$ excitation band

OH can be excited from the ground state (X) $\nu' = 0$ level to the excited state (A) $\nu'' = 0$ level by photons at around 308 nm. This scheme is attractive because 308 nm can be achieved with several types of lasers. In general, the fluorescence of the red-shifted (0,1) band is monitored. The fluorescence of the blue-shifted (1,0) band is stronger in some experiments, which may be due to collision-induced populations [76]. Although stronger, this fluorescence band is problematic because it is inherently dependent on gas composition, temperature and pressure.

3.7.1.2 The $A^2\Sigma^+-X^2\Pi(3, 0)$ excitation band

The transition from the ground state (X) $\nu' = 0$ to the excited state (A) $\nu'' = 3$ level is interesting due to its high pre-dissociation rate. If the pressure is sufficiently low, fluorescence is mainly competing against pre-dissociation and quenching effects can be neglected. This is highly interesting since the rate of pre-dissociation depends only on the nature of the excited molecule whereas quenching depends on gas composition, temperature, and pressure [77]. Therefore, quantitative laser-induced pre-dissociative fluorescence (LIPF) can be easier to achieve than other LIF schemes. However, relatively weak transitions in the (3,0) band make this unattractive for low NO concentrations.

3.7.1.3 The $A^2\Sigma^+-X^2\Pi(1, 0)$ excitation band

The last scheme is based again on a transition from the ground (X) $\nu' = 0$ level, but this time OH is excited to the (A) $\nu'' = 1$ level. The major drawback of this scheme is the absence of high power laser sources at the required wavelength (around 284 nm). Dye lasers with their higher tune-ability but lower power output must to be used. Fortunately, the fluorescence emission of two different vibrational transitions can be monitored: the A-X(1, 1) and (0, 0) transitions. The existence of a strong (0, 0) emission indicates extensive energy transfers [78]. Because this efficient detection scheme is at a shifted wavelength from the excitation laser pulse, this allows elimination of strong laser scattering. This scheme has been extensively applied for diffusion flames and a variety of applications such as diesel engines [79]. Thus, we chose this excitation scheme for the OH-PLIF laser setup.

3.7.2 Excitation Schemes for NO-PLIF

NO PLIF is often applied to low-pressure, seeded, ideal combustion systems due to attenuation of the laser and fluorescence signals. Thus, careful selection of the excitation and collection wavelengths is necessary.

3.7.2.1 *The $D^2\Sigma^+-X^2\Pi(0, 1)$ excitation band*

This scheme uses the D-X(0, 1) electronic-vibronic transition of nitric oxide with an excitation wavelength at 193 nm. The excitation laser can be obtained directly from an ArF excimer laser, allowing high laser powers. Moreover, the oscillator of this transition band has a strong signal. However, only NO signals at low pressure can be captured because hot CO₂ absorption leads to significant attenuation of the laser beam [80]. In addition, specialized optics are required for efficient transmission at the excitation wavelength of 193.377 nm. For these reasons, this excitation scheme was not selected for this work.

3.7.2.2 *The $A^2\Sigma^+-X^2\Pi(0, 2)$ excitation band*

From 2000, Hildenbrand et al. [81] focused on the use of the A-X(0,2) electronic-vibronic transition of nitric oxide to study 2-D NO-PLIF imaging. As the excitation wavelength of this band is around 248 nm, the relatively high energy output of available lasers (as much as twice the one of ArF) gave this approach a solid basis. The originality of the scheme came from the monitored wavelength. In order to avoid the high fluorescence contribution of hot oxygen (above 250 nm) and intermediate hydrocarbons (above 260 nm), a choice was made to monitor fluorescence shifted towards shorter wavelengths, including emission from the (0, 1) band at 237 nm. This

was necessary as analysis of emission spectra showed that fluorescence interference was especially high above 255 nm. However, laser energies at 248 nm for the current Nd:YAG-pump dye laser are comparable with other wavelengths which have stronger absorption cross sections.

3.7.2.3 The $A^2\Sigma^+-X^2\Pi(0,0)$ excitation band scheme

This scheme consists of exciting the first vibrational level of the ground state of NO into the lowest excited electronic state i.e. through the A-X (0, 0) electronic-vibronic transition at ~226 nm. The first vibrational level of the ground state is more populated than the second or third, as used in the two other schemes. This should result in stronger signals for the comparably lower excitation power available using the current Nd:YAG/dye-laser system.

Alatas et al. [82] first used a dye laser, but since dyes fluorescing in ultra violet are rare and have low conversion efficiencies, frequency conversion from the visible range was used to double the output frequency. Lee et al. [83] studied NO-PLIF imaging using a new multi-spectral strategy and optimized the excitation strategy. In this study, the main interference to the NO LIF signal came from LIF of O₂ and CO₂, with O₂ as the major interference at atmospheric pressure. By comparing five different transitions of the NO (0, 0) band at 224.82 nm, 225.25 nm, 225.58 nm, 226.03 nm and 226.87 nm, Di Rosa et al. [84] optimized the signal strength and minimized O₂ interference for high NO signal purity.

In the current work, the excitation wavelength of 226.030 nm is selected, which is the same as that found by Di Rosa *et al.* [84] to minimize oxygen absorption while being close to peak nitric oxide absorption. Polycyclic aromatic hydrocarbons (PAH)

fluorescence was found to be very low intensity and a filter system consisting of a series of 248 nm mirrors, as described previously, can carefully selected to isolate and collect the targeted NO signal.

3.8 Summary

This chapter is summarized as follows.

1. Qualitative OH-PLIF was successfully set up, including careful selection of optics, laser excitation scheme, ICCD camera, DAQ system, etc.
2. Quantitative NO-PLIF was successfully set up, including careful selection of laser optics, laser excitation scheme, ICCD camera, DAQ system, etc.
3. Concerning quantitative NO-PLIF setup, various excitation and detection schemes are discussed/compared. In particular, excitation in the A-X(0,0) band near 226.030 nm was selected, along with wavelength-shifted detection of the A-X (0,0), (0,1), and (0,2) bands centered at ~248 nm. Corrections for quenching rate and Boltzmann effects were also implemented.
4. In addition to the NO-PLIF experimental setup, calibration flames were set up to obtain absolute NO concentration. These are lean (equivalence ratio $\phi = 0.8$) premixed CH₄/O₂ flames diluted by N₂ with specific amounts of NO addition. Increases of NO concentration and corresponding increases in signal in the calibration flame were assumed to be due to NO addition to that flame. The flow fields of these calibration flames were assumed to be unperturbed by NO addition. These linear assumptions are validated later in this thesis by developing a corresponding calibration curve.

5. A tubular jet diffusion flame burner controlled by electronic mass flow controllers was built. CH₄ and syngas (F1: 45% CO, 45% H₂, and 10% CH₄; and F2: 50% CO and 50% H₂) diffusion flames were utilized in this set up.

CHAPTER 4 CHEMICAL KINETICS MODELING

This chapter describes the numerical model used to predict NO formation mechanisms and compare with experimental PLIF measurements. A two-dimensional axisymmetric time-dependent CFDC code (Computational Fluid Dynamics with Chemistry) known as UNICORN (UNsteady Ignition and COmbustion with ReactionS) has been developed over the past two decades to assist in understanding the flame dynamics [85]. UNICORN, which solves full equations of continuity/mass, momentum, species' mass fractions and energy in radial (r -) and axial (z -) directions, is one of the well-validated research codes of its kind. It successfully predicts ignition, extinction, and other dynamic characteristics of diffusion flames of hydrogen, methane, propane, and even higher hydrocarbon fuels. The current research uses this well-validated simulation together with PLIF to understand NO formation in laminar diffusion flames.

UNICORN successfully predicts flame dynamics (velocities, flow pattern) and scalars, such as density, temperature, and species distribution (e.g. OH, NO). Once incorporated with detailed chemical mechanisms (i.e., thermal data, transport data, and reaction rates of elementary reactions), it can be used to investigate major species (e.g., CH₄, H₂, CO, CO₂, N₂, etc.) , as well as minor species and intermediates (e.g., OH, CH_i, NO_x, N₂O, etc.).

UNICORN has been validated using a number of experimental configurations in the past two decades. For instance, NO formation was investigated in low-speed buoyant H₂/air diffusion flames [86], where it was found that local temperature and NO concentrations increase in the compressed region and decrease in the stretch regions of the flame. The temperature variation was due to non-unity of Lewis number and

curvature effects. To verify this prediction, experiments were carried out by Carter et al. [87] to measure OH and NO concentrations with PLIF and temperatures with Thin-Filament Pyrometry. Figure 4-1 shows the temperature, OH concentration, and NO concentration in this dynamic flame at an axial location of 80 mm from nozzle exit. Experimental data is shown on the left, with simulation data on the right. The excellent agreement between experiments and numerical simulation confirmed that UNICORN, combined with PLIF is a very powerful research tool to understand NO formation in diffusion flames.

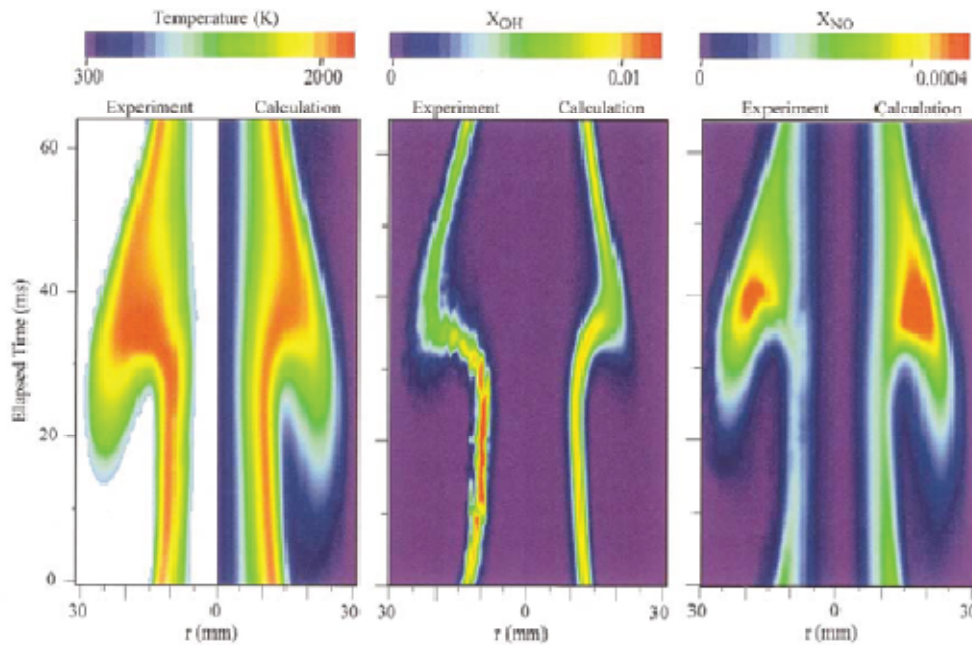


Figure 4-1: Evolution of temperature, OH concentration, and NO concentration in a H_2 /air jet diffusion flame at axial location 80 mm above nozzle exit. Contour table is given at the top.

The remainder of this chapter focuses on the CFD modeling of the combustion process. Computational Fluid Dynamics (CFD) is used for two purposes in this project.

Firstly, CFD is used to calculate important scalars, such as major species' concentrations and temperature in CH₄/air flames, as discussed later in Chapter 5. Secondly, relative contributions of each sub-mechanisms (thermal NO, prompt NO, fuel NO, N₂O intermediate, NNH, etc.) in CH₄ and syngas diffusion flames are studied numerically, as discussed in Chapters 5 and 6.

CFDC is used to numerically integrate the fluid-mechanics-related partial differential equations (PDEs), including energy and species conservations equations for the case with chemical reactions. In this way, a computational domain of interest needs to be determined first. Then the PDEs need to be discretized and solved in this domain both spatially and temporally with boundary conditions and initial conditions, respectively. Elements of the well-posed problem are listed as:

1. Governing equations, usually fluid-mechanics-related partial differential equations.
2. Temporal and spatial discretization of these governing equations.
3. An appropriate computational domain, whose properties (e.g. size) shouldn't affect the computational results.
4. Boundary conditions that specify variables and/or derivatives of variables on the boundaries of computational domain.
5. Initial conditions that specify variables initially applied within the domain. In our case of a steady state axisymmetric diffusion flame, this initial condition is trivial.

In the following sections, each element mentioned above is discussed in detail.

4.1 Governing Equations

The CFD approach computationally solves the time-dependent governing equations of reacting flow. Since it is an axisymmetric problem, the governing equations are deployed in cylindrical coordinates without azimuthal variable θ , i.e. two dimensionally in only the radial (r -) and axial (z -) directions and $\frac{\partial}{\partial \theta} = 0$, according to “axisymmetry”. These are generalized as:

$$\frac{\partial(\rho\phi)}{\partial t} + \frac{\partial(\rho v\phi)}{\partial r} + \frac{\partial(\rho u\phi)}{\partial z} = \frac{\partial}{\partial r} \left(\Gamma^\phi \frac{\partial\phi}{\partial r} \right) + \frac{\partial}{\partial z} \left(\Gamma^\phi \frac{\partial\phi}{\partial z} \right) - \frac{\rho v\phi}{r} + \frac{\Gamma^\phi}{r} \frac{\partial\phi}{\partial r} + S^\phi \quad (4.1)$$

where u and v represent the velocity components in the axial and radial directions, respectively.

Table 4-1: Variable ϕ , transport coefficients and source terms in governing equations.

Equations	ϕ	Γ^ϕ	S^ϕ
Continuity (4.2)	1	0	0
Axial Momentum (4.3)	u	μ	$-\frac{\partial P}{\partial z} + (\rho_0 - \rho)g + \frac{\partial}{\partial z} \left(\mu \frac{\partial u}{\partial z} \right) + \frac{\partial}{\partial r} \left(\mu \frac{\partial v}{\partial z} \right) + \frac{\mu}{r} \frac{\partial v}{\partial z}$ $-\frac{2}{3} \left(\frac{\partial}{\partial z} \left(\mu \frac{\partial u}{\partial z} \right) + \frac{\partial}{\partial z} \left(\mu \frac{\partial v}{\partial r} \right) \right) + \frac{\partial}{\partial z} \left(\mu \frac{v}{r} \right)$
Radial Momentum (4.4)	v	μ	$-\frac{\partial P}{\partial r} + \frac{\partial}{\partial r} \left(\mu \frac{\partial u}{\partial r} \right) + \frac{\partial}{\partial r} \left(\mu \frac{\partial v}{\partial r} \right) + \frac{\mu}{r} \frac{\partial v}{\partial r} - 2\mu \frac{v}{r^2}$ $-\frac{2}{3} \left(\frac{\partial}{\partial r} \left(\mu \frac{\partial u}{\partial z} \right) + \frac{\partial}{\partial r} \left(\mu \frac{\partial v}{\partial r} \right) \right) + \frac{\partial}{\partial r} \left(\mu \frac{v}{r} \right)$
Species mass fraction (4.5)	Y_i	ρD_{i-mix}	$\dot{\omega}_i$
Enthalpy (4.6)	H	$\frac{\lambda}{c_p}$	$\nabla \cdot \left(\frac{\lambda}{c_p} \sum_1^{N_s} \left((Le_i^{-1} - 1) H_i \nabla Y_i \right) \right) - \sum_1^{N_s} (h_{f,i}^0 \dot{\omega}_i) + q_{rad}$

This is a general form for mass/continuity, momentum, species and enthalpy equations with ϕ , Γ^ϕ , and S^ϕ taking different definitions. Hence, the above governing equation takes different forms, as summarized in Table 4-1. In the above equations, to calculate species mass fraction Y_i , the transport property D_{i-mix} represents the mixture-averaged diffusion coefficients of the i -th species in the gas mixture, where $i = 1, \dots, N_s$. N_s is the total number of chemical species in the chemical mechanism. To calculate energy, the sensible enthalpy H is calculated by the following equation:

$$H = \sum_{i=1}^{N_s} Y_i H_i = \sum_{i=1}^{N_s} Y_i (h_i - h_{f,i}^0) = \int_{T_0}^T c_p dT \quad (4.7)$$

where the h_i is the total enthalpy of the i -th species, $h_{f,i}^0$ is the i -th species' heat of formation at standard temperature T_0 . To calculate the enthalpy, the Lewis number is needed for each species, and it is defined in the following equation as:

$$Le_i = \frac{\lambda}{\rho c_{p,i} D_{i-mix}} \quad (4.8)$$

Thus, the total number of equations above is $N_s + 4$, with N_s representing the total number of species. However, the unknowns in the equations are the species mass fraction Y_i ($i = 1, \dots, N_s$), sensible enthalpy (H), temperature (T), density (ρ), pressure (P), axial velocity (u) and radial velocity (v). All these unknowns add up to a total number of $N_s + 6$. Hence, two more equations are needed to close this set of equation. One equations is:

$$Y_{N_2} = 1.0 - \sum_{i=1}^{N_s-1} Y_i, \quad (4.9)$$

which means that all of the mass fractions add up to unity. And since that N_2 is usually the largest major species, it is conventionally determined lastly to preserve the consistency of mass fractions. Another is the equation of state:

$$P = \rho T R_u \sum_{i=1}^{N_s} \left(\frac{Y_i}{MW_i} \right), \quad (4.10)$$

which is the multi-species version of the ideal gas law.

4.2 Chemical Kinetics

Each chemical species is considered as a passive scalar but with a source term $\dot{\omega}_i$, due to consumption or production of chemical reactions, as shown in Table 4-1. So, spatial distribution of i -th species is resolved by solving transport equation of its i -th mass fraction, Y_i , with its production/consumption rate, $\dot{\omega}_i$, as one of the source terms on the right hand side of the equation. With detailed chemical kinetics, which includes transport data and thermodynamics data for each species and numerous elementary reactions, $\dot{\omega}_i$ can be calculated accordingly as:

$$\dot{\omega}_i = \sum_{i=1}^{N_s} v_{i,k} q_j = (v''_{i,k} - v'_{i,k}) \left(k_{f,k} \prod_{i=1}^{N_s} [X_i]^{v''_{i,k}} - k_{b,k} \prod_{i=1}^{N_s} [X_i]^{v'_{i,k}} \right), \quad (4.11)$$

where $v''_{i,k}$ is the stoichiometric coefficient on the product side for the i -th species in the k -th reaction, and $v'_{i,k}$ is the stoichiometric coefficient from the reactant side for the i -th species in the k -th reaction. Similarly, $k_{f,k}$ is the forward reaction rate of the k -th reaction, and $k_{b,k}$ is the backward reaction rate. $k_{f,k}$ is calculated directly from modified Arrhenius Law as:

$$k_{f,k} = AT^N \exp\left(-\frac{E_a}{R_u T}\right), \quad (4.12)$$

where the pre-exponential coefficient A , temperature exponent N , and active energy E_a can be obtained directly from chemical mechanism being used. $k_{b,k}$ is deduced from equilibrium constant K_p as following:

$$K_p = \frac{k_{f,k}}{k_{b,k}} = \exp\left(-\frac{\Delta G_T^0}{R_u T}\right), \quad (4.13)$$

where the ΔG_T^0 is the standard gibbs energy and R_u is the universal gas constant.

In current CFD simulations, two chemical mechanisms were used. They are the GRI-Mech 3.0 and a detailed mechanism proposed by Tian et al. which is referred to here as the Tian mechanism. Details of these mechanism are presented in Chapter 2.

4.3 Thermodynamics and Transport Properties

The thermodynamic and transport properties are summarized in this section. For the i -th species, the total enthalpy (h_i), constant-pressure specific heat ($c_{p,i}$) and entropy (s_i) are calculated based on the thermodynamics and transport data being used with the corresponding chemical mechanism. The viscosity (μ_i), thermal conductivity (λ_i), and binary diffusivity coefficients (D_{i-j}) are calculated by Chapman-Enskog collision theory, respectively as [88]:

$$\mu_i = \left[2.669 \frac{\sqrt{MW_i T}}{\sigma_i^2 \Omega_v(T^*)} \right], \quad (4.14)$$

$$\lambda_i = \left(0.115 + 0.354 \cdot \frac{c_{p,i}}{R_u} \right) \left[8.322 \times 10^{-2} \frac{\sqrt{T}}{\sqrt{MW_i} \sigma_i^2 \Omega_v(T^*)} \right], \quad (4.15)$$

$$D_{i-j} = \left[\frac{0.2669 \times 10^{-6} T^{\frac{3}{2}}}{P \cdot \sigma_{ij}^2 \sqrt{MW_i} \Omega_D(T^*)} \right]. \quad (4.16)$$

Calculation of λ_i is corrected for internal energy storage, which makes it useful for calculation of polyatomic gases. The values of collision integrals $\Omega_v(T^*)$ and $\Omega_D(T^*)$ can be obtained from Neufeld et al. [89]. After obtaining each parameter from the above calculations for the i -th species, ϕ_{ij} , which is the approximation of ratio $\left(\frac{D_{ii}}{D_{ik}}\right)$ for nonpolar gases mixtures, can be calculated as:

$$\phi_{ij} = \frac{1}{2\sqrt{2}} \left[1 + \frac{MW_i}{MW_j} \right]^{-\frac{1}{2}} \left[1 + \left(\frac{\mu_i}{\mu_j} \right)^{\frac{1}{4}} \left(\frac{MW_i}{MW_j} \right)^{\frac{1}{4}} \right]^2. \quad (4.17)$$

Mixture properties are calculated using the following semi-empirical equations [90]:

$$\mu = \sum_{i=1}^N \frac{\mu_i}{1 + \sum_{\substack{k=1 \\ k \neq i}}^N \left(\frac{X_j}{X_i} \right) \phi_{ij}}, \quad (4.18)$$

$$\lambda = \sum_{i=1}^N \frac{\lambda_i}{1 + \sum_{\substack{k=1 \\ k \neq i}}^N 1.065 \left(\frac{X_j}{X_i} \right) \phi_{ij}}, \quad (4.19)$$

$$D_{i-m} = \frac{1 - X_i}{\sum_{\substack{j=1 \\ j \neq i}}^N 1 \left(\frac{X_j}{D_{ij}} \right)}, \quad (4.20)$$

To calculate thermal radiation, Planck mean absorption coefficients were needed for temperature-dependent curve fits. The absorption coefficients of H₂O, CO₂, CH₄, H₂, and CO were obtained from Grosshandler et al. [91].

4.4 Boundary Conditions

In this work, we applied three kinds of boundary conditions at each corresponding boundary of the computational domain. They are axisymmetric condition,

inflow condition, and outflow condition. As shown in Figure 4-2, the domain is bounded by four straight lines. The vertical straight line on the left is imposed with an axisymmetric boundary. The bottom horizontal line is the inlet of the entire domain, which consists of two inflow boundaries of the jet and coflow, respectively. Another vertical line on the right is the far-field boundary, whose boundary condition is though the same as the coflow condition. The top horizontal line is the outlet of the domain, which is composed of an outflow condition, where all gradients are set to zero across the boundary. The overall boundary conditions are presented in Figure 4-2.

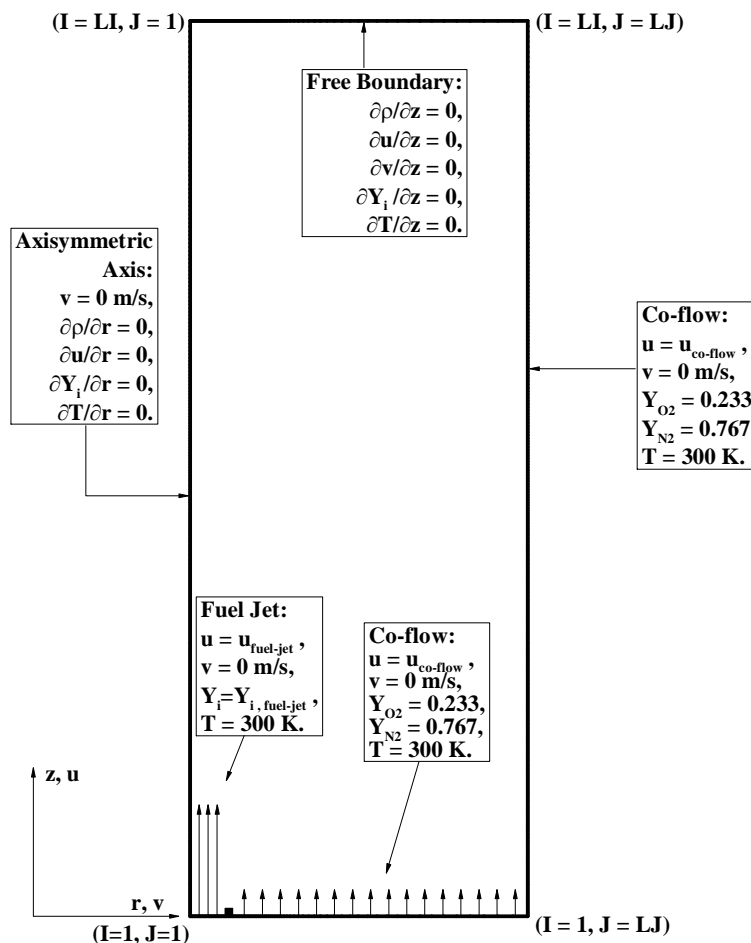


Figure 4-2: Detailed boundary conditions in the simulations.

As shown in the graph, the axisymmetric condition is applied at the left side of the domain. Since it is an axisymmetric boundary, there is no mass and momentum flux across this boundary, thus the radial velocity $v|_{r=0} = 0$ m/s. The “zero gradient” boundary condition is imposed by setting the values at $J = 1$ (axisymmetric axis) equal to those at $J = 2$ (grid points next to axisymmetric axis). It is mathematically expressed as $\frac{\partial \phi}{\partial r} = 0$, where “ ϕ ” represents primitive variables of density (ρ), axial velocity (u, v), mass fraction (Y_i), and temperature (T).

On the inflow type boundary conditions at the bottom, the variables are set constant. These variables include axial and radial velocities, temperature, pressure and species mass fraction ($\text{CH}_4, \text{H}_2, \text{O}_2, \text{N}_2, \text{CO}$ and CO_2). The velocity profiles can be either uniform or parabolic. There are two types of inflow boundary conditions used in this thesis: the fuel jet and co-flow conditions. The fuel-jet inflow condition is placed at the bottom of the computational domain in the section $0 \leq r \leq R_0$, with R_0 as the inner radius of the burner tube. In this boundary condition, a gaseous fuel composition is assigned, such as 40 vol% CO, 40 vol% H_2 , and 20 vol% CH_4 . The co-flow condition is placed at the bottom section $R_0 < r \leq R_{\text{domain}}$ and right vertical boundary, where air with a very small vertical velocity of 0.001 m/s, is imposed.

The free surface conditions are applied to the top boundary of the domain. All variables are set to have zero axial gradients, i.e. $\frac{\partial \phi}{\partial z} = 0$, where “ ϕ ” represents primitive variables of density (ρ), axial velocity (u, v), mass fraction (Y_i), and temperature (T).

4.5 Control Volume and Finite Difference Schemes

The discretization of the governing equations in the computational domain is a hybrid of the finite volume method (FVM) and the finite difference method (FDM).

A schematic of this approach is shown in Figure 4-3. The governing equations are integrated by the QUICKEST (Quadratic Upstream Interpolation for Convective Kinematics with Estimated Streaming Terms) scheme, developed by Leonard [92]. The finite-difference forms of the species and energy equations are obtained from the hybrid scheme of Spalding [93]. This scheme is third-order accurate both in space and time. This, along with very low numerical dissipation, is critical in simulating the buoyancy-driven and shear-driven structures of flames. The QUICKEST approach is implemented implicitly on a staggered grid. It is shown schematically in Figure 4-3. Suppose we are advancing from the N -th time step, when all of the variables are known, to the $(N + 1)$ -th time step, when variables are unknown. Then, with the governing equations and numerical fluxes across the boundaries of control volumes calculated, the finite difference forms of the governing equations can be written as:

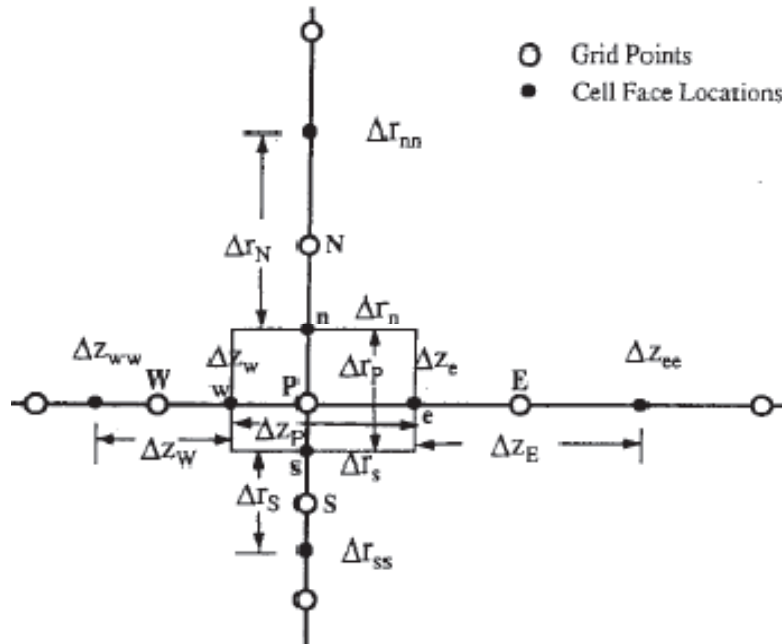


Figure 4-3: Schematic diagrams of the FVM/FDM schemes, courtesy of Katta et al. [94].

$$\begin{aligned}
 A_P \Phi_P^{N+1} + A_{EE} \Phi_{EE}^{N+1} + A_E \Phi_E^{N+1} + A_W \Phi_W^{N+1} + A_W \Phi_W^{N+1} + A_{NN} \Phi_{NN}^{N+1} + A_N \Phi_N^{N+1} + A_S \Phi_S^{N+1} \\
 + A_{SS} \Phi_{SS}^{N+1} = \Delta t \cdot S_P^\Phi + \rho_P \Phi_P^N
 \end{aligned}
 \quad (4.21)$$

This finite differencing represents four equations, which are solved individually by the iterative alternative direction implicit (ADI) technique. This involves obtaining solutions for pentadiagonal matrices in the r and z directions iteratively until the residual drops below a certain level. In the above equation, the time step Δt is maintained constant as $\Delta t = CFL \cdot \frac{\Delta l_{\min}}{|\vec{v}|_{\max}}$, where the CFL is the Courant-Friedrich-Lax number, Δl_{\min} is the minimal grid distance, and $|\vec{v}|_{\max}$ is the maximum velocity magnitude. The subscripts “E” and “W” represent the grid points immediately next to grid point P in the positive and negative z directions, respectively. In this way, the EE and WW denote the locations two grid points away from point P in the z directions. All of the coefficients A and the terms on the right hand side are calculated based on the N -th time step, as:

$$A_N = \frac{\Delta t}{\Delta r_p} \left[-(\rho_n v_n) \Delta r_n^2 \left(\frac{1}{6} - \gamma_n - \frac{1}{6} C_n^2 \right) c_1 \right], \quad (4.22)$$

$$A_{NN} = \frac{\Delta t}{\Delta r_p} \left\{ (\rho_n v_n) \left[\frac{1}{2} - \frac{C_n}{2} - \Delta r_n^2 \left(\frac{1}{6} - \gamma_n - \frac{1}{6} C_n^2 \right) c_2 \right] + (\rho_s v_s) \Delta r_s^2 \left(\frac{1}{6} - \gamma_s - \frac{1}{6} C_s^2 \right) d_1 - \frac{\Gamma_n}{r_n} \right\} - \frac{\Delta t}{r_p} \frac{\Gamma_p}{2 \Delta r_n}, \quad (4.23)$$

$$A_S = \frac{\Delta t}{\Delta r_p} \left\{ -(\rho_n v_n) \Delta r_n^2 \left(\frac{1}{6} - \gamma_n - \frac{1}{6} C_n^2 \right) c_4 - (\rho_s v_s) \left[\frac{1}{2} + \frac{C_s}{2} - \Delta r_s^2 \left(\frac{1}{6} - \gamma_s - \frac{1}{6} C_s^2 \right) d_3 \right] - \frac{\Gamma_s}{r_s} \right\} + \frac{\Delta t}{r_p} \frac{\Gamma_p}{2 \Delta r_s}, \quad (4.24)$$

$$A_{SS} = \frac{\Delta t}{\Delta r_p} \left[(\rho_s v_s) \Delta r_s^2 \left(\frac{1}{6} - \gamma_s - \frac{1}{6} C_s^2 \right) d_4 \right]. \quad (4.25)$$

The expressions for A_E, A_W, A_{EE}, A_{WW} can be written similarly. Then the coefficient A_P is:

$$A_P = \rho_P^N - (A_{NN} + A_N + A_{SS} + A_S + A_{WW} + A_W + A_{EE} + A_E). \quad (4.26)$$

The local Courant numbers (C_s, C_n) and the diffusion parameters are given by:

$$C_n = v_n \frac{\Delta t}{\Delta r_n} \quad (4.27)$$

$$C_s = v_s \frac{\Delta t}{\Delta r_s} \quad (4.28)$$

$$\gamma_n = \Gamma_n \frac{\Delta t}{\Delta r_n^2} \quad (4.29)$$

$$\gamma_s = \Gamma_s \frac{\Delta t}{\Delta r_s^2} \quad (4.30)$$

The coefficients c_i and d_i are determined on the directions of the velocities, v_n and v_s , or in another words based on upwind differencing. Other coefficients can be written similarly, such as

$$v_n \geq 0 \left\{ \begin{array}{l} c_1 = 0 \\ c_2 = \left(\frac{1}{\Delta r_p} \frac{1}{\Delta r_n} \right) \\ c_3 = - \left(\frac{1}{\Delta r_p} \frac{1}{\Delta r_n} + \frac{1}{\Delta r_p} \frac{1}{\Delta r_s} \right) \\ c_4 = \left(\frac{1}{\Delta r_p} \frac{1}{\Delta r_s} \right) \end{array} \right\}, \quad (4.31)$$

$$v_n < 0 \left\{ \begin{array}{l} c_1 = \left(\frac{1}{\Delta r_N} \frac{1}{\Delta r_{nn}} \right) \\ c_2 = - \left(\frac{1}{\Delta r_N} \frac{1}{\Delta r_{nn}} + \frac{1}{\Delta r_N} \frac{1}{\Delta r_n} \right) \\ c_3 = \left(\frac{1}{\Delta r_N} \frac{1}{\Delta r_n} \right) \\ c_4 = 0 \end{array} \right\}, \quad (4.32)$$

$$v_s \geq 0 \left\{ \begin{array}{l} d_1 = 0 \\ d_2 = \left(\frac{1}{\Delta r_s} \frac{1}{\Delta r_s} \right) \\ d_3 = - \left(\frac{1}{\Delta r_s} \frac{1}{\Delta r_s} + \frac{1}{\Delta r_s} \frac{1}{\Delta r_{ss}} \right) \\ d_4 = \left(\frac{1}{\Delta r_s} \frac{1}{\Delta r_{ss}} \right) \end{array} \right\}, \quad (4.33)$$

$$v_s < 0 \left\{ \begin{array}{l} d_1 = \left(\frac{1}{\Delta r_p} \frac{1}{\Delta r_n} \right) \\ d_2 = - \left(\frac{1}{\Delta r_p} \frac{1}{\Delta r_n} + \frac{1}{\Delta r_p} \frac{1}{\Delta r_s} \right) \\ d_3 = \left(\frac{1}{\Delta r_p} \frac{1}{\Delta r_s} \right) \\ d_4 = 0 \end{array} \right\}. \quad (4.34)$$

Base on the above equations, the governing equations can be numerically solved. The detailed numerical procedures in all iterations are described in the next section.

4.6 Numerical Procedure

The time step is determined by multiplying the minimum grid spacing by the CFL number and maximum velocity magnitude, as:

$$\Delta t = CFL \times \left(\frac{\Delta l_{\min}}{|\vec{v}|_{\max}} \right) \quad (4.35)$$

Usually 0.5 is selected as the *CFL* number. For our current grid system (151×61), $\Delta t = 0.15$ msec is used. For each iteration, the procedure is detailed as follows:

1. Calculate transport properties for each species and then the mixture.
2. Solve species and energy equations to get mass fractions, Y_i and sensible enthalpy H . A stable numerical-integration procedure is achieved by coupling the equations through the chemical reaction source terms.
3. Calculate the mixture temperature based on ideal gas theory.
4. Calculate the density based on the state equation.
5. Calculate the axial velocity from the u -momentum equation.
6. Calculate the radial velocity from the v -momentum equation.
7. Calculate the pressure by solving the Poisson equations.
8. Use the pressure gradients to correct the axial and radial velocities.

Steps 5 through 7 are to decouple the Navier-Stoke equations with continuity equation. The N-S equations are first solved assuming uniformly distributed pressure in the flow field. A complete decoupling is achieved using previous values of v in the u -momentum equation. Further details about the numerical model and the computational algorithm can be found in papers published by Katta and his coworkers [95-97].

4.7 Thermal Radiation Model

A sink term based on an optically thin gas assumption is incorporated in the energy equation to account for thermal radiation from the flame. The sink term is defined as $q_{\text{rad}} = -4\sigma K_p(T^4 - T_0^4)$, where T is the local flame temperature and K_p is the

absorption and emission sum from participating gaseous species (CO, H₂ and CH₄) [98].

It is expressed as:

$$K_p = P \sum_k X_i K_{p,i}, \quad (4.36)$$

where $K_{p,i}$ is the mean absorption coefficient of the i -th species, whose actual value can be obtained from a polynomial approximation to the experimental data [91].

4.8 Grid Size

Grid lines are clustered near the flame surfaces, in accordance with the steep gradients of the dependent variables. A study has been completed to confirm that the numerical solution is grid-independent. For this study, three sets of grid systems have been used to test the solution independence, they are 151×61 , 201×81 , and 251×101 . For each simulation, the chemical mechanism, boundary conditions, and initial conditions are identical to make sure that the only difference is the grid size. Since the solution along the centerline (axisymmetric axis on the left) of the simulated flames is of great interest, the temperature profiles along the centerline are investigated. Figure 4-4 shows the temperature profiles along the axisymmetric axis boundary. It is shown that the profile predicted by 151×61 is almost identical to the other two profiles within the region of interest, such as from 0 to 5 cm. The chemical kinetics mechanism used in these simulations is GRI-Mech 3.0.

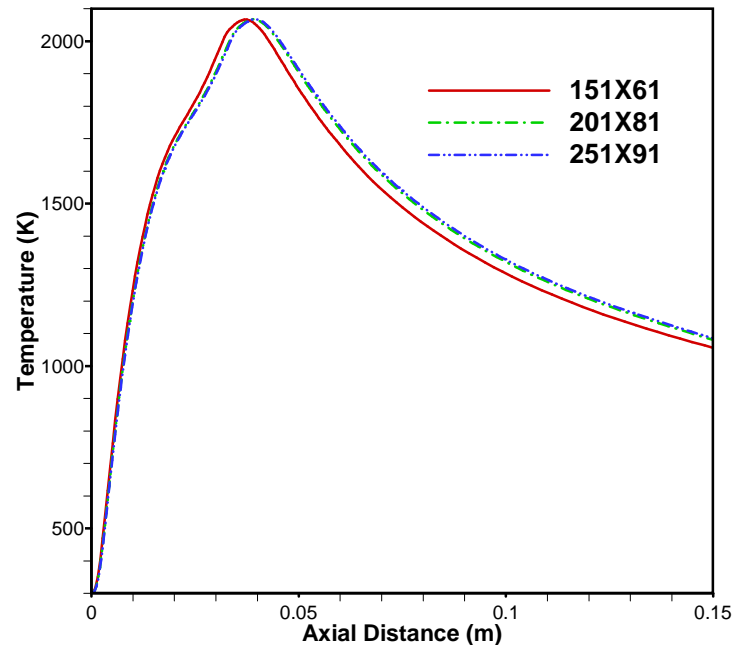


Figure 4-4: Temperature profiles along the "axisymmetric axis" boundary.

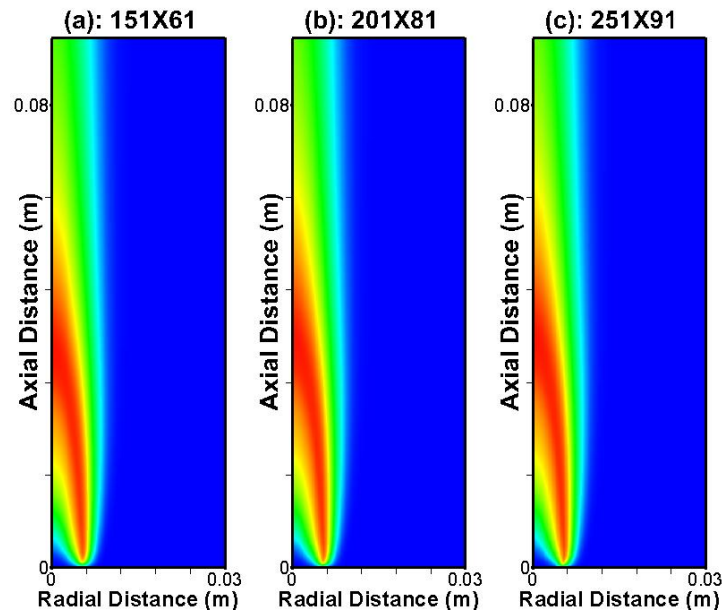


Figure 4-5: A comparison of 2-D temperature distribution, which shows that the temperature distributions are almost identical within the domain.

Figure 4-5 also shows the 2-D temperature distribution in the computational domain, and it is apparent that the distributions are identical to each other with the different sets of grid systems.

4.9 Physical Model

The physical domain used in this research is an 85 mm × 150 mm rectangle. The inner diameter of the jet is 7.747 mm (0.305"). The wall thickness of the tube is 0.889 mm $\left[\left(\frac{3}{8} - 0.305\right) = 0.07 \text{ inch}\right]$. It turned out that this wall thickness has trivial effect on the flow field, so in our research, this wall thickness isn't modeled and is assumed as zero. As mentioned earlier, the left boundary is the axisymmetric axis (centerline of the simulated flame). The right boundary is set as the coflow boundary, which extends from $\frac{7.747\text{mm}}{2} \approx 4.0 \text{ mm}$ to the right boundary at the bottom. The central jet condition extends along the bottom from zero to 4.0 mm. Figure 4-6 demonstrates the scheme of the physical domain and grids used in current research.

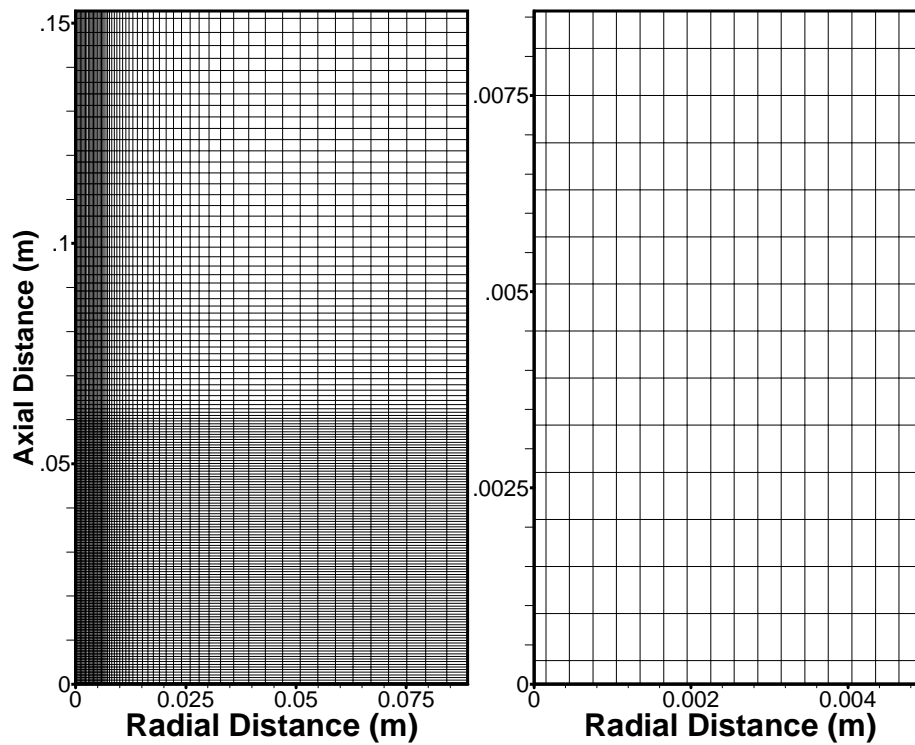
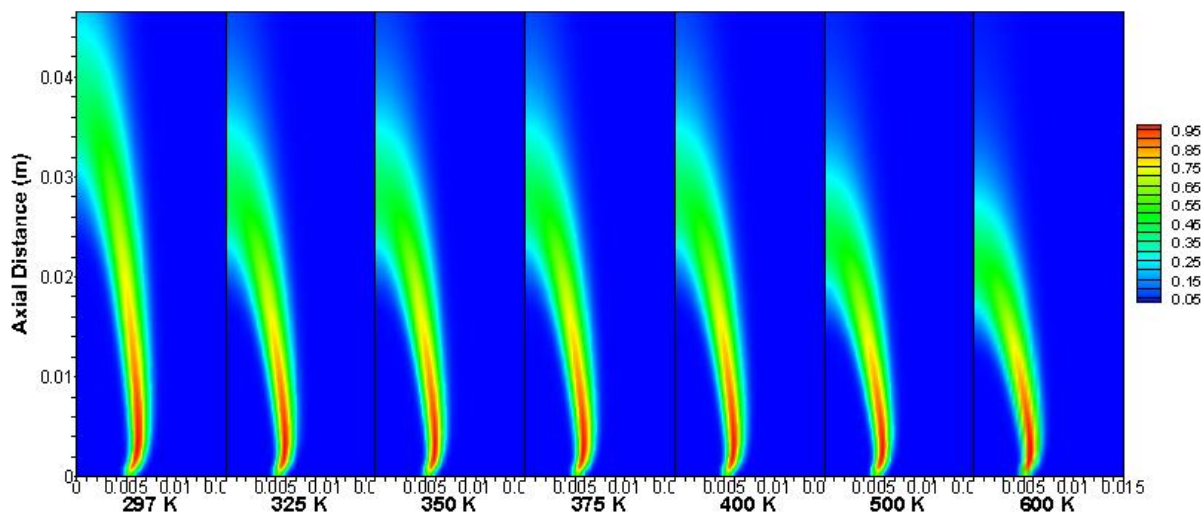


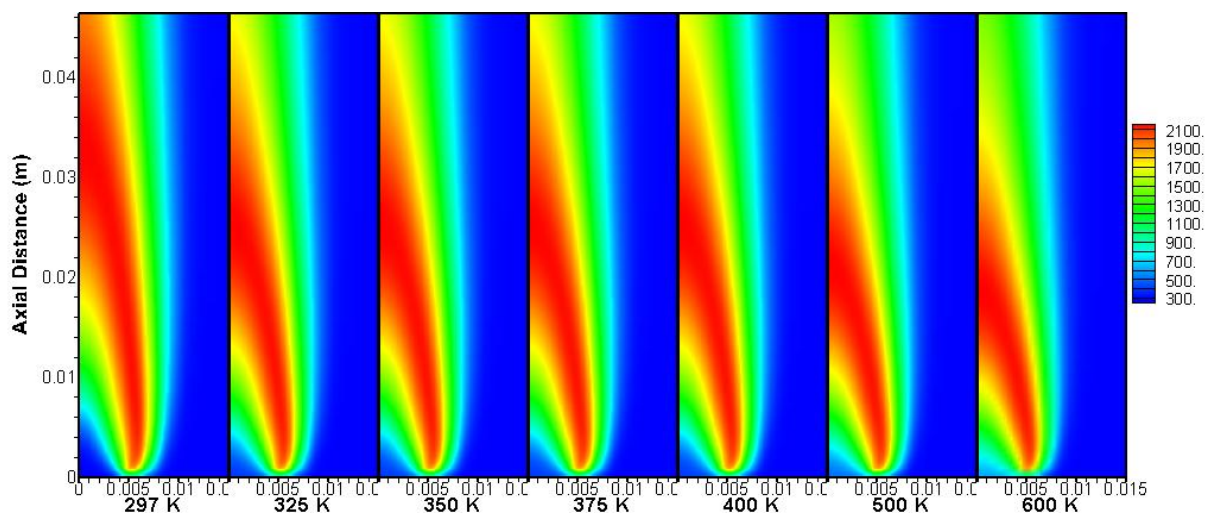
Figure 4-6: A schematic of the physical domain and grids used in the simulations.

4.10 Dependence of Inlet Temperature

As per the procedure for data acquisition described in Chapter 3, the laser sheet profiles were obtained between each data set using a cold flow of N_2 (10 SLPM) and 5000 ppm NO. This served to cool down the potentially preheated tube between data sets. Throughout the data acquisition, the tube was intermittently checked to verify that it was relatively cool. However, a series of CFD simulations were performed to investigate the potential effects of inlet temperature, T_{inlet} . As shown in Figure 4-7, T_{inlet} can have a significant effect on the flame length.



a) Simulated OH-PLIF signal in case of different T_{inlet} .



b) Temperature profile in case of different inlet temperature.

Figure 4-7: Top: Simulated OH-PLIF signal; Bottom: Temperature profile, $T(K)$, for different inlet temperatures.

As T_{inlet} increases, the flame length decreases. This trend is expected due to improved diffusivity. Nonetheless, as noted above, significant preheating was not observed during data acquisition. Furthermore, even for a heated tube, the gas flow will not reach the temperature of the tube itself. Finally, conservation of energy should also lead to a slightly cooler flame, which would counteract the effects of preheating.

4.11 Summary

This chapter is summarized as follows.

1. A two-dimensional axisymmetric, time-accurate CFDC (Computational Fluid Dynamics with Chemistry) code, known as UNICORN (UNsteady Ignition and COmbustion with ReactionNs) was used to solve the axial- and radial-momentum equations, continuity equation, enthalpy- and species-conservation equations to simulate a variety of CH₄ and syngas laminar diffusion flames in this research.
2. An appropriate computational domain, grid system, and boundary conditions were set up for these computations. A grid-independent study was performed to ensure that the converged solution is grid-independent. Grids were placed with higher density in the region of interest to resolve the structure of flames. The outer boundary is set to be far enough from the region of interest to make sure the flame is not affected by boundary effects.
3. Two chemical mechanisms, GRI-Mech 3.0 and the Tian mechanism, were incorporated into UNICORN to describe chemical reactions in the combustion process. GRI-Mech 3.0 is the latest version specially designed for CH₄ oxidation. It also contains elements of CO, H₂, and NH₃, although little information is present about the CH_{*i*} subset, NH_{*i*} subset and CH_{*i*}-NH_{*i*}-interaction subset. The Tian mechanism, compared to GRI-Mech 3.0, includes complete subsets of CH_{*i*}, NH_{*i*} and CH_{*i*}-NH_{*i*}-interaction, which are critical in predicting combustion involving NH₃ oxidation.

CHAPTER 5 RESULTS: LAMINAR CH₄/AIR DIFFUSION FLAMES

In this thesis, CH₄/air results serve as a starting point to verify and optimize our experimental setup, as well as to validate simulation models with familiar chemistry. In this chapter, we report an experimental and numerical investigation of laminar CH₄/air diffusion flames. The effects of NH₃ doping on the flame structure and emissions characteristics are evaluated based on the experimental and numerical results with different chemical kinetics mechanisms. Different amounts of NH₃ dopant were seeded to the fuel stream to understand the chemistry of fuel-N on NO formation. First, spatially resolved, semi-quantitative planar OH profiles of CH₄/air diffusion flames were obtained using Planar Laser-Induced Fluorescence (PLIF). The presence of OH within the flame zone made it a good marker to investigate flame structures and reaction zones for model validation. In addition, OH plays a critical role in NO chemistry and it is important to verify the proper prediction of OH distributions in the flame zone. Then, NO mole fraction profiles were recorded within the flame zone by quantitative PLIF Imaging. Quantities such as temperature, gas composition, laser sheet profiles, and laser power (or laser power density) were also necessary to correctly interpret the OH and NO PLIF images. Through careful post-processing of the experimental signals (discussed in Chapter 3), it was possible to obtain absolute mole fractions of NO in the flame zone for comparison with numerical simulations.

Computationally, the conservation equations of mass/continuity, momentum, species, and energy were solved with detailed transport and finite-rate chemistry incorporated to predict both major and minor species and temperature. Two chemical

kinetics models, GRI-Mech 3.0 and Tian et al., were incorporated into UNICORN as described in Chapters 2 and 4.

In the following sections, we first show comparisons of 2-D OH distributions between experimental and numerical data. Then, we show 2-D NO distributions and evaluate the NO distribution along the centerline based on both experimental and numerical data. Moreover, we discuss the effect of NH₃ addition on the NO formation. Finally, we show the relative contribution of each NO sub-mechanism, such as thermal NO, prompt NO, N₂O intermediate and other sub-mechanisms.

5.1 OH Profiles: Comparison of Experimental and Simulated PLIF Signals

As a starting point for model validation, we investigate OH distributions by PLIF. The 2-D OH spatial distribution shows the flame structure and the effects of NH₃ addition. Comparison of CFD calculations with both the GRI-Mech 3.0 and Tian et al. mechanisms shows which mechanism is more suitable for each condition.

Typically, as mentioned above interpretation of OH-PLIF signals into OH mole fractions requires knowledge of temperature and quenching species, which are technically difficult to achieve in our lab. Therefore, instead of conversion from experimental fluorescence signal to quantitative OH, the opposite conversion is implemented from the numerical OH to experimental OH fluorescence signal. Using the numerical OH mole fraction, with temperature and other species available in CFD calculation, a simulated fluorescence signal could be computed which is linearly proportional to experimental fluorescence signal, i.e.

$$S_{f,\text{simulated}} \propto S_{f,\text{experiment}} \quad (5.1a)$$

or

$$S_{f,\text{simulated}} = k \times S_{f,\text{experiment}}, \quad (5.1b)$$

where $k = \left(X_{\text{NO}} \times \frac{I_r}{LIF} \right)_{\text{cal}}$ is the calibration slope from Section 3.6.2. Hereafter, this quantity is called the “simulated” fluorescence signal or $S_{f,\text{simulated}}$. One comparison of this kind is shown in Figure 5-1. Since the comparison of experimental and “simulated” OH signals is to determine whether the current CFD approach produces the qualitatively correct flame structure and spatial distribution of OH, this semi-quantitative comparison of $S_{f,\text{simulated}}$ and $S_{f,\text{experiment}}$ is adequate. Figure 5-1 shows $S_{f,\text{simulated}}$ and signal $S_{f,\text{experiment}}$, both are normalized by their maximum values to facilitate comparison. Since the experimental fluorescence signal is noisy, it is normalized by its 99.9% percentile instead of its absolute maximum value.

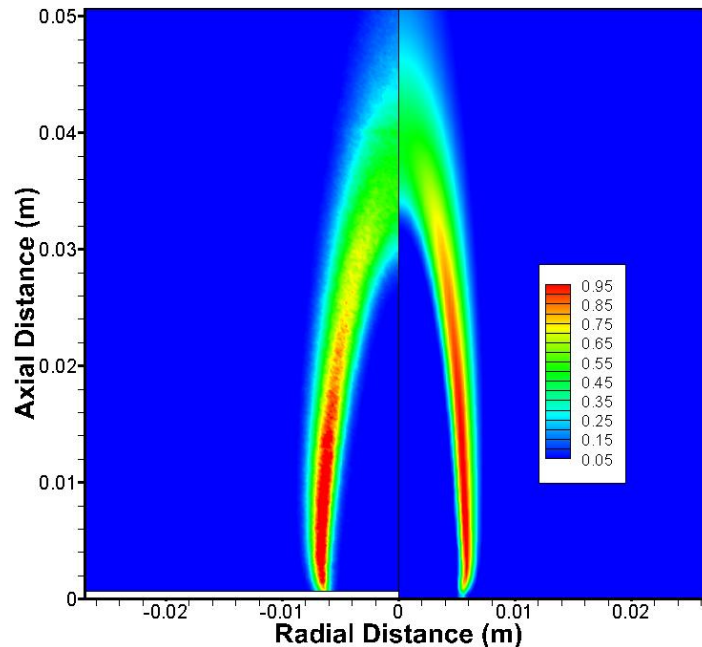


Figure 5-1: Experimental (left) and simulated (right) OH fluorescence signal of CH₄/air laminar diffusion flames without NH₃. The physical domain covers horizontally from the

centerline to 0.03m and axially from zero to 0.06m above the tube exit. This simulation was performed with GRI-Mech 3.0.

Figure 5-2 shows experimental OH-PLIF images for CH₄/air diffusion flames with varying amounts of NH₃. With the addition of NH₃, the flame length is shorter. This is due to the change in stoichiometric ratio change with NH₃ addition. This flame length, based on Burke-Schumann, is inversely proportional to the molar stoichiometric ratio S_{stoi} [1], which is defined as:

$$S_{\text{stoi}} = \left(\frac{\text{moles of oxidizers}}{\text{moles of fuel}} \right)_{\text{stoichiometric}} \quad (5.2)$$

For instance, without NH₃, one mole of CH₄ requires two moles of O₂ or $2 \times (1 + 3.76)$ moles of air to achieve the stoichiometric ratio, i.e. $S_{\text{stoi,CH}_4} = 2.0$ for oxygen or $S_{\text{stoi,CH}_4} = 9.42$ for air. For NH₃, however, one mole only requires 1.25 moles of oxygen to achieve complete combustion, i.e. $S_{\text{stoi,NH}_3} = 1.25$. Thus in case of NH₃ addition leads to $S_{\text{stoi,CH}_4+\text{NH}_3} < S_{\text{stoi,CH}_4}$, thus the reduced flame length. In other words, the addition of NH₃ requires less O₂ to reach complete combustion, so that the distance for the fuel/air mixture to reach the stoichiometric ratio (complete combustion), or equivalently the overall flame length, is reduced.

Each OH-PLIF image is an average of 50 snapshots taken consecutively at a sampling rate of 2 Hz (the repetition rate of laser was 10 Hz and the DAQ was running at a rate of 2 Hz with the parameter “Gates per Exposure” set to “1”). The overall agreement for flames without NH₃ between the experimental OH-PLIF and simulated OH-PLIF is good but not perfect. Both the experimental and simulation results have similar OH spatial distributions, with some differences in flame width, height, and shape.

In this case, the simulation shows around 10% over-prediction of flame length. However, the trend of higher OH intensity next to the tube rim and relatively broad but lower intensity closer to flame tip is captured by both the experimental measurements and the UNICORN simulation coupled with GRI-Mech 3.0.

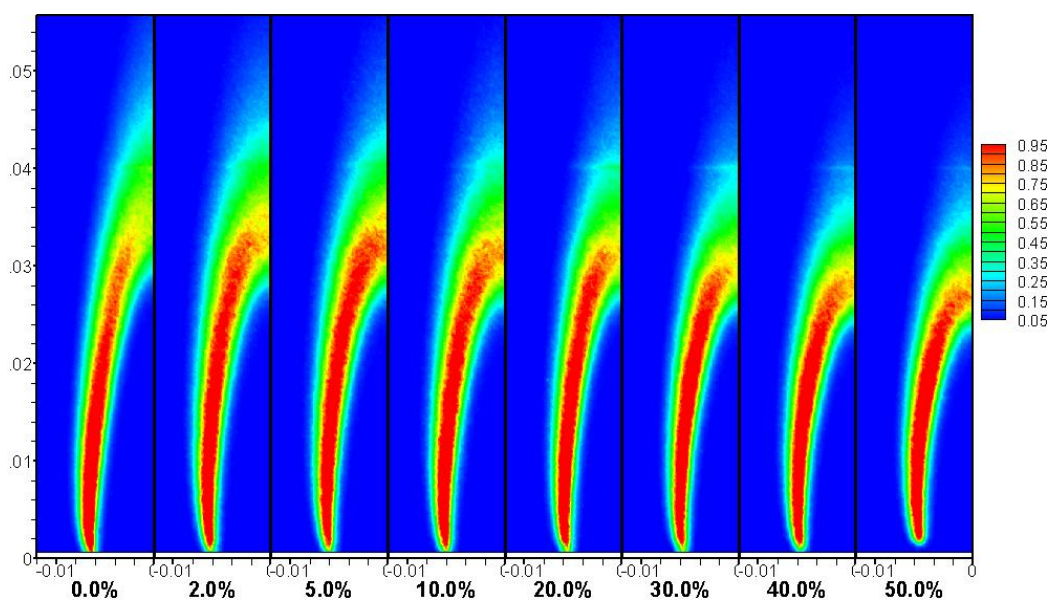


Figure 5-2: Experimental OH-PLIF images with different amounts of NH_3 seeding.

Figure 5-3 compares the experimental OH-PLIF signals with “simulated” signals from UNICORN with GRI-Mech 3.0 in the case of CH_4/air flames with 40 vol% ammonia seeded to the fuel. The overall agreement of flame length is good, although the flame length is 5% under-predicted. In this case, the vertical distribution of OH matches between the simulation and the experiment, but the horizontal distribution shows a wider OH layer for the experiment. This is likely due, in part, to the finite thickness of the laser sheet, slight flicker in the flame, and any potential misalignment from the flame axis. Similar to simulation results of flames without ammonia, the simulation with

ammonia predicts a stronger signal in the next-to-tube-exit region, which is another agreement between the “simulated” and experimental fluorescence signals.

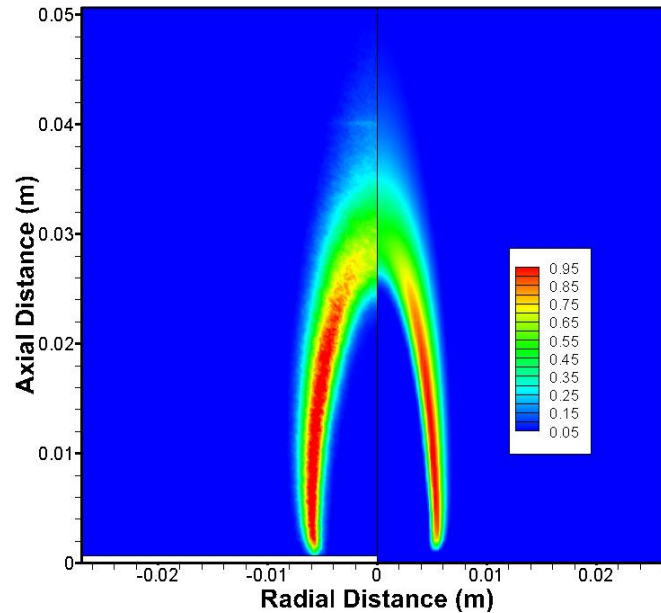


Figure 5-3: Experimental (left) and computational (right) OH profile of CH₄/air laminar diffusion flames with 40 vol% NH₃. CFD result incorporates the detailed chemical kinetics using GRI-Mech 3.0.

Figure 5-4 shows an overlay of simulated OH signals. Each profile is normalized by its own maximum values in domain so that the normalized signal ranges from 0 ~ 1. Again the color map is from 0.05 through 0.95. Comparing with Figure 5-2, we could see that the overall trend of flame length is captured by CFD calculations. Unfortunately, with more NH₃ seeding, the discrepancies of flame lengths between the CFD and PLIF signal increases. This is also shown in case of F1 and F2 syngas flames.

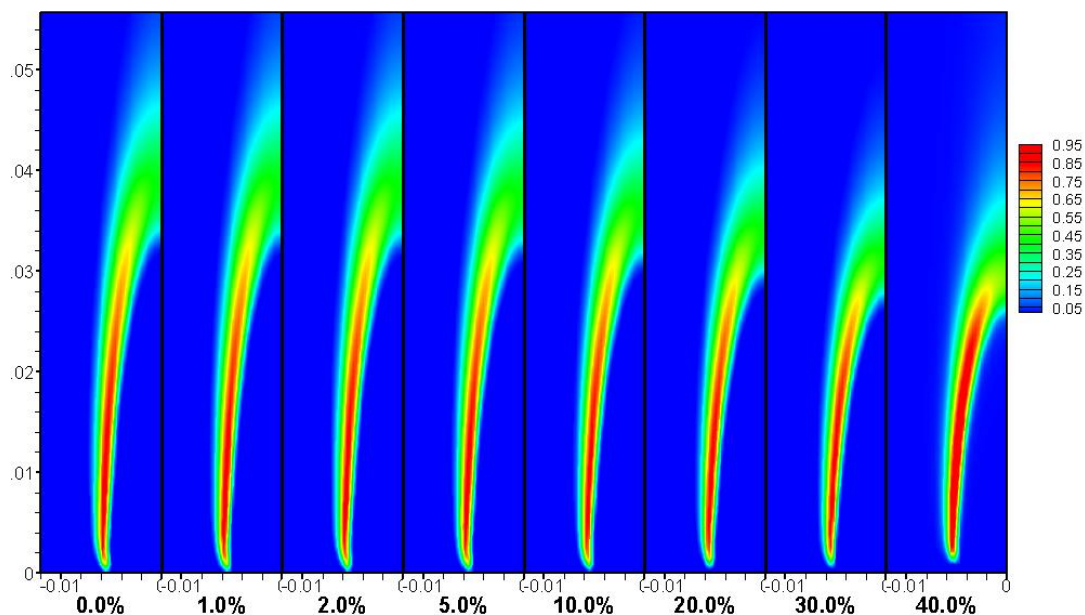


Figure 5-4: Simulated fluorescence signal with NH_3 seeding level ranging from 0.0% to 40%. The simulated signal does not show any fluctuation.

5.2 Mechanism Comparison for OH profiles (GRI-Mech 3.0 vs. Tian et al.)

Computationally, two chemical kinetics models, GRI-Mech 3.0 and Tian et al., were incorporated into UNICORN. The results are compared with PLIF results, as shown in the previous sections.

Figure 5-5 shows centerline temperature profiles with various amounts of NH_3 seeding by the GRI-Mech 3.0 and Tian mechanisms, respectively. These temperature profiles peak along the centerline at around 2000 K, and then decrease gradually in the downstream region.

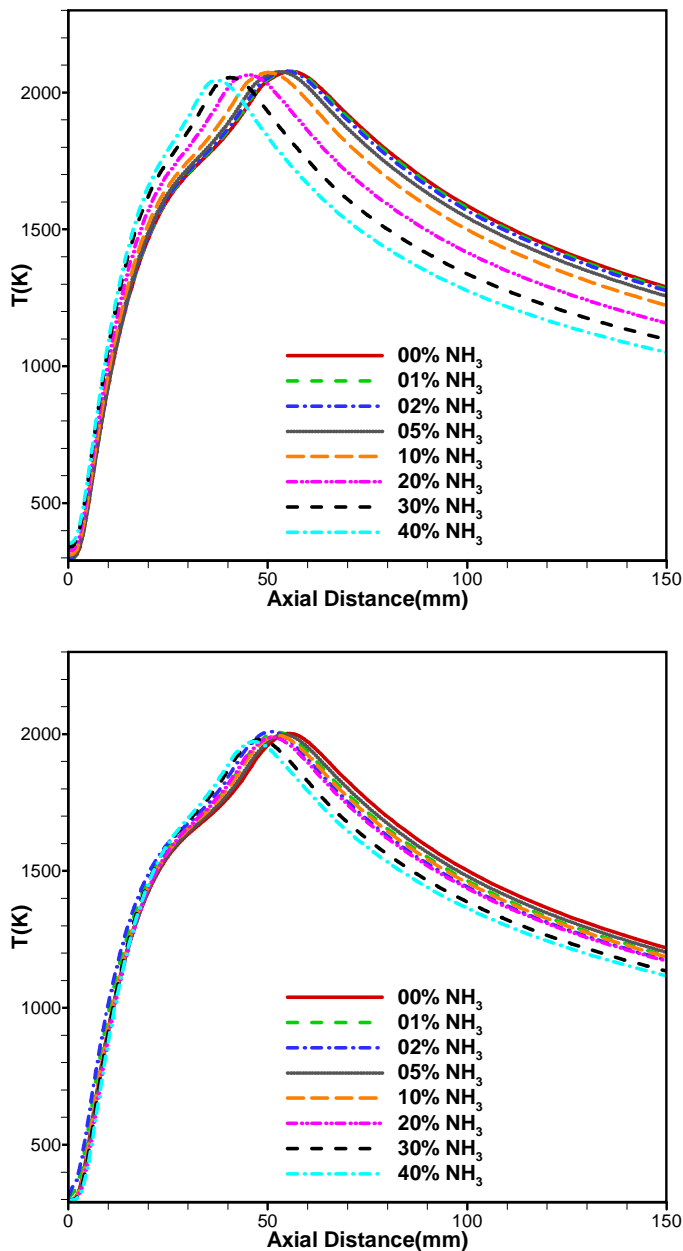


Figure 5-5: Comparison of simulated centerline temperature profiles for laminar diffusion flames with different amounts of NH₃ seeding using GRI-Mech 3.0 mechanism (top) and Tian mechanism (bottom). Horizontal axis is the distance from fuel nozzle, and vertical axis is the temperature. Only the temperature profiles at the centerlines are plotted for ease of comparison.

The GRI-Mech 3.0 temperature profiles are higher than those by the Tian mechanism. The temperature peaks shift closer to fuel nozzle mainly because of reduction of flame length with NH_3 seeding as noted above. With ammonia seeding, GRI-Mech 3.0 shows larger shifts of temperature peaks towards the fuel tube exit as compared with the Tian mechanism. Both mechanisms show that the temperatures decrease with higher amounts of NH_3 . However, the Tian mechanism predicts that this decrease is not monotonic with respect to NH_3 seeding level. The temperature first increases with no more than 2% NH_3 , then decreases with more NH_3 beyond 2%. This implies that two different reaction pathways are involved in NO formation.

Similar to the temperature profile, Figure 5-6 shows the OH profiles along the centerline using the GRI-Mech 3.0 and Tian mechanisms, respectively. GRI-Mech 3.0 shows higher OH mole fractions than the Tian mechanism. The OH peaks shift closer to the fuel nozzle because of the reduced length due to NH_3 . With NH_3 seeding, GRI-Mech 3.0 shows a larger shift of OH peaks closer to the fuel tube than the Tian mechanism. Although both mechanisms show that the OH peaks decrease with higher amounts of NH_3 seeding, the Tian mechanism predicts that this decrease isn't monotonic with increasing NH_3 , as can be seen from Figure 5-6.

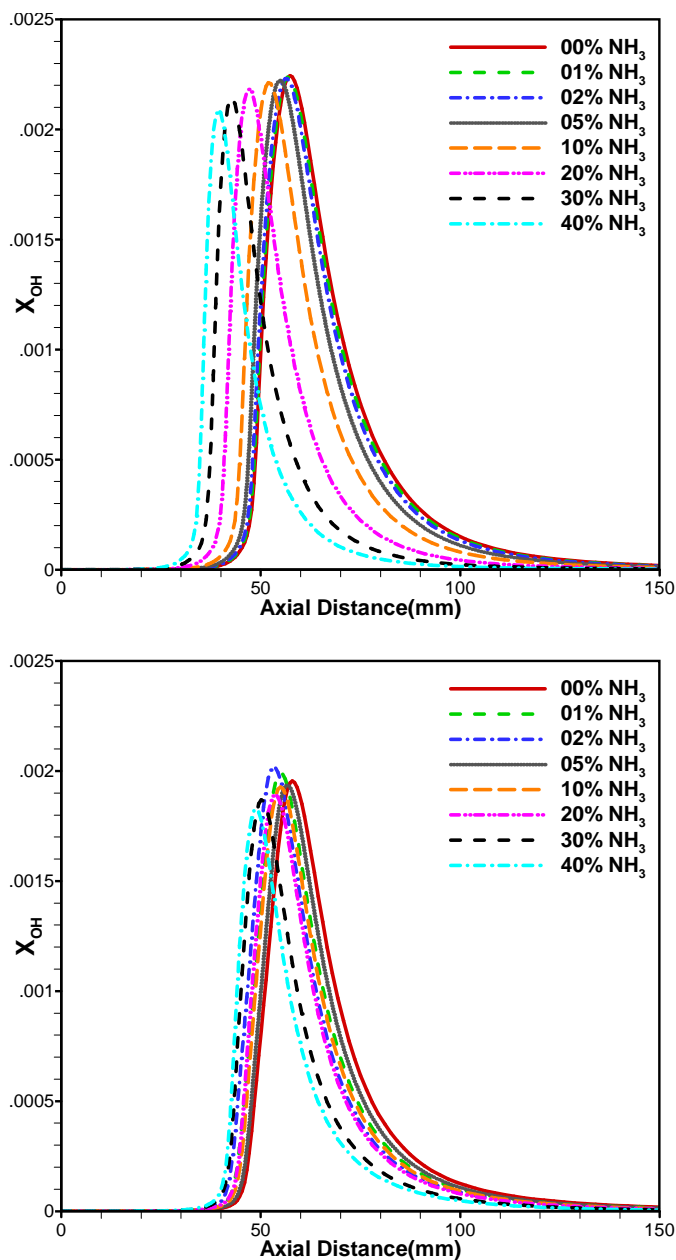


Figure 5-6: Comparison of simulated centerline OH mole fraction profiles for laminar diffusion flames with different amounts of NH₃ seeding using GRI-Mech 3.0 mechanism (top) and Tian mechanism (bottom). Only OH mole fraction profile in each flame centerline is plotted for ease of comparison.

5.3 NO-Profiles: Comparison of Experimental and Simulated Signals

As mentioned in Chapter 3, obtaining absolute NO concentration with NO-PLIF imaging requires additional data on the local temperature (for Boltzmann fraction) and major quenching species. These additional data are usually obtained in two ways: (1) by involving more instruments, such as CARS for temperature and major species; or (2) by exploiting numerical data from the CFD calculation. Since the numerical model predicts temperature and major species concentrations with a fair degree of accuracy (within ~10%), it is used for the derivation of absolute NO mole fractions that are within the experimental uncertainty. Hence, in this work, the numerical data are used for quenching and Boltzmann fraction corrections so that absolute NO concentration can be compared between experiments and simulations.

In addition to the methodology mentioned above, the “simulated” NO fluorescence signal, similar to the approach of obtaining “simulated” OH fluorescence, has been derived as well. Comparison between this “simulated” NO fluorescence signal and experimental signal is particularly useful for model validation as it requires that the model provide the correct concentration of NO as well as temperature and other major species concentrations. The derivation of absolute NO concentration is described in Section 3.6.2.

Figure 5-7 shows the calibration curve used for quantifying the NO fluorescence signals. This curve correlates the quantity, which is the fluorescence signal corrected for the laser sheet power density profile, with the NO mole fraction, i.e. $S_{f, \text{experiment}} \text{ v. s. } X_{\text{NO}}$. Further details on the calibration procedure are provided in Chapter 3.

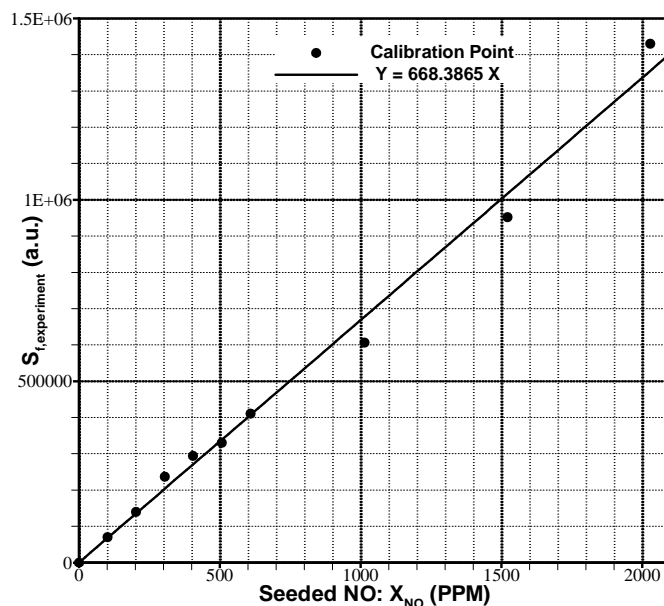


Figure 5-7: A premixed CH_4 /air calibration flame. Horizontal axis is the seeded NO concentration in ppm and vertical axis is the signal intensity in arbitrary units.

Figure 5-8 shows the experimental 2-D NO-PLIF signals in CH_4 /air diffusion flames from 100 ppm to 1% NH_3 doping in the fuel stream. Overall, with the increase of NH_3 doping amount, the NO signal also increases. In addition, using 1% NH_3 doping as representative, it is clearly observed that the NO-PLIF signals are not equally distributed in the flame. Rather, there is a colder, central region of the flame with lower NO-PLIF signals compared to the lower and the upper regions of the flame.

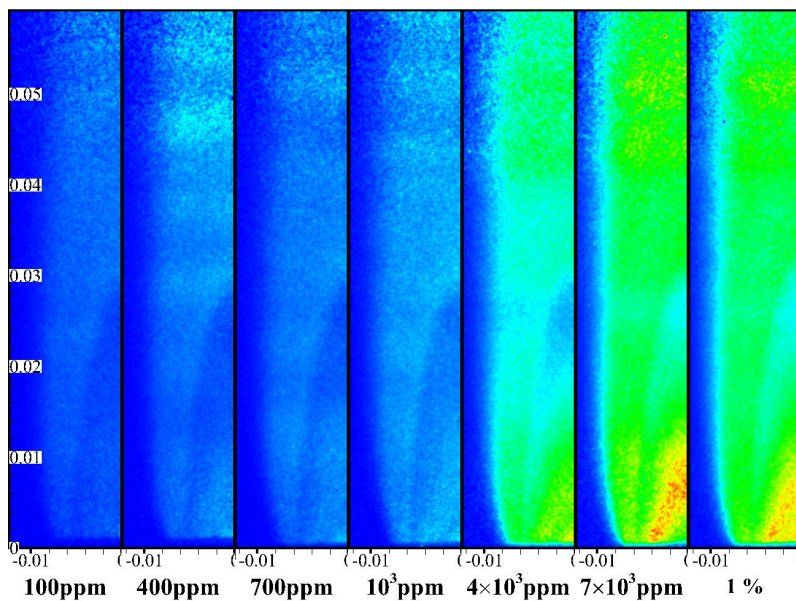


Figure 5-8: Experimental 2-D NO-PLIF signals in CH₄/air diffusion flames with different amounts of NH₃ seeding.

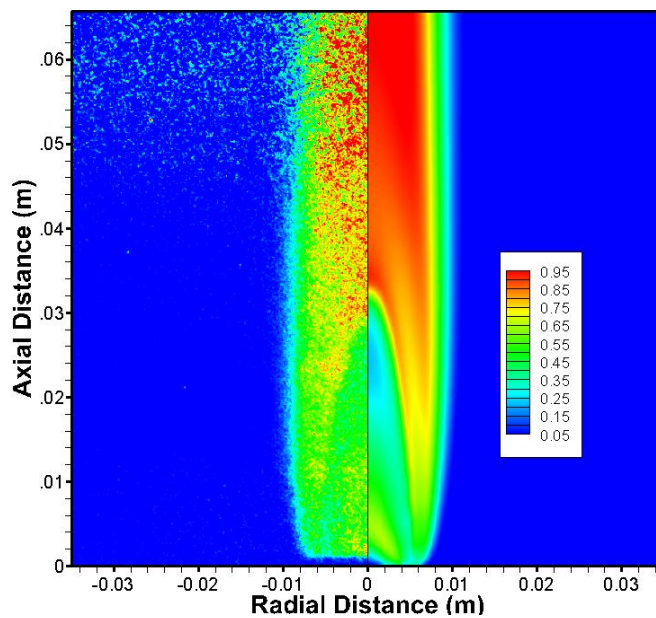


Figure 5-9: Comparison between 2-D NO-PLIF signal and 2-D simulated NO fluorescence signal in CH₄/air diffusion flame with 100-ppm NH₃ seeding.

Figure 5-9 shows a comparison of 2-dimensional experimental and "simulated" NO fluorescence signals in CH₄/air laminar diffusion flames with 100 ppm NH₃ doping. In this case, the CFD simulation used the GRI-Mech 3.0 mechanism. Since the experimental and "simulated" signals should be proportional, these two signals are normalized from 0 to 1.0. The color contours are adjusted from 0.05 through 0.95 in both cases for ease of comparison. As in the case of OH, good agreement (within 10%) is apparent in terms of flame length, structure and shapes between experimental and computational NO images. However, it is difficult to see fine details in the experimental data NO images due to low signal-to-noise ratio with lower amounts of NO seeding. Nonetheless, it is still possible to discern that NO is mainly found in the high temperature region.

Figure 5-10 shows similar agreement between experimental and "simulated" NO-PLIF signals of CH₄/air laminar diffusion flames with 1000 ppm NH₃. In the case of 1000 ppm NH₃, it can be seen that the signal-to-noise ratio is much higher than the 100 ppm NH₃ seeding level.

When an even higher amount of NH₃ is doped into the fuel stream, the flame is stretched and the internal NO contours change. Figure 5-11 shows the same comparison for a CH₄ laminar diffusion flame with 20% ammonia. Good agreement is again observed in terms of flame length and shape, with changes in the internal NO contours being qualitatively captured by the experimental measurement. The precise magnitude of the NO concentration is not matched between the experiment and the computation, with differences on the order 2x to 3x depending on the region of interest. However, it is clear in both the experiment and the computation that the region of high

NO concentration has moved downstream and that there is also a region of high NO concentration near the tube exit. More quantitative comparisons between the PLIF and numerical results are presented and discussed in the next section.

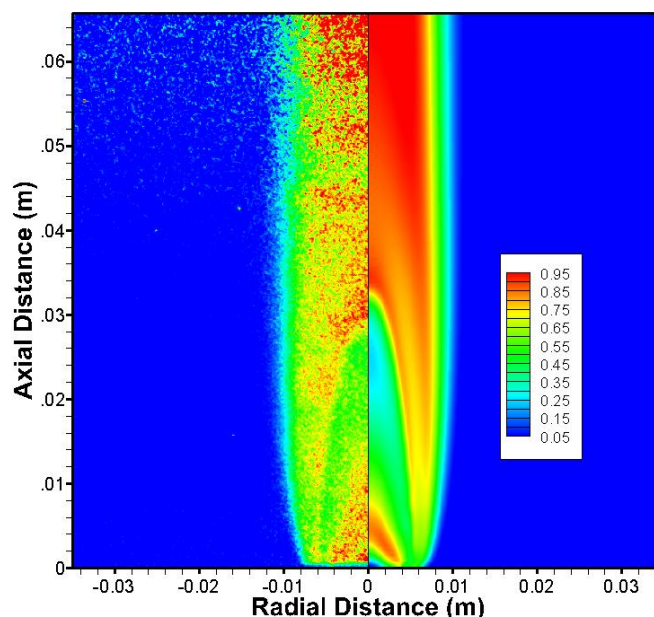


Figure 5-10: Experimental (left) and computational (right) NO fluorescence signal of CH_4/air laminar diffusion flames with 1000-ppm NH_3 doping. CFD simulation was performed using GRI-Mech 3.0 mechanism.

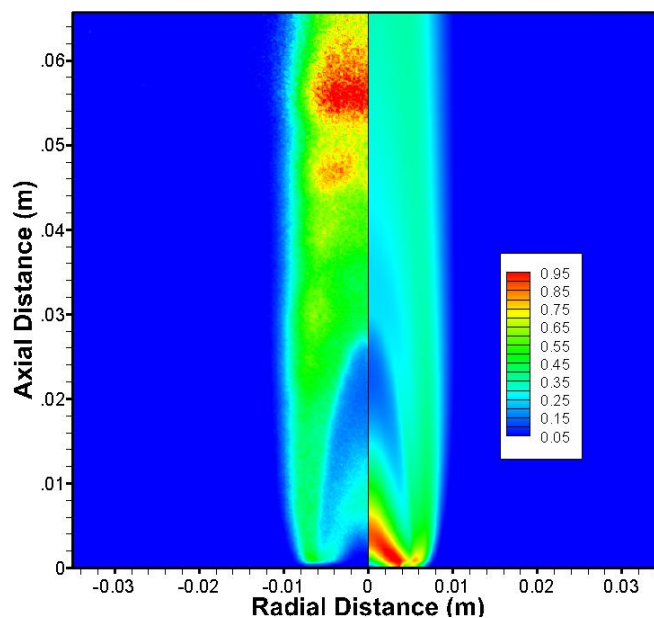


Figure 5-11: Experimental (left) and computational (right) NO fluorescence signal of CH_4/air laminar diffusion flames with 20 vol% NH_3 seeding. CFD simulation was performed using GRI-Mech 3.0 mechanism.

5.4 Mechanism Comparison for NO Profiles (GRI-Mech 3.0 vs. Tian et al.)

As noted earlier, two chemical kinetics models, GRI-Mech 3.0 and Tian et al., were incorporated into UNICORN. The 2-D data using GRI-Mech 3.0 were compared with PLIF images, as shown in the previous section. To obtain more insights into NO formation, such as which mechanism predicts NO formation more accurately, plots of experimentally measured NO mole fraction along the centerline of the CH_4/air diffusion flames are compared with the numerical predictions between the Tian and GRI-Mech 3.0 mechanisms. Figure 5-12, Figure 5-13 and Figure 5-14 compare the measured and computed NO concentrations along the centerline for 100 ppm, 1000 ppm, and 20 vol% NH_3 seeding into CH_4 . The green lines represent the GRI-Mech 3.0 mechanism, the blue lines are for the Tian mechanism, and the red lines indicate experimental data.

Generally speaking, numerical simulations qualitatively track the measured NO concentration and are not far from predicting the correct distribution. The Tian mechanism consistently under-predicts the NO concentration, especially at high NH₃ doping levels. With increased NH₃ doping levels, the peak NO predicted by Tian mechanism is only about 50% of the actual concentration measured from experimental data. This is somewhat surprising given the detailed NH₃ chemistry available in the Tian mechanism, but highlights the ability of GRI-Mech 3.0 to model CH₄ chemistry.

When the NH₃ doping level is low (100 and 1000 ppm), GRI-Mech 3.0 slightly under-predicts the NO concentration next to the fuel nozzle, and slightly over-predicts the NO close to the flame front at higher elevation. When the NH₃ doping level is high (20 vol% NH₃), excellent agreement exists along the centerline NO prediction between experimental and computational data with GRI-Mech 3.0 at the flame front, whereas at the lower region close to the fuel nozzle, GRI-Mech 3.0 over-predicts the NO concentration significantly.

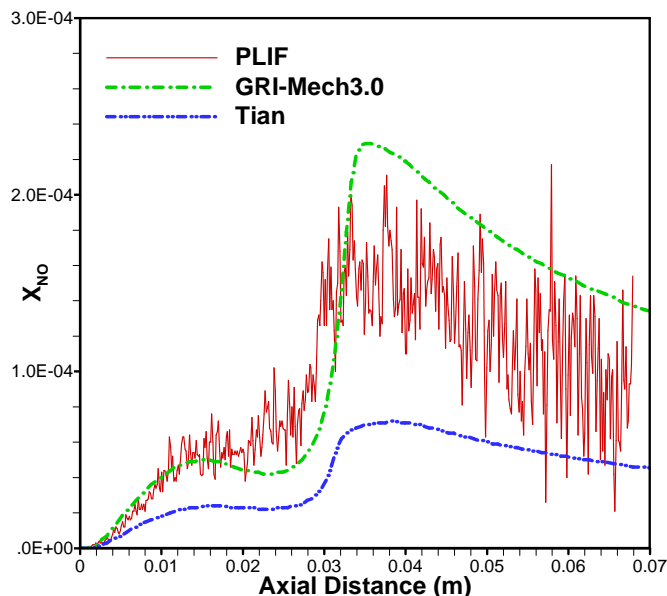


Figure 5-12: Comparison of measured and simulated NO concentration in the centerline of CH₄/air diffusion flames doped with 100-ppm NH₃. Green lines for GRI-Mech 3.0 mechanism. Blue lines for Tian mechanism

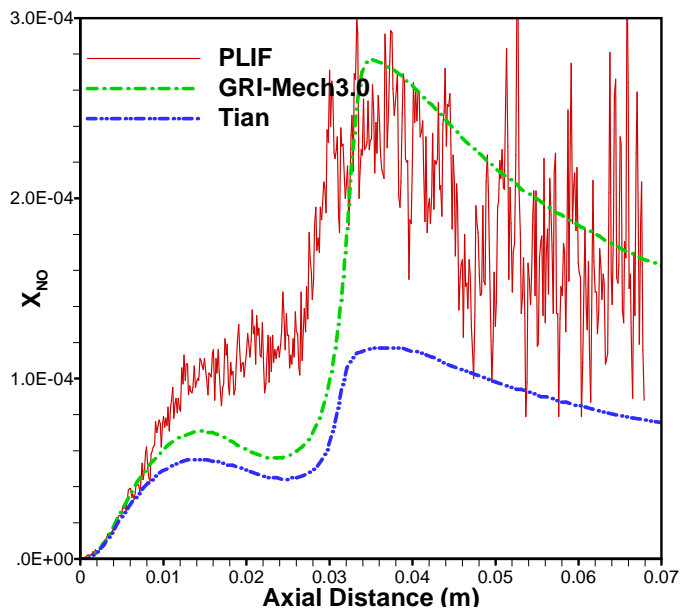


Figure 5-13: Comparison of measured and simulated NO concentration in the centerline of CH₄/air diffusion flames doped with 1000-ppm NH₃. Green lines for GRI-Mech 3.0 mechanism. Blue lines for Tian mechanism

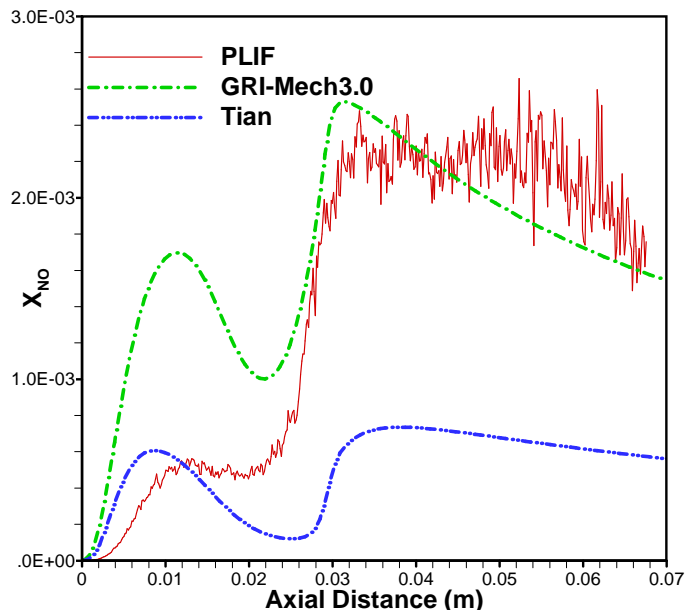
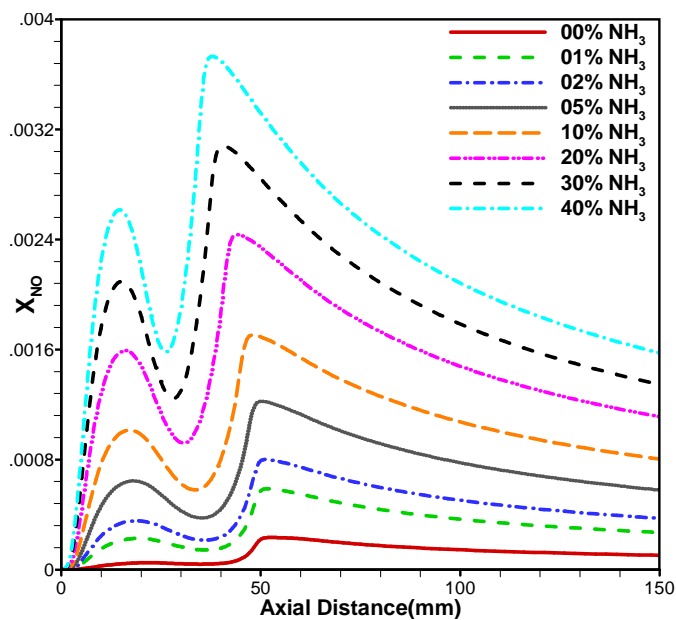


Figure 5-14: Comparison of measured and simulated NO concentration in the centerline of CH₄/air diffusion flames doped with 20 vol% NH₃. Green lines for GRI-Mech 3.0 mechanism. Blue lines are for Tian mechanism.

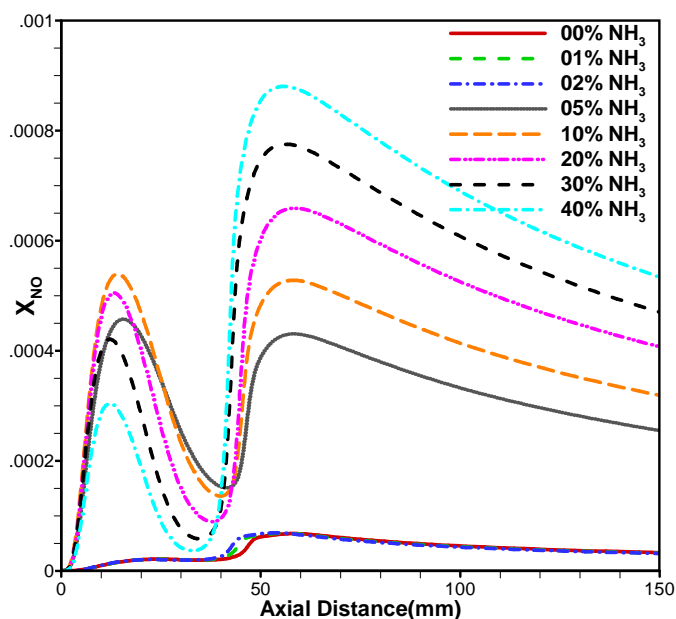
Figure 5-15 shows the NO profiles along the centerline for the full range of NH₃ seeding levels in the CH₄/air diffusion flames as computed using the GRI-Mech 3.0 and Tian mechanisms, respectively. Only the NO profile in each flame centerline is plotted for ease of comparison. GRI-Mech 3.0 shows a much higher peak NO level by ~4x as compared with the Tian mechanism. As shown previously in the 2-D images of NO from Section 5.3, there are two peaks in the NO profile, with the second peak higher than the first. The NO profile drops in the middle of the flame, perhaps because of the NO reburn mechanism. When NH₃ is seeded into the flow, both mechanisms show that the overall NO increases proportionally. Both mechanisms also predict that the maximum NO mole fraction shifts closer to the fuel nozzle with NH₃ seeding, which is mainly due to the shortening of flame length. Interestingly, the Tian mechanism shows no change in NO

for the first NO peak up a seeding level of 2% NH₃. However, if more NH₃ is seeded into the fuel, a tenfold increase in NO mole fraction in the first NO peak is observed. When 10% or more NH₃ is seeded into fuel, increasing the NH₃ seeding level only reduces the NO mole fraction in this region, even though the overall NO is increased downstream. This differs substantially from the GRI-Mech 3.0 mechanism, which shows monotonically increasing levels of NO in all regions of the flame.

Overall, in this study, GRI-Mech 3.0 mechanism appears to be more accurate than the Tian mechanism in predicting NO concentration in laminar CH₄/air diffusion flames with NH₃ seeding. The absolute NO concentration seems to be more accurately predicted, and the trend of increasing NO with NH₃ seeding appears to be true.



a) GRI-Mech 3.0.



b) Tian Mechanism.

Figure 5-15: Comparison of simulated centerline NO mole fraction profiles for laminar diffusion flames with different amounts of NH_3 seeding by GRI-Mech 3.0 mechanism (top) and by Tian mechanism (bottom).

5.5 Relative Contribution of NO Formation Sub-mechanisms

For CH₄/air diffusion flames studied in this work, it is important to understand the relative contribution of NO formation sub-mechanisms (e.g. Thermal NO, prompt NO, N₂O intermediate, NNH and fuel NO). To evaluate the effect of NH₃ in the total NO formation, we numerically investigated CH₄/air flames with two different NH₃ seeding levels: 0% and 1%. For each seeding level, individual contributions of NO formation sub-mechanisms to total NO were calculated using the GRI-Mech 3.0 mechanism. The contribution of each sub-mechanism is determined by the following procedure: (1) turning off the initiation reaction in that sub-mechanism and running the calculation with exactly the same condition, and (2) subtracting the total NO with the NO from step (1) In this manner, the difference is the contribution by that sub-mechanism.

In the case of zero NH₃ seeding, fuel NO isn't considered, and the NO centerline plots of the different sub-mechanisms are shown in Figure 5-16. Prompt NO is the most important, followed by Thermal NO; the N₂O intermediate, and NNH intermediate both contribute only a small amount of NO formation for this condition. It is reasonable that N₂O intermediate and NNH intermediate sub-mechanisms are not significant in this study since they are more relevant for lean premixed flames at low temperature. Prompt NO is dominant due to the mild flame temperature, which peaks no more than 2000K and the abundance of CH_i radicals.

When NH₃ is seeded into the fuel, the fuel NO mechanism becomes important. Figure 5-17 and Figure 5-18 show a comparison of the relative contributions of NO sub-mechanisms with NH₃ seeding of 1% into a CH₄/air diffusion flame using the GRI-Mech 3.0 and Tian mechanisms, respectively, According to the GRI-Mech 3.0 mechanism in

Figure 5-17, the relative contribution for NO formation in CH₄/air flames with 1% NH₃ seeding is fuel NO > Prompt NO > thermal NO ≫ N₂O intermediate > NNH intermediate. For the Tian mechanism in Figure 5-18, the relative contribution is fuel NO > Prompt NO ≈ thermal NO ≫ N₂O intermediate > NNH intermediate. From these data, we can conclude that the primary reason that the Tian mechanism under-predicts NO concentrations is mainly due to under-prediction of the fuel NO and Prompt NO sub-mechanisms.

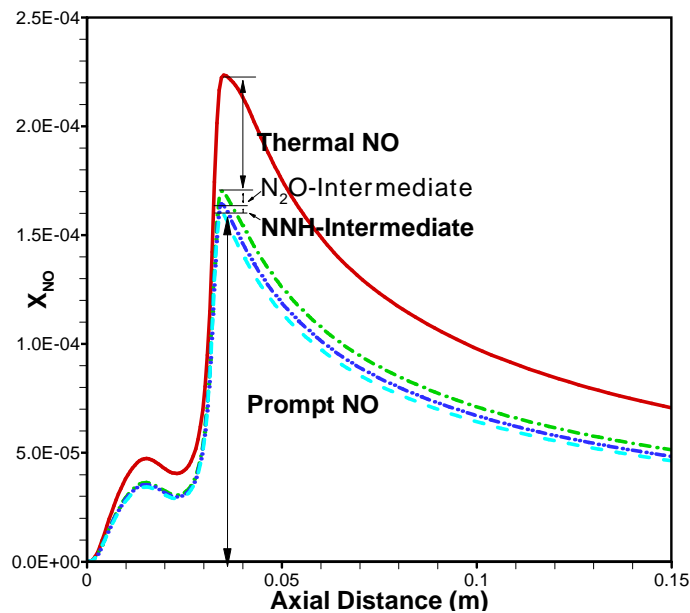


Figure 5-16: Relative contributions of NO-sub-mechanisms in CH₄/air diffusion flames without NH₃ seeding. CFD simulation was performed using GRI-Mech 3.0 mechanism.

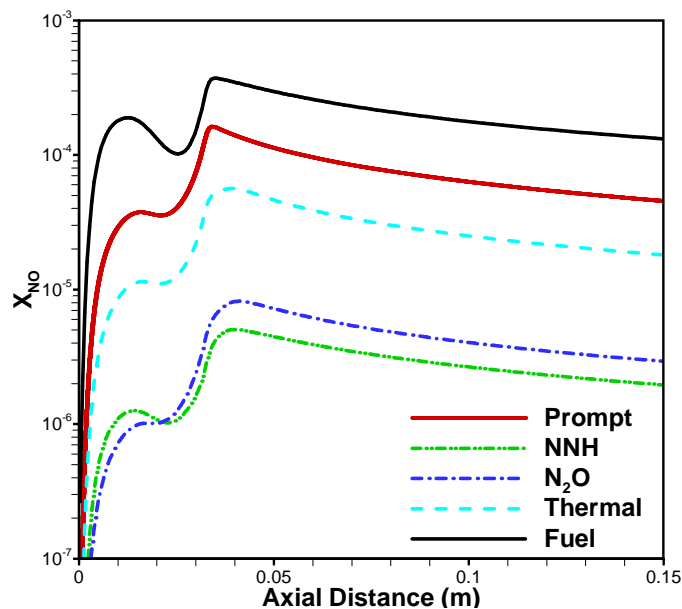


Figure 5-17: Relative contributions of NO-sub-mechanisms in CH₄/air diffusion flames with 1 vol% NH₃ seeding. CFD simulation was performed using GRI-Mech 3.0 mechanism.

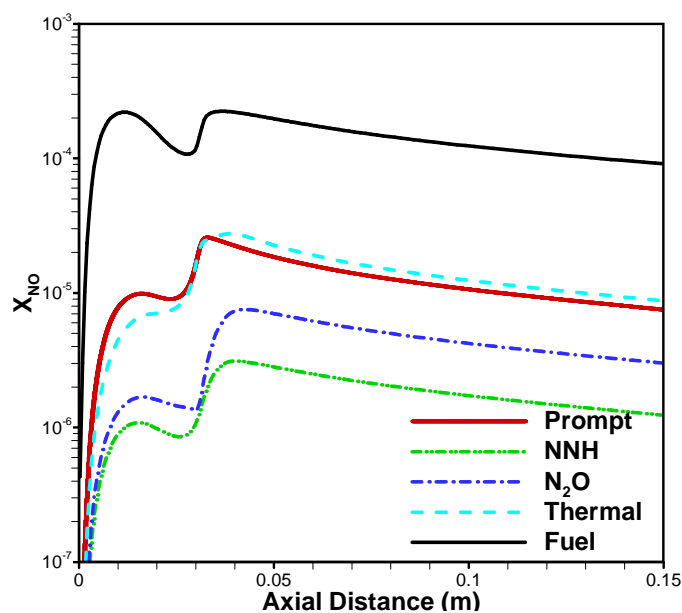


Figure 5-18: Relative contributions of NO-sub-mechanism in CH₄/air diffusion flames with 1 vol% NH₃ seeding. CFD was performed using Tian mechanism.

Table 5-1 shows percentages of fuel, thermal and prompt NO with 0% and 1% NH₃ doped. As can be seen in case of zero NH₃, the prompt NO (64%) is greater than (about 2 times) thermal NO(36%), which means that the first peak is mainly due to prompt NO. Surprisingly, the second peak is attributed to prompt NO (53%) even more than thermal (47%) as well. In case of 1% NH₃ doping, other than the dominant fuel NO, prompt NO (16%, 29%) is still ~3 times of thermal NO (5%, 9%).

Table 5-1: Percentages of NO sub-mechanisms in CH₄/air flames with 0% and 1% NH₃ doped for the first and second peaks in Fig. 5-15.

		Fuel	Thermal	Prompt	Prompt+N ₂ O+NNH
CH ₄ ,0% NH ₃	1st peak	N/A	36%	49%	64%
	2nd peak	N/A	47%	36%	53%
CH ₄ ,1% NH ₃	1st peak	79%	5%	15%	16%
	2nd peak	63%	9%	27%	29%

5.6 Summary

For CH₄/air diffusion flames, the OH distribution by both PLIF and CFD reveals that the flame exhibits a typical diffusion flame structure; i.e. after the fuel exits the fuel tube, it is convected into the flame sheet or flame zone, where the temperature begins to increase, and the fuel begins to decompose from CH₄ to CH_i radicals. In this region the calculated equivalence ratio ϕ is greater than 1.0, which means that the fuel is burning rich. As more oxidizer is entrained into the flame zone as the fuel/oxidizer mixture is convected downstream, the fuel/air ratio approaches the stoichiometric ratio. Thus the fuel/air mixture is burning at stoichiometric conditions, with temperature and OH radicals reaching their maximum values. Beyond this initial flame zone, additional

reactions can take place for reactions with CO and unburned hydrocarbons. Hence, the distribution of OH radicals in the flame zone is a good marker of the flame structure. Fortunately, the OH-PLIF measurements and CFD predictions using UNICORN show good agreement with regard to the flame structure.

As a result of this flame structure, the NO distribution exhibits a multi-peak structure, which means that once the fuel is discharged from the burner tube, the O₂ and CH_i radicals, which are decomposed from CH₄, react with entrained N₂ and form a significant amount of NO. This is the first NO peak, due to (1) in case of zero NH₃ doping, mainly the prompt NO formation mechanism; and (2) in case of 1 vol% NH₃ doping, mainly fuel NO then secondly prompt NO, which is 2~3 times that of thermal NO. With the flow convecting further, due to much higher flame temperature, a significant amount of NO is reformed again and results in the second NO “peak”. This second peak is again due to (1) in case of zero NH₃ doping, firstly the prompt NO formation mechanism (53%) and thermal NO (47%); and (2) in case of 1 vol% NH₃ doping, mainly fuel NO (63%) then secondly prompt NO (29%), which is ~3 times that of thermal NO (9%).

Two chemical mechanisms, GRI-Mech 3.0 and the Tian's mechanism are compared. Relatively speaking, GRI-Mech 3.0 appears to be more accurate than the Tian mechanism at predicting CH₄/air diffusion flames. This is true not only for the two-dimensional flame structure and flame length, but also the one dimensional NO profile along the centerline, $X_{NO,centerline}$. The $X_{NO,centerline}$ by GRI-Mech 3.0 and $X_{NO-PLIF}$ show better agreement than the case of Tian et al.

CHAPTER 6 RESULTS: LAMINAR SYNGAS DIFFUSION FLAMES

In this chapter, an experimental *in-situ* laser-based measurement of OH and NO, i.e. OH PLIF and NO PLIF are reported. Numerical modeling of laminar syngas diffusion flames is also reported. The effect of NH₃ doping on the flame structure and emission characteristics is investigated. The effect of syngas composition (or specifically the effect of CH₄ in syngas fuel) on the NO formation is also investigated.

Experimentally, different amounts of NH₃ dopant were added to the fuel stream to understand the chemistry of fuel-N on NO formation. First, spatially resolved planar OH concentration profiles of syngas diffusion flames were obtained using PLIF. Then, *in situ* NO concentration profiles were recorded by PLIF Imaging. In addition, two syngas compositions (F1: 45% H₂, 45% CO and 10% CH₄; F2: 50% H₂ and 50% CO) were tested by doping varying amount of NH₃, and *in-situ* NO measurements were compared to evaluate the effect of CH₄ in NO formation. Hereafter, the “F1” syngas refers to fuel compositions of 45 vol% H₂, 45 vol% CO and 10 vol% CH₄, “F2” refers to 50 vol% H₂ and 50 vol% CO.

In the following sections, we compare the 2-D numerical and experimental OH distributions, followed by the 2-D NO distributions in the same manner. We also evaluate NO profiles along the centerline of these syngas flames based on computational data. The effects of NH₃ addition on NO formation is discussed along with the relative contributions of NO sub-mechanisms.

The methodology used to study the syngas diffusion flame is basically the same as used for CH₄/air diffusion flames. The effects of NH₃ addition on the flame structure are investigated based on 2-D distribution of OH and NO radicals. Comparison of PLIF

data with CFD calculations by both the GRI-Mech and Tian's mechanism are used to determine which mechanism is suitable for various conditions.

6.1 OH Profiles: Comparison of Experimental and Simulated PLIF signals

As mentioned in the last chapter, conversion from NO/OH-PLIF signal to absolute NO concentration requires the information of major fluorescence quenching species and temperature distribution, which isn't available from the current experimental set up. Since these data can be estimated from the CFD calculation, conversion from 2-D numerical OH/NO to a 2-D "simulated" OH/NO fluorescence signal instead is implemented, as described in Chapter 5, i.e.

$$S_{f,\text{simulated}} \propto S_{f,\text{experiment}} \quad (5.1a)$$

or

$$S_{f,\text{simulated}} = k \times S_{f,\text{experiment}} \quad (5.1b)$$

where the $k = \left(X_{\text{NO}} \times \frac{I_r}{LIF} \right)_{\text{cal}}$ is the calibration slope. Hereafter, this quantity is called "simulated" fluorescence signal or $S_{f,\text{simulated}}$.

Conversion from a PLIF signal to absolute concentration is also implemented along the centerline of the flame (2-D conversion is relatively computationally expensive). However, this requires incorporating the major quenching species and temperature with experimental PLIF signal and another premix flame calibration. Figure 6-1 shows experimental and computational comparison of 2-D OH spatial distribution in syngas diffusion flames without NH_3 doping.

Each experimental OH-PLIF image is an average of 50 camera shots taken consecutively at a sampling rate of 2 Hz. The overall agreement for flames structure

without NH_3 is reasonable, although the simulation data shows around 5% over-prediction of flame length. As can be seen, the OH yield higher signal intensity next to the tube rim for both “simulated” and experimental fluorescence signals, whereas both are lower near flame tip. The flame sheet thicknesses are under-predicted by Tian mechanism.

The normalization of the images is performed by dividing the entire image by the maximum signal, so that the entire range is from 0.0 to 1.0 . However, since experimental data has inherent noise, it is normalized by its 99.99% percentile.

Comparing the experimental data of two compositions (F1 vs. F2), the F1 syngas flames have higher flame height, which is due to higher molar stoichiometric ratio S_{stoi} required for methane to reach complete combustion. The ratio S_{stoi} is defined as:

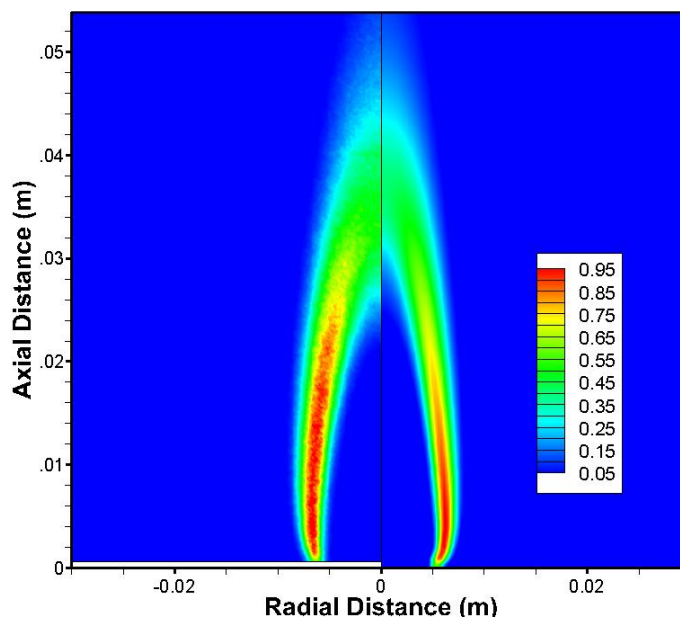
$$S_{\text{stoi}} = \left(\frac{\text{moles of oxidizers}}{\text{moles of fuel}} \right)_{\text{stoichiometric}}, \quad (5.3)$$

since flame length is proportional to the molar stoichiometric ratio, the more oxidizer is required, the longer the flame length.

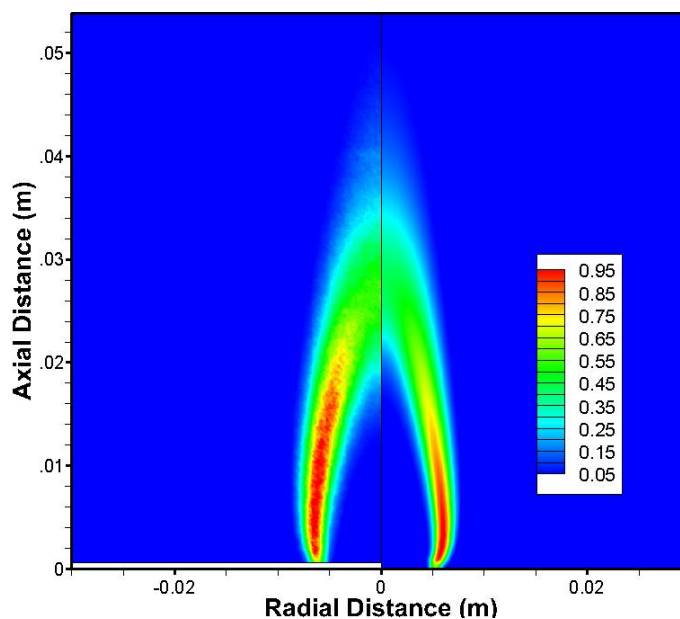
Figure 6-2 shows experimental OH-PLIF images for different NH_3 seeding levels. With the increasing addition of NH_3 , the flame length increases. This is due to the change of stoichiometric ratio S_{stoi} . The flame length of diffusion flames is inversely proportional to the molar stoichiometric ratio S_{stoi} , and the addition of NH_3 increases S_{stoi} , i.e. it requires more oxygen to reach complete combustion, thus, the overall flame length is enhanced. In addition to the flame length increasing, the OH flame layers become thinner with NH_3 addition.

Similar trends are shown in the simulated OH-PLIF images in Figure 6-3. The simulation incorporates Tian's mechanism to describe the chemical reaction. As was the case for CH₄ flames in Chapter 5, the overall agreement in flames heights with NH₃ seeding between experimental and simulated OH PLIF is reasonable. Both experimental and numerical results have similar OH spatial distributions, with similar flame structure shapes. While the absolute OH layer thicknesses are not in agreement between the experiment and the CFD prediction, both show the flame becoming thinner with NH₃ addition.

Figure 6-4 shows experimental and "simulated" OH-PLIF signals for syngas flames with up to 50% NH₃, which is the maximum amount of NH₃ that can be added to maintain a flame. The simulation result shows 10% under-prediction on flame length. Again, the absolute OH layer thicknesses are not in agreement between the experiment and the CFD prediction.

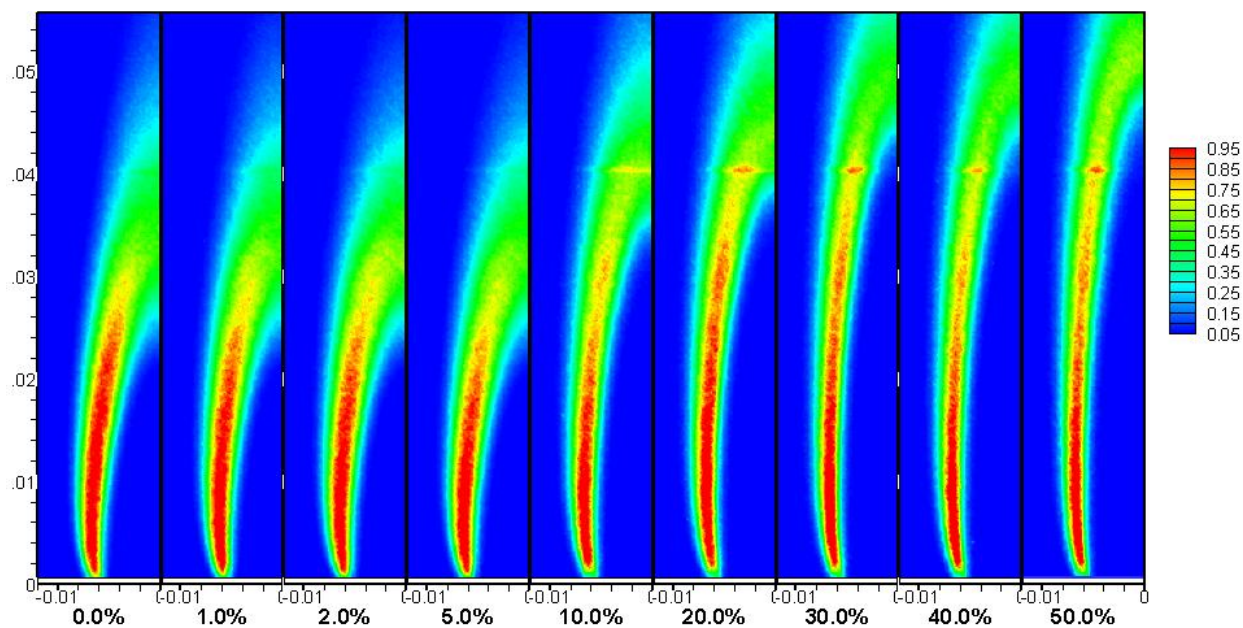


a) F1 syngas, 45% H_2 , 45% CO , 10% CH_4

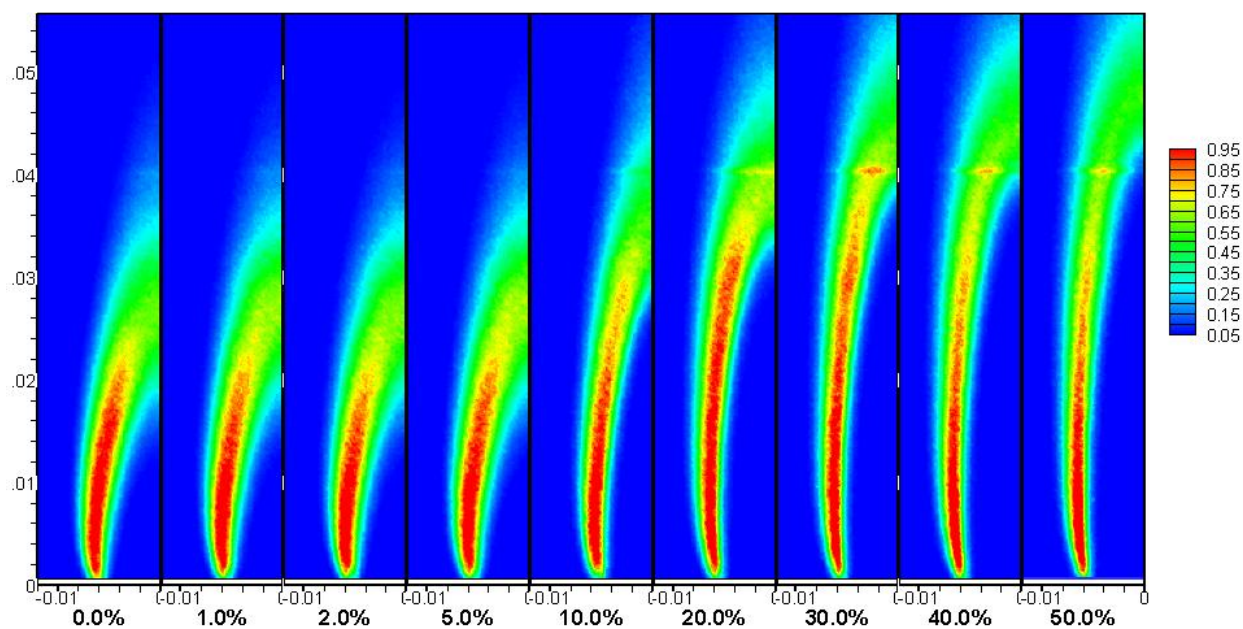


b) F2 syngas, 50% H_2 , 50% CO

Figure 6-1: Experimental (left) and computational (right) OH profile of syngas diffusion flames without NH_3 seeding. CFD simulation was performed using Tian's mechanism.

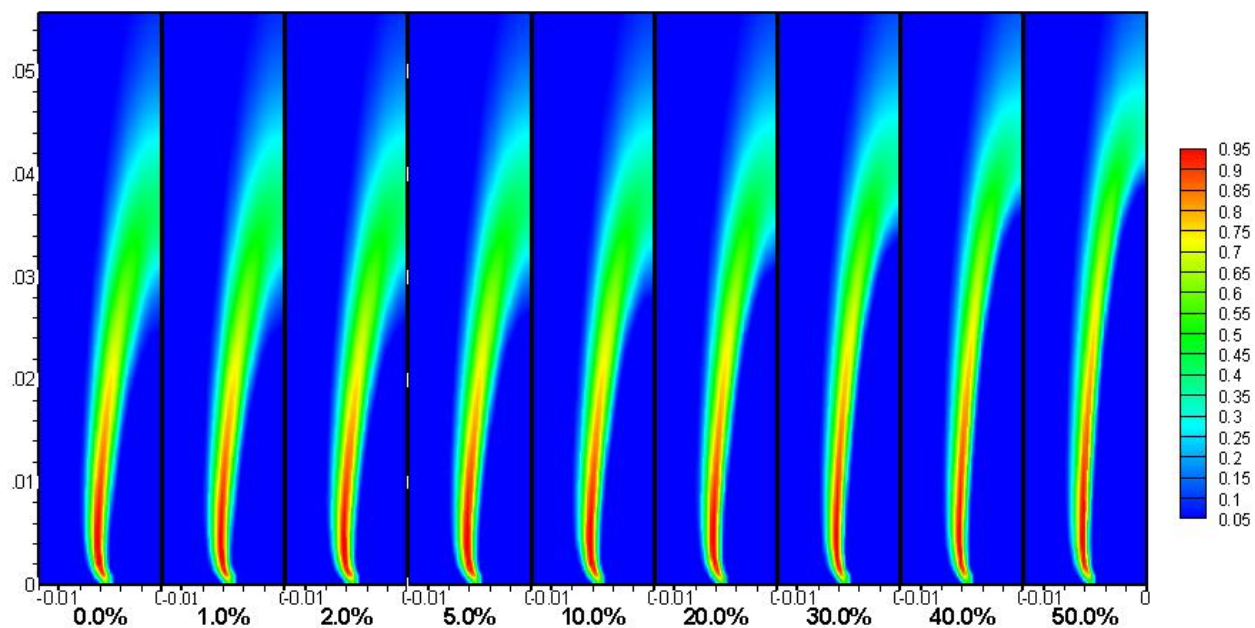
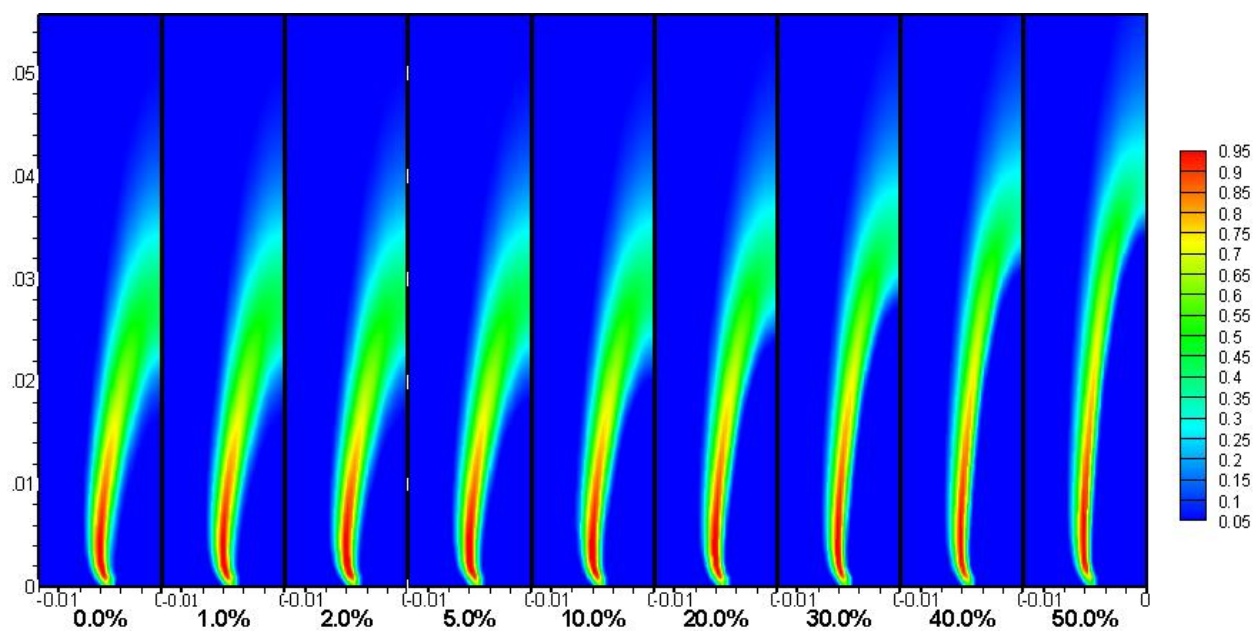


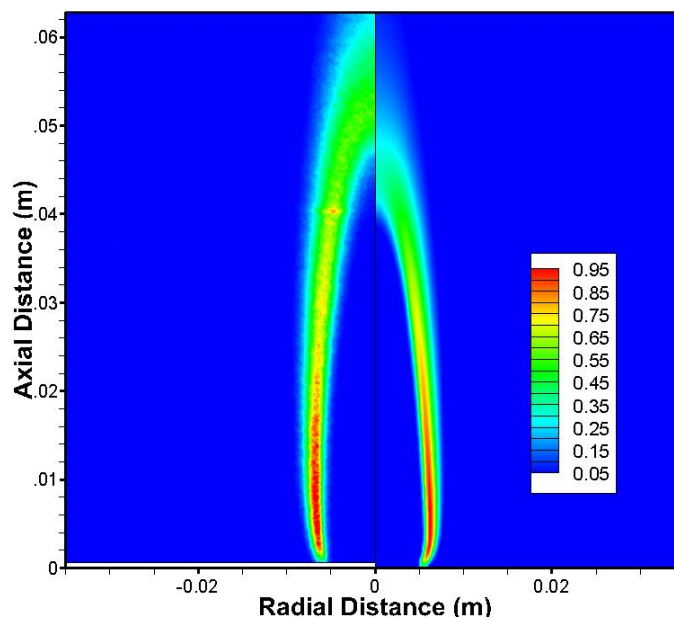
a) 45% H₂, 45% CO, 10% CH₄



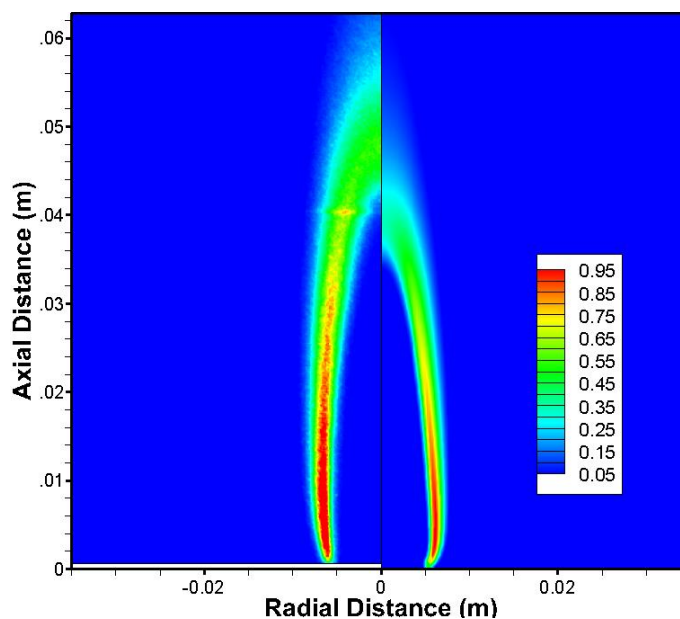
b) 50% H₂, 50% CO

Figure 6-2: Experimental OH-PLIF images from 0% to 50% NH₃ seeding.

a) F1: 45% H₂, 45% CO, 10% CH₄.b) F2: 50% H₂, 50% CO.Figure 6-3: Simulated OH-PLIF images from 0% to 50% NH₃ seeding.



a) F1: 45% H₂, 45% CO 10% CH₄.



b) F2: 50% H₂, 50% CO.

Figure 6-4: Experimental (left) and computational (right) OH profile of syngas laminar diffusion flames with 50% NH₃. CFD simulation was performed using Tian's mechanism.

6.2 NO profiles: Comparison of Experimental and Simulated Signals

As mentioned in previous sections, obtaining absolute NO concentration with NO-PLIF image requires information of local temperature, major quenching species, etc., because quenching corrections and Boltzmann corrections must be taken into consideration, as mentioned in Chapter 3. This additional data is obtained from the CFD results.

“Simulated” NO fluorescence signal, similar to the OH counterparts in the previous section, have been derived as well. Comparison between this “simulated” NO fluorescence signal and experimental signal can then be made for validation of CFD calculations. Details about the calibration data was presented previously in Chapter 3. For ease of comparison, both experimental and “simulated” fluorescence signals are normalized to the 0 ~ 1 range and plotted in the range of 0.05 ~ 0.95.

Figure 6-5 shows the experimental 2-D NO-PLIF signals from 100 ppm to 1% NH_3 in the fuel stream. Both syngas compositions (F1: 45% CO, 45% H_2 , 10% CH_4 and F2: 50% CO, 50% H_2) are shown. Overall, with increasing NH_3 , the NO signal also increases. In addition, using 1% NH_3 doping as the representative, the NO-PLIF signals are not equally distributed within the flame zone. Instead, there is a darker, central region inside the flame.

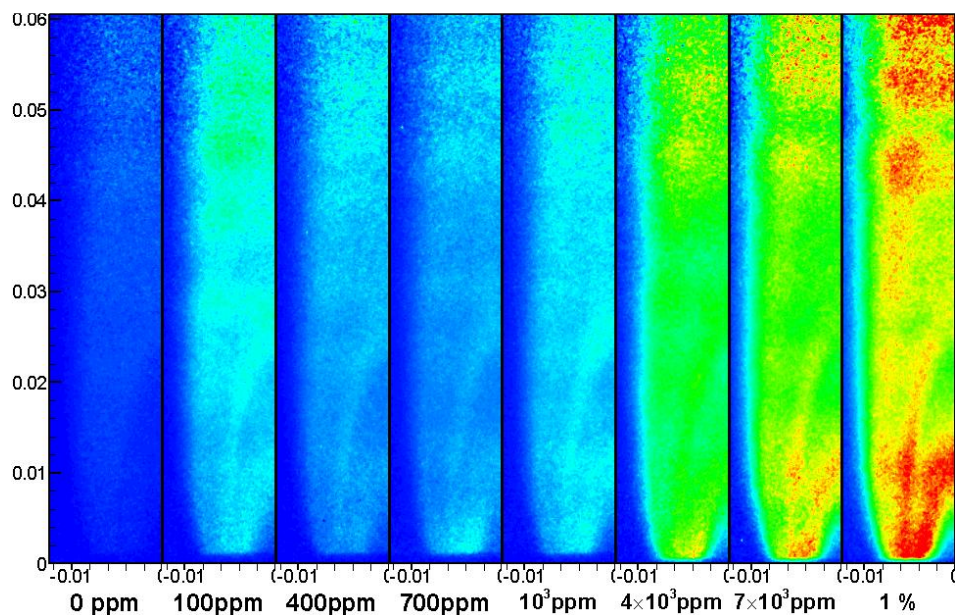
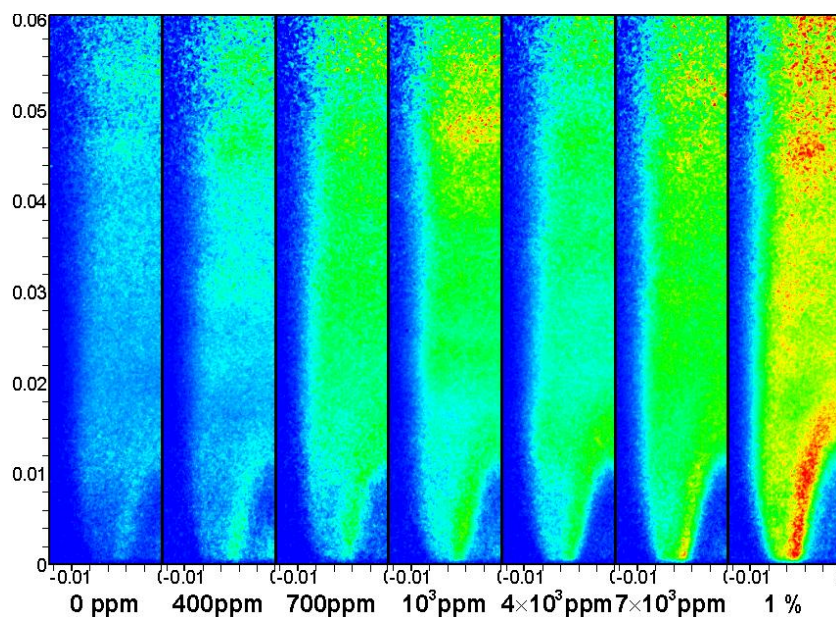
a) F1: % CO 10% CH₄b) F2: 50% H₂ 50% CO

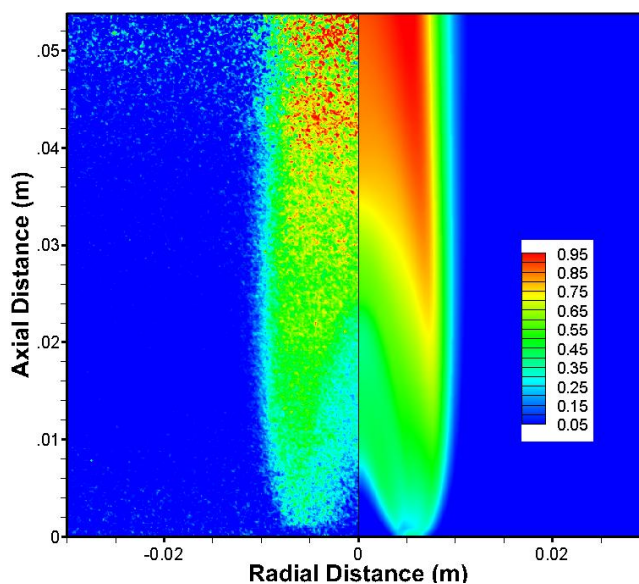
Figure 6-5: Experimental 2-D NO-PLIF signals with different amounts of NH₃ seeding. Since these laminar diffusion flames are symmetric, only halves on left are shown.

Two different compositions are shown in the figure. Reasonable agreement can be seen with respect to flame length and structure between experimental and computational data. Again as seen in the last chapter of CH_4 diffusion flame, the experimental data doesn't show smooth NO spatial distribution, background signal obviously has random "roughness" inherently due to low signal-to-noise ratio. Nonetheless, it still could be seen that NO is mainly formed in the high temperature region. With regard to model validation, the internal flame structures are comparable for the experimental and numerical results. Similarly, the growth of the NO signal at higher flame heights is tracked in both cases.

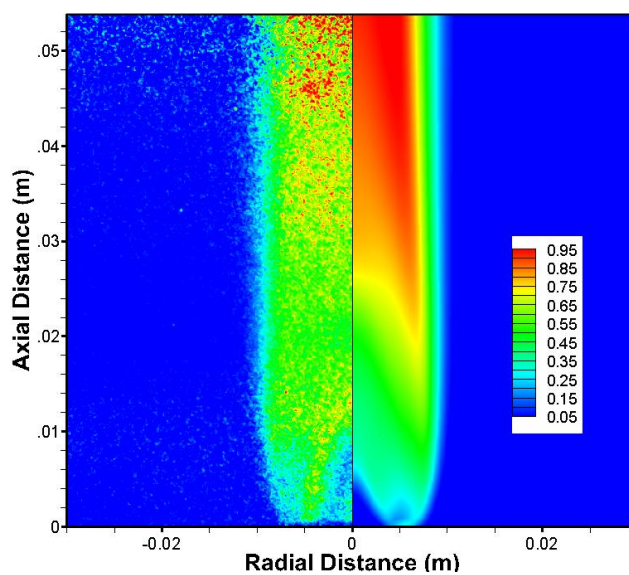
Similarly, in case of 1% NH_3 seeded in the fuel stream as shown in Figure 6-7: Experimental (left) and computational (right) NO profile of syngas laminar diffusion flames with 1% NH_3 . CFD simulation was performed using Tian mechanism., reasonable agreement can be seen in terms of flame length and structure. Since the signal-to-noise ratio is highly improved in this case, the background looks much "clearer" than that of 100 ppm NH_3 seeding. NO is mainly found in both the high temperature region (upper part of the flame) and the bottom part of the flame (next to the tube exit).

When larger amount of NH_3 doped into the flame, flames are stretched and change in shape, as shown in Figure 6-8: Experimental (left) and computational (right) NO profile of syngas laminar diffusion flames with 30% NH_3 . CFD simulation was performed using Tian's mechanism. Again, reasonable agreement can be seen in terms of flame length and internal structure. However, with 30% NH_3 doping, there are still some discrepancies with the NO distribution. For example, the simulated NO signal is

higher next to the fuel tube “rim” (not the “entire” exit but the tube rim), whereas the experimental data shows NO is still higher further from the tube.

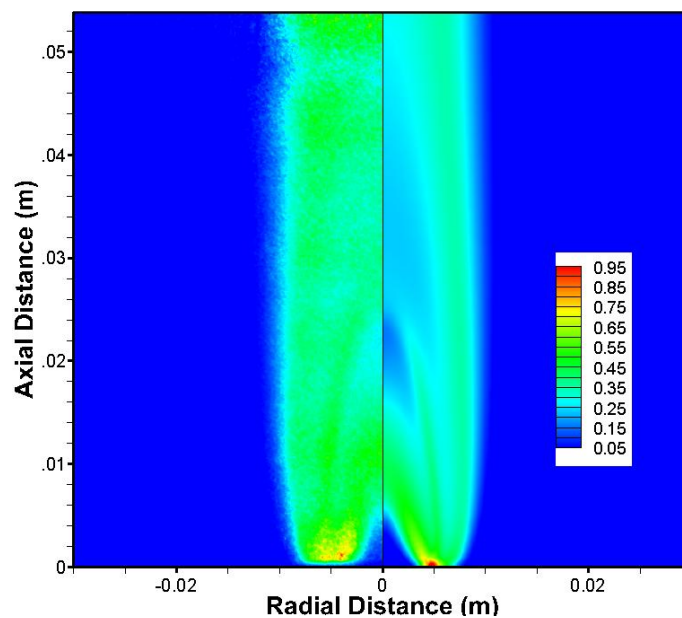


a) F1: 45% H₂, 45% CO, 10% CH₄

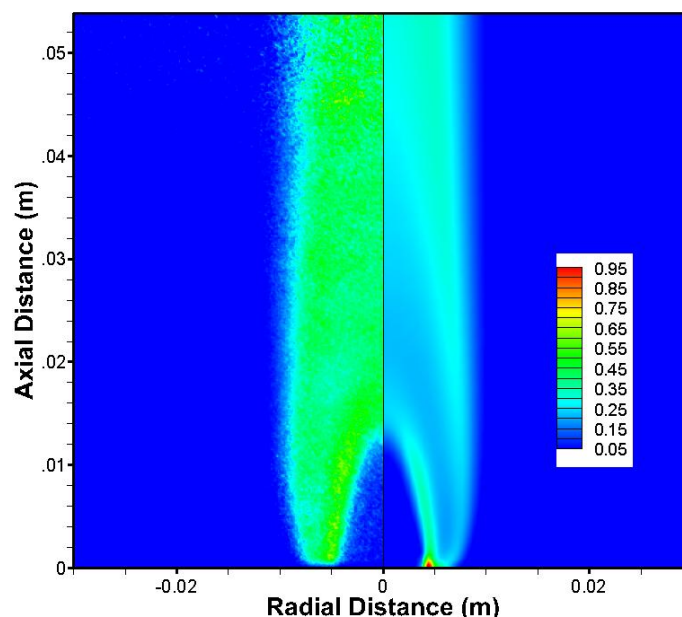


b) F2: 50% H₂, 50% CO

Figure 6-6: Experimental (left) and computational (right) NO profile of syngas laminar diffusion flames without NH₃. CFD simulation was performed using Tian mechanism.

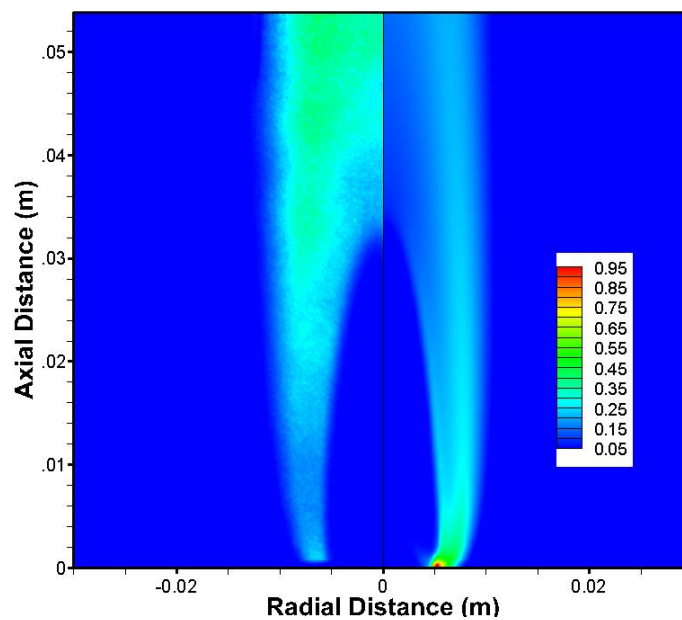


a) F1: 45% H₂, 45% CO, 10% CH₄

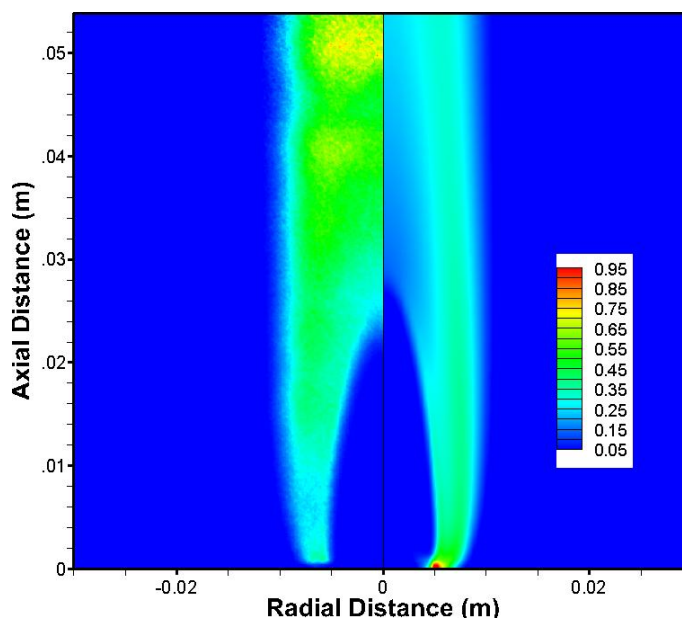


b) F2: 50% H₂, 50% CO

Figure 6-7: Experimental (left) and computational (right) NO profile of syngas laminar diffusion flames with 1% NH₃. CFD simulation was performed using Tian mechanism.



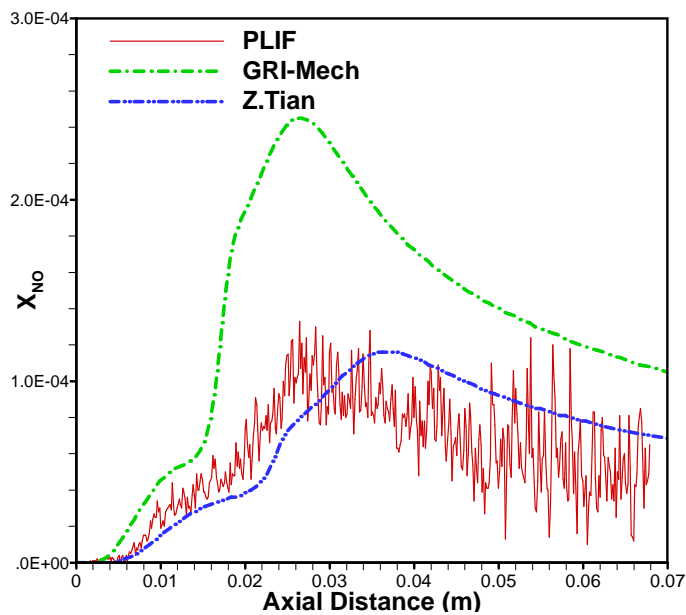
a) F1: 45% H₂, 45% CO, 10% CH₄



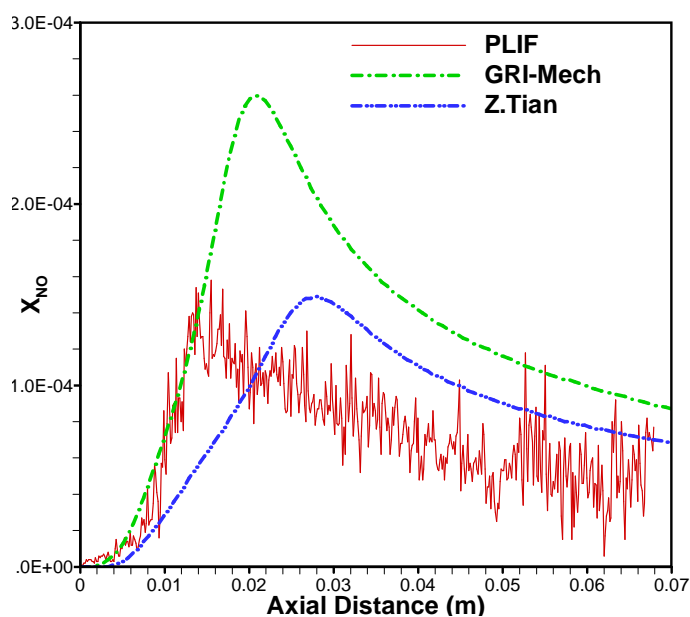
b) F2: 50% H₂, 50% CO

Figure 6-8: Experimental (left) and computational (right) NO profile of syngas laminar diffusion flames with 30% NH₃. CFD simulation was performed using Tian's mechanism.

To better understand the details of NO formation and evaluate which chemical mechanism predicts the NO formation more accurately, several NO profiles along the centerline of the flames are plotted in Figure 6-9, Figure 6-10 and Figure 6-11: Comparison of measured NO concentration in centerline with 30% NH₃ doped flames with CFD. Green lines for GRI-Mech mechanism. Blue lines for . In each figure, both the F1 and F2 syngas flames are compared. Generally speaking, the GRI-Mech 3.0 mechanism always over-predicts the NO mole fraction, especially at higher NH₃ doping levels. With increasing NH₃ doping levels, the peak NO predicted by the GRI-Mech 3.0 mechanism shows two times higher NO than those measured from the experimental data. When the NH₃ doping level is low, the NO profile of the Tian mechanism is shifted downstream of the experimental data. When NH₃ doping level is high, excellent agreement can be found using the Tian's mechanism, especially near the flame front. The Tian's mechanism not only correctly predicts the peak NO levels, but also predicts accurately the overall NO distribution throughout the flame centerline. Comparing syngas flames between two types of compositions, the Tian mechanism seems to be slightly more accurate with F2 syngas flames.

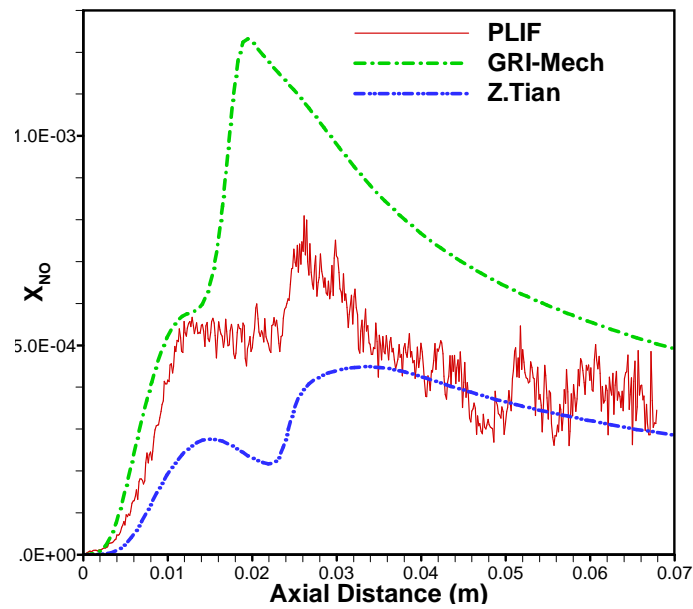


a) F1: 45% H₂, 45% CO, 10% CH₄

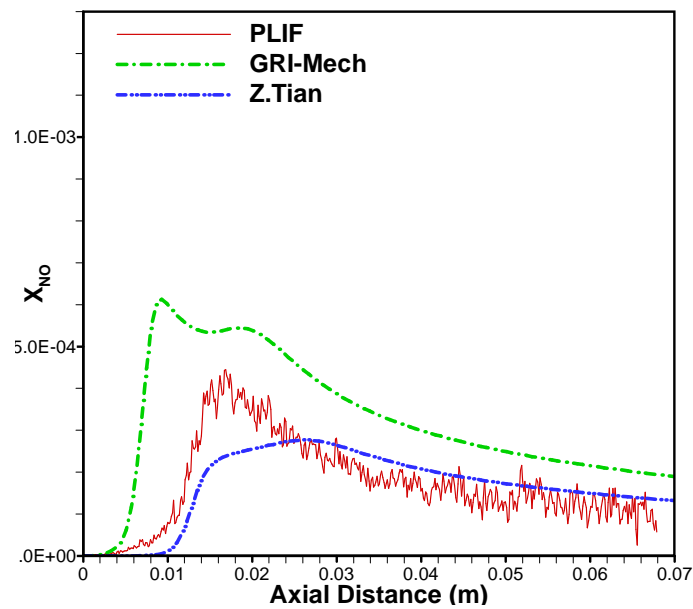


b) F2: 50% H₂, 50% CO

Figure 6-9: Comparison of absolute NO concentration in centerline un-doped flames with CFD. Green lines for GRI-Mech 3.0 mechanism. Blue lines for Tian mechanism



a) F1: 45% H₂, 45% CO, 10% CH₄



b) F2: 50% H₂, 50% CO

Figure 6-10: Comparison of measured NO concentration in centerline 1% NH₃ flames with CFD. Green lines use GRI-Mech 3.0 mechanism. Blue lines use Tian mechanism.

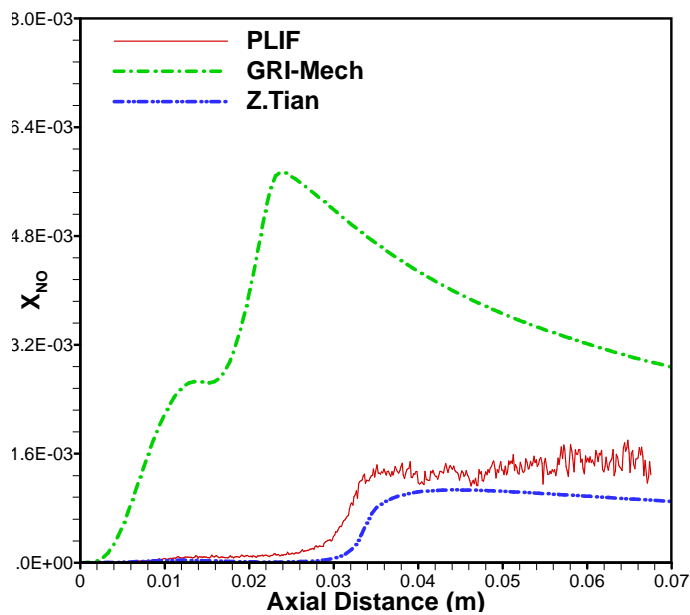
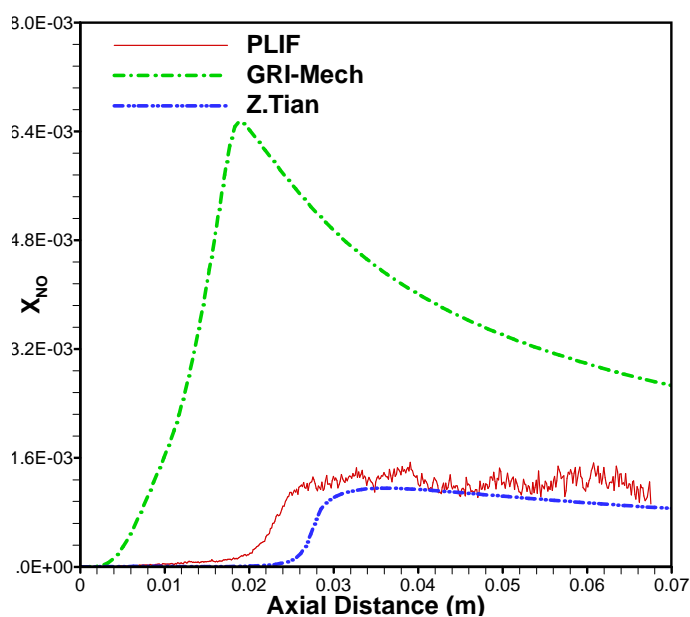
a) 45% H₂, 45% CO, 10% CH₄b) 50% H₂, 50% CO

Figure 6-11: Comparison of measured NO concentration in centerline with 30% NH₃ doped flames with CFD. Green lines for GRI-Mech mechanism. Blue lines for Tian mechanism

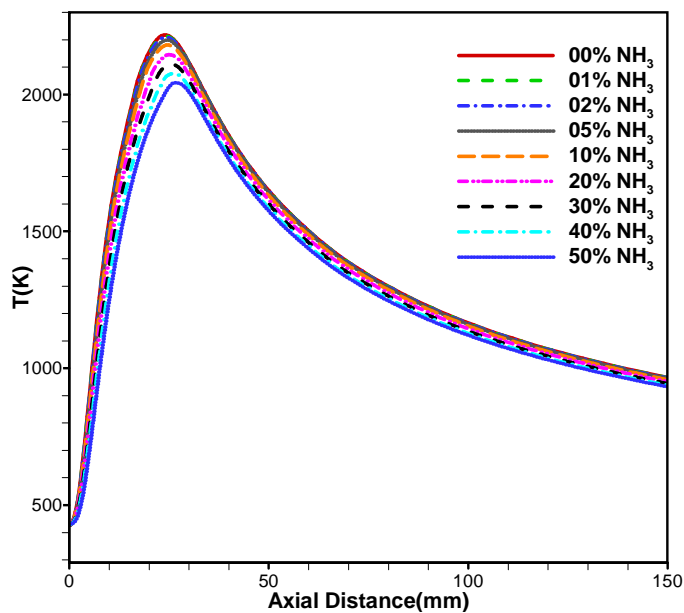
6.3 Mechanism Comparison for OH Profiles (GRI-Mech 3.0 vs. Tian et al.)

Figure 6-12 shows the overlay of centerline temperature profiles in the F1 (45% H_2 , 45% CO , 10% CH_4) syngas diffusion flame with varying levels of NH_3 , using the GRI-Mech 3.0 and Tian mechanisms. Only the temperature profile along the centerline is plotted for ease of comparison. Both mechanisms yield similar temperature profiles. The profile quickly peaks, and then decreases gradually in the downstream direction. The maximum temperature reaches around 2000K, with the GRI-Mech 3.0 prediction being higher than that of the Tian mechanism. The addition of NH_3 reduces the maximum temperature in both mechanisms, but the Tian mechanism predicts that the peak temperature shifted to the flame front further away from the fuel nozzle; this shift of peak temperature is mainly due to the increase in flame length with addition of NH_3 .

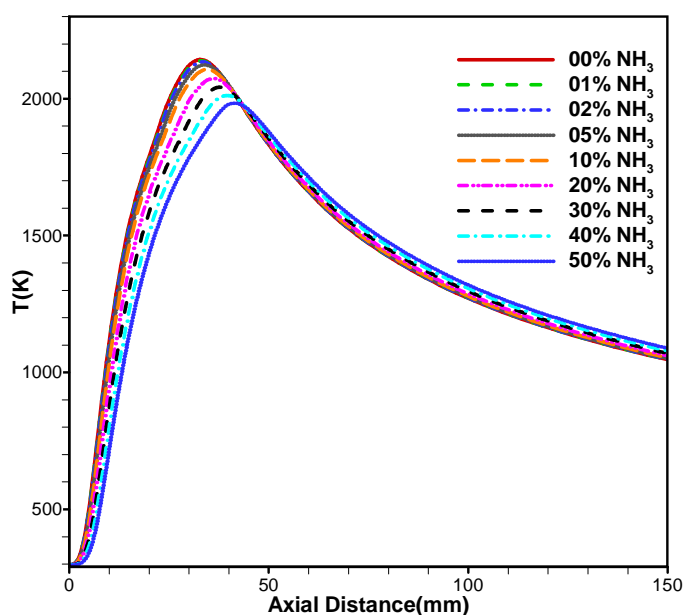
Similar to the temperature profile, Figure 6-13 shows the overlay of centerline OH profiles in F1 (45% H_2 , 45% CO , 10% CH_4) syngas diffusion flames using GRI-Mech 3.0 and Tian mechanisms, respectively. Only the OH profile along each flame centerline is plotted for ease of comparison. GRI-Mech 3.0 showed higher peak OH than prediction by Tian's mechanism. The OH decreases gradually with NH_3 addition. The Tian mechanism also predicts that the peak OH shifts to the flame front further away from fuel nozzle with NH_3 addition because of the increase in flame length .

Similar to the OH profile, Figure 6-14 shows the overlay of centerline NO profiles in F1 (45% H_2 , 45% CO , 10% CH_4) syngas diffusion flames using the GRI-Mech 3.0 and Tian's mechanisms. Only the NO mole fraction profile along the centerline is plotted for ease of comparison. GRI-Mech 3.0 shows higher NO peak mole fraction than the Tian's mechanism. The NO mole fraction increases near the exit of the fuel nozzle, followed by

a steep drop before it achieves another peak and decreases gradually downstream. The NO mole fraction drop in the middle of the flame may be due to the lower temperature in the central region of the flame and the NO-reburn mechanism [32, 34], which is addressed later in this chapter. The overall NO mole fraction increases proportionally with NH_3 addition. Both mechanisms predict that the peak NO mole fraction shifts the flame front further away from the fuel nozzle. The shift of OH mole fraction was mainly due to the elongation of flame with an increase in NH_3 seeding. The interesting point is the prediction by the Tian mechanism. It shows a tenfold increase in NO mole fraction in the region near the nozzle when only 1% NH_3 was doped. Increasing the NH_3 level only reduced the NO mole fraction in this region, even though the overall NO was increased.

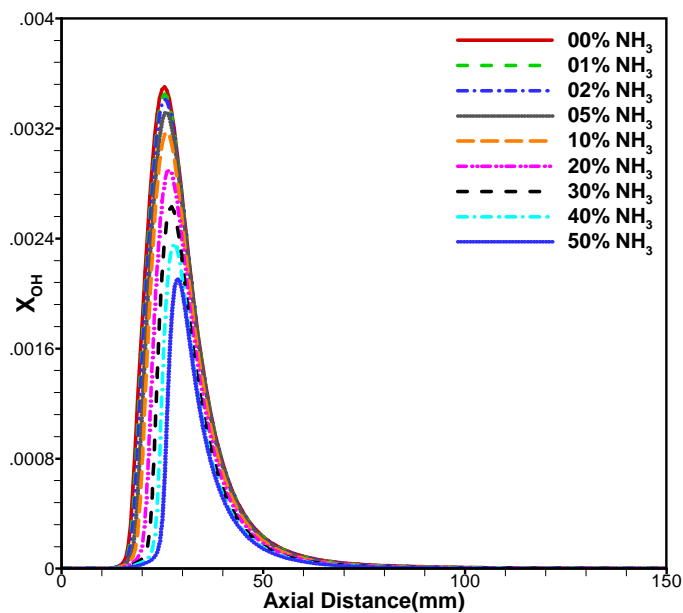


a) GRI-Mech 3.0 mechanism

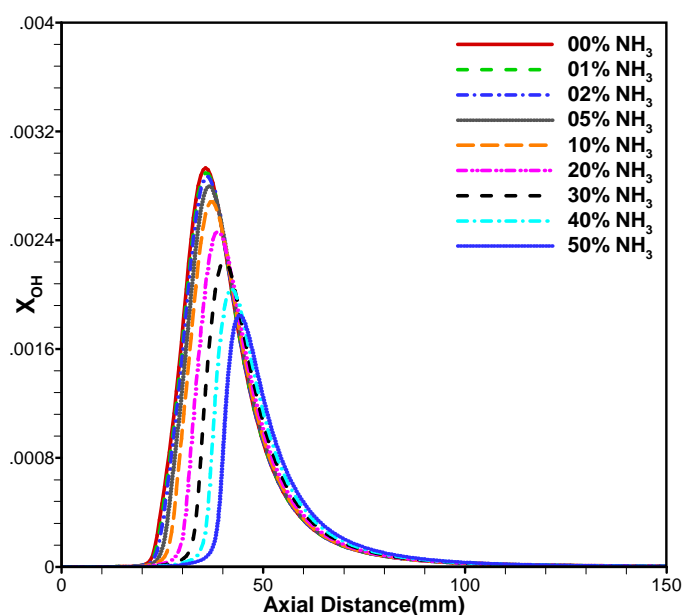


b) Tian's mechanism

Figure 6-12: Comparison of simulated centerline temperature profiles for laminar syngas (45% H₂, 45% CO, 10% CH₄) diffusion flames with various amounts of NH₃ seeding by two mechanisms. X axis is the axial distance from fuel nozzle, and Y axis is the temperature.

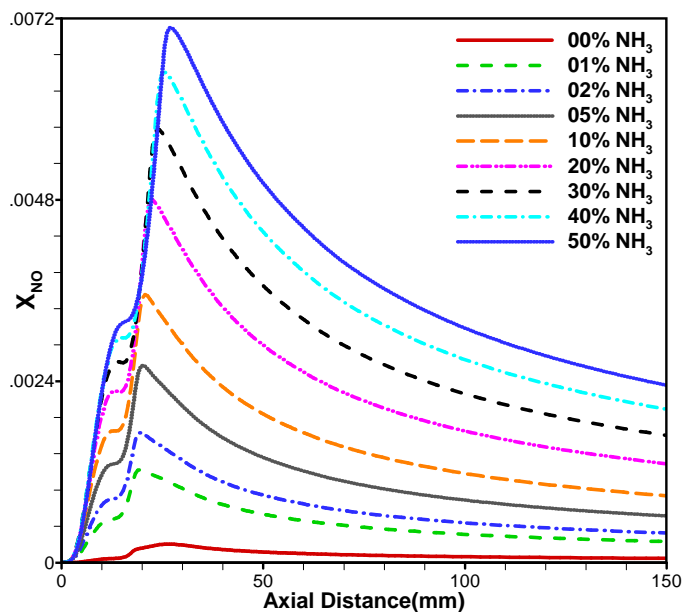


a) GRI-Mech 3.0 Mechanism

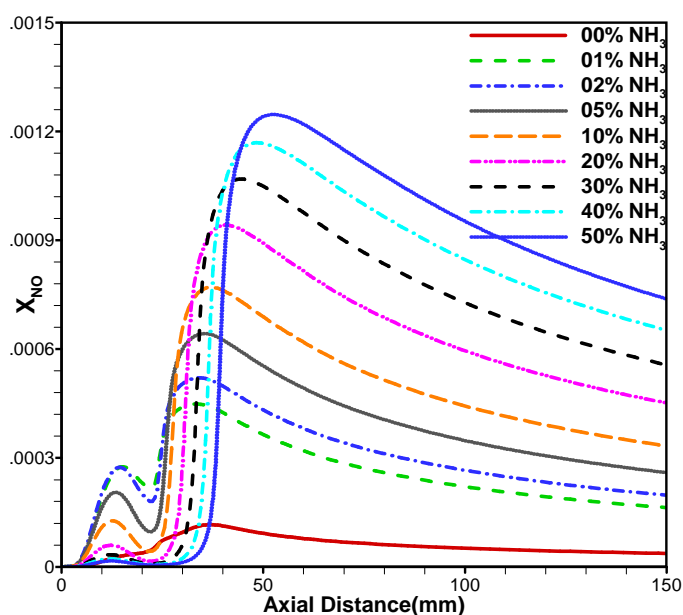


b) Tian's mechanism

Figure 6-13: Comparison of simulated centerline OH mole fraction profiles for laminar syngas (45% H_2 , 45% CO , 10% CH_4) diffusion flames with different amounts of NH_3 seeding using GRI-Mech 3.0 mechanism (top) and by Tian mechanism (bottom).



a) GRI-Mech 3.0 mechanism



b) Tian's mechanism

Figure 6-14: Comparison of simulated centerline NO mole fraction profiles for laminar (45% H₂, 45% CO, 10% CH₄) syngas diffusion flames with different amounts of NH₃ seeding using GRI-Mech 3.0 mechanism (top) and by Tian mechanism (bottom). Only NO mole fraction profile in each flame centerline is plotted for ease of comparison.

6.4 Effects of Syngas Composition with Various Levels of NH₃ Seeding

Two representative syngas mixtures are chosen based on the composition used in typical power generation systems [66]. One contains 45% H₂, 45% CO and 10% CH₄ by volume, which is denoted as “F1”, and the other contains 50% H₂ and 50% CO by volume, which is denoted as “F2”. By comparing flame structures and NO formation characteristics of these two syngas mixtures, further understanding can be achieved regarding the effects of methane and (CH_i) on NO formation in laminar syngas diffusion flames.

The Tian mechanism contains several subsets including the CH_i contribution, NH_i contribution, and interaction between NH_i and CH_i, which are absent in GRI-Mech 3.0. Moreover, the Tian mechanism includes detailed oxidation of both NH₃ and CH₄, whereas GRI-Mech 3.0 was specifically designed for CH₄ oxidation. In addition, our 2-D OH-PLIF and NO-PLIF results presented earlier indicated that the Tian mechanism predicts more accurate flame shapes and flame lengths in syngas diffusion flames compared to GRI-Mech 3.0. Thus, in the following syngas composition studies, syngas combustion chemistry was modeled using Tian mechanism.

To evaluate the CH_i contribution to NO formation in syngas diffusion flames, it is reasonable to compare two syngas (F1 vs. F2) compositions without the NH₃ addition first. Figure 6-15 shows the temperature and major species of two syngas flames without NH₃ doping predicted using Tian mechanism. Both flames show similar reaction zones, with fuel species being transported into the reaction zone, followed by an increase of temperature. As fuel species gradually decrease and approach the reaction zone, major products (e.g. H₂O, CO₂) gradually increase. Mole fractions of major

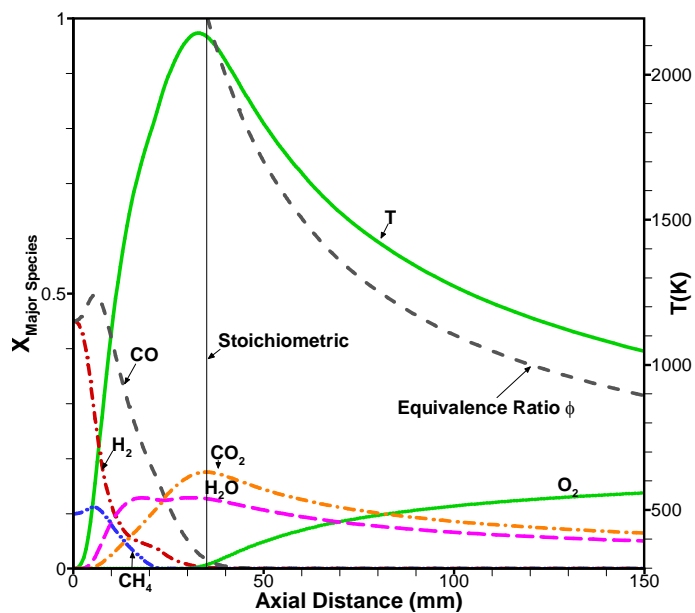
species and temperature reach the maximum near the stoichiometric point. Figure 6-15 (a) contains fuel species CH_4 , as shown in red circle, whereas Figure 6-15 (b) only contains H_2 and CO as the fuel species.

Similarly, Figure 6-16 shows the temperature and minor species of two syngas flames without NH_3 doping predicted using Tian mechanism. Both syngas mixtures show typical hydrocarbon diffusion flame characteristics with H , CH and C_2H_2 radicals peaking upstream of the stoichiometric point, whereas OH and O radicals peak slightly downstream of the stoichiometric point. However, comparing the peak C_2H_2 levels in these two syngas flames, the F1 syngas flame generates 10^5 fold of more C_2H_2 radicals than F2. The F1 flame also produces 10 to 100 fold of more CH radicals than F2. The large amount of CH and C_2H_2 radicals in the F1 syngas flame is very important to NO formation, because CH and C_2H_2 are key radicals in the formation of prompt NO . This implies that NO formation in syngas flames with CH_4 would expect a higher contribution from prompt NO .

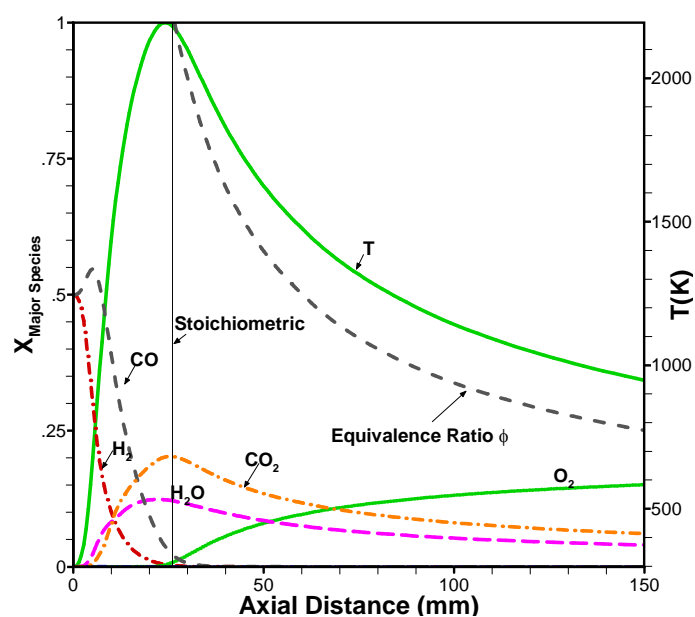
Figure 6-17 and Figure 6-18 show the major and minor species of two syngas flames with 1% NH_3 doping respectively. Same trends still hold for both major and minor species if compared with those without NH_3 doping. For major species, mole fractions of major species reach the maximum near the stoichiometric point. Major species change similarly in the reaction zone except for the existence of CH_4 in F1. For minor species, the F1 syngas flame generates 10^5 fold of more C_2H_2 radicals than F2. The F1 flame also produces 10 to 100 fold of more CH radicals than F2. All the above observations indicate that the existence of large amount of CH and C_2H_2 radicals are due to difference between F1 and F2 syngas flames, and are not related to NH_3 doping levels.

To further support this, Figure 6-19 and Figure 6-20 are plotted to show the major and minor species of two syngas flames with 2% NH_3 doping respectively, and the results indicate that C_2H_2 and CH radicals do not change with more NH_3 doping.

Figure 6-21 compares the predicted temperature of the two syngas mixtures with various levels of NH_3 doping. The data for F1 is repeated from the comparison of chemical mechanisms shown previously in Figure 6-12 b). Without NH_3 doping, the peak temperature for syngas with 10% CH_4 is $\sim 2100\text{K}$, whereas the peak temperature for syngas without CH_4 is $\sim 2200\text{K}$. With 50% NH_3 doping, both syngas flames show a temperature drop of $\sim 300\text{K}$ and a shift in the peak further downstream due to the increase in flame length with NH_3 addition. The flame location as determined by the peak temperature appears to be closer to the tube exit for the case of the F2 (50% H_2 and 50% CO) flame.

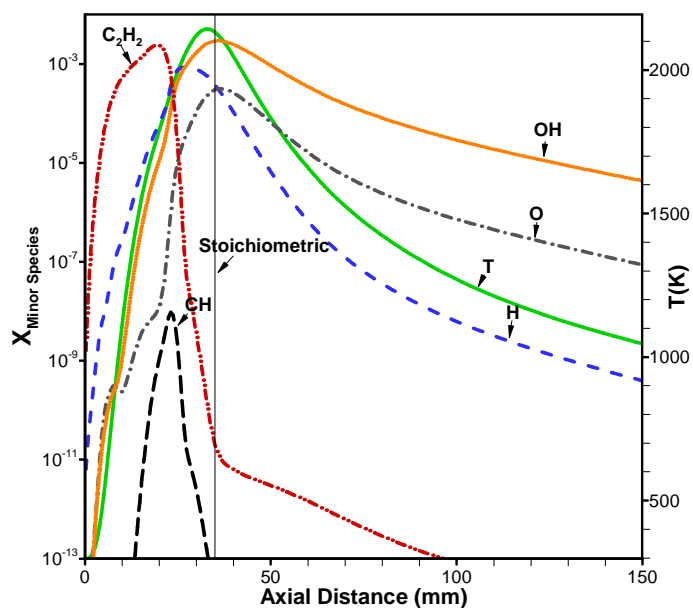


a) 45% H₂, 45% CO, 10% CH₄ (F1)

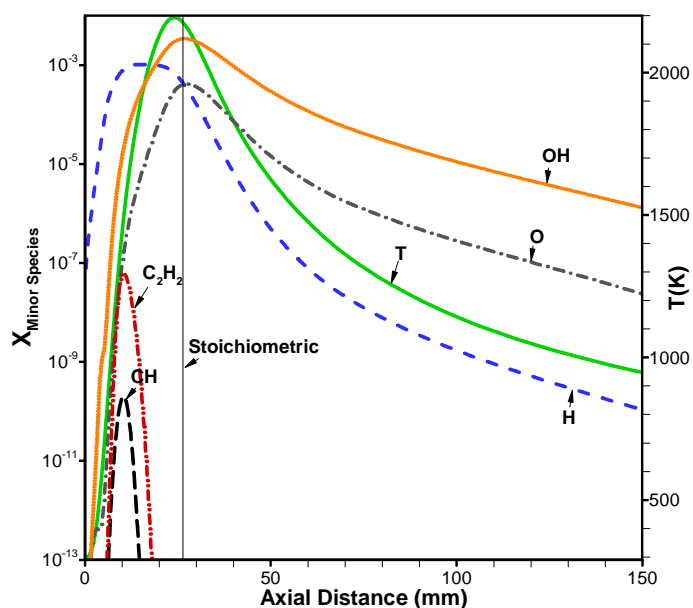


b) 50% H₂ 50% CO (F2)

Figure 6-15: Comparison of the predicted major species and temperature of two syngas mixtures without NH₃ seeding

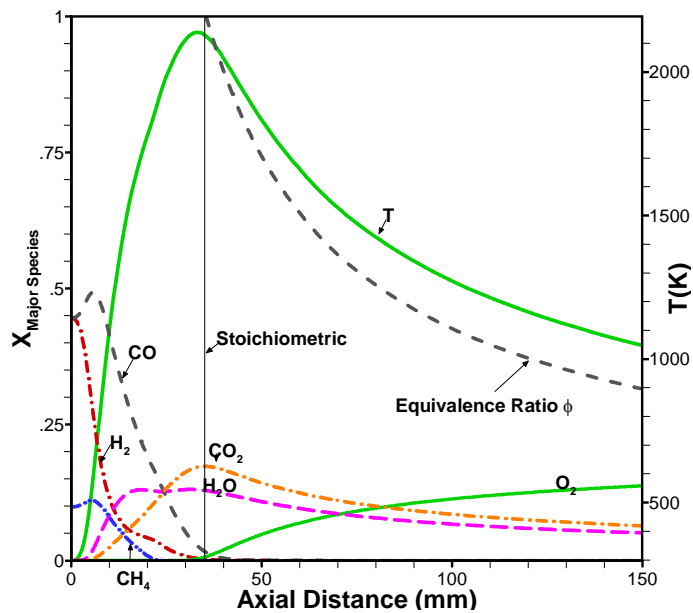


a) 45% H₂, 45% CO, 10% CH₄ (F1)

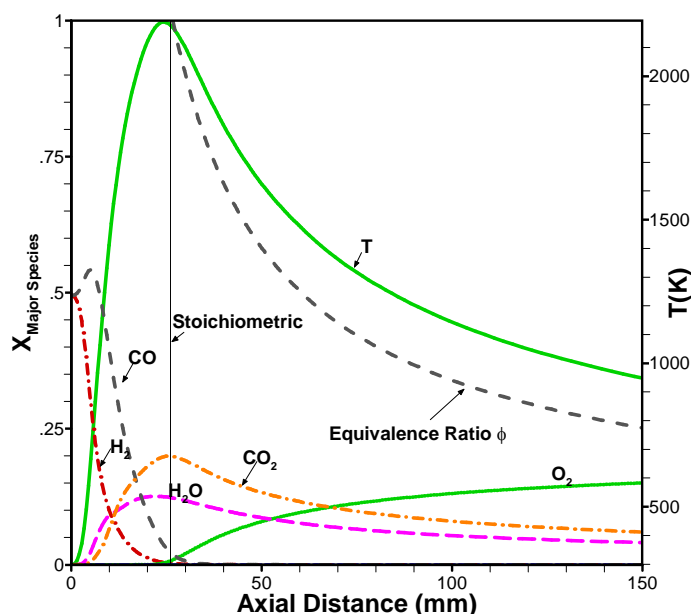


b) 50% H₂, 50% CO (F2)

Figure 6-16: Comparison of the predicted minor species and temperature of two syngas mixtures without NH₃ seeding.

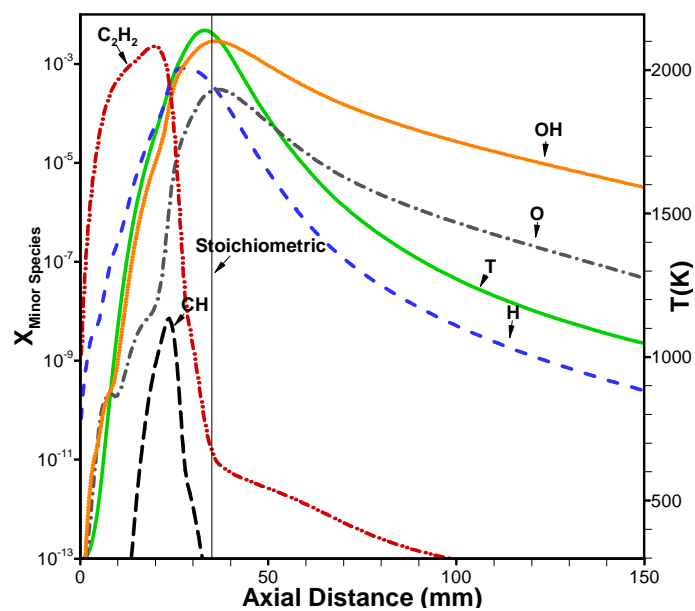


a) 45% H₂, 45% CO, 10% CH₄ (F1)

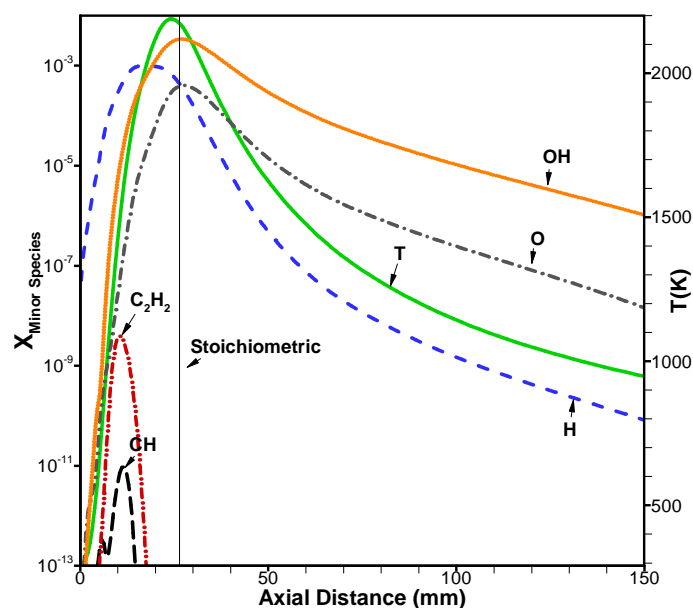


b) 50% H₂, 50% CO (F2)

Figure 6-17: Comparison of the predicted major species and temperature of two syngas mixtures with 1 vol% NH₃ seeding in fuel stream.

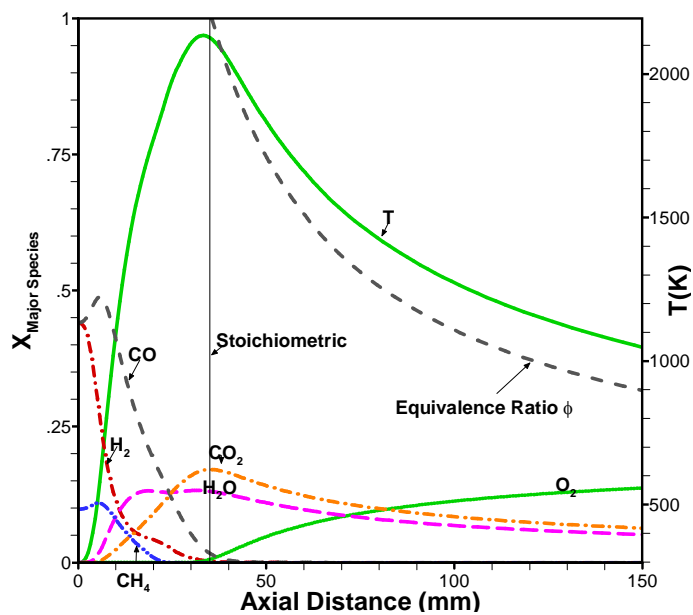


a) 45% H₂, 45% CO, 10% CH₄ (F1)

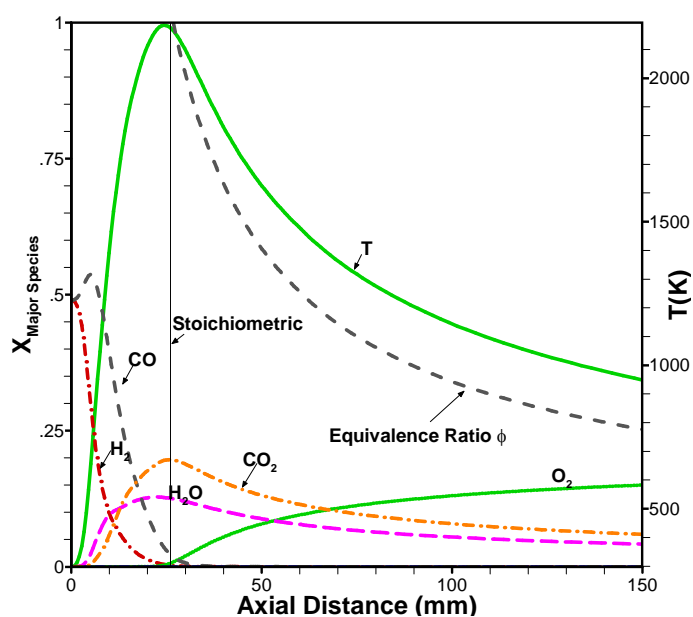


b) 50% H₂, 50% CO (F2)

Figure 6-18: Comparison of the predicted minor species and temperature of two syngas mixtures with 1 vol% NH₃ seeding in fuel stream.

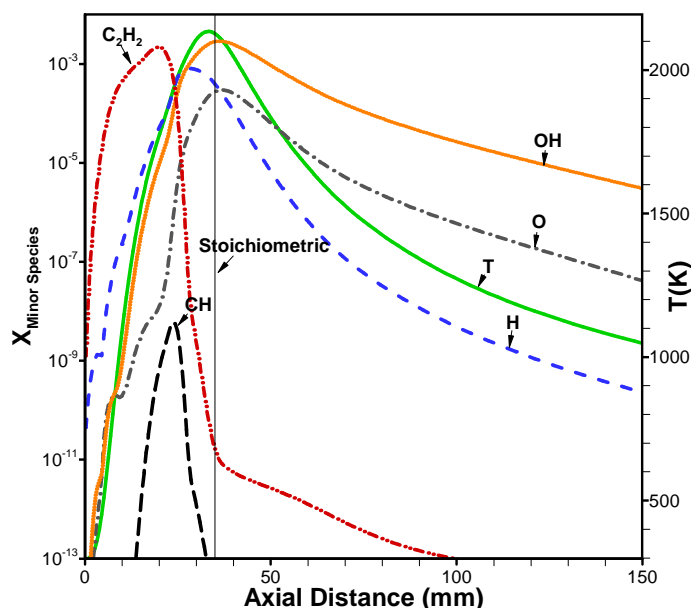


a) 45% H₂, 45% CO, 10% CH₄ (F1)

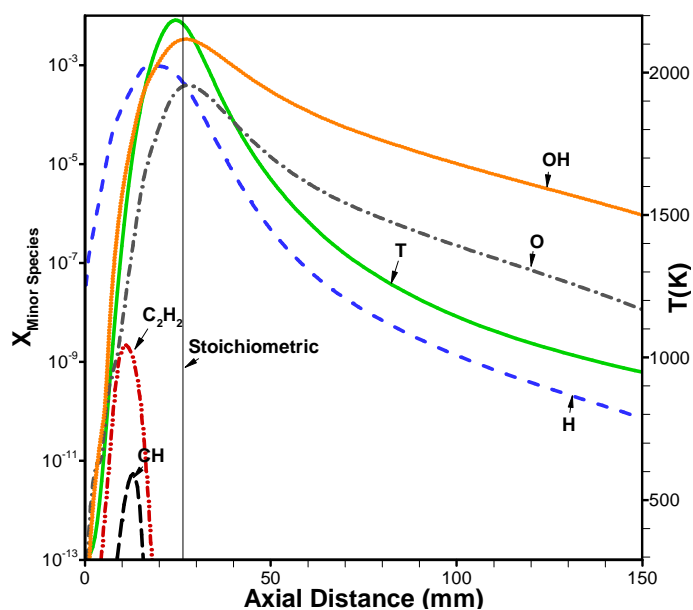


b) 50% H₂, 50% CO (F2)

Figure 6-19: Comparison of the predicted major species and temperature of two syngas mixtures with 2 vol% NH₃ seeding in fuel stream.

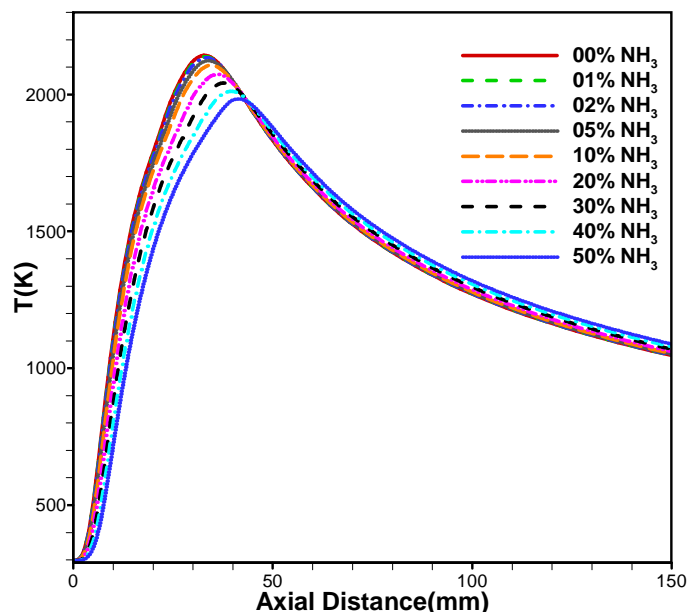


a) 45% H₂, 45% CO, 10% CH₄ (F1)

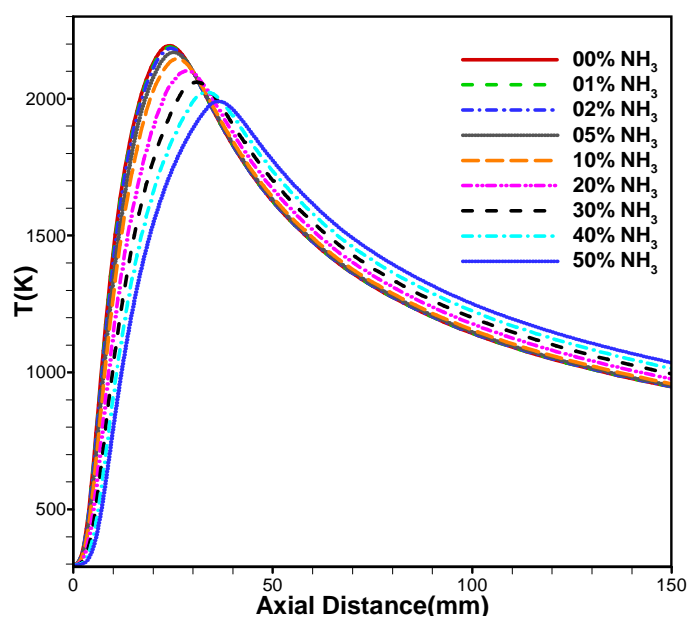


b) 50% H₂, 50% CO (F2)

Figure 6-20: Comparison of the predicted minor species and temperature of two syngas mixtures with 2 vol% NH₃ seeding in fuel stream.



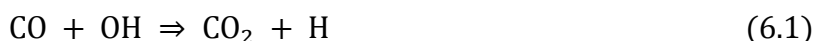
a) 45% H₂, 45% CO, 10% CH₄ (F1)



b) 50% H₂, 50% CO (F2)

Figure 6-21: Comparison of the predicted temperature of two syngas mixtures with various levels of NH₃ seeding.

Figure 6-22 compares the predicted OH mole fraction of the two syngas mixtures along the centerline with various levels of NH₃ seeding. The data for F1 is repeated from the comparison of chemical mechanisms shown previously in Figure 6-13 b). Without NH₃ seeding, the peak OH mole fraction for F1 syngas is 0.0029, whereas the peak OH mole fraction for F2 syngas is 0.0034. The presence of CH₄ inhibits the oxidation of CO [79], which primarily proceeds via the reaction



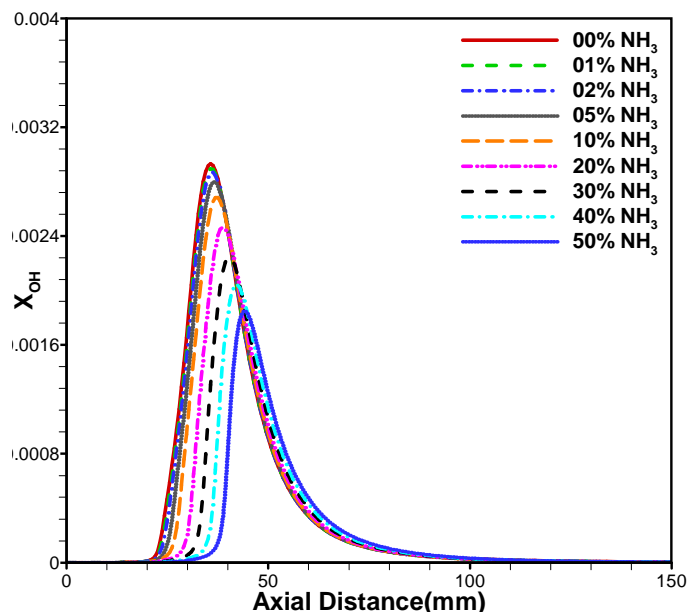
With an increase of NH₃ doping, OH mole fractions of both syngas flames show that the mole fraction drops gradually. At 50% NH₃, OH mole fractions of both syngas flames are ~0.0002. With NH₃ doping, the locations of peak OH also shift further downstream with NH₃ addition, following the same trend as temperature, discussed above.

Figure 6-23 compares the predicted NO mole fraction of two syngas mixtures along the centerline with various levels of NH₃ doping. The data for F1 is repeated from the comparison of chemical mechanisms shown previously in Fig. 6-14 (b). Without NH₃ doping, the peak NO mole fraction in F1 flame is 0.0001, whereas the peak NO mole fraction in F2 flame is slightly higher. The presence of CH₄ favors the prompt NO formation, [79] which primarily proceeds via the following several reactions

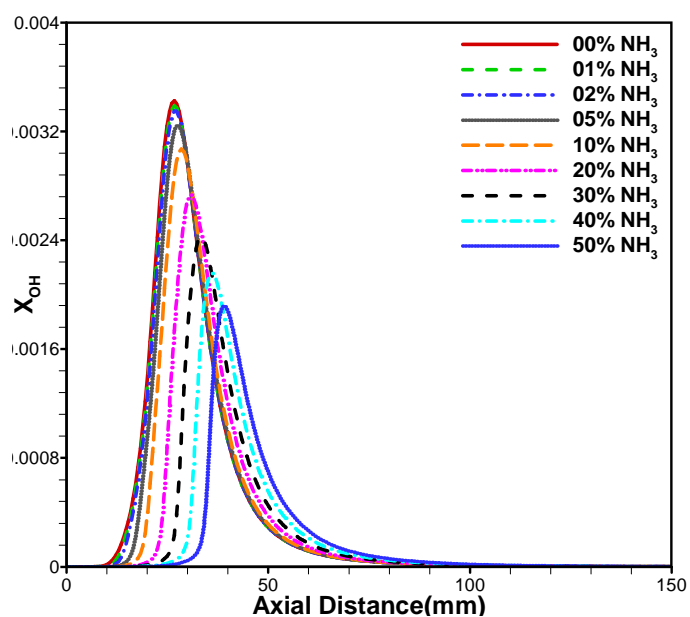


With a slight increase in NH_3 to 1%, the NO mole fractions increase significantly. With further addition, up to 50%, NO mole fractions of both syngas flames increase more gradually. At 50% NH_3 doping, NO mole fractions of both syngas flames are ~ 0.0012 . With NH_3 doping, the shift in the peak NO further downstream mimics that of the shift in temperature further downstream..

The presence of CH_4 not only amplifies the NH_3 seeding effect with more total NO production, but also changes the spatial distribution of NO mole fraction. As discussed in the previous chapter, with the presence of CH_4 , NO profiles for the F1 flame show two peaks along the centerline. For flame F2 (50% H_2 , 50% CO), the addition of NH_3 also leads to a significant increase in NO mole fraction, but the dual-peak structure is not apparent. The detailed NO sub-mechanisms that lead to these differences will be discussed in detail in the next section.

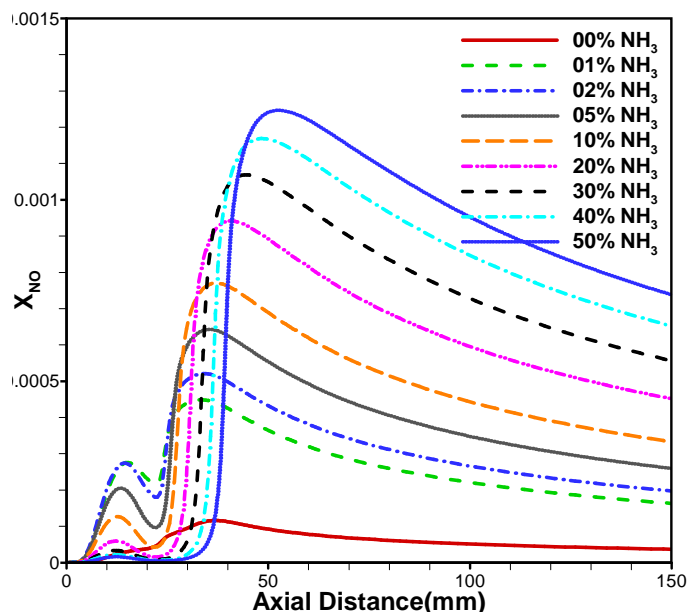


a) 45% H_2 , 45% CO , 10% CH_4 (F1)

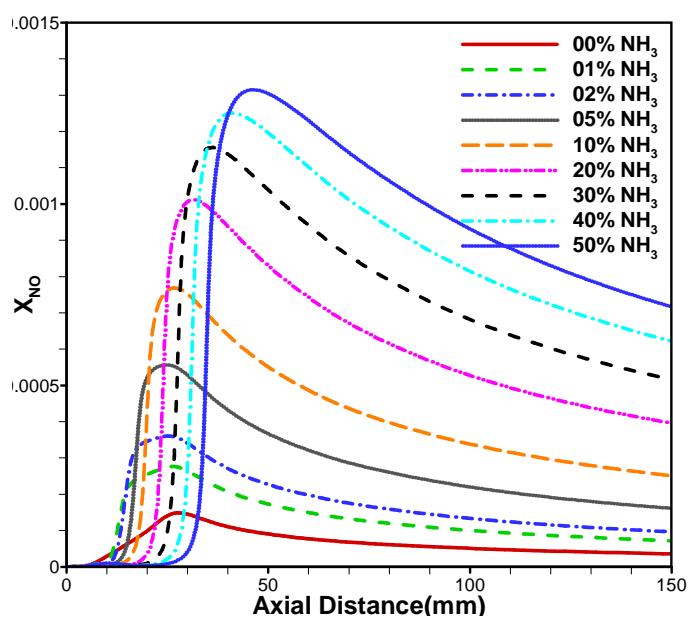


b) 50% H_2 , 50% CO (F2)

Figure 6-22: Comparison of the predicted OH mole fraction of two syngas mixtures with various levels of NH_3 seeding.



a) 45% H_2 , 45% CO , 10% CH_4 (F1)



b) 50% H_2 , 50% CO (F2)

Figure 6-23: Comparison of the predicted NO mole fraction of two syngas mixtures with various levels of NH_3 seeding.

As can be seen above, the major difference between F1 and F2 syngas is their composition, and consequently the availability of CH_i radicals. Figure 6-24 shows the minor species CH and C_2H_2 radicals on the centerline of the flame, along with NO. A log-scale is used on the left y-axis to include the minor species CH_i radicals in both F1 and F2 flames. A linear scale is used on the right y-axis for X_{NO} . The CH profiles (CH_{F1}) in case of the F1 syngas flame (with 0%, 1% and 2% NH_3 seeded to the fuel stream) are ~ 50 times of the magnitude of the CH_{F2} in the F2 flame. The radical $\text{C}_2\text{H}_{2,\text{F1}}$ is $\sim 10^4$ times higher than that of $\text{C}_2\text{H}_{2,\text{F2}}$. In case of 0% NH_3 seeding, the $X_{\text{NO},\text{F1}}$ and $X_{\text{NO},\text{F2}}$ are closer to each other, and $X_{\text{NO},\text{F2}}$ has an even higher peak value than $X_{\text{NO},\text{F1}}$. However, once NH_3 is seeded to the fuel, the $X_{\text{NO},\text{F1}}$ profiles are roughly double the $X_{\text{NO},\text{F2}}$ profiles, which shows clearly the effects of CH_i radicals on the NO formation. Hence, NO formation is enhanced by the combination of NH_3 seeding and with CH_i (F1 vs. F2) radicals available in the fuel stream.

To further investigate the effects of CH_i radicals, the mole fractions of CH, C_2H_2 and CH_3 are plotted in Figure 6-25 as well as the net production rate of NO by Reactions 551, 552 and 566 in the Tian Mechanism (see Appendix B). These elemental reactions are listed below as:



As mentioned in the Chapter 2, HNO is a key pathway to the production of NO in the presence of NH_3 . HNO reacts with CH_i radicals (mainly from decomposition of CH_4) and form NO. For the case of Reaction 566, the net production rate, ω_{566} , in the case of

F1 is about 6 orders of magnitude higher than for F2. Furthermore, ω_{566} , increase substantially next to the tube exit. This helps to explain why the fuel NO in F1 increases rapidly at the tube exit. The difference in fuel NO in the F1 and F2 flames could be explained by Reactions 551 and 552. For example, ω_{551} for F1 is about 4 orders of magnitude higher than for F2, while ω_{552} for F1 is 2 orders of magnitude higher than for F2. This leads to an overall increase in fuel NO for the F1 flame (with CH₄) as compared with the F2 flame (without CH₄).

6.5 Relative Contribution of NO Formation Sub-mechanisms

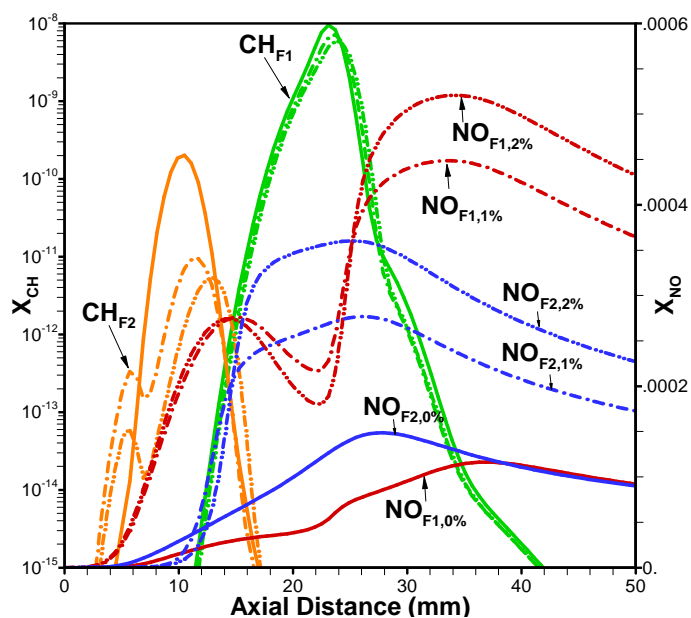
Nitrogen oxides are produced by mainly four different sub-mechanisms: thermal NO, prompt NO, N₂O intermediate and NNH intermediate if fuel NO isn't applicable. When fuel-N (e.g. from coal, or biomass) is involved in the combustion process, the fuel-NO sub-mechanism should be also considered. Without NH₃, all nitrogen chemistry comes from N₂, so fuel NO is not considered. In this section, the relative contributions of these NO formation sub-mechanisms were calculated from simulation results using the Tian mechanism. For ease of comparison, only NO along the flame centerline is plotted and analyzed.

Figure 6-26 shows individual contributions of thermal, prompt, NNH-intermediate, and N₂O-intermediate sub-mechanisms to the total NO. The relative contribution to NO formation is similar between the F1 and F2 syngas flames, showing Thermal NO > N₂O intermediate > NNH intermediate. However, these two differ substantially with regard to prompt NO formation. The magnitude of prompt NO formation for the case with CH₄ is much higher than the case without CH₄, as expected due to the increase of CH in the

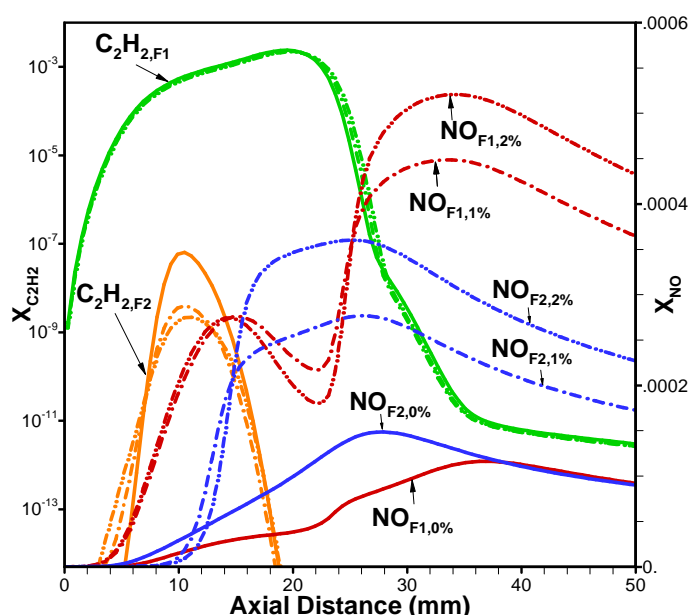
F1 flame. The CH radicals inhibit the oxidation of CO, decrease the temperature, and promote prompt NO formation.

When NH_3 is doped in the fuel stream, the fuel NO mechanism becomes an important factor promoting NO formation. Figure 6-27 a) and b) compare the relative contributions of the NO sub-mechanisms with NH_3 seeding of 1 vol% for the F1 (45% H_2 , 45% CO, 10% CH_4) and F2 (50% H_2 , 50% CO) flames, respectively. According to Figure 6-27, sub-mechanisms other than fuel NO remain nearly the same in terms of magnitude.

The fuel NO appears to be more dominant for the F1 flame compared to F2 flame. In addition to reaching a higher level of NO, the F1 flame also shows a significantly higher rate of increase in fuel NO near the fuel-tube exit as compared to the F2 flame without CH_4 .



a) CH radical and NO profiles on centerline



b) C_2H_2 radicals and NO profiles on centerline

Figure 6-24: CH radical (top) and C_2H_2 radical (bottom) profiles on centerline of F1 and F2 diffusion flames. Solid lines “—” denote the quantities without NH_3 seeding, dash-dot lines “- . -” denote the quantities with 1 vol% NH_3 seeding and dash-dot-dot lines “- .. -” denote the quantities with 2 vol% NH_3 seeding.

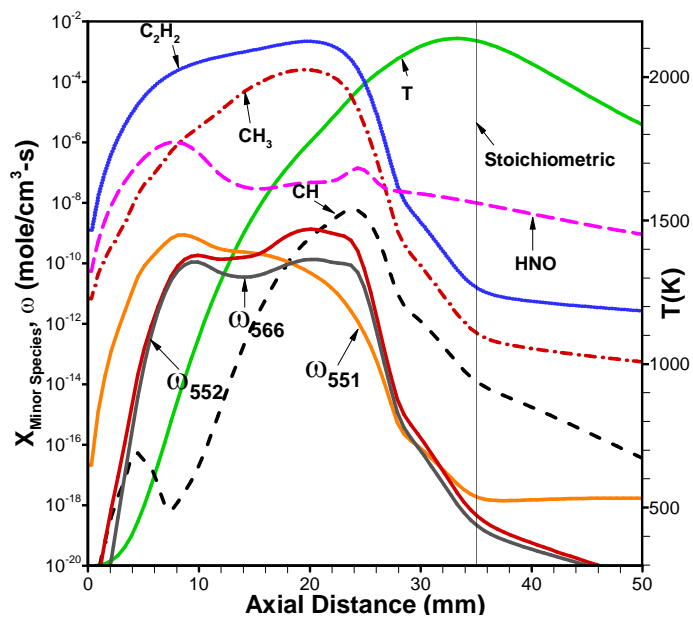
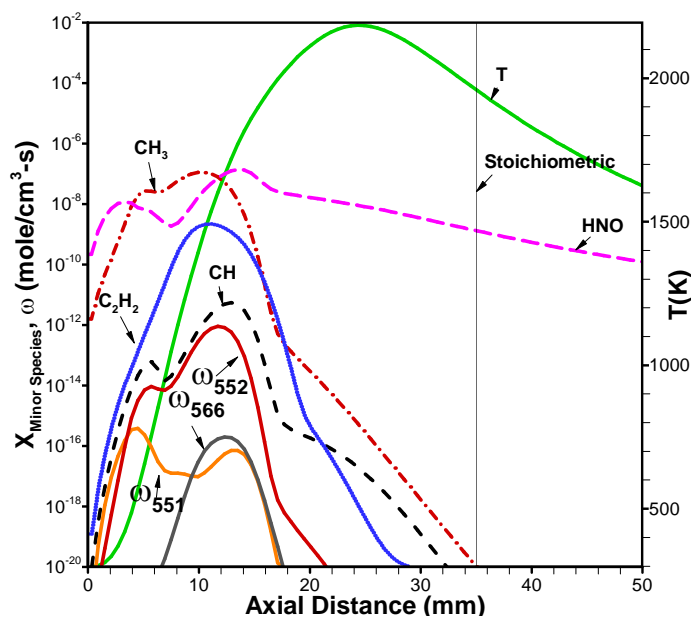
a) 45% H₂, 45% CO, 10% CH₄ (F1)b) CO50%, H₂ 50% (F2)

Figure 6-25: CH, C₂H₂, CH₃ radicals and net production rate of NO by reaction 551, 552 and 566 in Tian's mechanism in case of 1% NH₃ doped in the syngas fuel stream. Top figure is in case of F1 and bottom is in case of F2 flame.

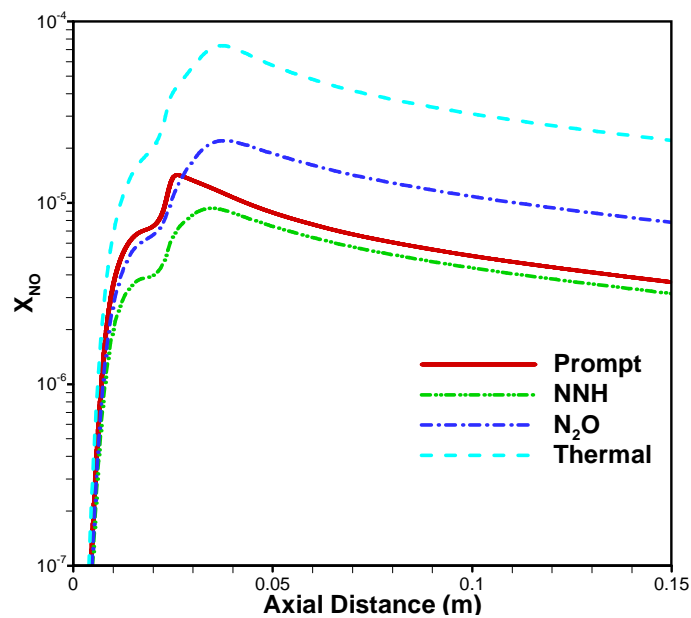
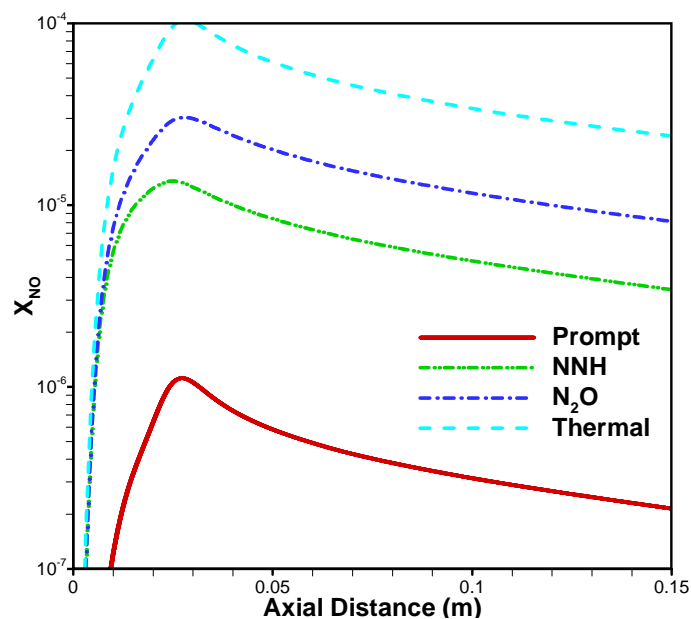
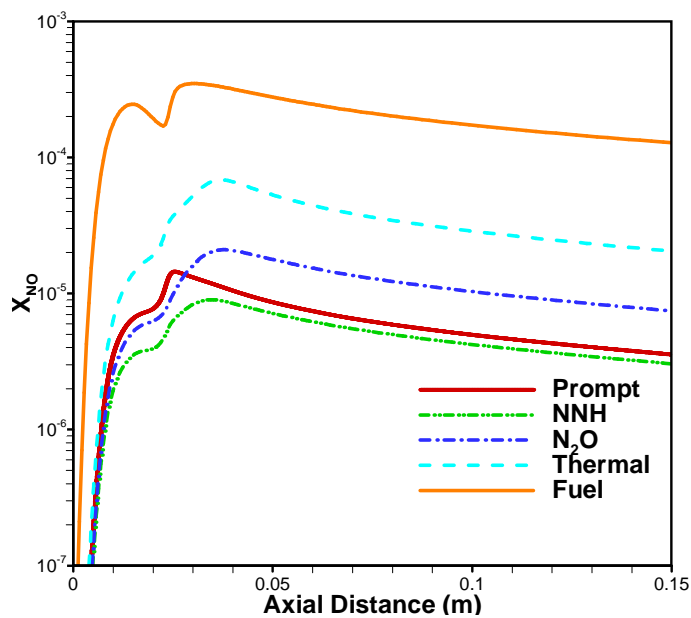
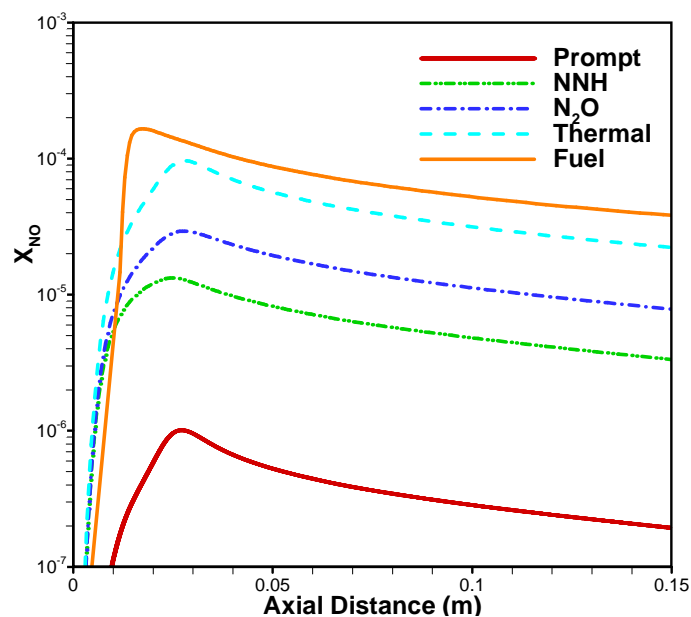
a) 45% H₂, 45% CO, 10% CH₄ (F1)b) 50% H₂, 50% CO (F2)

Figure 6-26: Comparison of the relative contribution of NO-sub-mechanism in two syngas mixtures without NH₃ seeding.



a) 45% H₂, 45% CO, 10% CH₄ (F1)



b) 50% H₂, 50% CO (F2)

Figure 6-27: Comparison of the relative contribution of NO-sub-mechanism in two syngas mixtures with 1 vol% NH₃ seeding in the fuel stream.

It is interesting to investigate the percentages of each sub-mechanisms to the single-peak and dual-peak structure in the F1 syngas diffusion flames with and without NH_3 seeding. Figure 6-28 shows the percentages of sub-mechanisms of F1 syngas flame without any NH_3 seeded to fuel stream. It is shown that once the gaseous fuel exits the tube, all of the sub-mechanisms take effect, with thermal NO as the biggest contributor and prompt NO the second. However, if we consider the contribution of “traditional” prompt NO, which in our case is the total contribution of “prompt”, “ N_2O ” and “NNH”, then the traditional prompt NO is definitely dominant, which is consistent with the “traditional” definition of prompt NO that refers to the amount of prompt-formed NO instead of slowly-formed thermal NO. Nonetheless, the total NO contribution is minimal at the tube exit, so comparison between sub-mechanisms at this location is trivial. As the flow is convected downstream, the thermal NO is increasingly dominant and peaks at the $x = 0.0369$ m, where the X_{NO} peaks. This means that in case of zero NH_3 doping, the single NO peak in the F1 syngas flame is dominated by the thermal NO sub-mechanism.

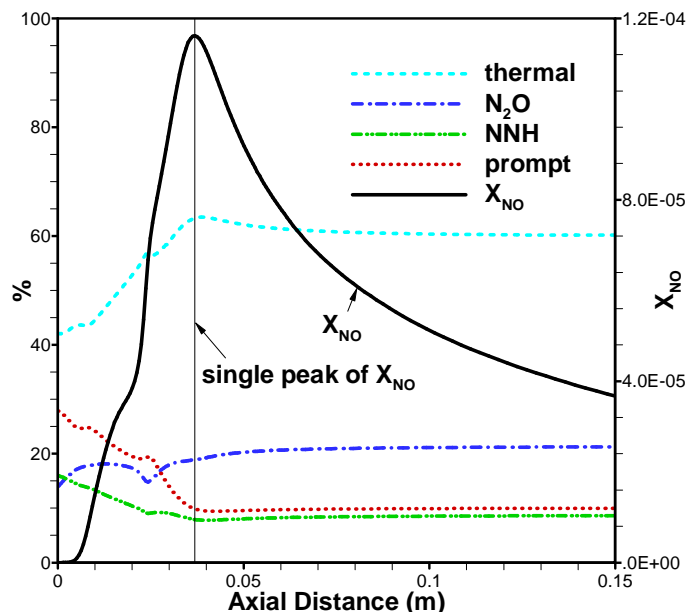


Figure 6-28: Percentages of each NO formation sub-mechanisms to the total NO mole fraction on the centerline of the F1 flame without NH₃ seeding.

Figure 6-29 and Figure 6-30 show the percentage contributions of sub-mechanisms in the case of 1 vol% and 5 vol% NH₃ seeded into the fuel stream for the F1 syngas diffusion flame. In both cases, fuel NO is dominant throughout the centerline extent. A notable difference between these two scenarios is the effect of NH₃ on NO formation. In case of 1 vol% NH₃ as shown in Figure 6-29, the fuel NO doesn't go lower than 75% of total NO formation; however, for the case of 5 vol% NH₃ seeding, this number goes below 60%. This dip in fuel NO contribution explains the deeper valley between the two X_{NO} peaks. For higher levels of NH₃ seeding, it is even possible for the NH₃ to actually suppress the NO formation instead of contributing to it. Figure 6-30 shows the overlap of this dip with the valley of X_{NO} for the case of 20 vol% NH₃, in which the high amount of NH₃ reduces the NO formed by thermal NO and other sub-mechanisms.

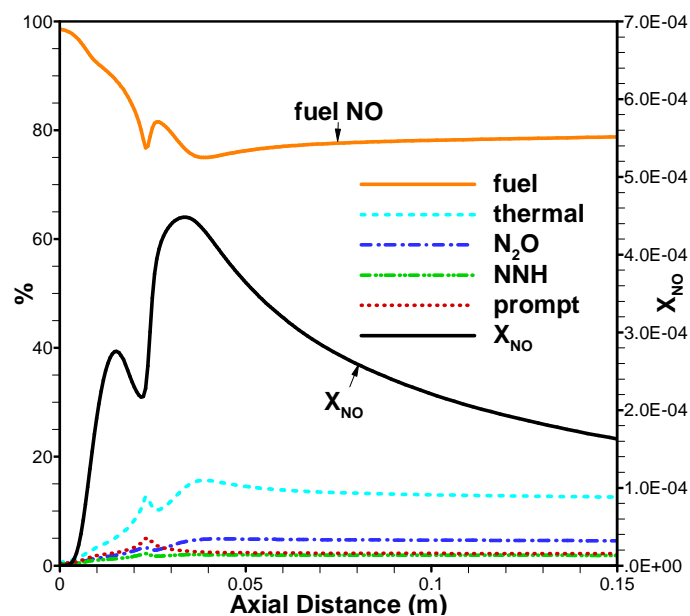


Figure 6-29: Percentage contributions of NO formation sub-mechanisms to the total NO mole fraction along the centerline of the F1 flame with 1 vol% NH_3 in the fuel stream.

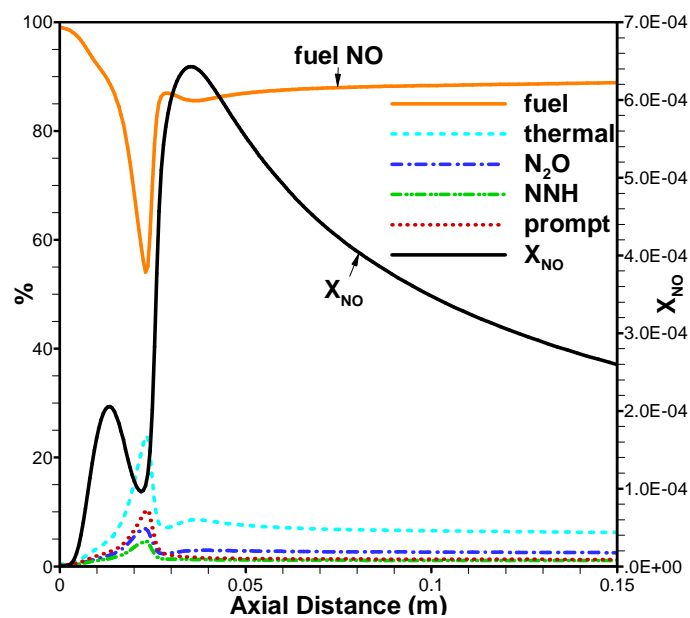


Figure 6-30: Percentage contributions of NO formation sub-mechanisms to the total NO mole fraction along the centerline of the F1 flame with 5 vol% NH_3 in the fuel stream.

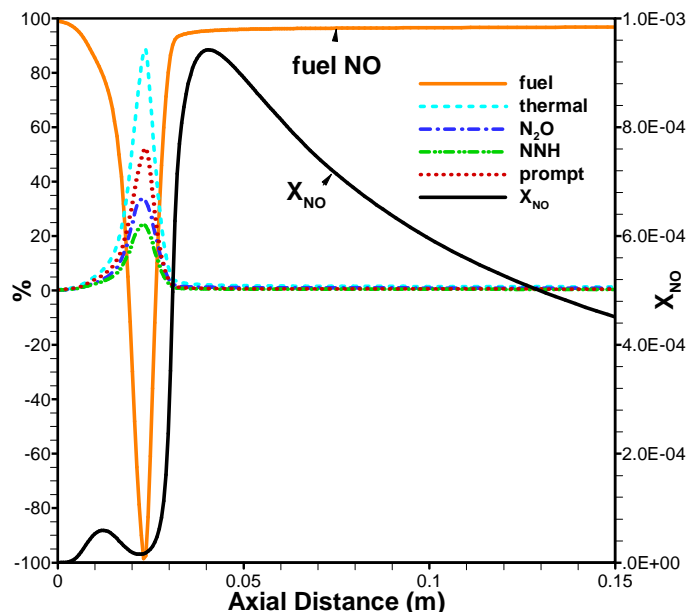


Figure 6-31: Percentage contributions of NO formation sub-mechanisms to the total NO mole fraction along the centerline of the F1 flame with 20 vol% NH_3 in the fuel stream.

Note that in Figure 6-31, the y-axis ranges from -100% to 100%, and the dip of fuel NO coincides with that of X_{NO} , indicating that the high amount of NH_3 suppresses the NO formation.

It is also of interest to investigate the relative contributions of NO formation sub-mechanism to the peak(s) of X_{NO} along the centerline of the flames. Table 6-1 shows the percentages of fuel, thermal, and prompt sub-mechanisms to the total X_{NO} . Note that for F1 syngas without NH_3 seeding, there is only a single peak. Fuel NO always dominates both peaks with small amounts of NH_3 seeded into the fuel. However, with NH_3 beyond 20 vol%, the contribution of fuel NO to the first peak decreases, but increases for the second peak. With higher levels of NH_3 seeding, the thermal NO also decreases, potentially due to higher amounts of NH_3 decreasing flame temperature, as

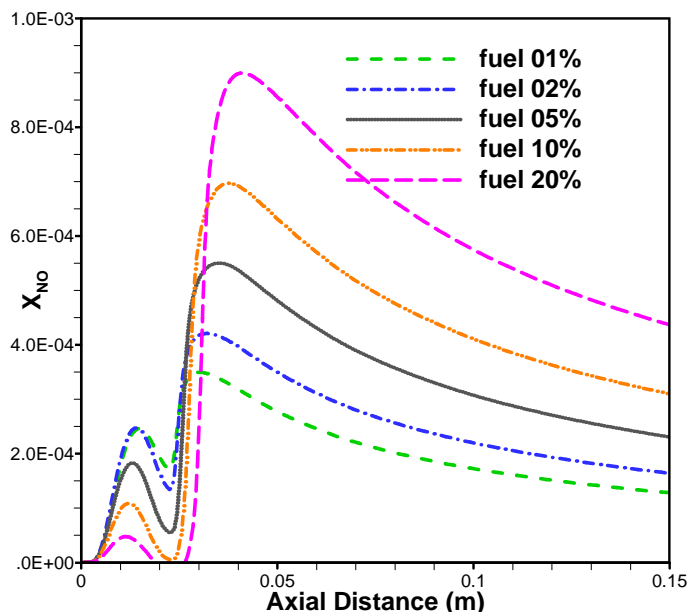
well as removing O, H and OH radicals, which are essential for the thermal NO mechanism.

Table 6-1: Percentage contributions of NO sub-mechanisms to peak(s) of X_{NO} along centerlines of flames.

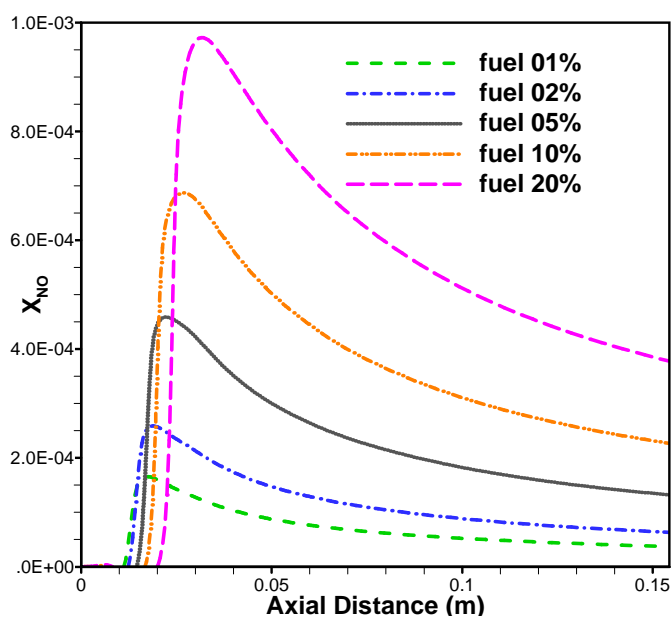
		Fuel	Thermal	Prompt	Prompt+N ₂ O+NNH
F1,0% NH ₃	1st peak	N/A	63%	10%	37%
	2nd peak	N/A	N/A	N/A	N/A
F1,1% NH ₃	1st peak	89%	5%	2%	6%
	2nd peak	76%	14%	3%	9%
F1,5% NH ₃	1st peak	89%	5%	3%	6%
	2nd peak	86%	8%	2%	6%
F1,20% NH ₃	1st peak	78%	8%	6%	14%
	2nd peak	95%	2%	1%	2%

Based on Table 6-1, the prompt NO sub-mechanism is not dominant for either X_{NO} peak in the dual-peak structure and is on the same order of magnitude as the thermal NO sub-mechanism. With a high amounts of NH₃, prompt NO plays an important role in first X_{NO} peak(14%) compared to the second peak(2%).

Effect of NH₃ doping on submechanisms were also investigated as shown in Figure 6-32 through Figure 6-36. The fuel NO is the only sub-mechanism that increases with NH₃. Thermal NO decreases with NH₃ due to that the flame temperature decreased with NH₃. Prompt, N₂O and NNH-intermediate also decrease with NH₃.

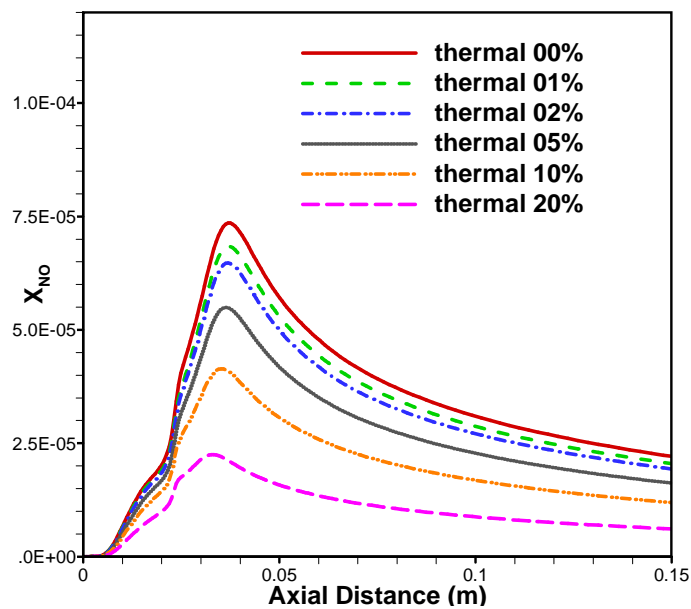


a) 45% H₂, 45% CO, 10% CH₄ (F1)

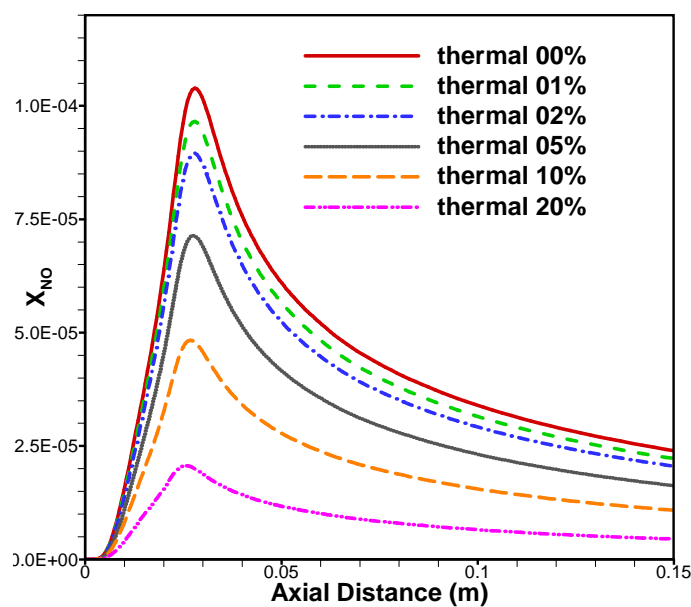


b) 50% H₂, 50% CO (F2)

Figure 6-32: Fuel NO with respect to NH₃ doping in case of F1 (top) and F2 (bottom).

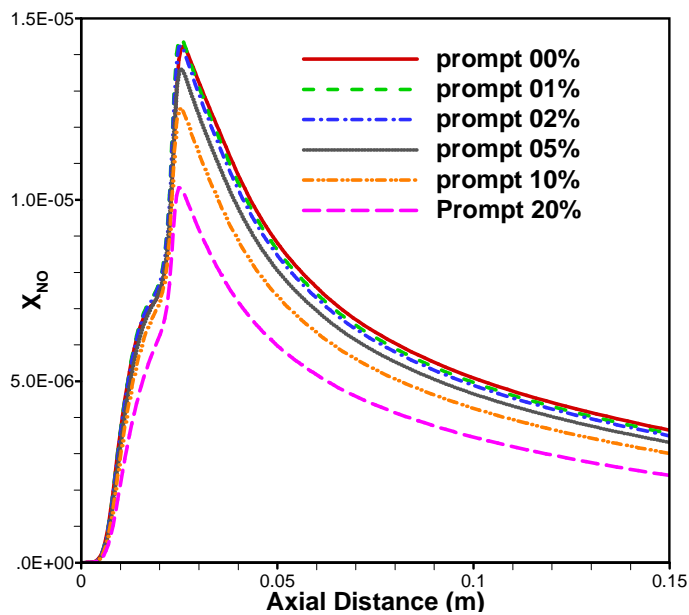


a) 45% H₂, 45% CO, 10% CH₄ (F1)

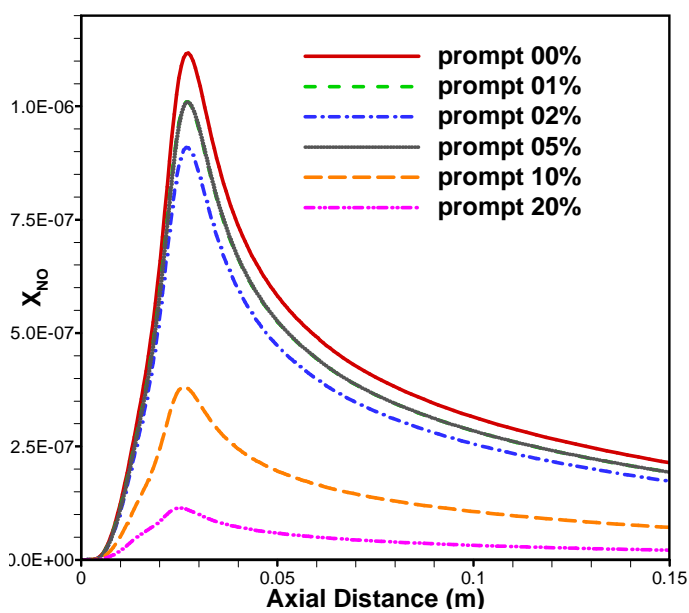


b) 50% H₂, 50% CO (F2)

Figure 6-33: Thermal vs. NH₃ doping in case of F1 (top) and F2 (bottom).

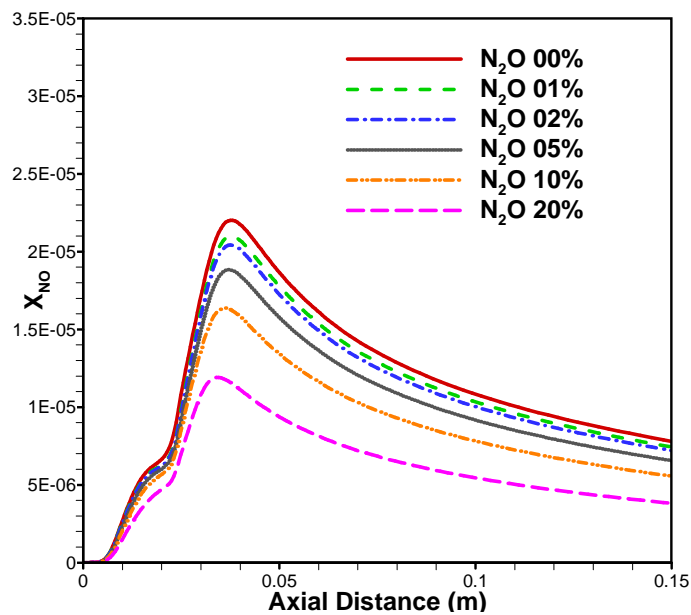


a) 45% H₂, 45% CO, 10% CH₄ (F1).

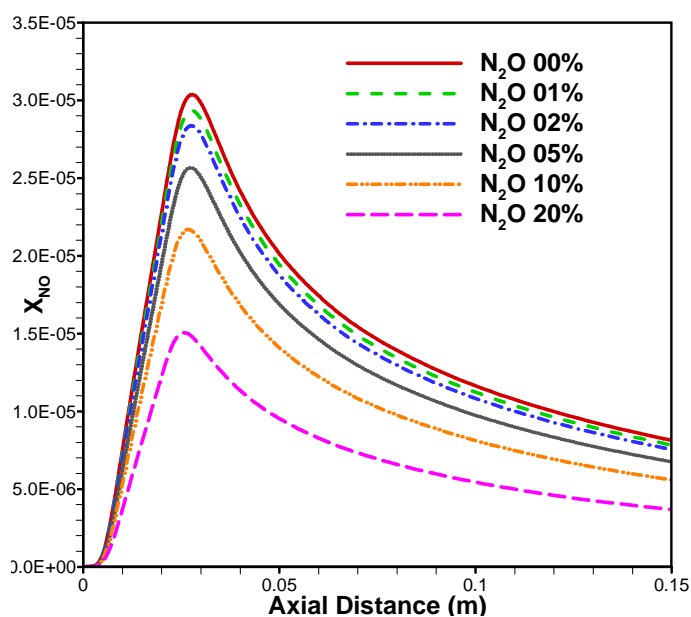


b) 50% H₂, 50% CO (F2).

Figure 6-34: Prompt NO vs. NH₃ seeding in case of F1 (top) and F2 (bottom).

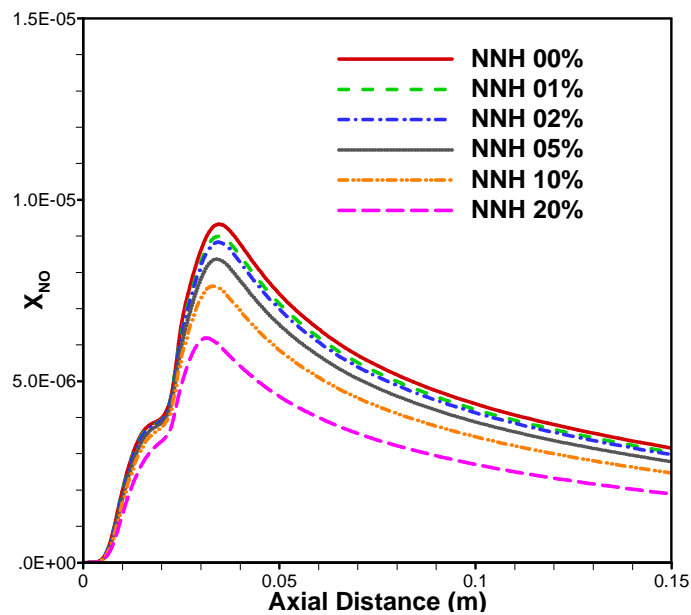


a) 45% H₂, 45% CO, 10% CH₄ (F1).

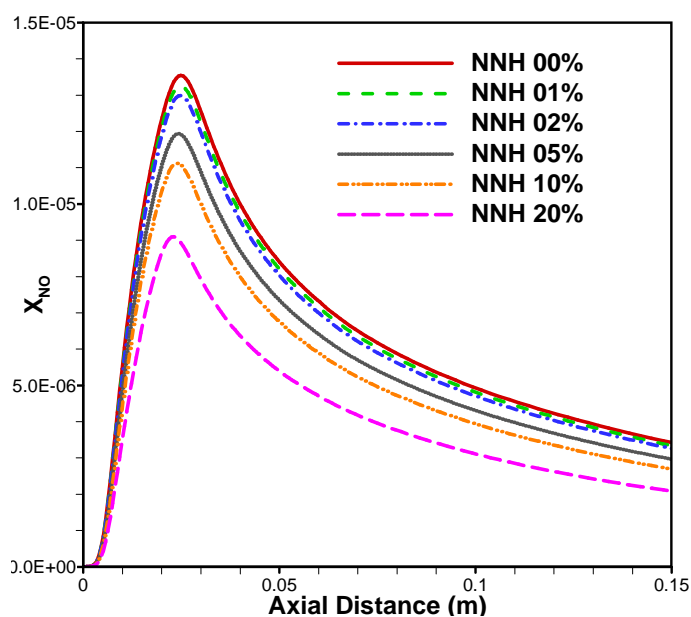


b) 50% H₂, 50% CO (F2).

Figure 6-35: N₂O-intermediate vs. NH₃ doping in case of F1 (top) and F2 (bottom).



a) 45% H₂, 45% CO, 10% CH₄ (F1).



b) 50% H₂, 50% CO (F2).

Figure 6-36: NNH-intermediate vs. NH₃ doping in case of F1 (top) and F2 (bottom).

6.6 Summary

Two syngas/air diffusion flames, referred to here as the F1 (45% H₂, 45% CO, 10% CH₄) and F2 (50% H₂, 50% CO) flames, are investigated with varying levels of NH₃ to determine the relevant NO formation mechanisms. As was the case for the CH₄/air diffusion flames in Chapter 5, the ability of CFD simulation to capture the flame structure is demonstrated by comparison with the OH distribution as revealed using planar laser-induced fluorescence (PLIF). Without NH₃ seeding, the CFD simulation using the Tian chemical mechanism compares favorably with the measured OH distribution. With the highest levels of NH₃ seeding of 50%, the numerical calculations underestimate the flame length by about 10-20%, indicating that the CFD model used in the current work is most reliable for lower levels of NH₃ seeding.

For the syngas/air diffusion flames, NO formation is investigated in terms of the two dimensional NO distribution on the meridian plane of the flames, and for the one-dimensional NO profile along the centerline of the flame. In the case of zero NH₃ added to the fuel stream, this NO distribution exhibits a single-peak structure. With increasing amounts of NH₃ addition, a dual-peak structure develops for the F1 flame but not the F2 flame. Once the fuel is discharged from the burner tube for the F1 syngas, CH_i radicals, which are decomposed from CH₄, react with entrained N₂ and NH₃ to form significant amount of NO, this results in the first NO "peak". In case of zero NH₃, this first peak is caused by both thermal and prompt NO formation, with prompt NO being less than thermal NO. With NH₃ seeding, prompt NO exceeds thermal NO, but both are much less than the contribution from fuel NO. Further downstream, in terms of the second NO peak, the "thermal" NO mechanism becomes more important than prompt NO, but fuel

NO is still significant due to NH_3 doping. In the downstream of second peak, the thermal NO is usually greater than prompt NO. However, in terms of F2 syngas, with a smaller source of CH_i radicals, the prompt NO is not as significant and does not result in a second peak in NO.

Fuel NO is dominant once NH_3 is present in the fuel stream. Comparison between F1 and F2 shows that the fuel NO in F1 is about 2 ~ 3 times of that in F2. Also the fuel NO of F1 picks up drastically next to burner exit comparing to F2. Net production rates of NO by each elementary reaction were investigated, it turned out that reactions 551, 552 and 566 in Tian mechanism make significant difference between F1 and F2 flames, as depicted in last the section.

The relative contributions of different NO formation sub-mechanisms are investigated. These sub-mechanisms include fuel NO, thermal NO, prompt NO, N_2O intermediate, and NNH intermediate, etc. In the case of zero NH_3 addition to the fuel stream, along the centerline, the contributions of the sub-mechanisms for the F1 flame are sorted as: thermal NO > N_2O intermediate > prompt NO > NNH intermediate. For the F2 flame, they are sorted as thermal NO > NNH intermediate > N_2O intermediate >> prompt NO. While prompt NO can play a significant role early in the F1 flame, when CH_4 is absent in the F2 fuel stream, prompt NO is negligible

Fuel NO is also investigated based on CFD calculations. Fuel N refers the nitrogen available in the fuel, mainly in the forms of NH_3 and HCN. NH_3 is seeded into the fuel stream to simulate the fuel NO. In case of $X_{\text{NH}_3} = 1.0\%$ in the fuel stream, the corresponding X_{NO} is enhanced by four times from ~120 ppm to ~500 ppm.

NH_3 doping effect on the NO sub-mechanisms were investigated. With increasing NH_3 , fuel NO increases, while other submechanism decreases.

Two chemical mechanisms, the GRI-Mech 3.0 and Tian mechanisms are compared. Relatively speaking, the Tian mechanism is better than GRI-Mech 3.0 in predicting the NO mole fractions and centerline profile of NO for the syngas/air diffusion flames.

CHAPTER 7 CONCLUSIONS AND RECOMMENDATIONS FOR FUTURE WORK

7.1 Conclusions

Four aspects of CH₄/air and syngas/air diffusion flames are examined in this thesis, they are:

- 1) the basic diffusion flame structure, height, shape, etc.
- 2) characteristics of the NO distribution on the meridian plane,
- 3) relative contributions of NO formation sub-mechanisms,
- 4) comparison of two detailed chemical kinetic mechanisms.

Experimental aspects of the current research involve primarily planar laser-induced fluorescence (PLIF) of OH and NO, while computational work involved the use of a CFDC (Computational Fluid Dynamics with Chemistry) research code known as UNICORN (UNsteady Ignition and COmbustion with ReactionNs). The experimental and numerical tools are presented in Chapters 3 and 4, respectively. Chapter 5 presents the results of CH₄/air diffusion flames, while chapter 6 presents the syngas/air diffusion flames. The main conclusions of the current research are summarized below.

Firstly, the basic diffusion flame structure is validated by OH PLIF and the CFDC approach. On the centerline of the flame, temperature increases from ambient temperature, approaches the adiabatic flame temperature and drops down back slowly to ambient temperature in the far downstream. CH_i and OH radicals occur on the fuel and product sides, respectively, of the stoichiometric region. The experimental OH distributions are confirmed by PLIF in the case with low amounts of NH₃ seeding. For high levels of NH₃, CFDC predictions of the flame height can differ from experimental measurements by 10-20%.

Secondly, the NO distribution on meridian plane and centerline may exhibit single-peak or dual-peak structures, depending on type of fuel or presence of additives (CH_4 and NH_3). CH_4 /air diffusion flames always exhibit the two-peak structure. Both the first and second peak are mainly due to the fuel NO with NH_3 seeding, then secondly attributed to prompt NO, which is 1.3 ~ 3 times of thermal NO.

The baseline F1 (45% H_2 , 45% CO , 10% CH_4) syngas/air flames do not exhibit a two-peak structure until NH_3 is seeded to fuel stream. With NH_3 seeded to the fuel stream, both the first and second peaks are due to fuel NO, then secondly attributed to prompt or thermal NO. In these cases, the prompt and thermal NO are comparable with each other, and no great disparity is expected. The F2 (50% H_2 , 50% CO) syngas/air diffusion flame doesn't exhibit any multi-peak structure at all.

Thirdly, the effect of NH_3 seeding on NO formation depends on the amount of NH_3 in the fuel mixture. For the CH_4 /air and F2 syngas/air diffusion flames, the NO profile on centerline increases monotonically with NH_3 seeding level. However, for the F1 syngas/air diffusion flame, the first NO peak increases up to 2% of NH_3 seeding but then decreases with increasing levels of NH_3 . In contrast, the second peak increases monotonically throughout the entire range of NH_3 seeding.

Fourthly, comparison of relative contributions of NO formation is summarized in Table 7-1. Without CH_4 in the fuel stream, prompt NO is negligible because of the lack of CH_i radicals. In case of syngas diffusion flames, when CO and H_2 are the major fuel species instead of CH_4 . The N_2O and NNH intermediate sub-mechanisms are more significant than in CH_4 diffusion flames.

Table 7-1: Relative contributions of NO sub-mechanisms.

Fuel/Oxidizer	Without NH ₃	1% NH ₃
CH ₄ /air	prompt NO > thermal NO » N ₂ O intermediate > NNH intermediate	fuel NO > prompt NO > thermal NO » N ₂ O intermediate > NNH intermediate
F1 (45% H ₂ , 45% CO, 10% CH ₄) syngas/air	thermal NO > N ₂ O intermediate > prompt NO > NNH intermediate	fuel NO > thermal NO > N ₂ O intermediate > prompt NO > NNH intermediate
F2 (50% H ₂ , 50% CO) syngas/air	thermal NO > NNH intermediate > N ₂ O intermediate » prompt NO	fuel NO > thermal NO > N ₂ O intermediate > NNH intermediate » prompt NO

Lastly, the GRI-Mech 3.0 mechanism is successful in predicting the structure of the CH₄/air diffusion flame, while the Tian's mechanism is more effective in syngas/air diffusion flames. This determination is made in terms of (1) the NO spatial distribution on the meridian plane of flame, and (2) NO spatial profile along the centerline of the flames.

7.2 Recommendations for Future Work

The diffusion flames investigated in the current research consisted of simple jet flames. A "classical" flame structure that could eliminate the effects of curvature and apply a known strain at a one-dimensional flame surface is the counterflow flame, which has been studied extensively. Numerically, with jet velocity U_{jet} fixed, the co-flow velocity $U_{co-flow}$ can be varied to determine if the strain rate affects the spatial

distribution or flame structure. It would be of interest to study this flame configuration by employing similar mixtures as well as the experimental and numerical techniques utilized in the current work.

Since the jet flow field is complicated and couldn't be simplified as a one dimensional flow, other than two dimensional distribution and centerline profile, profiles in the radial direction could be made to investigate the entrainment of the oxidizer into the flame zone and how this affects the NO formation.

Analysis of the NO sub-mechanisms can also be extended. In the current work, certain chemical reactions corresponding to each NO formation sub-mechanism were turned on and off to determine the relative contributions of each. However, this approach assumes that the inter-dependence or interactions between sub-mechanisms are minimal. This may not be true for all conditions, and it would be helpful to perform reaction path analysis within the CFDC to visualize the sub-mechanism pathways more clearly.

Finally, it would be of interest to include the effects of exhaust-gas recirculation on the NO formation sub-mechanisms. Recirculation is known to significantly affect NO formation. It should be possible to establish a laminar recirculating flame to study these effects and thereby better represent practical (e.g., swirl stabilized) flames.

REFERENCES

- [1] Turns, S., 2000, An Introduction to Combustion : Concepts and Applications, WCB/McGraw Hill, Boston.
- [2] Kuo, K., 2005, Principles of Combustion, John Wiley, Hoboken, N.J.
- [3] Eckbreth, A. C., 1996, Laser Diagnostics for Combustion Temperature and Species, Gordon and Breach Publishers, Amsterdam, The netherlands.
- [4] Zhang, H., Eddings, E., and Whitty, K., 2009, Pollutant Formation and Control, Synthesis Gas Combustion, CRC Press.
- [5] Bowman, C. T., 1992, "Control of Combustion-Generated Nitrogen Oxide Emissions: Technology Driven by Regulation," Proc. 24th Int. Symp. Combust., pp. 859-78.
- [6] Nishioka, M., Nakagawa, S., Ishikawa, Y., and Takeno, T., 1994, "No Emission Characteristics of Methane-Air Bunsen-Type Burner Flames Were Studied Numerically in Terms of Counterflow Flame," Combust. Flame, 98(1-2), pp. 127-38.
- [7] Ravikrishna, R. V., Cooper, C. S., and Laurendeau, N. M., 1999, "Comparison of Saturated and Linear Laser-Induced Fluorescence Measurements of Nitric Oxide in Counterflow Diffusion Flames," Combust. Flame, 117(4), pp. 810-820.
- [8] Ravikrishna, R. V., and Laurendeau, N. M., 2000, "Laser-Induced Fluorescence Measurements and Modeling of Nitric Oxide in Counterflow Partially Premixed Flames," Combust. Flame, 122(4), pp. 474-482.
- [9] Drake, M. C., Ratcliffe, J. W., Blint, R. J., Carter, C. D., and Laurendeau, N. M., 1991, "Measurements and Modeling of Flamefront Nitric Oxide Formation and Superequilibrium Radical Concentrations in Laminar High-Pressure Premixed Flames," Proc. 23rd Int. Symp. Combust., pp. 387-95.

- [10] Miller, J. A., and Bowman, C. T., 1989, "Mechanism and Modeling of Nitrogen Chemistry in Combustion," *Prog. Energy Combust. Sci.*, 15(4), pp. 287-338.
- [11] Drake, M. C., and Blint, R. J., 1991, "Relative Importance of Nitric Oxide Formation Mechanisms in Laminar Opposed-Flow Diffusion Flames," *Combust. Flame*, 83(1-2), pp. 185-203.
- [12] Glarborg, P., Miller, J. A., and Kee, R. J., 1986, "Kinetic Modeling and Sensitivity Analysis of Nitrogen Oxide Formation in Well-Stirred Reactors," *Combust. Flame*, 65(2), pp. 177-202.
- [13] Pratt, D. T., and Malte, P. C., 1975, "Formation of Thermal and Prompt Nitrogen Oxide (NO_x) in a Jet-Stirred Combustor," *AIChE Symp. Ser.*, 71(148), pp. 150-7.
- [14] Drake, M. C., and Blint, R. J., 1988, "Structure of Laminar Opposed-Flow Diffusion Flames with Carbon Monoxide/Hydrogen/Nitrogen Fuel," *Combust. Sci. Technol.*, 61(4-6), pp. 187-224.
- [15] Glarborg, P., Jensen, A. D., and Johnsson, J. E., 2003, "Fuel Nitrogen Conversion in Solid Fuel Fired Systems," *Prog. Energy Combust. Sci.*, 29(2), pp. 89-113.
- [16] Bozzelli, J. W., and Dean, A. M., 1995, "O + NNH: A Possible New Route for NO_x Formation in Flames," *Int. J. Chem. Kinet.*, 27(11), pp. 1097-1109.
- [17] Daily, J. W., 1997, "Laser Induced Fluorescence Spectroscopy in Flames," *Prog. Energy Combust. Sci.*, 23(2), pp. 133-199.
- [18] Paul, P. H., Gray, J. A., Durant, J. L., Jr., and Thoman, J. W., Jr., 1994, "Collisional Quenching Corrections for Laser-Induced Fluorescence Measurements of $\text{NO A}^2\sigma^+$," *aIAA J.*, 32(8), pp. 1670-5.

- [19] Gibaud, C., Snyder, J. A., Sick, V., and Lindstedt, R. P., 2005, "Laser-Induced Fluorescence Measurements and Modeling of Absolute CH Concentrations in Strained Laminar Methane/Air Diffusion Flames," *Proc. Combust. Inst.*, 30(Pt. 1), pp. 455-463.
- [20] Hirano, A., Tsujishita, M., Nishigaki, M., and Fujimaru, N., 1996, "NO_x Formation Diagnostics in Natural-Gas Combustion by Planar Laser-Induced Fluorescence," *Proc. Int. Gas Res. Conf.*, Vol. 2, pp. 1607-1615.
- [21] Plessing, T., Peters, N., and Wunning, J. G., 1998, "Laser Optical Investigation of Highly Preheated Combustion with Strong Exhaust Gas Recirculation," *Proc. 27th Int. Symp Combust.*, Vol. 2, pp. 3197-3204.
- [22] Heberle, N. H., Smith, G. P., Jeffries, J. B., Crosley, D. R., and Dibble, R. W., 2000, "Simultaneous Laser-Induced Fluorescence and Rayleigh Scattering Measurements of Structure in Partially Premixed Flames," *Appl. Phys. B Lasers Opt.*, 71(5), pp. 733-740.
- [23] Naik, S. V., and Laurendeau, N. M., 2004, "Measurements of Absolute CH Concentrations by Cavity Ring-Down Spectroscopy and Linear Laser-Induced Fluorescence in Laminar, Counterflow Partially Premixed and Non-Premixed Flames at Atmospheric Pressure," *Appl. Opt.*, 43(26), pp. 5116-5125.
- [24] Kychakoff, G., Howe, R. D., and Hanson, R. K., 1984, "Quantitative Flow Visualization Technique for Measurements in Combustion Gases," *Appl. Opt.*, 23(5), pp. 704-712.
- [25] Charlston-Goch, D., Chadwick, B. L., Morrison, R. J. S., Campisi, A., Thomsen, D. D., and Laurendeau, N. M., 2001, "Laser-Induced Fluorescence Measurements and Modeling of Nitric Oxide in Premixed Flames of CO+H₂+CH₄ and Air at High Pressures I. Nitrogen Fixation," *Combust. Flame*, 125(1/2), pp. 729-743.

- [26] Thomsen, D. D., and Laurendeau, N. M., 2001, "LIF Measurements and Modeling of Nitric Oxide Concentration in Atmospheric Counterflow Premixed Flames," *Combust. Flame*, 124(3), pp. 350-369.
- [27] Dec, J. E., and Canaan, R. E., 1998, "PLIF Imaging of NO Formation in a DI Diesel Engine,".
- [28] Sarofim, A. F., Pohl, J. H., and Taylor, B. R., 1978, "Strategies for Controlling Nitrogen Oxide Emissions During Combustion of Nitrogen-Bearing Fuels," *AIChE Symp. Ser.*, 74(175), pp. 67-92.
- [29] Smooke, M. D., Mitchell, R. E., and Keyes, D. E., 1989, "Numerical Solution of Two-Dimensional Axisymmetric Laminar Diffusion Flames," *Combust. Sci. Technol.*, 67(4-6), pp. 85-122.
- [30] Bennett, B. A. V., Mcenally, C. S., Pfefferle, L. D., Smooke, M. D., and Colket, M. B., 2001, "Computational and Experimental Study of Axisymmetric Coflow Partially Premixed Ethylene/Air Flames," *Combust. Flame*, 127(1/2), pp. 2004-2022.
- [31] Nishioka, M., Takemoto, Y., Yamashita, H., and Takeno, T., 1996, "Effects of Multi-Dimensionality on a Diffusion Flame," *Proc. 26th Int. Symp. Combust.*, Vol. 1, pp. 1071-1077.
- [32] Sullivan, N., Jensen, A., Glarborg, P., Day, M. S., Grcar, J. F., Bell, J. B., Pope, C. J., and Kee, R. J., 2002, "Ammonia Conversion and NOx Formation in Laminar Coflowing Nonpremixed Methane-Air Flames," *Combust. Flame*, 131(3), pp. 285-298.
- [33] Glarborg, P., Alzueta, M. U., Dam-Johansen, K., and Miller, J. A., 1998, "Kinetic Modeling of Hydrocarbon/Nitric Oxide Interactions in a Flow Reactor," *Combust. Flame*, 115 (1/2), pp. 1-27.

- [34] Bell, J. B., Day, M. S., Grcar, J. F., Bessler, W. G., Schulz, C., Glarborg, P., and Jensen, A. D., 2002, "Detailed Modeling and Laser-Induced Fluorescence Imaging of Nitric Oxide in a NH_3 -Seeded Non-Premixed Methane/Air Flame," Proc. Combust. Inst., 29(Pt. 2), pp. 2195-2202.
- [35] Bowman, C. T., 1970, "An Experimental and Analytical Investigation of the High-Temperature Oxidation Mechanisms of Hydrocarbon Fuels," Combust. Sci. Technol., 2(2), pp. 161 - 172.
- [36] Cooke, D. F., and Williams, A., 1971, "Shock-Tube Studies of the Ignition and Combustion of Ethane and Slightly Rich Methane Mixtures with Oxygen," International Symposium on Combustion, 13(1), pp. 757-766.
- [37] Westbrook, C. K., Dryer, F. L., and Schug, K. P., 1982, "A Comprehensive Mechanism for the Pyrolysis and Oxidation of Ethylene," International Symposium on Combustion, 19(1), pp. 153-166.
- [38] Westbrook, C. K., and Dryer, F. L., 1984, "Chemical Kinetic Modeling of Hydrocarbon Combustion," Prog. Energy Combust. Sci., 10(1), pp. 1-57.
- [39] Dagaut, P., Lecomte, F., Chevailler, S., and Cathonnet, M., 1998, "Experimental and Detailed Kinetic Modeling of Nitric Oxide Reduction by a Natural Gas Blend in Simulated Reburning Conditions," Combust. Sci. Technol., 139(1), pp. 329 - 363.
- [40] Baulch, D. L., Cobos, C. J., Cox, R. A., Esser, C., Frank, P., Just, T., Kerr, J. A., Pilling, M. J., Troe, J., Walker, R. W., and Warnatz, J., 1992, "Evaluated Kinetic Data for Combustion Modelling," Journal of Physical and Chemical Reference Data, 21 (3), pp. 411-734.

- [41] Baulch, D. L., Cobos, C. J., Cox, R. A., Frank, P., Hayman, G., Just, T., Kerr, J. A., Murrells, T., Pilling, M. J., Troe, J., Walker, R. W., and Warnatz, J., 1994, "Evaluated Kinetic Data for Combustion Modeling. Supplement I," *Journal of Physical and Chemical Reference Data*, 23(6), pp. 847-848.
- [42] Frenklach, M., Wang, H., and Rabinowitz, M. J., 1992, "Optimization and Analysis of Large Chemical Kinetic Mechanisms Using the Solution Mapping Method--Combustion of Methane," *Prog. Energy Combust. Sci.*, 18(1), pp. 47-73.
- [43] Smith, G. P., Golden, D. M., Frenklach, M., Moriarty, N. W., Eiteneer, B., Goldenberg, M., Bowman, C. T., Hanson, R. K., Song, S. S., Gardiner, W. C., Lissianski, V. V., and Qin, Z., 1996, "{Gri-Mech} 3.0,".
- [44] Tian, Z., Li, Y., Zhang, L., Glarborg, P., and Qi, F., 2009, "An Experimental and Kinetic Modeling Study of Premixed $\text{NH}_3/\text{CH}_4/\text{O}_2/\text{Ar}$ Flames at Low Pressure," *Combust. Flame*, 156(7), pp. 1413-1426.
- [45] Rasmussen, C. L., Jakobsen, J. G., and Glarborg, P., 2008, "Experimental Measurements and Kinetic Modeling of CH_4/O_2 and $\text{CH}_4/\text{C}_2\text{H}_6/\text{O}_2$ Conversion at High Pressure," *Int. J. Chem. Kinet.*, 40(12), pp. 778-807.
- [46] Skreiberg, O., Kilpinen, P., and Glarborg, P., 2004, "Ammonia Chemistry Below 1400 K under Fuel-Rich Conditions in a Flow Reactor," *Combust. Flame*, 136 (4), pp. 501-518.
- [47] Dagaut, P., Glarborg, P., and Alzueta, M. U., 2008, "The Oxidation of Hydrogen Cyanide and Related Chemistry," *Prog. Energy Combust. Sci.*, 34(1), pp. 1-46.
- [48] Rasmussen, C. L., Rasmussen, A. E., and Glarborg, P., 2008, "Sensitizing Effects of NO_x on CH_4 Oxidation at High Pressure," *Combust. Flame*, 154(3), pp. 529-545.

- [49] Dean, A. M., and Bozzelli, J. W., 2000, Combustion Chemistry of Nitrogen, Gas-Phase Combustion Chemistry, Springer, New York.
- [50] Konnov, 2009, "Implementation of the NCN Pathway of Prompt-NO Formation in the Detailed Reaction Mechanism," Combust. Flame, 156(11), pp. 2093-2105.
- [51] Konnov, A. A., Dyakov, I. V., and De Ruyck, J., 2006, "Probe Sampling Measurements of No in CH₄+O₂+N₂ Flames Doped with NH₃," Combust. Sci. Technol., 178(6), pp. 1143-1164.
- [52] Knyazkov, D. A., Shmakov, A. G., Dyakov, I. V., Korobeinichev, O. P., De Ruyck, J., and Konnov, A. A., 2009, "Formation and Destruction of Nitric Oxide in Methane Flames Doped with NO at Atmospheric Pressure," Proc. Combust. Inst., 32(1), pp. 327-334.
- [53] Duynslaegher, C., Jeanmart, H., and Vandooren, J., 2010, "Ammonia Combustion at Elevated Pressure and Temperature Conditions," Fuel, 89(11), pp. 3540-3545.
- [54] Shmakov, A. G., Korobeinichev, O. P., Rybitskaya, I. V., Chernov, A. A., Knyazkov, D. A., Bolshova, T. A., and Konnov, A. A., 2010, "Formation and Consumption of NO in H₂+O₂+N₂ Flames Doped with NO or NH₃ at Atmospheric Pressure," Combust. Flame, 157(3), pp. 556-565.
- [55] Yetter, R., Ribert, G., Yang, V., Wang, Z., and Thakre, P., 2009, Fundamental Combustion Characteristics of Syngas, Synthesis Gas Combustion, CRC Press,
- [56] Allen, M. T., Yetter, R. A., and Dryer, F. L., 1997, "High Pressure Studies of Moist Carbon Monoxide/Nitrous Oxide Kinetics," Combust. Flame, 109(3), pp. 449-470.
- [57] Drake, M. C., and Blint, R. J., 1989, "Thermal Nitrogen Oxide (NO_x) in Stretched Laminar Opposed-Flow Diffusion Flames with Carbon Monoxide/Hydrogen/Nitrogen Fuel," Combust. Flame, 76(2), pp. 151-67.

- [58] Hasegawa, T., and Sato, M., 1998, "Study of Ammonia Removal from Coal-Gasified Fuel," *Combust. Flame*, 114(1/2), pp. 246-258.
- [59] Chung, S. H., and Williams, F. A., 1990, "Asymptotic Structure and Extinction of Carbon Monoxide-Hydrogen Diffusion Flames with Reduced Kinetic Mechanisms," *Combust. Flame*, 82(3-4), pp. 389-410.
- [60] Fotache, C. G., Tan, Y., Sung, C. J., and Law, C. K., 2000, "Ignition of CO/H₂/N₂ Versus Heated Air in Counterflow: Experimental and Modeling Results," *Combust. Flame*, 120(4), pp. 417-426.
- [61] Rumminger, M. D., and Linteris, G. T., 2000, "Inhibition of Premixed Carbon Monoxide-Hydrogen-Oxygen-Nitrogen Flames by Iron Pentacarbonyl," *Combust. Flame*, 120(4), pp. 451-464.
- [62] Natarajan, J., Lieuwen, T., and Seitzman, J., 2007, "Laminar Flame Speeds of H₂/CO Mixtures: Effect of CO₂ Dilution, Preheat Temperature, and Pressure," *Combust. Flame*, 151(1/2), pp. 104-119.
- [63] Natarajan, J., Kochar, Y., Lieuwen, T., and Seitzman, J., 2009, "Pressure and Preheat Dependence of Laminar Flame Speeds of H₂/CO/CO₂/O₂/He Mixtures," *Proc. Combust. Inst.*, 32(Pt. 1), pp. 1261-1268.
- [64] Braun-Unkhoff, M., Slavinskaya, N., and Aigner, M., 2010, "A Detailed and Reduced Reaction Mechanism of Biomass-Based Syngas Fuels," *J. Eng. Gas Turbines Power*, 132(9), pp. 091401-9.
- [65] Ahn, S. Y., Go, S. M., Lee, K. Y., Kim, T. H., Seo, S. I., Choi, G. M., and Kim, D. J., 2011, "The Characteristics of NO Production Mechanism on Flue Gas Recirculation in Oxy-Firing Condition," *Applied Thermal Engineering*, 31(6-7), pp. 1163-1171.

- [66] Giles, D. E., and Aggarwal, S. K., 2006, "NO_x Emission Characteristics of Counterflow Syngas Diffusion Flames with Airstream Dilution," *Fuel*, 85(12-13), pp. 1729-1742.
- [67] Alavandi, S., and Agrawal, A. K., 2008, "Experimental Study of Combustion of Hydrogen-Syngas/Methane Fuel Mixture in a Porous Burner," *International Journal of Hydrogen Energy*, 33(1/2), pp. 1407-1415.
- [68] Williams, T. C., Shaddix, C. R., and Schefer, R. W., 2008, "Effect of Syngas Composition and CO₂-Diluted Oxygen on Performance of a Premixed Swirl-Stabilized Combustor," *Combust. Sci. Technol.*, 180 (pp. 64-88).
- [69] Sick, V., 1999, "Deriving Quantitative Concentration Distributions from Planar Laser-Induced Fluorescence Measurements in Engines," *J. Flow Visualization & Image Processing*, 6(4), pp. 313-331.
- [70] Mokhov, A. V., Levinsky, H. B., and Van Der Meij, C. E., 1997, "Temperature Dependence of Laser-Induced Fluorescence of Nitric Oxide in Laminar Premixed Atmospheric-Pressure Flames," *Appl. Opt.*, 36(15), pp. 3233-3243.
- [71] Berg, P. A., Smith, G. P., Jeffries, J. B., and Crosley, D. R., 1998, "Nitric Oxide Formation and Reburn in Low-Pressure Methane Flames," *Proc. 27th Int. Symp. Combust.*, Vol. 1, pp. 1377-1384.
- [72] Bessler, W. G., Hildenbrand, F., and Schulz, C., 2001, "Two-Line Laser-Induced Fluorescence Imaging of Vibrational Temperatures in a No-Seeded Flame," *Appl. Opt.*, 40(6), pp. 748-756.

- [73] Bockle, S., Kazenwadel, J., Kunzelmann, T., and Schulz, C., 2000, "Laser-Diagnostic Multi-Species Imaging in Strongly Swirling Natural Gas Flames," *Appl. Phys. B Lasers Opt.*, 71(5), pp. 741-746.
- [74] Tamura, M., Berg, P. A., Harrington, J. E., Luque, J., Jeffries, J. B., Smith, G. P., and Crosley, D. R., 1998, "Collisional Quenching of CH(a), OH(a), and NO(a) in Low Pressure Hydrocarbon Flames," *Combust. Flame*, 114(3/4), pp. 502-514.
- [75] Bessler, W. G., Hildenbrand, F., and Schulz, C., 2001, "Two-Line Laser-Induced Fluorescence Imaging of Vibrational Temperatures in a NO-Seeded Flame," *Appl Opt*, 40(6), pp. 748-56.
- [76] Böckle, S., Einecke, S., Hildenbrand, F., Orlemann, C., Schulz, C., Wolfrum, J., and Sick, V., 1999, "Laser-Spectroscopic Investigation of OH-Radical Concentrations in the Exhaust Plane of Jet Engines," *Geophys. Res. Lett.*, 26(13), pp. 1849-1852.
- [77] Andresen, P., Meijer, G., Schlüter, H., Voges, H., Koch, A., Hentschel, W., Oppermann, W., and Rothe, E., 1990, "Fluorescence Imaging inside an Internal Combustion Engine Using Tunable Excimer Lasers," *Appl. Opt.*, 29(16), pp. 2392-2404.
- [78] Allen, M. G., Mcmanus, K. R., Sonnenfroh, D. M., and Paul, P. H., 1995, "Planar Laser-Induced-Fluorescence Imaging Measurements of OH and Hydrocarbon Fuel Fragments in High-Pressure Spray-Flame Combustion," *Appl. Opt.*, 34(27), pp. 6287-6300.
- [79] Luque, J., Jeffries, J. B., Smith, G. P., Crosley, D. R., Walsh, K. T., Long, M. B., and Smooke, M. D., 2000, "CH(a-X) and OH(a-X) Optical Emission in an Axisymmetric Laminar Diffusion Flame," *Combust. Flame*, 122(1-2), pp. 172-175.

- [80] Hildenbrand, F., and Schulz, C., 2001, "Measurements and Simulation of in-Cylinder UV-Absorption in Spark Ignition and Diesel Engines," *Appl. Phys. B: Lasers Opt.*, 73, pp. 173-180.
- [81] Hildenbrand, F., Schulz, C., Wolfrum, J., Keller, F., and Wagner, E., 2000, "Laser Diagnostic Analysis of NO Formation in a Direct Injection Diesel Engine with Pump-Line-Nozzle and Common Rail Injection Systems," *Proc. Combust. Inst.*, 28(Pt. 1), pp. 1137-1143.
- [82] Alatas, B., Santavicca, D. A., Bandaru, R. V., and Turns, S. R., 1993, "Semi-Quantitative One-Dimensional Measurements of Nitric Oxide Concentration in Turbulent Hydrocarbon-Air Diffusion Flames Using Laser Induced Fluorescence," *Chem. Phys. Processes Combust.*, pp. 145-8.
- [83] Lee, T., Jeffries, J. B., and Hanson, R. K., 2007, "Experimental Evaluation of Strategies for Quantitative Laser-Induced-Fluorescence Imaging of Nitric Oxide in High-Pressure Flames (1-60 bar)," *Proc. Combust. Inst.*, 31(1), pp. 757-764.
- [84] Di, R. M. D., Klavuhn, K. G., and Hanson, R. K., 1996, "LIF Spectroscopy of NO and O₂ in High-Pressure Flames," *Combust. Sci. Technol.*, 118(pp. 257-283).
- [85] Katta, V. R., and Roquemore, W. M., 1995, "On the Structure of a Stretched/Compressed Laminar Flamelet-Influence of Preferential Diffusion," *Combust. Flame*, 100(pp. 61-70).
- [86] Katta, V. R., Goss, L. P., and Roquemore, W. M., 1994, "Effect of Nonunity Lewis Number and Finite-Rate Chemistry on the Dynamics of a Hydrogen-Air Jet Diffusion Flame," *Combust. Flame*, 96(pp. 60-74).

- [87] Carter, C. D., and Barlow, R. S., 1994, "Simultaneous Measurements of NO, OH, and the Major Species in Turbulent Flames," *Opt. Lett.*, 19(4), pp. 299-301.
- [88] Poling, B. E., Prausnitz, J. M., and Connell, J. P., 2001, *The Properties of Gases and Liquids*, McGraw-Hill New York,
- [89] Neufeld, P. D., Janzen, A. R., and Aziz, R. A., 1972, "Empirical Equations to Calculate 16 of the Transport Collision Integrals $\Omega(1,S)^*$ for the Lennard-Jones (12-6) Potential," *J. Chem. Phys.*, 57 (pp. 1100-102).
- [90] Gardiner, W. C., and Burcat, A., 1984, *Combustion Chemistry*, Springer-Verlag,
- [91] Grosshandler, W., 1995, *Radcal: A Narrow-Band Model for Radiation Calculations in Combustion Environment*.
- [92] Leonard, B. P., 1979, "A Stable and Accurate Convective Modelling Procedure Based on Quadratic Upstream Interpolation," *Computer Methods in Applied Mechanics and Engineering*, 19(1), pp. 59-98.
- [93] Spalding, D. B., 1972, "A Novel Finite Difference Formulation for Differential Expressions Involving Both First and Second Derivatives," *International Journal for Numerical Methods in Engineering*, 4(4), pp. 551-559.
- [94] Katta, R., V., Goss, P., L., Roquemore, and M., W., 1994, "Numerical Investigations of Transitional H_2/N_2 Jet Diffusion Flames", American Institute of Aeronautics and Astronautics, Reston, VA, ETATS-UNIS.
- [95] Roquemore, W., and Katta, V., 2000, "Role of Flow Visualization in the Development of Unicorn," *Journal of Visualization*, 2(3), pp. 257-272.
- [96] Katta, V. R., and Roquemore, W. M., 1998, "Simulation of Dynamic Methane Jet Diffusion Flames Using Finite Rate Chemistry Models," *AIAA J.*, 36(11), pp. 2044-2054.

- [97] Katta, V. R., Forlines, R. A., Roquemore, W. M., Anderson, W. S., Zelina, J., Gord, J. R., Stouffer, S. D., and Roy, S., 2011, "Experimental and Computational Study on Partially Premixed Flames in a Centerbody Burner," *Combust. Flame*, 158(3), pp. 511-524.
- [98] Howell, J. R., Siegel, R., and Mengüç, M. P., 2011, *Thermal Radiation Heat Transfer*, John R. Howell, Robert Siegel, M. Pinar Mengüç, CRC Press, Boca Raton, Fla.
- [99] Baulch, D. L., Cobos, C. J., Cox, R. A., Esser, C., Frank, P., Th. Just, Kerr, J. A., Pilling, M. J., Troe, J., Walker, R. W., and Warnatz, J., "Evaluated Kinetic Data for Combustion Modeling", 1992, *J. Phys. Chem. Ref. Data*, 21, pp. 411-429.
- [100] Glarborg, P., Alzueta, M. U., Dam-Johansen, K., and Miller, J. A., 1998, "Kinetic Modeling of Hydrocarbon/Nitric Oxide Interactions in a Flow Reactor", *Combust. Flame*, 115, pp. 1-27.
- [101] Bauer, W., Becker, K. H., and Meuser, R., 1985, "Laser Induced Fluorescence Studies on C_2O and CH Radicals", *Ber. Bunsenges. Phys. Chem.*, 89, pp. 340-341.
- [102] Skreiberg, Kilpinen, P., and Glarborg, P., 2004, "Ammonia Chemistry below 1400 K under fuel-rich conditions in a flow reactor", *Combust. Flame*, 136, pp. 501-518.
- [103] Dean, A. M., and Bozzelli, J. W., *Combustion chemistry of nitrogen*. In *Gas-Phase Combustion Chemistry*, W.C. Gardiner, Jr., Ed. Springer, NY, 2000; pp.125-341.
- [104] Atakan, B., Kocis, D., and Wolfrum, J., "Direct Investigation of the Kinetics of the Reaction of CN Radicals with N Atoms and 3CH_2 Radicals with NO ", 1992, *Proc. Combust. Inst.*, 24, pp. 691-699.

[105] Fikri, M., Meyer, S., Roggenbuck, J., and Temps, F., "An Experimental and Theoretical Study of the Product Distribution of the Reaction $\text{CH}_2 (\tilde{\text{X}}^3\text{B}_1) + \text{NO}$ ", 2001, Faraday Discuss. Roy. Soc., 119, pp. 223-242.

[106] Dagaut, P., Glarborg, P., and Alzueta, M. U., 2008, "The Oxidation of Hydrogen Cyanide and Related Chemistry", Prog. Energy Combust. Sci., 34, pp. 1-46.

APPENDIX A: ERROR ANALYSIS

A.1 Flame Length Adjustment:

As can be seen in the chapters 5 and 6, the lengths of the experimental and numerical flame simulation aren't and probably couldn't be perfectly matched. In this section, the effect of flame length difference on the experimentally measured flame structure and X_{NO} distribution along centerline is investigated.

Data reduction of for NO PLIF imaging requires the availability of temperature and concentrations of major quenching species, such as O_2 , CO_2 , N_2 , OH , CO , etc. These data are used to calculate the Boltzmann fraction f_B , quenching correction rate or fluorescence efficiency η_{fluor} of the NO-PLIF signals and Tamura's procedure[74] is followed,

$$f_B = f_B(T, X_i), \quad (A.1)$$

$$\eta_{fluor} = \eta_{fluor}(T, X_i). \quad (A.2)$$

In current research, the temperature and species data are obtained from CFD simulation, thus compounding discrepancies of flame lengths into the data reduction. The discrepancies of flame lengths as replotted in Figure A-1.

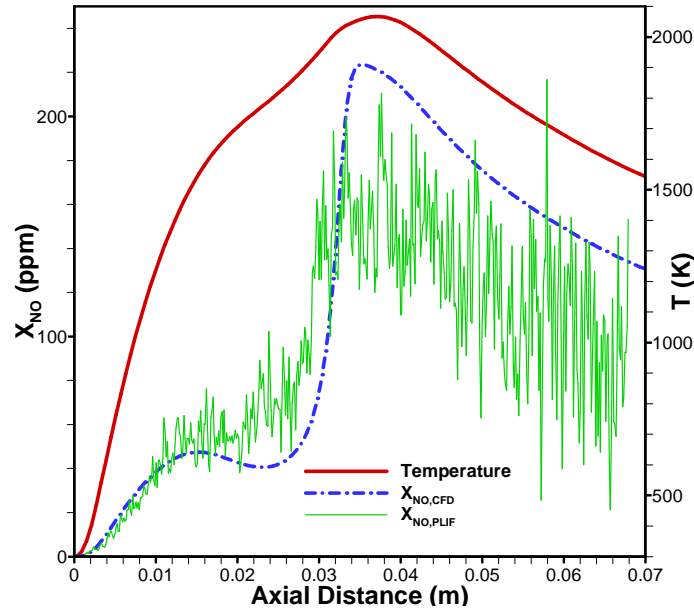


Figure A-1: X_{NO} on centerline of CH_4 /air diffusion flame with 100 ppm NH_3 seeding into the fuel stream.

As can be seen, both the $X_{NO,CFD}$ and $X_{NO,PLIF}$ agree on the “two-peak” structure, which means that there are two peaks of X_{NO} on the centerline of flames. This structure is confirmed by both the $X_{NO,CFD}$ and $X_{NO,PLIF}$. The $X_{NO,CFD}$ overpredicts the second peak of X_{NO} distribution. This second peak approximately overlaps with the temperature above 2,000 K, which confirms that this peak is primarily due to the thermal-NO mechanism. Correspondingly, the first peak is in the region where the temperature is below 1,900 K, indicating that this peak is formed by the prompt-NO mechanism. Figure A-3 shows the Boltzmann corrections f_B , fluorescence efficiency η_{fluor} , total correction $\times 10^6$ and temperature profiles. The total correction here is $\frac{f_B \eta_{fluor}}{T}$, which also accounts for the variation of gas density, assuming that the atmospheric flame has uniform pressure everywhere.

The discrepancy in the flame lengths is also apparent in this figure. The step transition in front of the second peak doesn't occur at the same axial distances. X_{NO-CFD} predicts steep gradient at higher elevation than $X_{NO-PLIF}$ does. This brings up a question when temperature and major quenching species are used for data reduction (i.e., to calculate the Boltzmann correction f_B and fluorescence efficiency η_{fluor}), which is that if the temperature profile or the flame length needs to be adjusted or stretched before data reduction. The effect of this adjustment is shown in Figure A-2.

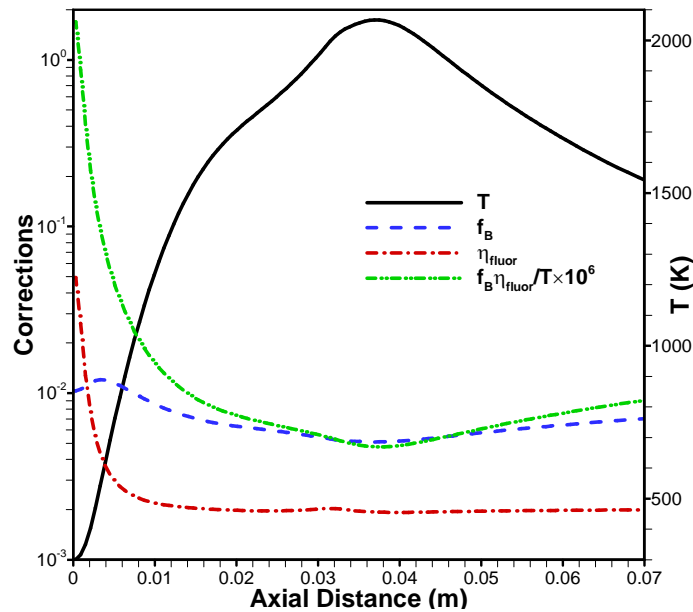


Figure A-2: The Boltzmann fraction f_B , fluorescence efficiency η_{fluor} , total corrections $\times 10^6$ and temperature on the centerline of CH₄/air diffusion flame, with zero NH₃ seeded to fuel stream.

Figure A-3 shows the stretched temperature $T_{CFD,STRETCHED}$, original temperature T_{CFD} , stretched, original $X_{NO-PLIF}$ $X_{NO-PLIF,STRETCHED}$ and X_{NO-CFD} . The $X_{NO-PLIF,STRETCHED}$ is

obtained by using stretched temperature profile $T_{CFD,STRETCHED}$ and corresponding stretched major quenching species. Comparison between the $X_{NO-PLIF,STRETCHED}$ and $X_{NO-PLIF}$ shows that first of all, the two-peak structure is again obtained, and the magnitudes of these two profiles are identical. The only difference is the locations of the steep gradients. This means that even the temperature or flame length is accounted for, it doesn't change the structure of $X_{NO,PLIF}$ but just the spatial scale.

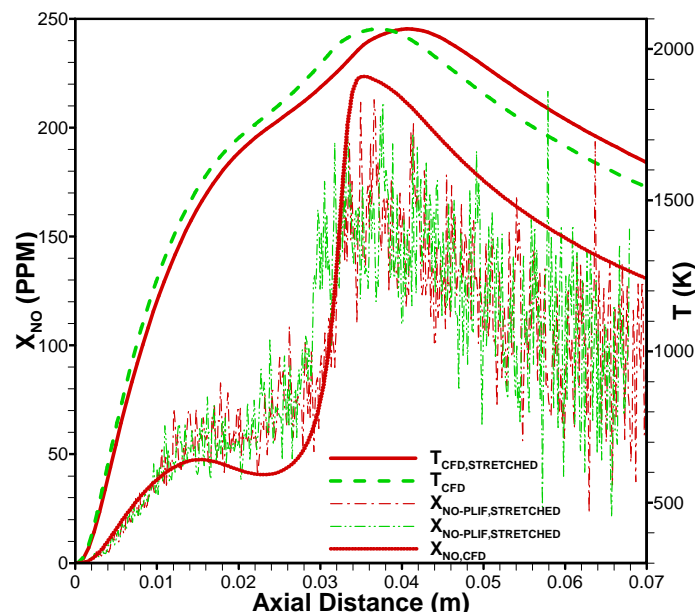


Figure A-3: The stretched temperature $T_{CFD,STRETCHED}$, original temperature T_{CFD} ; The stretched and original $X_{NO-PLIF}$; The stretched $X_{NO-PLIF,STRETCHED}$ and and $X_{NO,CFD}$.

A.2 Laser Profile Curve Fitting

Since the laser profile out of the dye laser is not perfectly Gaussian, additional curve fitting is needed to fit the profile for image normalization, i.e. to obtain the term

$\left(\frac{LIF}{I_r}\right)_{flame}$ in the derivation of quantitative X_{NO} . In this term, I_r is the profile of laser sheet

or laser irradiance. The sheet profile, its curve fitting, and the fitting error are plotted in

Figure A-4. The laser-sheet profile is fitted with 7-Gaussian functions using the curve fitting tool in MatLab as:

$$I_r \triangleq \sum_{i=1}^7 a_i \exp \left[- \left(\frac{(x - b_i)}{c_i} \right)^2 \right]. \quad (\text{A. 3})$$

The 7-Gaussian curve is chosen because there are multiple peaks or modes in the laser profile and 7 Gaussians are found to be sufficient. As shown below, the fitting error is fairly constant throughout the entire domain.

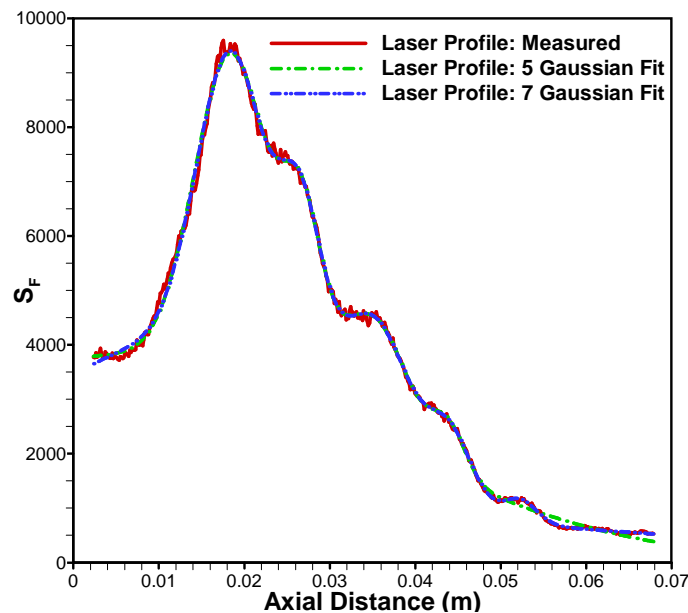


Figure A-4: Laser profile, its curve fitting and fitting error.

This explains to some extent the relatively large uncertainty/fluctuation of X_{NO} distribution in the upper region beyond 3 cm in Figure A-1 and Figure A-3. Since the NO fluorescence signal and total correction are fairly constant beyond 1 cm, the variation of laser profile plays a significant role in X_{NO} fluctuation. The $X_{NO,PLIF}$ is found from:

$$[\text{NO}]_{\text{PLIF}} = \frac{1}{k} \frac{LIF}{I_r} \frac{(\text{total correction})_{\text{cal}}}{(\text{total correction})_{\text{flame}}}, \quad (\text{A. 4})$$

with the calibration slope k , fluorescence signal LIF , and total corrections fairly constant.

The the uncertainty of $X_{NO,PLIF}$ is, based on an error propagation equation,

$$u([NO]_{PLIF}) \propto \sqrt{\left[\frac{\partial[NO]_{PLIF}}{\partial I_r} u(I_r)\right]^2} = \text{abs}\left\{\frac{\partial[NO]_{PLIF}}{\partial I_r} u(I_r)\right\} = \frac{[NO]_{PLIF}}{I_r} u(I_r) \quad (A.5)$$

where $u(\circ)$ is the uncertainty of quantity “ \circ ”. The relative uncertainty of $X_{NO,PLIF}$ is:

$$\frac{u([NO]_{PLIF})}{[NO]_{PLIF}} \propto \frac{u(I_r)}{I_r}, \quad (A.6)$$

which means the relative uncertainty of $X_{NO,PLIF}$ is proportional to that of the laser profile.

Since the uncertainty of the laser sheet profile is fairly constant, its relative uncertainty increases with respect to height, which results in the greater uncertainty/fluctuations of X_{NO} at higher elevation in the flame.

Since the laser sheet profile is a temporal average collected by accumulating shots on the camera chip, an estimate of the uncertainty due to temporal fluctuations of the laser sheet profile $u(I_r)$ is not available from measurement.

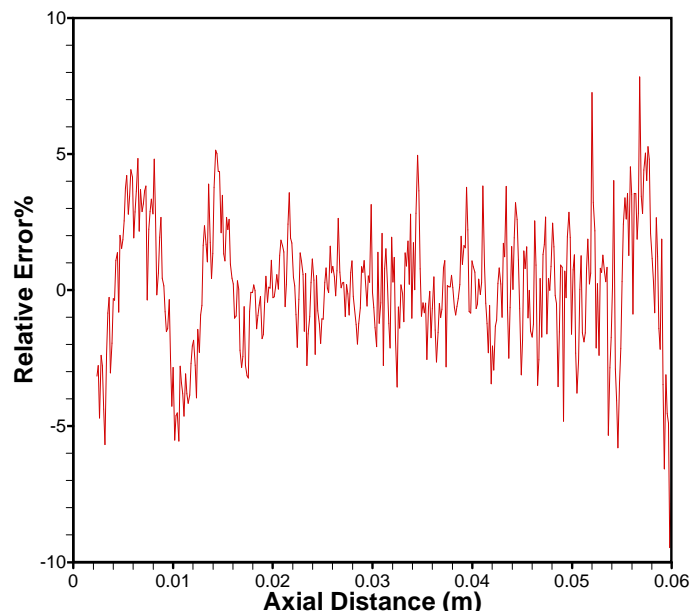


Figure A-5: The relative spatial error introduced by multi-gaussian curve fitting.

The relative spatial error introduced by multi-gaussian curve fitting is calculated and shown in Figure A-5. Basically this error is less than 5%

A.3 An Overall Estimate of Spatial Uncertainty

An analysis of spatial uncertainty is implemented to roughly estimate the overall uncertainty of X_{NO} using PLIF. In order to remove the high spatial noise, a low-pass filter with a cut-off wave length of 5.46 mm was applied, i.e. $\lambda_{cut-off} = 5.46$ mm. The filtered X_{NO} and original X_{NO} are shown in Figure A-1. As shown at the bottom of Figure A-1, the error between the original signal X_{NO} and its filtered version $X_{NO,FILTERED}$ increases with axial distance because of diminishing laser intensity (see Figure A-4).

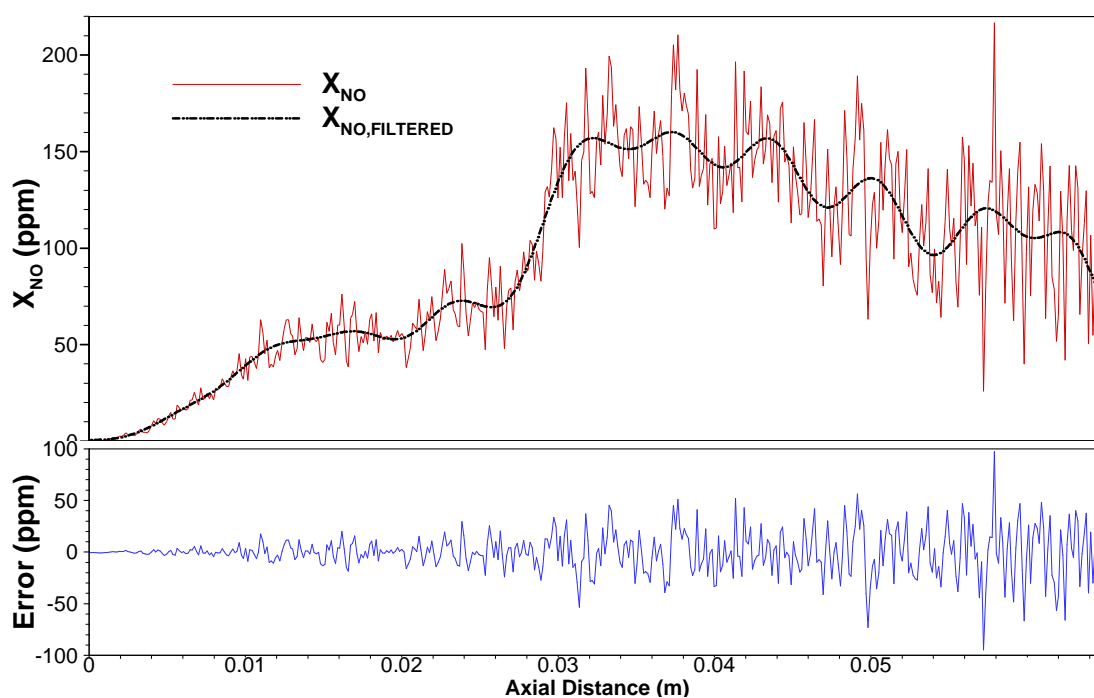


Figure A-6: Top: The original X_{NO} and its filtered signal, in case of zero NH_3 doping. Bottom: The difference between the original and filtered signal.

An overall RMS (root mean square) value is calculated based on the difference between X_{NO} and $X_{NO,FILTERED}$, i.e.

$$RMS = \sqrt{\frac{1}{N-1} \sum_{i=1}^N (X_{NO,i} - X_{NO,FILTERED,i})^2}, \quad (A.7)$$

$$RMS = 20.66 \text{ ppm}, \quad (A.8)$$

where the N is the total number of samples, which in our case includes data along the entire axial distance. It is also possible to estimate the RMS for different regions of the flow. With a coverage factor of 2, the relative uncertainty in the lower regions of the flame (where the signal is ~50 ppm from 0.01 m to 0.02 m) is estimated as

$$\frac{u(X_{NO})}{X_{NO}} \approx \frac{2 * RMS_{lower}}{X_{NO}} = \frac{2 * 7.81}{50} = 31\%,$$

where 7.81 is the estimated RMS value in that region. While in the upper region (where the signal is ~150 from 0.03 m to 0.04 m), the relative uncertainty is estimated as

$$\frac{u(X_{NO})}{X_{NO}} \approx \frac{2 * RMS_{upper}}{X_{NO}} = \frac{2 * 22.40}{150} = 29\%.$$

Note that the flow condition with no NH_3 seeded in the flow gives the weakest NO-PLIF signal level. With NH_3 seeding, the signal level and consequently the relative spatial noise are expected to be significantly reduced. For example, with a seeding level of 2% NH_3 , the relative uncertainty due to spatial noise is less than 10%.

APPENDIX B: DETAILED REACTION PATHWAYS OF TIAN MECHANISM

ELEMENTS	ATOMIC
CONSIDERED	WEIGHT
1. O	15.9994
2. H	1.00797
3. C	12.0112
4. N	14.0067
5. AR	39.9480

SPECIES	S	G	MOLECULAR	TEMPERATURE			ELEMENT COUNT			
				WEIGHT	LOW	HIGH	OH	C	N	AR
1. H	G	0	1.0080E+00	200	6000	0	1	0	0	0
2. O	G	0	1.5999E+01	200	6000	1	0	0	0	0
3. OH	G	0	1.7007E+01	200	6000	1	1	0	0	0
4. H2	G	0	2.0159E+00	200	6000	0	2	0	0	0
5. O2	G	0	3.1999E+01	200	6000	2	0	0	0	0

6. HO2	G 0	3.3007E+01	200	6000	2	1	0	0	0
7. H2O	G 0	1.8015E+01	200	6000	1	2	0	0	0
8. H2O2	G 0	3.4015E+01	200	6000	2	2	0	0	0
9. CO	G 0	2.8011E+01	200	6000	1	0	1	0	0
10. CO2	G 0	4.4010E+01	200	6000	2	0	1	0	0
11. HOCO	G 0	4.5018E+01	200	3000	2	1	1	0	0
12. CH4	G 0	1.6043E+01	200	6000	0	4	1	0	0
13. CH3	G 0	1.5035E+01	200	6000	0	3	1	0	0
14. CH2	G 0	1.4027E+01	200	6000	0	2	1	0	0
15. CH2(S)	G 0	1.4027E+01	200	6000	0	2	1	0	0
16. CH	G 0	1.3019E+01	200	6000	0	1	1	0	0
17. C	G 0	1.2011E+01	200	3500	0	0	1	0	0
18. CH3OH	G 0	3.2042E+01	200	6000	1	4	1	0	0
19. CH3O	G 0	3.1034E+01	200	6000	1	3	1	0	0
20. CH2OH	G 0	3.1034E+01	200	6000	1	3	1	0	0
21. CH2O	G 0	3.0026E+01	200	6000	1	2	1	0	0
22. HCO	G 0	2.9019E+01	200	6000	1	1	1	0	0
23. C2H6	G 0	3.0070E+01	200	6000	0	6	2	0	0
24. C2H5	G 0	2.9062E+01	200	6000	0	5	2	0	0
25. C2H4	G 0	2.8054E+01	200	6000	0	4	2	0	0
26. C2H3	G 0	2.7046E+01	200	6000	0	3	2	0	0
27. C2H2	G 0	2.6038E+01	200	6000	0	2	2	0	0
28. H2CC	G 0	2.6038E+01	200	6000	0	2	2	0	0

29. C2H	G 0	2.5030E+01	200	6000	0	1	2	0	0
30. C2	G 0	2.4022E+01	200	6000	0	0	2	0	0
31. CH3CH2OH	G 0	4.6070E+01	200	6000	1	6	2	0	0
32. CH3CH2O	G 0	4.5062E+01	200	6000	1	5	2	0	0
33. CH3CHOH	G 0	4.5062E+01	200	6000	1	5	2	0	0
34. CH2CH2OH	G 0	4.5062E+01	200	6000	1	5	2	0	0
35. CH3CHO	G 0	4.4054E+01	200	6000	1	4	2	0	0
36. cC2H4O	G 0	4.4054E+01	200	6000	1	4	2	0	0
37. HCCOH	G 0	4.2038E+01	200	6000	1	2	2	0	0
38. CH3CO	G 0	4.3046E+01	200	6000	1	3	2	0	0
39. CH2CHO	G 0	4.3046E+01	200	6000	1	3	2	0	0
40. CH2CO	G 0	4.2038E+01	200	6000	1	2	2	0	0
41. HCCO	G 0	4.1030E+01	200	6000	1	1	2	0	0
42. C2O	G 0	4.0022E+01	300	4000	1	0	2	0	0
43. OCHCHO	G 0	5.8037E+01	300	3000	2	2	2	0	0
44. NO	G 0	3.0006E+01	200	6000	1	0	0	1	0
45. NO2	G 0	4.6005E+01	200	6000	2	0	0	1	0
46. NO3	G 0	6.2005E+01	200	6000	3	0	0	1	0
47. N2O	G 0	4.4013E+01	300	5000	1	0	0	2	0
48. HNO	G 0	3.1014E+01	200	6000	1	1	0	1	0
49. HON	G 0	3.1014E+01	300	5000	1	1	0	1	0
50. HONO	G 0	4.7013E+01	200	6000	2	1	0	1	0
51. HNO2	G 0	4.7013E+01	300	4000	2	1	0	1	0

52. H2NO	G 0	3.2022E+01	300	4000	1	2	0	1	0
53. HNOH	G 0	3.2022E+01	300	4000	1	2	0	1	0
54. HONO2	G 0	6.3013E+01	200	6000	3	1	0	1	0
55. CH3NO	G 0	4.5041E+01	200	6000	1	3	1	1	0
56. NH3	G 0	1.7031E+01	300	5000	0	3	0	1	0
57. NH2	G 0	1.6023E+01	300	5000	0	2	0	1	0
58. NH	G 0	1.5015E+01	200	6000	0	1	0	1	0
59. N	G 0	1.4007E+01	300	5000	0	0	0	1	0
60. N2H4	G 0	3.2045E+01	300	5000	0	4	0	2	0
61. N2H3	G 0	3.1037E+01	300	5000	0	3	0	2	0
62. N2H2	G 0	3.0029E+01	300	5000	0	2	0	2	0
63. H2NN	G 0	3.0029E+01	300	5000	0	2	0	2	0
64. NNH	G 0	2.9021E+01	250	4000	0	1	0	2	0
65. NH2OH	G 0	3.3030E+01	300	5000	1	3	0	1	0
66. HCN	G 0	2.7026E+01	300	4000	0	1	1	1	0
67. HNC	G 0	2.7026E+01	300	5000	0	1	1	1	0
68. CN	G 0	2.6018E+01	200	6000	0	0	1	1	0
69. HNCO	G 0	4.3025E+01	300	5000	1	1	1	1	0
70. HOCN	G 0	4.3025E+01	300	5000	1	1	1	1	0
71. HCNO	G 0	4.3025E+01	300	5000	1	1	1	1	0
72. NCO	G 0	4.2017E+01	300	5000	1	0	1	1	0
73. H2CN	G 0	2.8034E+01	300	4000	0	2	1	1	0
74. HCNH	G 0	2.8034E+01	300	4000	0	2	1	1	0

75. CH ₃ NH ₂	G	0	3.1058E+01	300	5000	0	5	1	1	0
76. CH ₃ NH	G	0	3.0050E+01	300	5000	0	4	1	1	0
77. CH ₂ NH ₂	G	0	3.0050E+01	300	5000	0	4	1	1	0
78. CH ₂ NH	G	0	2.9042E+01	300	5000	0	3	1	1	0
79. CH ₃ CN	G	0	4.1053E+01	200	6000	0	3	2	1	0
80. CH ₂ CN	G	0	4.0045E+01	200	6000	0	2	2	1	0
81. NCCN	G	0	5.2036E+01	300	5000	0	0	2	2	0
82. NCN	G	0	4.0025E+01	300	4000	0	0	1	2	0
83. AR	G	0	3.9948E+01	200	6000	0	0	0	0	1
84. N ₂	G	0	2.8013E+01	200	6000	0	0	0	2	0

$$(k = A T^{**b} \exp(-E/RT))$$

REACTIONS CONSIDERED	A	b	E
1. H+O ₂ =O+OH	3.60E+15	-0.4	16600.0
2. H+H+M=H ₂ +M	7.00E+17	-1.0	0.0
N ₂	Enhanced by	0.000E+00	
H ₂ O	Enhanced by	0.000E+00	
H ₂	Enhanced by	0.000E+00	
3. H+H+N ₂ =H ₂ +N ₂	5.40E+18	-1.3	0.0
4. H+H+H ₂ =H ₂ +H ₂	1.00E+17	-0.6	0.0
5. H+H+H ₂ O=H ₂ +H ₂ O	1.00E+19	-1.0	0.0

6. H+O+M=OH+M	6.20E+16	-0.6	0.0
H2O	Enhanced by	5.000E+00	
7. H+O2(+M)=HO2(+M)	1.50E+12	0.6	0.0
Low pressure limit:	0.35000E+17	-0.41000E+00	-0.11160E+04
TROE centering:	0.50000E+00	0.10000E-29	0.10000E+31
N2	Enhanced by	0.000E+00	
AR	Enhanced by	0.000E+00	
H2O	Enhanced by	1.100E+01	
H2	Enhanced by	2.000E+00	
O2	Enhanced by	7.800E-01	
8. H+O2(+AR)=HO2(+AR)	1.50E+12	0.6	0.0
Low pressure limit:	0.90400E+20	-0.15000E+01	0.49000E+03
TROE centering:	0.50000E+00	0.10000E-29	0.10000E+31
9. H+O2(+N2)=HO2(+N2)	1.50E+12	0.6	0.0
Low pressure limit:	0.63700E+21	-0.17200E+01	0.52000E+03
TROE centering:	0.80000E+00	0.10000E-29	0.10000E+31
10. O+O+M=O2+M	1.90E+13	0.0	-1788.0
N2	Enhanced by	1.500E+00	
O2	Enhanced by	1.500E+00	
H2O	Enhanced by	1.000E+01	
11. O+H2=OH+H	3.80E+12	0.0	7948.0
Declared duplicate reaction...			
12. O+H2=OH+H	8.80E+14	0.0	19175.0

Declared duplicate reaction...

13. $\text{OH}+\text{OH}=\text{O}+\text{H}_2\text{O}$ 4.30E+03 2.7 -1822.0

14. $\text{OH}+\text{H}+\text{M}=\text{H}_2\text{O}+\text{M}$ 4.50E+22 -2.0 0.0

AR Enhanced by 3.800E-01

H2 Enhanced by 7.300E-01

H2O Enhanced by 1.200E+01

15. $\text{OH}+\text{H}_2=\text{H}+\text{H}_2\text{O}$ 2.10E+08 1.5 3449.0

16. $\text{H}_2+\text{O}_2=\text{HO}_2+\text{H}$ 7.40E+05 2.4 53502.0

17. $\text{HO}_2+\text{H}=\text{OH}+\text{OH}$ 8.40E+13 0.0 400.0

18. $\text{HO}_2+\text{H}=\text{H}_2\text{O}+\text{O}$ 1.40E+12 0.0 0.0

19. $\text{HO}_2+\text{O}=\text{OH}+\text{O}_2$ 1.60E+13 0.0 -445.0

20. $\text{HO}_2+\text{OH}=\text{H}_2\text{O}+\text{O}_2$ 3.60E+21 -2.1 9000.0

Declared duplicate reaction...

21. $\text{HO}_2+\text{OH}=\text{H}_2\text{O}+\text{O}_2$ 2.00E+15 -0.6 0.0

Declared duplicate reaction...

22. $\text{HO}_2+\text{OH}=\text{H}_2\text{O}+\text{O}_2$ -2.2E96 -24.0 49000.0

Declared duplicate reaction...

23. $\text{HO}_2+\text{HO}_2=\text{H}_2\text{O}_2+\text{O}_2$ 1.90E+11 0.0 -1408.0

Declared duplicate reaction...

24. $\text{HO}_2+\text{HO}_2=\text{H}_2\text{O}_2+\text{O}_2$ 1.00E+14 0.0 11034.0

Declared duplicate reaction...

25. $\text{H}_2\text{O}_2(+\text{M})=\text{OH}+\text{OH}(+\text{M})$ 4.00E+11 0.0 37137.0

Low pressure limit: 0.22910E+17 0.00000E+00 0.43638E+05

TROE centering: 0.50000E+00 0.10000E-29 0.10000E+31 0.10000E+31

H2O Enhanced by 1.200E+01

H2 Enhanced by 2.500E+00

AR Enhanced by 6.400E-01

26. H2O2+H=H2O+OH	1.00E+13	0.0	3580.0
27. H2O2+H=HO2+H2	1.70E+12	0.0	3760.0
28. H2O2+O=HO2+OH	9.60E+06	2.0	3970.0
29. H2O2+OH=H2O+HO2	1.90E+12	0.0	427.0

Declared duplicate reaction...

30. H2O2+OH=H2O+HO2	1.60E+18	0.0	29410.0
---------------------	----------	-----	---------

Declared duplicate reaction...

31. CO+O(+M)=CO2(+M)	1.80E+10	0.0	2384.0
----------------------	----------	-----	--------

Low pressure limit: 0.13500E+25 -0.27900E+01 0.41910E+04

TROE centering: 0.10000E+01 0.10000E-29 0.10000E+31 0.10000E+31

H2 Enhanced by 2.500E+00

H2O Enhanced by 1.200E+01

CO Enhanced by 1.900E+00

CO2 Enhanced by 3.800E+00

32. CO+O2=CO2+O	4.70E+12	0.0	60500.0
33. CO+HO2=CO2+OH	1.60E+05	2.2	17943.0
34. CO+OH=CO2+H	9.30E+10	0.0	0.0

Declared duplicate reaction...

35. CO+OH=CO2+H	7.10E+05	1.8	1133.0
-----------------	----------	-----	--------

Declared duplicate reaction...

36. CO+OH=HOCO	1.00E+25	-6.0	2981.0
37. HOCO=CO2+H	1.60E+55	-15.0	46500.0

Declared duplicate reaction...

38. HOCO=CO2+H	1.20E+68	-18.0	60000.0
----------------	----------	-------	---------

Declared duplicate reaction...

39. HOCO+OH=CO2+H2O	4.60E+12	0.0	-89.0
---------------------	----------	-----	-------

Declared duplicate reaction...

40. HOCO+OH=CO2+H2O	9.50E+06	2.0	-89.0
---------------------	----------	-----	-------

Declared duplicate reaction...

41. HOCO+O2=CO2+HO2	9.90E+11	0.0	0.0
42. CH2O(+M)=HCO+H(+M)	8.00E+15	0.0	87726.0

Low pressure limit: 0.37340E+16 0.00000E+00 0.73479E+05

43. CH2O(+M)=CO+H2(+M)	3.70E+13	0.0	71969.0
------------------------	----------	-----	---------

Low pressure limit: 0.56610E+16 0.00000E+00 0.65849E+05

44. CH2O+H=HCO+H2	4.10E+08	1.5	2444.0
45. CH2O+O=HCO+OH	4.20E+11	0.6	2760.0
46. CH2O+O2=HCO+HO2	2.40E+05	2.5	36461.0
47. CH2O+OH=HCO+H2O	7.80E+07	1.6	-1055.0
48. CH2O+HO2=HCO+H2O2	4.10E+04	2.5	10206.0
49. CH2O+CH3=HCO+CH4	3.20E+01	3.4	4310.0
50. HCO=H+CO	6.10E+10	-0.9	16755.0
51. HCO+H=CO+H2	1.10E+14	0.0	0.0

52. HCO+O=CO+OH	3.00E+13	0.0	0.0
53. HCO+O=CO ₂ +H	3.00E+13	0.0	0.0
54. HCO+OH=CO+H ₂ O	1.10E+14	0.0	0.0
55. HCO+O ₂ =CO+HO ₂	3.40E+12	0.0	0.0
56. HCO+HO ₂ =CO ₂ +OH+H	3.00E+13	0.0	0.0
57. HCO+HCO=CO+CH ₂ O	2.70E+13	0.0	0.0
58. CH ₃ +H(+M)=CH ₄ (+M)	2.10E+14	0.0	0.0

Low pressure limit: 0.64670E+24 -0.18000E+01 0.00000E+00

TROE centering: 0.63760E+00 0.10000E-29 0.32300E+04 0.10000E+31

CH₄ Enhanced by 1.900E+00

C₂H₆ Enhanced by 4.800E+00

59. CH ₄ +H=CH ₃ +H ₂	4.10E+03	3.2	8755.0
60. CH ₄ +O=CH ₃ +OH	4.40E+05	2.5	6577.0
61. CH ₄ +OH=CH ₃ +H ₂ O	1.00E+06	2.2	2506.0
62. CH ₄ +HO ₂ =CH ₃ +H ₂ O ₂	4.70E+04	2.5	21000.0
63. CH ₄ +CH ₂ =CH ₃ +CH ₃	4.30E+12	0.0	10030.0
64. CH ₄ +CH ₂ (S)=CH ₃ +CH ₃	4.30E+13	0.0	0.0
65. CH ₂ +H(+M)=CH ₃ (+M)	3.80E+16	-0.8	0.0

Low pressure limit: 0.48000E+28 -0.31400E+01 0.12300E+04

TROE centering: 0.68000E+00 0.78000E+02 0.19950E+04 0.55900E+04

N₂ Enhanced by 1.000E+00

H₂O Enhanced by 6.000E+00

AR Enhanced by 7.000E-01

66. CH ₃ +H=CH ₂ +H ₂	9.00E+13	0.0	15100.0
67. CH ₂ (S)+H ₂ =CH ₃ +H	7.20E+13	0.0	0.0
68. CH ₃ +O=CH ₂ O+H	6.90E+13	0.0	0.0
69. CH ₃ +O=H ₂ +CO+H	1.50E+13	0.0	0.0
70. CH ₃ +OH=CH ₂ +H ₂ O	1.10E+03	3.0	2780.0
71. CH ₃ +OH=CH ₂ (S)+H ₂ O	4.40E+13	-0.3	-727.0
72. CH ₃ +HO ₂ =CH ₄ +O ₂	1.80E+03	2.8	-3730.0
73. CH ₃ +HO ₂ =CH ₃ O+OH	2.00E+13	0.0	1075.0
74. CH ₃ +O ₂ =CH ₃ O+O	7.50E+12	0.0	28297.0
75. CH ₃ +O ₂ =CH ₂ O+OH	1.90E+11	0.0	9842.0
76. CH ₃ +HCO=CH ₄ +CO	2.80E+13	0.0	0.0
77. CH ₃ +CH ₃ =C ₂ H ₅ +H	5.40E+13	0.0	16055.0
78. CH ₃ +CH ₃ (+M)=C ₂ H ₆ (+M)	3.60E+13	0.0	0.0

Low pressure limit: 0.12690E+42 -0.70000E+01 0.27620E+04

TROE centering: 0.62000E+00 0.73000E+02 0.11800E+04 0.10000E+31

79. CH ₂ +M=CH+H+M	5.60E+15	0.0	89000.0
80. CH ₂ +M=C+H ₂ +M	5.80E+12	0.5	68500.0
81. CH ₂ +H=CH+H ₂	1.20E+14	0.0	0.0
82. CH ₂ +O=CO+H+H	1.20E+14	0.0	536.0
83. CH ₂ +O=CO+H ₂	8.00E+13	0.0	536.0
84. CH ₂ +OH=CH ₂ O+H	2.80E+13	0.1	-161.0
85. CH ₂ +OH=CH+H ₂ O	8.60E+05	2.0	6776.0
86. CH ₂ +O ₂ =CO+H ₂ O	1.80E+11	0.0	0.0

87. CH ₂ +O ₂ =CO ₂ +H+H	3.80E+11	0.0	0.0
88. CH ₂ +O ₂ =CH ₂ O+O	2.90E+11	0.0	0.0
89. CH ₂ +O ₂ =CO ₂ +H ₂	3.40E+11	0.0	0.0
90. CH ₂ +O ₂ =CO+OH+H	6.10E+11	0.0	0.0
91. CH ₂ +CO ₂ =CO+CH ₂ O	1.00E+11	0.0	1000.0
92. CH ₂ (S)+M=CH ₂ +M	1.00E+13	0.0	0.0
N ₂	Enhanced by	0.000E+00	
H ₂ O	Enhanced by	0.000E+00	
AR	Enhanced by	0.000E+00	
H	Enhanced by	0.000E+00	
93. CH ₂ (S)+N ₂ =CH ₂ +N ₂	1.30E+13	0.0	430.0
94. CH ₂ (S)+AR=CH ₂ +AR	1.50E+13	0.0	884.0
95. CH ₂ (S)+H=CH ₂ +H	2.00E+14	0.0	0.0
96. CH ₂ (S)+H=CH+H ₂	3.00E+13	0.0	0.0
97. CH ₂ (S)+O=CO+2H	3.00E+13	0.0	0.0
98. CH ₂ (S)+OH=CH ₂ O+H	3.00E+13	0.0	0.0
99. CH ₂ (S)+O ₂ =CH ₂ +O ₂	3.10E+13	0.0	0.0
100. CH ₂ (S)+H ₂ O=CH ₂ +H ₂ O	3.00E+13	0.0	0.0
101. CH ₂ (S)+CO ₂ =CH ₂ O+CO	1.10E+13	0.0	0.0
102. CH+H=C+H ₂	1.50E+14	0.0	0.0
103. CH+O=CO+H	5.70E+13	0.0	0.0
104. CH+OH=HCO+H	3.00E+13	0.0	0.0
105. CH+OH=C+H ₂ O	4.00E+07	2.0	3000.0

106. CH+O2=HCO+O	3.30E+13	0.0	0.0
107. CH+H2O=CH2O+H	5.70E+12	0.0	-755.0
108. CH+CO2=HCO+CO	8.80E+06	1.8	-1040.0
109. C+OH=CO+H	5.00E+13	0.0	0.0
110. C+O2=CO+O	2.00E+13	0.0	0.0
111. CH3OH(+M)=CH3+OH(+M)	2.10E+18	-0.6	92540.0

Low pressure limit: 0.26000E+50 -0.88000E+01 0.10150E+06

TROE centering: 0.76560E+00 0.19100E+04 0.59510E+02 0.93740E+04

112. CH3OH(+M)=CH2(S)+H2O(+M)	3.10E+18	-1.0	91712.0
-------------------------------	----------	------	---------

Low pressure limit: 0.54000E+24 -0.83446E+01 0.99596E+05

TROE centering: 0.99220E+00 0.94300E+03 0.47310E+05 0.47110E+05

113. CH3OH+H=CH2OH+H2	2.90E+09	1.2	4491.0
114. CH3OH+H=CH3O+H2	5.10E+08	1.2	4491.0
115. CH3OH+O=CH2OH+OH	2.10E+13	0.0	5305.0
116. CH3OH+O=CH3O+OH	3.70E+12	0.0	5305.0
117. CH3OH+OH=CH2OH+H2O	1.50E+08	1.4	113.0
118. CH3OH+OH=CH3O+H2O	2.70E+07	1.4	113.0
119. CH3OH+HO2=CH2OH+H2O2	2.00E+13	0.0	15000.0
120. CH3OH+O2=CH2OH+HO2	6.00E+13	0.0	46600.0
121. CH3OH+O2=CH3O+HO2	6.00E+13	0.0	54800.0
122. CH2OH(+M)=CH2O+H(+M)	2.80E+14	-0.7	32820.0

Low pressure limit: 0.60100E+34 -0.53900E+01 0.36200E+05

TROE centering: 0.96000E+00 0.67600E+02 0.18550E+04 0.75430E+04

H2	Enhanced by	2.000E+00		
H2O	Enhanced by	5.000E+00		
CO	Enhanced by	2.000E+00		
CO2	Enhanced by	3.000E+00		
123. CH2OH+H=CH2O+H2		4.00E+06	1.9	147.0
124. CH2OH+H=CH3+OH		1.80E+14	0.2	111.0
125. CH2OH+H(+M)=CH3OH(+M)		4.30E+15	-0.8	0.0
Low pressure limit: 0.38440E+38 -0.62100E+01 0.13330E+04				
TROE centering: 0.25000E+00 0.21000E+03 0.14340E+04 0.10000E+31				
126. CH2OH+O=CH2O+OH		6.60E+13	0.0	-693.0
127. CH2OH+OH=CH2O+H2O		2.40E+13	0.0	0.0
128. CH2OH+HO2=CH2O+H2O2		1.20E+13	0.0	0.0
129. CH2OH+O2=CH2O+HO2		7.20E+13	0.0	3736.0
Declared duplicate reaction...				
130. CH2OH+O2=CH2O+HO2		2.90E+16	-1.5	0.0
Declared duplicate reaction...				
131. CH2OH+HCO=CH3OH+CO		1.00E+13	0.0	0.0
132. CH2OH+HCO=CH2O+CH2O		1.50E+13	0.0	0.0
133. CH2OH+CH2O=CH3OH+HCO		5.50E+03	2.8	5862.0
134. CH2OH+CH2OH=CH3OH+CH2O		4.80E+12	0.0	0.0
135. CH2OH+CH3O=CH3OH+CH2O		2.40E+12	0.0	0.0
136. CH2OH+CH4=CH3OH+CH3		2.20E+01	3.1	16227.0
137. CH3O(+M)=CH2O+H(+M)		6.80E+13	0.0	26154.0

Low pressure limit: 0.18670E+26 -0.30000E+01 0.24291E+05

TROE centering: 0.50000E+00 0.10000E+04 0.20000E+04

138. CH3O+H=CH2O+H2	7.60E+08	1.5	-519.0
139. CH3O+H=CH3+OH	4.60E+13	0.3	28.0
140. CH3O+H(+M)=CH3OH(+M)	2.40E+12	0.5	50.0

Low pressure limit: 0.46600E+42 -0.74400E+01 0.14080E+05

TROE centering: 0.70000E+00 0.10000E+03 0.90000E+05 0.10000E+05

N2 Enhanced by 1.000E+00

H2 Enhanced by 2.000E+00

H2O Enhanced by 6.000E+00

CH4 Enhanced by 2.000E+00

CO Enhanced by 1.500E+00

CO2 Enhanced by 2.000E+00

C2H6 Enhanced by 3.000E+00

141. CH3O+O=CH2O+OH	3.80E+12	0.0	0.0
142. CH3O+OH=CH2O+H2O	1.80E+13	0.0	0.0
143. CH3O+HO2=CH2O+H2O2	3.00E+11	0.0	0.0
144. CH3O+O2=CH2O+HO2	2.20E+10	0.0	1749.0
145. CH3O+CO=CH3+CO2	9.50E+25	-4.9	9080.0
146. CH3O+CH3=CH2O+CH4	2.40E+13	0.0	0.0
147. CH3O+CH4=CH3OH+CH3	1.30E+14	0.0	15073.0
148. CH3O+CH2O=CH3OH+HCO	1.00E+11	0.0	2981.0
149. CH3O+CH3O=CH3OH+CH2O	6.00E+13	0.0	0.0

150. C2H6+H=C2H5+H2	9.80E+13	0.0	9220.0
151. C2H6+O=C2H5+OH	1.10E-07	6.5	274.0
152. C2H6+OH=C2H5+H2O	9.20E+06	2.0	990.0
153. C2H6+HO2=C2H5+H2O2	1.10E+05	2.5	16850.0
154. C2H6+O2=C2H5+HO2	7.30E+05	2.5	49160.0
155. C2H6+CH3=C2H5+CH4	5.60E+10	0.0	9418.0

Declared duplicate reaction...

156. C2H6+CH3=C2H5+CH4	8.40E+14	0.0	22250.0
------------------------	----------	-----	---------

Declared duplicate reaction...

157. C2H6+CH2(S)=C2H5+CH3	1.20E+14	0.0	0.0
158. C2H4+H(+M)=C2H5(+M)	1.40E+09	1.5	1355.0

Low pressure limit: 0.20000E+40 -0.66420E+01 0.57690E+04

TROE centering: -0.56900E+00 0.29900E+03 0.91470E+04 0.15240E+03

159. C2H5+H(+M)=C2H6(+M)	5.20E+17	-1.0	1580.0
--------------------------	----------	------	--------

Low pressure limit: 0.19900E+42 -0.70800E+01 0.66850E+04

TROE centering: 0.84220E+00 0.12500E+03 0.22190E+04 0.68820E+04

N2 Enhanced by 1.000E+00

H2 Enhanced by 2.000E+00

H2O Enhanced by 6.000E+00

CH4 Enhanced by 2.000E+00

CO Enhanced by 1.500E+00

CO2 Enhanced by 2.000E+00

C2H6 Enhanced by 3.000E+00

AR	Enhanced by	7.000E-01		
160. C2H5+O=CH3+CH2O	4.20E+13	0.0	0.0	
161. C2H5+O=CH3CHO+H	5.30E+13	0.0	0.0	
162. C2H5+O=C2H4+OH	3.10E+13	0.0	0.0	
163. C2H5+OH=C2H4+H2O	2.40E+13	0.0	0.0	
164. C2H5+HO2=CH3CH2O+OH	3.10E+13	0.0	0.0	
165. C2H5+O2=C2H4+HO2	1.40E+07	1.1	-1975.0	
166. C2H5+CH2O=C2H6+HCO	5.50E+03	2.8	5860.0	
167. C2H5+HCO=C2H6+CO	4.30E+13	0.0	0.0	
168. C2H5+CH3=C2H4+CH4	9.00E+11	0.0	0.0	
169. C2H5+C2H5=C2H6+C2H4	1.50E+12	0.0	0.0	
170. C2H3+H(+M)=C2H4(+M)	3.90E+13	0.2	0.0	

Low pressure limit: 0.21000E+25 -0.13000E+01 0.00000E+00

TROE centering: 0.50000E+00 0.10000E-29 0.10000E+31 0.10000E+31

171. C2H4(+M)=H2CC+H2(+M)	8.00E+12	0.4	88800.0	
---------------------------	----------	-----	---------	--

Low pressure limit: 0.70000E+51 -0.93100E+01 0.99900E+05

TROE centering: 0.73500E+00 0.18000E+03 0.10350E+04 0.54170E+04

H2O Enhanced by 6.000E+00

AR Enhanced by 7.000E-01

172. C2H4+H=C2H3+H2	2.40E+02	3.6	11266.0	
173. CH4+CH=C2H4+H	3.00E+13	0.0	-400.0	
174. CH3+CH2=C2H4+H	1.20E+15	-0.3	153.0	
175. CH3+CH2(S)=C2H4+H	2.00E+13	0.0	0.0	

176. C2H4+O=CH3+HCO	3.90E+12	0.0	1494.0
Declared duplicate reaction...			
177. C2H4+O=CH3+HCO	6.20E+13	0.0	6855.0
Declared duplicate reaction...			
178. C2H4+O=CH2CHO+H	1.70E+12	0.0	1494.0
Declared duplicate reaction...			
179. C2H4+O=CH2CHO+H	2.80E+13	0.0	6855.0
Declared duplicate reaction...			
180. C2H4+OH=C2H3+H2O	1.30E-01	4.2	-860.0
181. C2H4+OH=CH3+CH2O	3.20E+01	2.7	-1172.0
182. C2H4+OH=CH3CHO+H	8.70E-05	4.6	-618.0
183. C2H4+HO2=cC2H4O+OH	2.20E+12	0.0	17200.0
184. C2H4+O2=C2H3+HO2	7.10E+13	0.0	60010.0
185. C2H4+CH3=C2H3+CH4	6.00E+07	1.6	16630.0
186. C2H2+H(+M)=C2H3(+M)	1.70E+10	1.3	2709.0
Low pressure limit: 0.63000E+32 -0.46640E+01 0.37800E+04			
TROE centering: 0.78780E+00 -0.10212E+05 0.10000E+31			
H2	Enhanced by	2.000E+00	
CO	Enhanced by	2.000E+00	
CO2	Enhanced by	3.000E+00	
H2O	Enhanced by	5.000E+00	
187. C2H3+H=C2H2+H2	4.50E+13	0.0	0.0
188. CH3+CH=C2H3+H	3.00E+13	0.0	0.0

189.	$C_2H_3+O=CH_2CO+H$	3.00E+13	0.0	0.0
190.	$C_2H_3+OH=C_2H_2+H_2O$	2.00E+13	0.0	0.0
191.	$C_2H_3+HO_2=CH_2CHO+OH$	3.00E+13	0.0	0.0
192.	$C_2H_3+O_2=CH_2O+HCO$	1.10E+15	-0.8	179.0
193.	$C_2H_3+O_2=CH_2CHO+O$	6.40E+08	1.0	-197.0
194.	$C_2H_3+O_2=C_2H_2+HO_2$	9.70E+00	3.1	-272.0
195.	$C_2H_3+O_2=CH_3O+CO$	5.40E+13	-0.8	179.0
196.	$C_2H_3+O_2=CH_3+CO_2$	6.00E+12	-0.8	179.0
197.	$C_2H_3+CH_2O=C_2H_4+HCO$	5.40E+03	2.8	5860.0
198.	$C_2H_3+HCO=C_2H_4+CO$	9.00E+13	0.0	0.0
199.	$C_2H_3+CH_3=C_2H_2+CH_4$	9.00E+12	0.0	-765.0
200.	$C_2H_3+CH=CH_2+C_2H_2$	5.00E+13	0.0	0.0
201.	$C_2H_3+C_2H_3=C_2H_4+C_2H_2$	1.50E+13	0.0	0.0
202.	$C_2H_3+C_2H=C_2H_2+C_2H_2$	3.00E+13	0.0	0.0
203.	$C_2H_2+M=C_2H+H+M$	9.10E+30	-3.7	127138.0
	H2	Enhanced by	2.000E+00	
	CO	Enhanced by	2.000E+00	
	CO2	Enhanced by	3.000E+00	
	H2O	Enhanced by	5.000E+00	
204.	$CH_3+C=C_2H_2+H$	5.00E+13	0.0	0.0
205.	$CH_2+CH=C_2H_2+H$	4.00E+13	0.0	0.0
206.	$CH_2+CH_2=C_2H_2+H+H$	7.00E+13	0.0	8.0
207.	$CH_2+CH_2=C_2H_2+H_2$	1.80E+13	0.0	8.0

208. $C_2H_2+O=HCCO+H$	1.40E+07	2.0	1900.0
209. $C_2H_2+O=CH_2+CO$	6.10E+06	2.0	1900.0
210. $C_2H_2+O=C_2H+OH$	3.20E+15	-0.6	15000.0
211. $C_2H_2+OH=CH_3+CO$	1.30E+09	0.7	2579.0
212. $C_2H_2+OH=HCCOH+H$	2.40E+06	2.0	12713.0
213. $C_2H_2+OH=CH_2CO+H$	7.50E+06	1.6	2106.0
214. $C_2H_2+HO_2=CH_2O+HCO$	3.00E+12	0.0	10000.0
215. $C_2H_2+HO_2=CH_2CHO+O$	3.00E+12	0.0	10000.0
216. $C_2H_2+O_2=HCO+HCO$	2.20E+07	1.5	33100.0
217. $C_2H_2+CH_2(S)=C_2H_2+CH_2$	4.00E+13	0.0	0.0
218. $H_2CC=C_2H_2$	1.00E+07	0.0	0.0
219. $H_2CC+H=C_2H_2+H$	1.00E+14	0.0	0.0
220. $H_2CC+OH=CH_2CO+H$	2.00E+13	0.0	0.0
221. $H_2CC+O_2=CH_2+CO_2$	1.00E+13	0.0	0.0
222. $C_2+H_2=C_2H+H$	4.00E+05	2.4	1000.0
223. $CH_2+C=C_2H+H$	5.00E+13	0.0	0.0
224. $C_2H+O=CH+CO$	5.00E+13	0.0	0.0
225. $C_2H+OH=HCCO+H$	2.00E+13	0.0	0.0
226. $C_2H+OH=C_2+H_2O$	4.00E+07	2.0	8000.0
227. $C_2H+H_2=C_2H_2+H$	4.10E+05	2.4	864.0
228. $C_2H+O_2=CO+CO+H$	4.70E+13	-0.2	0.0
229. $C_2H+CH_4=CH_3+C_2H_2$	7.20E+12	0.0	976.0
230. $C_2+M=C+C+M$	1.50E+16	0.0	142300.0

231. C2+O=C+CO	1.00E+14	0.0	0.0
232. C2+OH=C2O+H	5.00E+13	0.0	0.0
233. C2+O2=CO+CO	9.00E+12	0.0	980.0
234. CH3CHO(+M)=CH3+HCO(+M)	4.30E+22	-1.9	85480.0

Low pressure limit: 0.22200E+77 -0.11810E+02 0.95040E+05

TROE centering: 0.23000E+00 0.80000E+02 0.70000E+04 0.10000E+31

235. CH3CHO+H=CH3CO+H2	4.70E+13	-0.3	3000.0
236. CH3CHO+H=CH2CHO+H2	1.90E+12	0.4	5359.0
237. CH3CHO+O=CH3CO+OH	1.80E+18	-1.9	2975.0
238. CH3CHO+O=CH2CHO+OH	3.70E+13	-0.2	3556.0
239. CH3CHO+OH=CH3CO+H2O	2.40E+11	0.3	-1000.0
240. CH3CHO+OH=CH2CHO+H2O	3.00E+13	-0.6	800.0
241. CH3CHO+HO2=CH3CO+H2O2	2.40E+19	-2.2	14030.0
242. CH3CHO+HO2=CH2CHO+H2O2	2.30E+11	0.4	14864.0
243. CH3CHO+O2=CH3CO+HO2	1.20E+05	2.5	37554.0
244. CH3CHO+CH3=CH3CO+CH4	3.90E-07	5.8	2200.0
245. CH3CHO+CH3=CH2CHO+CH4	2.50E+01	3.1	5727.0
246. CH2CHO=CH2CO+H	2.40E+25	-4.8	43424.0
247. CH2CHO=CH3+CO	1.20E+30	-6.1	41332.0
248. CH2CHO+H=CH3+HCO	1.00E+14	0.0	0.0
249. CH2CHO+H=CH3CO+H	3.00E+13	0.0	0.0
250. CH2CHO+H=CH2CO+H2	2.00E+13	0.0	0.0
251. CH2CHO+O=CH2CO+OH	5.00E+13	0.0	0.0

252. CH ₂ CHO+OH=CH ₂ CO+H ₂ O	2.00E+13	0.0	0.0
253. CH ₂ CHO+OH=CH ₂ OH+HCO	1.00E+13	0.0	0.0
254. CH ₂ CHO+O ₂ =CH ₂ O+CO+OH	5.70E+17	-1.8	11067.0
255. CH ₂ CHO+CH ₃ =C ₂ H ₅ +CO+H	4.90E+14	-0.5	0.0
256. CH ₂ CHO+HO ₂ =CH ₂ O+HCO+OH	7.00E+12	-0.5	0.0
257. CH ₂ CHO+HO ₂ =CH ₃ CHO+O ₂	3.00E+12	-0.5	0.0
258. CH ₂ CHO+CH ₂ =C ₂ H ₄ +HCO	5.00E+13	0.0	0.0
259. CH ₂ CHO+CH=C ₂ H ₃ +HCO	1.00E+14	0.0	0.0
260. CH ₃ CO=CH ₃ +CO	6.90E+14	-2.0	14584.0
261. CH ₂ CO+H=CH ₃ CO	2.30E+08	1.6	2627.0
262. CH ₃ CO+H=CH ₃ +HCO	2.10E+13	0.0	0.0
263. CH ₃ CO+H=CH ₂ CO+H ₂	1.20E+13	0.0	0.0
264. CH ₃ CO+O=CH ₃ +CO ₂	1.60E+14	0.0	0.0
265. CH ₃ CO+O=CH ₂ CO+OH	5.30E+13	0.0	0.0
266. CH ₃ CO+OH=CH ₂ CO+H ₂ O	1.20E+13	0.0	0.0
267. CH ₃ CO+CH ₃ =C ₂ H ₆ +CO	3.30E+13	0.0	0.0
268. CH ₃ CO+CH ₃ =CH ₂ CO+CH ₄	5.30E+13	0.0	0.0
269. CH ₃ CO+O ₂ =CH ₂ O+CO+OH	1.90E+12	0.0	0.0
270. CH ₂ +CO(+M)=CH ₂ CO(+M)	8.10E+11	0.5	4510.0

Low pressure limit: 0.26900E+34 -0.51100E+01 0.70950E+04

TROE centering: 0.59070E+00 0.27500E+03 0.12260E+04 0.51850E+04

N₂ Enhanced by 1.000E+00

H₂O Enhanced by 6.000E+00

AR	Enhanced by	7.000E-01		
271. CH ₂ CO+H=CH ₃ +CO		3.30E+10	0.9	2840.0
272. CH ₂ CO+H=HCCO+H ₂		3.00E+07	2.0	10000.0
273. CH+CH ₂ O=CH ₂ CO+H		9.50E+13	0.0	-517.0
274. CH ₂ CO+O=CO ₂ +CH ₂		1.80E+12	0.0	1350.0
275. CH ₂ CO+O=HCCO+OH		2.00E+07	2.0	10000.0
276. CH ₂ CO+OH=CH ₂ OH+CO		1.00E+12	0.0	-1013.0
277. CH ₂ CO+OH=CH ₃ +CO ₂		6.70E+11	0.0	-1013.0
278. CH ₂ CO+OH=HCCO+H ₂ O		1.00E+07	2.0	3000.0
279. CH ₂ CO+CH ₂ (S)=C ₂ H ₄ +CO		1.60E+14	0.0	0.0
280. HCCOH+H=HCCO+H ₂		3.00E+07	2.0	1000.0
281. HCCOH+O=HCCO+OH		2.00E+07	2.0	1900.0
282. HCCOH+OH=HCCO+H ₂ O		1.00E+07	2.0	1000.0
283. CH+CO(+M)=HCCO(+M)		5.00E+13	0.0	0.0

Low pressure limit: 0.27000E+29 -0.37400E+01 0.19360E+04

TROE centering: 0.57570E+00 0.23700E+03 0.16520E+04 0.50690E+04

N₂ Enhanced by 1.000E+00

H₂O Enhanced by 6.000E+00

AR Enhanced by 7.000E-01

H₂ Enhanced by 2.000E+00

CH₄ Enhanced by 2.000E+00

CO Enhanced by 1.500E+00

CO₂ Enhanced by 2.000E+00

C2H6	Enhanced by	3.000E+00			
284. HCCO+H=CH2(S)+CO	1.50E+14	0.0	0.0	[99]	
285. HCCO+O=CO+CO+H	1.00E+14	0.0	0.0		
286. HCCO+OH=HCO+HCO	1.00E+13	0.0	0.0		
287. HCCO+OH=C2O+H2O	6.00E+13	0.0	0.0		
288. HCCO+O2=CO2+CO+H	4.90E+12	-0.1	1150.0		
289. HCCO+O2=CO+CO+OH	1.60E+11	0.0	1020.0		
290. HCCO+O2=HCO+CO+O	2.20E+02	2.7	3540.0		
291. HCCO+CH2=C2H3+CO	3.00E+13	0.0	0.0		
292. HCCO+CH=C2H2+CO	5.00E+13	0.0	0.0		
293. HCCO+HCCO=C2H2+CO+CO	1.00E+13	0.0	0.0		
294. C2O+M=C+CO+M	2.00E+15	0.0	44200.0		
295. C2O+H=CH+CO	1.30E+13	0.0	0.0		
296. C2O+O=CO+CO	5.20E+13	0.0	0.0		
297. C2O+OH=CO+CO+H	2.00E+13	0.0	0.0		
298. C2O+O2=CO+CO+O	1.00E+13	0.0	2600.0		
299. C2O+O2=CO+CO2	1.00E+13	0.0	2600.0		
300. C2O+C=CO+C2	1.00E+14	0.0	0.0		
301. OCHCHO(+M)=CO+CO+H2(+M)	1.10E+14	0.0	55000.0		
Low pressure limit: 0.26000E+17 0.00000E+00 0.38400E+05					
302. OCHCHO+H=CH2O+HCO	3.00E+13	0.0	0.0		
303. OCHCHO+OH=>HCO+CO+H2O	4.00E+06	2.0	-1630.0		
304. HNO+H=NO+H2	4.40E+11	0.7	650.0		

305. HNO+O=NO+OH	2.30E+13	0.0	0.0
306. HNO+OH=NO+H2O	3.60E+13	0.0	0.0
307. HNO+O2=HO2+NO	2.00E+13	0.0	16000.0
308. HNO+HNO=N2O+H2O	9.00E+08	0.0	3100.0
309. HNO+NO2=HONO+NO	4.40E+04	2.6	4040.0
310. NO+H(+M)=HNO(+M)	1.50E+15	-0.4	0.0

Low pressure limit: 0.24000E+15 0.20600E+00 -0.15500E+04

TROE centering: 0.82000E+00 0.10000E-29 0.10000E+31 0.10000E+31

N2 Enhanced by 1.600E+00

311. NO+O(+M)=NO2(+M)	1.30E+15	-0.8	0.0
-----------------------	----------	------	-----

Low pressure limit: 0.47200E+25 -0.28700E+01 0.15500E+04

TROE centering: 0.88000E+00 0.10000E+04 0.10000E+05 0.10000E+31

AR Enhanced by 0.000E+00

312. NO+O(+AR)=NO2(+AR)	1.30E+15	-0.8	0.0
-------------------------	----------	------	-----

Low pressure limit: 0.75600E+20 -0.14100E+01 0.00000E+00

TROE centering: 0.75000E+00 0.10000E+04 0.10000E+06 0.10000E+31

313. NO+OH(+M)=HONO(+M)	1.10E+14	-0.3	0.0
-------------------------	----------	------	-----

Low pressure limit: 0.33920E+24 -0.25000E+01 0.00000E+00

TROE centering: 0.75000E+00 0.10000E-29 0.10000E+31 0.10000E+31

314. NO+HO2=NO2+OH	2.10E+12	0.0	-497.0
--------------------	----------	-----	--------

315. NO2+H=NO+OH	1.30E+14	0.0	362.0
------------------	----------	-----	-------

316. NO2+O=NO+O2	1.10E+14	-0.5	0.0
------------------	----------	------	-----

317. NO2+O(+M)=NO3(+M)	3.50E+12	0.2	0.0
------------------------	----------	-----	-----

Low pressure limit: 0.25000E+21 -0.15000E+01 0.00000E+

TROE centering: 0.71000E+00 0.10000E-29 0.17000E+04 0.10000E+31

318. NO₂+OH(+M)=HONO₂(+M) 3.00E+13 0.0 0.0

Low pressure limit: 0.29380E+26 -0.30000E+01 0.00000E+00

TROE centering: 0.40000E+00 0.10000E-29 0.10000E+31 0.10000E+31

319. NO₂+HO₂=HONO+O₂ 1.90E+00 3.3 3044.0

320. NO₂+HO₂=HNO₂+O₂ 1.90E+01 3.3 4983.0

321. NO₂+H₂=HONO+H 1.30E+04 2.8 29770.0

322. NO₂+H₂=HNO₂+H 2.40E+00 3.7 32400.0

323. NO₂+NO₂=NO+NO+O₂ 4.50E+12 0.0 27599.0

324. NO₂+NO₂=NO₃+NO 9.60E+09 0.7 20900.0

325. HONO+H=HNO+OH 5.60E+10 0.9 5000.0

326. HONO+H=NO+H₂O 8.10E+06 1.9 3850.0

327. HONO+O=NO₂+OH 1.20E+13 0.0 5960.0

328. HONO+OH=NO₂+H₂O 1.70E+12 0.0 -520.0

329. HONO+NO₂=HONO₂+NO 2.00E+11 0.0 32700.0

330. HONO+HONO=NO+NO₂+H₂O 3.50E-01 3.6 12140.0

331. HNO₂(+M)=HONO(+M) 2.50E+14 0.0 32300.0

Low pressure limit: 0.31000E+19 0.00000E+00 0.31500E+05

TROE centering: 0.11490E+01 0.10000E-29 0.31250E+04 0.10000E+31

332. HNO₂+O=NO₂+OH 1.70E+08 1.5 2000.0

333. HNO₂+OH=NO₂+H₂O 4.00E+13 0.0 0.0

334. NO₃+H=NO₂+OH 6.00E+13 0.0 0.0

335. $\text{NO}_3+\text{O}=\text{NO}_2+\text{O}_2$	1.00E+13	0.0	0.0
336. $\text{NO}_3+\text{OH}=\text{NO}_2+\text{HO}_2$	1.40E+13	0.0	0.0
337. $\text{NO}_3+\text{HO}_2=\text{NO}_2+\text{O}_2+\text{OH}$	1.50E+12	0.0	0.0
338. $\text{NO}_3+\text{NO}_2=\text{NO}+\text{NO}_2+\text{O}_2$	5.00E+10	0.0	2940.0
339. $\text{HONO}_2+\text{H}=\text{H}_2+\text{NO}_3$	5.60E+08	1.5	16400.0
340. $\text{HONO}_2+\text{H}=\text{H}_2\text{O}+\text{NO}_2$	6.10E+01	3.3	6285.0
341. $\text{HONO}_2+\text{H}=\text{OH}+\text{HONO}$	3.80E+05	2.3	6976.0
342. $\text{HONO}_2+\text{OH}=\text{H}_2\text{O}+\text{NO}_3$	1.00E+10	0.0	-1240.0
343. $\text{N}_2\text{O}(+\text{M})=\text{N}_2+\text{O}(+\text{M})$	1.30E+12	0.0	62570.0
Low pressure limit: 0.40000E+15 0.00000E+00 0.56600E+05			
N2	Enhanced by	1.700E+00	
O2	Enhanced by	1.400E+00	
CO2	Enhanced by	3.000E+00	
H2O	Enhanced by	1.200E+01	
344. $\text{N}_2\text{O}+\text{H}=\text{N}_2+\text{OH}$	3.30E+10	0.0	4729.0
Declared duplicate reaction...			
345. $\text{N}_2\text{O}+\text{H}=\text{N}_2+\text{OH}$	4.40E+14	0.0	19254.0
Declared duplicate reaction...			
346. $\text{N}_2\text{O}+\text{O}=\text{NO}+\text{NO}$	9.20E+13	0.0	27679.0
347. $\text{N}_2\text{O}+\text{O}=\text{N}_2+\text{O}_2$	3.70E+12	0.0	15936.0
348. $\text{N}_2\text{O}+\text{OH}=\text{N}_2+\text{HO}_2$	1.30E-02	4.7	36560.0
349. $\text{N}_2\text{O}+\text{OH}=\text{HNO}+\text{NO}$	1.20E-04	4.3	25080.0
350. $\text{N}_2\text{O}+\text{NO}=\text{NO}_2+\text{N}_2$	5.30E+05	2.2	46280.0

351. $\text{NH}_3+\text{M}=\text{NH}_2+\text{H}+\text{M}$	2.20E+16	0.0	93470.0
352. $\text{NH}_3+\text{H}=\text{NH}_2+\text{H}_2$	6.40E+05	2.4	10171.0
353. $\text{NH}_3+\text{O}=\text{NH}_2+\text{OH}$	9.40E+06	1.9	6460.0
354. $\text{NH}_3+\text{OH}=\text{NH}_2+\text{H}_2\text{O}$	2.00E+06	2.0	566.0
355. $\text{NH}_3+\text{HO}_2=\text{NH}_2+\text{H}_2\text{O}_2$	3.00E+11	0.0	22000.0
356. $\text{NH}_2+\text{H}=\text{NH}+\text{H}_2$	7.20E+05	2.3	799.0
357. $\text{NH}_2+\text{O}=\text{HNO}+\text{H}$	6.60E+13	0.0	0.0
358. $\text{NH}_2+\text{O}=\text{NH}+\text{OH}$	7.00E+12	0.0	0.0
Declared duplicate reaction...			
359. $\text{NH}_2+\text{O}=\text{NH}+\text{OH}$	8.60E-01	4.0	1673.0
Declared duplicate reaction...			
360. $\text{NH}_2+\text{OH}=\text{NH}+\text{H}_2\text{O}$	4.00E+06	2.0	1000.0
361. $\text{NH}_2+\text{HO}_2=\text{H}_2\text{NO}+\text{OH}$	5.00E+13	0.0	0.0
362. $\text{NH}_2+\text{HO}_2=\text{NH}_3+\text{O}_2$	9.20E+05	1.9	-1152.0
363. $\text{NH}_2+\text{O}_2=\text{H}_2\text{NO}+\text{O}$	2.50E+11	0.5	29586.0
364. $\text{NH}_2+\text{O}_2=\text{HNO}+\text{OH}$	6.20E+07	1.2	35100.0
365. $\text{NH}_2+\text{NH}_2=\text{NH}_3+\text{NH}$	5.00E+13	0.0	10000.0
366. $\text{NH}_2+\text{NH}=\text{N}_2\text{H}_2+\text{H}$	5.00E+13	0.0	0.0
367. $\text{NH}_2+\text{NH}=\text{NH}_3+\text{N}$	9.20E+05	1.9	2444.0
368. $\text{NH}_2+\text{N}=\text{N}_2+\text{H}+\text{H}$	7.00E+13	0.0	0.0
369. $\text{NH}_2+\text{HNO}=\text{NH}_3+\text{NO}$	3.60E+06	1.6	-1250.0
370. $\text{NH}_2+\text{NO}=\text{N}_2+\text{H}_2\text{O}$	2.80E+20	-2.7	1258.0
371. $\text{NH}_2+\text{NO}=\text{NNH}+\text{OH}$	2.30E+10	0.4	-814.0

372. $\text{NH}_2 + \text{HONO} = \text{NH}_3 + \text{NO}_2$	7.10E+01	3.0	-4940.0
373. $\text{NH}_2 + \text{NO}_2 = \text{N}_2\text{O} + \text{H}_2\text{O}$	1.60E+16	-1.4	268.0
374. $\text{NH}_2 + \text{NO}_2 = \text{H}_2\text{NO} + \text{NO}$	6.50E+16	-1.4	268.0
375. $\text{NH} + \text{H} = \text{N} + \text{H}_2$	3.00E+13	0.0	0.0
376. $\text{NH} + \text{O} = \text{NO} + \text{H}$	9.20E+13	0.0	0.0
377. $\text{NH} + \text{OH} = \text{HNO} + \text{H}$	2.00E+13	0.0	0.0
378. $\text{NH} + \text{OH} = \text{N} + \text{H}_2\text{O}$	5.00E+11	0.5	2000.0
379. $\text{NH} + \text{O}_2 = \text{HNO} + \text{O}$	4.60E+05	2.0	6500.0
380. $\text{NH} + \text{O}_2 = \text{NO} + \text{OH}$	1.30E+06	1.5	100.0
381. $\text{NH} + \text{NH} = \text{N}_2 + \text{H} + \text{H}$	2.50E+13	0.0	0.0
382. $\text{NH} + \text{N} = \text{N}_2 + \text{H}$	3.00E+13	0.0	0.0
383. $\text{NH} + \text{NO} = \text{N}_2\text{O} + \text{H}$	2.90E+14	-0.4	0.0
Declared duplicate reaction...			
384. $\text{NH} + \text{NO} = \text{N}_2\text{O} + \text{H}$	-2.2E13	-0.2	0.0
Declared duplicate reaction...			
385. $\text{NH} + \text{NO} = \text{N}_2 + \text{OH}$	2.20E+13	-0.2	0.0
386. $\text{NH} + \text{HONO} = \text{NH}_2 + \text{NO}_2$	1.00E+13	0.0	0.0
387. $\text{NH} + \text{NO}_2 = \text{N}_2\text{O} + \text{OH}$	1.00E+13	0.0	0.0
388. $\text{N} + \text{OH} = \text{NO} + \text{H}$	3.80E+13	0.0	0.0
389. $\text{N} + \text{O}_2 = \text{NO} + \text{O}$	6.40E+09	1.0	6280.0
390. $\text{N} + \text{NO} = \text{N}_2 + \text{O}$	2.10E+13	0.0	0.0
391. $\text{NNH} = \text{N}_2 + \text{H}$	6.50E+07	0.0	0.0
392. $\text{NNH} + \text{H} = \text{N}_2 + \text{H}_2$	1.00E+14	0.0	0.0

393. NNH+O=N2O+H	1.00E+14	0.0	0.0
394. NNH+O=N2+OH	8.00E+13	0.0	0.0
395. NNH+O=NH+NO	5.00E+13	0.0	0.0
396. NNH+OH=N2+H2O	5.00E+13	0.0	0.0
397. NNH+O2=N2+HO2	2.00E+14	0.0	0.0
398. NNH+O2=N2+H+O2	5.00E+13	0.0	0.0
399. NNH+NH=N2+NH2	5.00E+13	0.0	0.0
400. NNH+NH2=N2+NH3	5.00E+13	0.0	0.0
401. NNH+NO=N2+HNO	5.00E+13	0.0	0.0
402. NH2+NH2=N2H4	5.60E+48	-11.3	11882.0
403. N2H4+H=N2H3+H2	7.00E+12	0.0	2500.0
404. N2H4+O=NH2OH+NH	2.90E+11	0.0	-1270.0
405. N2H4+O=N2H3+OH	1.50E+11	0.0	-1270.0
406. N2H4+OH=N2H3+H2O	1.30E+13	0.0	-318.0
407. N2H4+NH2=N2H3+NH3	3.90E+12	0.0	1500.0
408. N2H3=N2H2+H	3.60E+47	-10.4	69009.0
409. NH2+NH2=N2H3+H	1.20E+12	0.0	10084.0
410. N2H3+H=N2H2+H2	2.40E+08	1.5	-10.0
411. N2H3+O=N2H2+OH	1.70E+08	1.5	-646.0
412. N2H3+O=NH2+HNO	3.00E+13	0.0	0.0
413. N2H3+O=>NH2+NO+H	3.00E+13	0.0	0.0
414. N2H3+OH=N2H2+H2O	1.20E+06	2.0	-1192.0
415. N2H3+OH=H2NN+H2O	3.00E+13	0.0	0.0

416.	$N_2H_3+OH=NH_3+HNO$	1.00E+12	0.0	15000.0
417.	$N_2H_3+HO_2=N_2H_2+H_2O_2$	1.40E+04	2.7	-1600.0
418.	$N_2H_3+HO_2=N_2H_4+O_2$	9.20E+05	1.9	2126.0
419.	$N_2H_3+NH_2=N_2H_2+NH_3$	9.20E+05	1.9	-1152.0
420.	$N_2H_3+NH_2=H_2NN+NH_3$	3.00E+13	0.0	0.0
421.	$N_2H_3+NH=N_2H_2+NH_2$	2.00E+13	0.0	0.0
422.	$N_2H_2+M=NNH+H+M$	1.90E+27	-3.0	66107.0
	H2O Enhanced by 7.000E+00			
423.	$N_2H_2+H=NNH+H_2$	8.50E+04	2.6	230.0
424.	$N_2H_2+O=NNH+OH$	3.30E+08	1.5	497.0
425.	$N_2H_2+O=NH_2+NO$	1.00E+13	0.0	0.0
426.	$N_2H_2+OH=NNH+H_2O$	5.90E+01	3.4	1360.0
427.	$N_2H_2+NH_2=NNH+NH_3$	8.80E-02	4.0	1610.0
428.	$N_2H_2+NH=NNH+NH_2$	2.40E+06	2.0	-1192.0
429.	$N_2H_2+NO=N_2O+NH_2$	4.00E+12	0.0	11922.0
430.	$NH_2+NH_2=H_2NN+H_2$	1.20E+21	-3.1	3368.0
431.	$H_2NN=NNH+H$	3.40E+26	-4.8	46228.0
432.	$H_2NN+H=NNH+H_2$	4.80E+08	1.5	-894.0
433.	$H_2NN+H=N_2H_2+H$	7.00E+13	0.0	0.0
434.	$H_2NN+O=NNH+OH$	3.30E+08	1.5	-894.0
435.	$H_2NN+O=NH_2+NO$	7.00E+13	0.0	0.0
436.	$H_2NN+OH=NNH+H_2O$	2.40E+06	2.0	-1192.0
437.	$H_2NN+OH=>NH_2+NO+H$	2.00E+12	0.0	0.0

438. $\text{H}_2\text{NN}+\text{HO}_2\Rightarrow\text{NH}_2+\text{NO}+\text{OH}$	9.00E+12	0.0	0.0
439. $\text{H}_2\text{NN}+\text{HO}_2=\text{NNH}+\text{H}_2\text{O}_2$	2.90E+04	2.7	-1600.0
440. $\text{H}_2\text{NN}+\text{O}_2=\text{NH}_2+\text{NO}_2$	1.50E+12	0.0	5961.0
441. $\text{H}_2\text{NN}+\text{NH}_2=\text{NNH}+\text{NH}_3$	1.80E+06	1.9	-1152.0
442. $\text{H}_2\text{NO}+\text{M}=\text{HNO}+\text{H}+\text{M}$	2.80E+24	-2.8	64915.0
H2O Enhanced by	1.000E+01		
443. $\text{H}_2\text{NO}+\text{M}=\text{HNOH}+\text{M}$	1.10E+29	-4.0	44000.0
H2O Enhanced by	1.000E+01		
444. $\text{H}_2\text{NO}+\text{H}=\text{HNO}+\text{H}_2$	3.00E+07	2.0	2000.0
445. $\text{H}_2\text{NO}+\text{H}=\text{NH}_2+\text{OH}$	5.00E+13	0.0	0.0
446. $\text{H}_2\text{NO}+\text{O}=\text{HNO}+\text{OH}$	3.00E+07	2.0	2000.0
447. $\text{H}_2\text{NO}+\text{OH}=\text{HNO}+\text{H}_2\text{O}$	1.00E+14	0.0	0.0
448. $\text{H}_2\text{NO}+\text{HO}_2=\text{HNO}+\text{H}_2\text{O}_2$	2.90E+04	2.7	-1600.0
449. $\text{H}_2\text{NO}+\text{O}_2=\text{HNO}+\text{HO}_2$	3.00E+12	0.0	25000.0
450. $\text{H}_2\text{NO}+\text{NH}_2=\text{HNO}+\text{NH}_3$	3.00E+12	0.0	1000.0
451. $\text{H}_2\text{NO}+\text{NO}=\text{HNO}+\text{HNO}$	2.00E+04	2.0	13000.0
452. $\text{H}_2\text{NO}+\text{NO}_2=\text{HONO}+\text{HNO}$	6.00E+11	0.0	2000.0
453. $\text{HNOH}+\text{M}=\text{HNO}+\text{H}+\text{M}$	2.00E+24	-2.8	58934.0
H2O Enhanced by	1.000E+01		
454. $\text{HNOH}+\text{H}=\text{NH}_2+\text{OH}$	4.00E+13	0.0	0.0
455. $\text{HNOH}+\text{H}=\text{HNO}+\text{H}_2$	4.80E+08	1.5	378.0
456. $\text{HNOH}+\text{O}=\text{HNO}+\text{OH}$	7.00E+13	0.0	0.0

Declared duplicate reaction...

457. HNOH+O=HNO+OH	3.30E+08	1.5	-358.0
Declared duplicate reaction...			
458. HNOH+OH=HNO+H2O	2.40E+06	2.0	-1192.0
459. HNOH+HO2=HNO+H2O2	2.90E+04	2.7	-1600.0
460. HNOH+O2=HNO+HO2	3.00E+12	0.0	25000.0
461. HNOH+NH2=N2H3+OH	1.00E+01	3.5	-467.0
462. HNOH+NH2=H2NN+H2O	8.80E+16	-1.1	1113.0
463. HNOH+NH2=NH3+HNO	1.80E+06	1.9	-1152.0
464. HNOH+NO2=HONO+HNO	6.00E+11	0.0	2000.0
465. HCN+M=H+CN+M	3.40E+35	-5.1	133000.0
N2	Enhanced by	0.000E+00	
O2	Enhanced by	1.500E+00	
H2O	Enhanced by	1.000E+01	
466. HCN+N2=H+CN+N2	3.60E+26	-2.6	124890.0
467. HCN+M=HNC+M	1.60E+26	-3.2	54600.0
AR	Enhanced by	7.000E-01	
H2O	Enhanced by	7.000E+00	
CO2	Enhanced by	2.000E+00	
468. CN+H2=HCN+H	1.10E+05	2.6	1908.0
469. HCN+O=NCO+H	1.40E+04	2.6	4980.0
470. HCN+O=CN+OH	4.20E+10	0.4	20665.0
471. HCN+O=NH+CO	3.50E+03	2.6	4980.0
472. HCN+OH=CN+H2O	3.90E+06	1.8	10300.0

473. HCN+OH=HOCN+H	5.90E+04	2.4	12500.0
474. HCN+OH=HNCO+H	2.00E-03	4.0	1000.0
475. HCN+OH=NH ₂ +CO	7.80E-04	4.0	4000.0
476. HCN+O ₂ =CN+HO ₂	3.00E+13	0.0	75100.0
477. HCN+CN=NCCN+H	1.50E+07	1.7	1530.0
478. HNC+H=HCN+H	7.80E+13	0.0	3600.0
479. HNC+O=NH+CO	4.60E+12	0.0	2200.0
480. HNC+OH=HNCO+H	2.80E+13	0.0	3700.0
481. HNC+CN=NCCN+H	1.00E+13	0.0	0.0
482. CN+O=CO+N	1.90E+12	0.5	723.0
483. CN+OH=NCO+H	1.00E+15	-0.4	0.0
484. CN+O ₂ =NCO+O	7.20E+12	0.0	-417.0
Declared duplicate reaction...			
485. CN+O ₂ =NCO+O	-2.8E17	-2.0	0.0
Declared duplicate reaction...			
486. CN+O ₂ =NO+CO	2.80E+17	-2.0	0.0
487. CN+NO=NCO+N	9.60E+13	0.0	42100.0
488. CN+NO ₂ =NCO+NO	5.30E+15	-0.8	344.0
489. CN+NO ₂ =CO+N ₂ O	4.90E+14	-0.8	344.0
490. CN+NO ₂ =N ₂ +CO ₂	3.70E+14	-0.8	344.0
491. CN+HNO=HCN+NO	1.80E+13	0.0	0.0
492. CN+HONO=HCN+NO ₂	1.20E+13	0.0	0.0
493. CN+N ₂ O=NCN+NO	3.80E+03	2.6	3700.0

494. CN+HNCO=HCN+NCO	1.00E+13	0.0	0.0
495. CN+NCO=NCN+CO	1.80E+13	0.0	0.0
496. HNCO+M=CO+NH+M	1.10E+16	0.0	86000.0
N2	Enhanced by	1.500E+00	
497. HNCO+H=NH2+CO	3.60E+04	2.5	2345.0
498. HNCO+H=NCO+H2	9.00E+07	1.7	13900.0
499. HNCO+O=NCO+OH	2.20E+06	2.1	11430.0
500. HNCO+O=NH+CO2	9.60E+07	1.4	8520.0
501. HNCO+O=HNO+CO	1.50E+08	1.6	44012.0
502. HNCO+OH=NCO+H2O	3.60E+07	1.5	3600.0
503. HNCO+HO2=NCO+H2O2	3.00E+11	0.0	22000.0
504. HNCO+O2=HNO+CO2	1.00E+12	0.0	35000.0
505. HNCO+NH=NH2+NCO	3.00E+13	0.0	23700.0
506. HOCN+H=HNCO+H	3.10E+08	0.8	1917.0
507. HOCN+H=NH2+CO	1.20E+08	0.6	2076.0
508. HOCN+H=H2+NCO	2.40E+08	1.5	6617.0
509. HOCN+O=OH+NCO	1.70E+08	1.5	4133.0
510. HOCN+OH=H2O+NCO	1.20E+06	2.0	-248.0
511. HOCN+NH2=NCO+NH3	9.20E+05	1.9	3646.0
512. HCNO=HCN+O	2.00E+30	-6.0	60733.0
513. HCNO+H=HCN+OH	7.20E+10	0.8	8612.0
514. HCNO+O=HCO+NO	6.30E+13	0.0	0.0
515. HCNO+OH=CH2O+NO	1.00E+12	0.0	0.0

516. HCNO+O=NCO+OH	7.00E+12	0.0	0.0
517. HCNO+OH=NO+CO+H2	6.50E+12	0.0	0.0
518. HCNO+OH=NCO+H+OH	4.50E+12	0.0	0.0
519. HCNO+OH=NCO+H2O	3.50E+12	0.0	0.0
520. HCNO+OH=HCO+HNO	4.50E+12	0.0	0.0
521. HCNO+CN=HCN+NCO	6.00E+13	0.0	0.0
522. NCO+M=N+CO+M	2.20E+14	0.0	54050.0
N2	Enhanced by	1.500E+00	
523. NCO+H=CO+NH	7.20E+13	0.0	1000.0
524. NCO+O=NO+CO	2.00E+15	-0.5	0.0
525. NCO+OH=HON+CO	5.30E+12	-0.1	5126.0
526. NCO+OH=H+CO+NO	8.30E+12	-0.1	18042.0
527. NCO+HO2=HNCO+O2	2.00E+13	0.0	0.0
528. NCO+O2=NO+CO2	1.00E+13	0.0	10000.0
529. NCO+NO=N2O+CO	4.00E+19	-2.2	1743.0
530. NCO+NO=N2+CO2	1.50E+21	-2.7	1824.0
531. NCO+NO2=CO+NO+NO	2.50E+11	0.0	-707.0
532. NCO+NO2=CO2+N2O	3.00E+12	0.0	-707.0
533. NCO+HNO=HNCO+NO	1.80E+13	0.0	0.0
534. NCO+HONO=HNCO+NO2	3.60E+12	0.0	0.0
535. NCO+NH3=HNCO+NH2	2.80E+04	2.5	980.0
536. NCO+N=N2+CO	2.00E+13	0.0	0.0
537. NCO+NCO=CO+CO+N2	1.80E+13	0.0	0.0

538. CO+NO ₂ =NO+CO ₂	9.00E+13	0.0	33800.0
539. CO+N ₂ O=N ₂ +CO ₂	2.70E+11	0.0	20237.0
540. HOCO+NO=CO+HONO	1.50E+12	0.0	0.0
541. CH ₂ O+NO ₂ =HONO+HCO	1.40E-07	5.6	9220.0
542. CH ₂ O+NO ₂ =HNO ₂ +HCO	1.10E-01	4.2	19850.0
543. HCO+NO=HNO+CO	6.90E+12	0.0	0.0
544. HCO+NO ₂ =NO+CO ₂ +H	2.30E+13	0.0	0.0
545. HCO+NO ₂ =HONO+CO	5.00E+12	0.0	0.0
546. HCO+NO ₂ =NO+CO+OH	5.00E+12	0.0	0.0
547. HCO+HNO=NO+CH ₂ O	5.80E-01	3.8	115.0
548. CH ₄ +NO ₂ =HONO+CH ₃	6.50E+14	0.0	45800.0
549. CH ₄ +NO ₂ =HNO ₂ +CH ₃	6.00E+14	0.0	37600.0
550. CH ₃ +NO(+M)=CH ₃ NO(+M)	9.00E+12	0.0	192.0

Low pressure limit: 0.25000E+17 0.00000E+00 -0.28410E+04

TROE centering: 0.50000E+01 0.10000E-29 0.12000E+03 0.10000E+31

551. CH ₃ +NO ₂ =CH ₃ O+NO	1.10E+13	0.0	0.0
552. CH ₃ +HNO=NO+CH ₄	2.30E+14	0.0	8400.0
553. CH ₃ OH+NO ₂ =HONO+CH ₂ OH	1.50E+02	3.3	20035.0
554. CH ₃ OH+NO ₂ =HNO ₂ +CH ₂ OH	2.40E+03	2.9	27470.0
555. CH ₃ O+NO=HNO+CH ₂ O	7.50E+12	0.0	2017.0

Declared duplicate reaction...

556. CH ₃ O+NO=HNO+CH ₂ O	2.50E+18	-2.6	0.0
---	----------	------	-----

Declared duplicate reaction...

557. CH ₃ O+HNO=NO+CH ₃ OH	3.20E+13	0.0	0.0
558. CH ₂ OH+NO=CH ₂ O+HNO	1.30E+12	0.0	0.0
559. CH ₂ OH+NO ₂ =HONO+CH ₂ O	5.00E+12	0.0	0.0
560. CH ₂ OH+HNO=NO+CH ₃ OH	3.00E+13	0.0	0.0
561. C ₂ H ₆ +NO ₂ =HONO+C ₂ H ₅	6.50E+14	0.0	41400.0
562. C ₂ H ₆ +NO ₂ =HNO ₂ +C ₂ H ₅	6.00E+14	0.0	33200.0
563. C ₂ H ₅ +NO ₂ =NO+CH ₃ CH ₂ O	4.00E+13	-0.2	0.0
564. C ₂ H ₄ +NO ₂ =HONO+C ₂ H ₃	6.50E+14	0.0	41400.0
565. C ₂ H ₄ +NO ₂ =HNO ₂ +C ₂ H ₃	6.00E+14	0.0	33200.0
566. C ₂ H ₃ +NO=C ₂ H ₂ +HNO	1.00E+12	0.0	1000.0
567. C ₂ H ₃ +NO ₂ =NO+CH ₂ CHO	7.70E+14	-0.6	0.0
568. CH ₂ CHO+NO ₂ =CH ₂ CO+HONO	8.90E+12	0.0	-159.0
569. CH ₃ CO+NO ₂ =>CH ₃ +CO ₂ +NO	1.50E+13	0.0	0.0
570. CO ₂ +CN=NCO+CO	3.70E+06	2.2	26900.0
571. CH ₂ O+CN=HCO+HCN	1.70E+03	2.7	-1427.0
572. CH ₂ O+NCO=HNCO+HCO	6.00E+12	0.0	0.0
573. HCO+NCO=HNCO+CO	3.60E+13	0.0	0.0
574. CH ₄ +NH ₂ =CH ₃ +NH ₃	1.50E+03	3.0	9940.0
575. CH ₄ +CN=CH ₃ +HCN	8.60E+05	2.3	-32.0
576. CH ₄ +NCO=CH ₃ +HNCO	9.80E+12	0.0	8120.0
577. CH ₃ +NH ₂ =CH ₃ NH ₂	1.30E+54	-12.7	15608.0
578. CH ₃ +NH ₂ =CH ₂ NH ₂ +H	1.10E+13	-0.1	9905.0
579. CH ₃ +NH ₂ =CH ₃ NH+H	1.20E+13	-0.1	16144.0

580. CH ₃ +NH ₂ =CH ₂ NH+H ₂	2.10E+11	-0.1	19095.0
581. CH ₃ +NH ₂ =CH ₄ +NH	2.80E+06	1.9	9210.0
582. CH ₃ +NH ₂ =CH ₂ +NH ₃	1.60E+06	1.9	7570.0
583. CH ₃ +NH=CH ₂ NH+H	4.00E+13	0.0	0.0
584. CH ₃ +NH=N+CH ₄	8.20E+05	1.9	5852.0
585. CH ₃ +N=H ₂ CN+H	7.10E+13	0.0	0.0
586. CH ₃ +N ₂ H ₂ =NNH+CH ₄	1.60E+06	1.9	2971.0
587. CH ₃ +H ₂ NN=CH ₄ +NNH	1.60E+06	1.9	129.0
588. CH ₃ +N ₂ H ₄ =N ₂ H ₃ +CH ₄	3.30E+06	1.9	5325.0
589. CH ₃ +N ₂ H ₃ =N ₂ H ₂ +CH ₄	8.20E+05	1.9	1818.0
590. CH ₃ +N ₂ H ₃ =H ₂ NN+CH ₄	3.00E+13	0.0	0.0
591. CH ₃ +NO=HCN+H ₂ O	1.50E-01	3.5	3950.0
592. CH ₃ +NO=H ₂ CN+OH	1.50E-01	3.5	3950.0
593. CH ₃ +H ₂ NO=CH ₃ O+NH ₂	2.00E+13	0.0	0.0
594. CH ₃ +H ₂ NO=CH ₄ +HNO	1.60E+06	1.9	2961.0
595. CH ₃ +CN=CH ₂ CN+H	1.00E+14	0.0	0.0
596. CH ₃ +HOCN=CH ₃ CN+OH	5.00E+12	0.0	2000.0
597. CH ₂ +N=HCN+H	5.00E+13	0.0	0.0
598. CH ₂ +NO=HCNO+H	3.10E+12	0.0	-378.0
599. CH ₂ +NO=HCN+OH	3.90E+11	0.0	-378.0
600. CH ₂ +NO ₂ =CH ₂ O+NO	5.90E+13	0.0	0.0
601. CH ₂ +N ₂ =HCN+NH	1.00E+13	0.0	74000.0
602. CH ₂ (S)+NO=HCN+OH	2.00E+13	0.0	0.0

603. CH ₂ (S)+NO=CH ₂ +NO	1.00E+14	0.0	0.0
604. CH ₂ (S)+N ₂ O=CH ₂ O+N ₂	3.80E+13	0.0	0.0
605. CH ₂ (S)+NH ₃ =CH ₂ NH ₂ +H	1.00E+14	0.0	0.0
606. CH ₂ (S)+NH ₂ =CH ₂ NH+H	3.00E+13	0.0	0.0
607. CH ₂ (S)+HCN=CH ₂ CN+	1.80E+14	0.0	0.0
608. CH+NH ₃ =H ₂ CN+H+H	4.40E+13	0.0	-630.0
609. CH+NH ₂ =H ₂ CN+H	3.00E+13	0.0	0.0
610. CH+NH=HCN+H	3.00E+13	0.0	0.0
611. CH+N=CN+H	1.30E+13	0.0	0.0
612. CH+NO=CO+NH	9.10E+12	0.0	0.0
613. CH+NO=NCO+H	1.80E+13	0.0	0.0
614. CH+NO=HCN+O	7.90E+13	0.0	0.0
615. CH+NO=CN+OH	1.10E+12	0.0	0.0
616. CH+NO=HCO+N	6.80E+12	0.0	0.0
617. CH+NO ₂ =HCO+NO	1.00E+14	0.0	0.0
618. CH+N ₂ O=HCN+NO	1.90E+13	0.0	-511.0
619. CH+N ₂ =NCN+H	3.70E+07	1.4	20723.0
620. C+NO=CN+O	2.00E+13	0.0	0.0
621. C+NO=CO+N	2.80E+13	0.0	0.0
622. C+N ₂ O=CN+NO	4.80E+12	0.0	0.0
623. CN+N=C+N ₂	5.90E+14	-0.4	0.0
624. C ₂ H ₆ +NH ₂ =C ₂ H ₅ +NH ₃	4.50E+01	3.5	5600.0
625. C ₂ H ₆ +CN=C ₂ H ₅ +HCN	1.20E+08	1.8	-994.0

626. $C_2H_6+NCO=C_2H_5+HNCO$	1.50E-09	6.9	-2910.0
627. $C_2H_5+N=C_2H_4+NH$	4.30E+13	0.0	0.0
628. $C_2H_5+N=CH_3+H_2CN$	2.30E+13	0.0	0.0
629. $C_2H_4+NH_2=C_2H_3+NH_3$	5.30E+12	0.0	10274.0
630. $C_2H_3+NO=HCN+CH_2O$	7.00E+21	-3.4	1025.0
631. $C_2H_2+NCO=HCCO+HCN$	1.40E+12	0.0	1815.0
632. $C_2H+NH_3=C_2H_2+NH_2$	7.20E+12	0.0	-735.0
633. $C_2H+NO=HCN+CO$	6.00E+13	0.0	570.0
634. $C_2+NO=C_2O+N$	2.30E+13	0.0	8640.0
635. $C_2+N_2=CN+CN$	1.50E+13	0.0	41730.0
636. $HCCO+N=HCN+CO$	5.00E+13	0.0	0.0
637. $HCCO+NO=HCNO+CO$	5.90E+12	0.1	-457.0
638. $HCCO+NO=HCN+CO_2$	3.70E+14	-0.8	-90.0
639. $HCCO+NO_2=HCNO+CO_2$	1.60E+13	0.0	0.0
640. $C_2O+NO=CO+NCO$	1.00E+14	0.0	670.0
641. $C_2O+NO_2=CO_2+NCO$	5.10E+13	0.0	125.0
642. $NCN+H=HCN+N$	1.00E+14	0.0	0.0
643. $NCN+O=CN+NO$	1.00E+14	0.0	0.0
644. $NCN+OH=HCN+NO$	5.00E+13	0.0	0.0
645. $NCN+O_2=NO+NCO$	4.40E+09	0.5	24580.0
646. $CH_3NH_2+M=CH_2NH+H_2+M$	2.40E+13	0.0	107260.0
647. $CH_3NH_2+H=CH_2NH_2+H_2$	5.60E+08	1.5	5464.0
648. $CH_3NH_2+H=CH_3NH+H_2$	4.80E+08	1.5	9706.0

649. $\text{CH}_3\text{NH}_2 + \text{O} = \text{CH}_2\text{NH}_2 + \text{OH}$	4.00E+08	1.5	5196.0
650. $\text{CH}_3\text{NH}_2 + \text{O} = \text{CH}_3\text{NH} + \text{OH}$	3.30E+08	1.5	6348.0
651. $\text{CH}_3\text{NH}_2 + \text{OH} = \text{CH}_2\text{NH}_2 + \text{H}_2\text{O}$	1.00E+13	0.0	0.0
652. $\text{CH}_3\text{NH}_2 + \text{OH} = \text{CH}_3\text{NH} + \text{H}_2\text{O}$	2.40E+06	2.0	447.0
653. $\text{CH}_3\text{NH}_2 + \text{CH}_3 = \text{CH}_2\text{NH}_2 + \text{CH}_4$	1.50E+06	1.9	9170.0
654. $\text{CH}_3\text{NH}_2 + \text{CH}_3 = \text{CH}_3\text{NH} + \text{CH}_4$	1.60E+06	1.9	8842.0
655. $\text{CH}_3\text{NH}_2 + \text{NH}_2 = \text{CH}_2\text{NH}_2 + \text{NH}_3$	2.80E+06	1.9	5494.0
656. $\text{CH}_3\text{NH}_2 + \text{NH}_2 = \text{CH}_3\text{NH} + \text{NH}_3$	1.80E+06	1.9	7143.0
657. $\text{CH}_2\text{NH}_2 = \text{CH}_2\text{NH} + \text{H}$	1.10E+45	-10.2	47817.0
658. $\text{CH}_2\text{NH}_2 + \text{H} = \text{CH}_2\text{NH} + \text{H}_2$	4.80E+08	1.5	-894.0
659. $\text{CH}_2\text{NH}_2 + \text{O} = \text{CH}_2\text{O} + \text{NH}_2$	7.00E+13	0.0	0.0
660. $\text{CH}_2\text{NH}_2 + \text{O} = \text{CH}_2\text{NH} + \text{OH}$	3.30E+08	1.5	-894.0
661. $\text{CH}_2\text{NH}_2 + \text{OH} = \text{CH}_2\text{OH} + \text{NH}_2$	4.00E+13	0.0	0.0
662. $\text{CH}_2\text{NH}_2 + \text{OH} = \text{CH}_2\text{NH} + \text{H}_2\text{O}$	2.40E+06	2.0	-1192.0
663. $\text{CH}_2\text{NH}_2 + \text{O}_2 = \text{CH}_2\text{NH} + \text{HO}_2$	1.00E+22	-3.1	6756.0
664. $\text{CH}_2\text{NH}_2 + \text{CH}_3 = \text{C}_2\text{H}_5 + \text{NH}_2$	2.00E+13	0.0	2702.0
665. $\text{CH}_2\text{NH}_2 + \text{CH}_3 = \text{CH}_2\text{NH} + \text{CH}_4$	1.60E+06	1.9	-626.0
666. $\text{CH}_3\text{NH} = \text{CH}_2\text{NH} + \text{H}$	1.60E+36	-7.9	36342.0
667. $\text{CH}_3\text{NH} + \text{H} = \text{CH}_2\text{NH} + \text{H}_2$	7.20E+08	1.5	-894.0
668. $\text{CH}_3\text{NH} + \text{O} = \text{CH}_2\text{NH} + \text{OH}$	5.00E+08	1.5	-894.0
669. $\text{CH}_3\text{NH} + \text{OH} = \text{CH}_2\text{NH} + \text{H}_2\text{O}$	3.60E+06	2.0	-1192.0
670. $\text{CH}_3\text{NH} + \text{CH}_3 = \text{CH}_2\text{NH} + \text{CH}_4$	2.40E+06	1.9	-1113.0
671. $\text{CH}_2\text{NH} + \text{H} = \text{H}_2\text{CN} + \text{H}_2$	2.40E+08	1.5	7322.0

672. CH ₂ NH+H=HCNH+H ₂	3.00E+08	1.5	6130.0
673. CH ₂ NH+O=H ₂ CN+OH	1.70E+08	1.5	4630.0
674. CH ₂ NH+O=HCNH+OH	2.20E+08	1.5	5404.0
675. CH ₂ NH+O=CH ₂ O+NH	1.70E+06	2.1	0.0
676. CH ₂ NH+OH=H ₂ CN+H ₂ O	1.20E+06	2.0	-89.0
677. CH ₂ NH+OH=HCNH+H ₂ O	2.40E+06	2.0	457.0
678. CH ₂ NH+CH ₃ =H ₂ CN+CH ₄	8.20E+05	1.9	7123.0
679. CH ₂ NH+CH ₃ =HCNH+CH ₄	5.30E+05	1.9	9687.0
680. CH ₂ NH+NH ₂ =H ₂ CN+NH ₃	9.20E+05	1.9	4441.0
681. CH ₂ NH+NH ₂ =HCNH+NH ₃	1.80E+06	1.9	6090.0
682. H ₂ CN=HCN+H	1.30E+29	-6.0	29894.0
683. H ₂ CN+H=HCN+H ₂	2.40E+08	1.5	-894.0
684. H ₂ CN+O=HCN+OH	1.70E+08	1.5	-894.0
685. H ₂ CN+OH=HCN+H ₂ O	2.10E+17	-1.7	318.0
Declared duplicate reaction...			
686. H ₂ CN+OH=HCN+H ₂ O	1.20E+06	2.0	-1192.0
Declared duplicate reaction...			
687. H ₂ CN+O ₂ =CH ₂ O+NO	3.00E+12	0.0	5961.0
688. H ₂ CN+NH ₂ =HCN+NH ₃	9.20E+05	1.9	-1152.0
689. H ₂ CN+NH=HCN+NH ₂	1.70E+08	1.5	-894.0
690. H ₂ CN+N=CH ₂ +N ₂	2.00E+13	0.0	0.0
691. HCNH=HCN+H	7.70E+25	-5.2	21986.0
692. HCNH+H=H ₂ CN+H	2.00E+13	0.0	0.0

693. $\text{HCNH} + \text{H} = \text{HCN} + \text{H}_2$	2.40E+08	1.5	-894.0
694. $\text{HCNH} + \text{O} = \text{HNCO} + \text{H}$	7.00E+13	0.0	0.0
695. $\text{HCNH} + \text{O} = \text{HCN} + \text{OH}$	1.70E+08	1.5	-894.0
696. $\text{HCNH} + \text{OH} = \text{HCN} + \text{H}_2\text{O}$	1.20E+06	2.0	-1192.0
697. $\text{HCNH} + \text{CH}_3 = \text{HCN} + \text{CH}_4$	8.20E+05	1.9	-1113.0
698. $\text{CH}_3\text{CN} + \text{H} = \text{HCN} + \text{CH}_3$	4.00E+07	2.0	2000.0
699. $\text{CH}_3\text{CN} + \text{H} = \text{CH}_2\text{CN} + \text{H}_2$	3.00E+07	2.0	1000.0
700. $\text{CH}_3\text{CN} + \text{O} = \text{NCO} + \text{CH}_3$	1.50E+04	2.6	4980.0
701. $\text{CH}_3\text{CN} + \text{OH} = \text{CH}_2\text{CN} + \text{H}_2\text{O}$	2.00E+07	2.0	2000.0
702. $\text{CH}_2\text{CN} + \text{O} = \text{CH}_2\text{O} + \text{CN}$	1.00E+14	0.0	0.0
703. $\text{CH}_2\text{OH} + \text{CN} = \text{CH}_2\text{CN} + \text{OH}$	5.00E+13	0.0	0.0

NOTE: A units mole-cm-sec-K, E units cal/mole